A boost current source inverter based generator-converter topology for direct drive wind turbines

by

Akanksha Singh

B.E., Bengal Engineering and Science University, 2010

AN ABSTRACT OF A DISSERTATION

submitted in partial fulfillment of the requirements for the degree

DOCTOR OF PHILOSOPHY

Department of Electrical and Computer Engineering
College of Engineering

KANSAS STATE UNIVERSITY
Manhattan, Kansas

2017

Abstract

In this dissertation, a new topology for Direct-Drive Wind Turbines (DDWTs) with a new power electronics interface and a low-voltage generator design is presented. In the presented power electronics interface, the grid - side converter is replaced by a boost Current Source Inverter (CSI) which eliminates the required dc-bus capacitors resulting in an increase in the lifetime of DDWTs. The inherently required dc-link inductor for this topology is eliminated by utilizing the inductance of the Permanent Magnet Synchronous Generator (PMSG). The proposed three-phase boost CSI is equipped with Reverse-Blocking IGBTs (RB-IGBT) and the Phasor Pulse Width Modulation (PPWM) switching pattern to provide a 98% efficiency and high boost ratios (V_{LL}/V_{dc}) up to 3.5 in a single stage. In this dissertation, Phasor Pulse Width Modulation (PPWM) pattern for the boost – CSI is also modified and verified through simulation and experimental results. In order to realize potential capabilities of the boost inverter and to assist its penetration into renewable energy systems, the boost inverter dynamic behaviors are studied in this dissertation. Then, the developed models are verified using circuit simulations and experiments on a laboratory-scale boost – CSI equipped with RB-IGBTs. The developed dynamic models are used to study the stability of the boost – CSI through root locus of small signal poles (eigenvalues) as control inputs and load parameters vary within the boost inverter's operating limits. The dynamic models are also used to design the control schemes for the boost – CSI

for both stand-alone and grid-tied modes of operation. The developed controllers of the boost – CSI are verified through simulation and experimental results. In this dissertation, the boost – CSI steady-state characterization equations are also developed and verified. The developed boost – CSI is used to replace the grid - side converter in a DDWT. A reliability analysis on the power electronics interface of an existing and developed topology is presented to demonstrate the increase in the mean time between failures. The boost – CSI enables conversion of a low dc voltage to a higher line-to-line voltage enabling the implementation of a low-voltage generator. This further enables a reduction in the number poles required in DDWT generators. The feasibility of the presented low-voltage generator is investigated through finite element computations. In this dissertation, a 1.5MW low-voltage generator designed for the proposed topology is compared with an existing $1.5\,MW$ permanent magnet synchronous generator for DDWTs to demonstrate the reduction in the volume, weight, and amount of permanent magnet materials required in the generator. The feasibility of the developed system is supported by a set of MATLAB/Simulink simulations and laboratory experiments on the closed-loop stand-alone and grid-tied systems.

A boost current source inverter based generator-converter topology for direct drive wind turbines

by

Akanksha Singh

B.E., Bengal Engineering and Science University, 2010

A DISSERTATION

submitted in partial fulfillment of the requirements for the degree

DOCTOR OF PHILOSOPHY

Department of Electrical and Computer Engineering
College of Engineering

KANSAS STATE UNIVERSITY
Manhattan, Kansas

2017

Approved by:

Major Professor
Dr. Behrooz Mirafzal

Copyright

© Akanksha Singh 2017.

Abstract

In this dissertation, a new topology for Direct-Drive Wind Turbines (DDWTs) with a new power electronics interface and a low-voltage generator design is presented. In the presented power electronics interface, the grid - side converter is replaced by a boost Current Source Inverter (CSI) which eliminates the required dc-bus capacitors resulting in an increase in the lifetime of DDWTs. The inherently required dc-link inductor for this topology is eliminated by utilizing the inductance of the Permanent Magnet Synchronous Generator (PMSG). The proposed three-phase boost CSI is equipped with Reverse-Blocking IGBTs (RB-IGBT) and the Phasor Pulse Width Modulation (PPWM) switching pattern to provide a 98% efficiency and high boost ratios (V_{LL}/V_{dc}) up to 3.5 in a single stage. In this dissertation, Phasor Pulse Width Modulation (PPWM) pattern for the boost – CSI is also modified and verified through simulation and experimental results. In order to realize potential capabilities of the boost inverter and to assist its penetration into renewable energy systems, the boost inverter dynamic behaviors are studied in this dissertation. Then, the developed models are verified using circuit simulations and experiments on a laboratory-scale boost – CSI equipped with RB-IGBTs. The developed dynamic models are used to study the stability of the boost – CSI through root locus of small signal poles (eigenvalues) as control inputs and load parameters vary within the boost inverter's operating limits. The dynamic models are also used to design the control schemes for the boost – CSI

for both stand-alone and grid-tied modes of operation. The developed controllers of the boost – CSI are verified through simulation and experimental results. In this dissertation, the boost – CSI steady-state characterization equations are also developed and verified. The developed boost – CSI is used to replace the grid - side converter in a DDWT. A reliability analysis on the power electronics interface of an existing and developed topology is presented to demonstrate the increase in the mean time between failures. The boost – CSI enables conversion of a low dc voltage to a higher line-to-line voltage enabling the implementation of a low-voltage generator. This further enables a reduction in the number poles required in DDWT generators. The feasibility of the presented low-voltage generator is investigated through finite element computations. In this dissertation, a 1.5MW low-voltage generator designed for the proposed topology is compared with an existing $1.5\,MW$ permanent magnet synchronous generator for DDWTs to demonstrate the reduction in the volume, weight, and amount of permanent magnet materials required in the generator. The feasibility of the developed system is supported by a set of MATLAB/Simulink simulations and laboratory experiments on the closed-loop stand-alone and grid-tied systems.

Table of Contents

List of Figures

List of Tables

Acknowledgments

This dissertation is a huge accomplishment and it would not have been possible without the support, guidance, and motivation received from several people. I would like to thank my parents for their constant encouragement, support and endurance during the course of this dissertation. I would also like to thank my brother, Shubham for his support. I sincerely thank my family for believing in me and encouraging me all the way to the end. My own success is a reflection of the love and support they have given me throughout my life.

I would like to express my heartfelt gratitude and appreciation to my advisor, Dr. Behrooz Mirafzal for trusting my abilities and his constant motivation. I sincerely thank him for his guidance, encouragement, constructive criticism, and patience throughout this work which has lead to this achievement. Dr. Mirafzal spent countless hours helping me with research and writing papers. This dissertation would not have been possible without his help and advice.

I would like to express my sincere thanks to Dr. Anil Pahwa, Dr. Noel Schulz, and Dr. Warren White for serving on my dissertation committee and providing valuable suggestions. I appreciate their participation and enthusiasm to be a part of my dissertation committee.

I would like to thank my friends Mr. Jacob Lamb and Mr. Aswad Adib for all their help and discussions on the research topic. I would also thank them for their patience

when I bothered them time and again.

I would like to thank my friend Mr. Vivek K. Singh for his unconditional support throughout this endeavor. I will also express thanks to my friends Tania, Shailaja, and Avantika for their care and support throughout.

Dedication

To my parents...

Chapter 1

Introduction

This chapter provides an introduction to the dissertation. The motivations and objectives of the proposed generator-converter topology for the Direct-Drive Wind Turbines (DDWTs) are discussed in this chapter. The state-of-the-art DDWTs are also reviewed as a background for presenting contributions of the dissertation in this chapter. This chapter contains three sections. Section 1.1 presents the motivations and objectives of the presented research. The literature review providing a background about the existing state of the art technology is presented in Section 1.2. Finally, the contributions made in this dissertation are presented in Section 1.3.

1.1 Motivations and Objectives

The continuous growth in the energy demand around the globe, and the limited availability of fossil fuels along with the increased awareness in the society about the impact of these fossil fuels on the environment has resulted in exploring of the renewable energy sources (for e.g., photovoltaic cells). Nowadays, renewable energy resources such as photovoltaic panels and wind turbines play an important role in the electric power

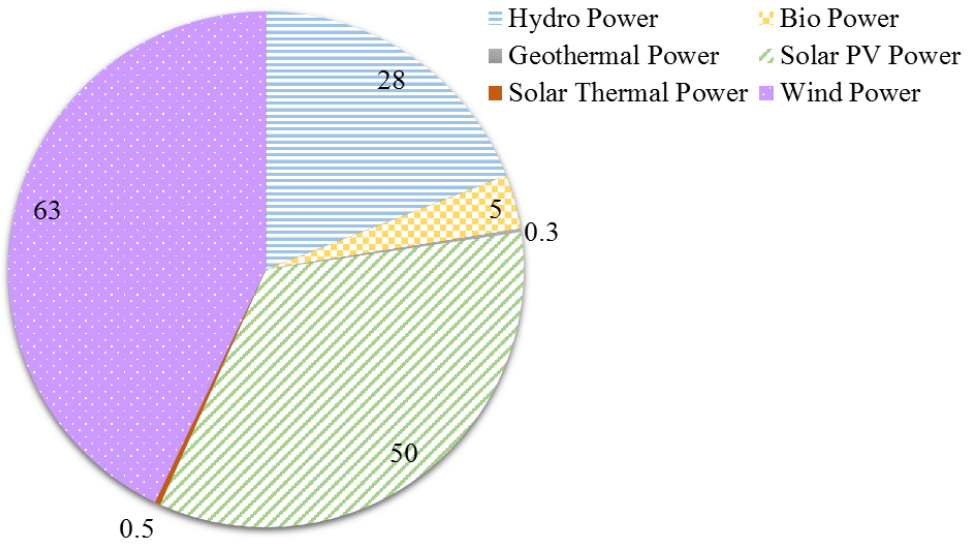

Fig. 1.1: Increase in installed capacity of renewable energy system in 2015 [1].

generation system. Connecting these energy resources to the power grid helps reduce the dependency of the electric grid to the price and availability of fossil fuels. Furthermore, sustainable energy sources have attracted the attention of many societies because the generated power is environmentally friendly, and the sources are not subject to the instability of price and availability that are typical of conventional energy sources such as oil, natural gas, etc. Advancements in sustainable energy technologies such as in photovoltaic panels, wind generators, fuel cells and energy storage devices, are increasing the penetration of distributed generation into the existing energy infrastructure. Wind power is the fastest growing renewable energy resource nationally and globally. Over the past decade, the global capacity of wind energy has increased from 30 GW to 300 GW [1], that is approximately equal to more than 200,000 new wind turbines in the energy infrastructure. In 2012, the United States increased its wind energy capacity by 60GW, exceeding natural gas for the first time ever [1]. 60 GW is enough to power the equivalent of 15.2 million U.S. homes. The increase in global renewable energy installed capacity for the year 2015 is shown in Figure 1.1. As

can be seen in Figure 1.1, wind power generation, and photovoltaic power generation installed capacity increased by 63GW and 50GW, respectively. Wind energy system and photovoltaic energy system are the major growing renewable energy conversion systems. However, while the energy produced by them is in a form that cannot be directly connected to the power grid, power electronics interface circuits are required to convert their output to a compatible form with the electric grid and local loads. Solid-state device based converters are used as an interface between sustainable energy sources and the grid. In the past several decades, primary advances in power converters have been achieved because of new semiconductor materials and high-speed solid-state switches. As a result, solid-state converters have become the enabling technology to realize a wide range of critical technologies, such as fuel-cells, wind and solar energy conversion systems [2–6].

1.1.1 Reliability of the Power Electronics Interface in DDWTs

Renewable energy technologies are clean energy sources that have a very low environmental impact as compared to conventional fossil fuel-based energy sources. These technologies produce power in the form which cannot be directly connected to the grid or local load and require an interface for converting the available power to a grid-compatible form. Such power conversion is obtained through solid-state based power converters. The primary advances in power converters that have been achieved by new semiconductor materials and high-speed solid-state switches have resulted in solid-state converters becoming one of the most crucial parts to execute many technologies, such as solar or wind energy conversion systems.

In most renewable energy conversion systems, either a low dc voltage provided from the source must be typically boosted and converted to an ac voltage with a fixed frequency and fixed amplitude or a variable frequency ac input is converted to dc-voltage

and the dc voltage is then converted to a symmetrical three-phase ac output. The power electronics interface in most wind turbines consists of a rectifier, an inverter, and an energy stored element, which is generally a dc-bus buffer formed by electrolytic capacitors [7, 8]. For DDWTs, the back-to-back converter is the most failure prone component [9–12]. However, the point of failure within this power electronics interface is well known; electrolytic capacitors failures can account for over 60% of failures in power electronics interfaces [13, 14]. Many complex methods which try to determine the remaining lifespan of electrolytic capacitors exist [15–17], but these methods do not serve to extend the life of the capacitors. Thus, although faults become more predictable using these methods, the capacitors must still be manually replaced, resulting in high maintenance costs. Furthermore, the methods used to determine the remaining lifespan of electrolytic capacitors require the use of expensive monitoring systems [16], and so any system which uses electrolytic capacitors is expensive to monitor, maintain, and has a shorter life span than a system which does not use these capacitors. The failure of these electrolytic capacitors determines the frequency of maintenance and thus adds to the system operation and maintenance costs. Therefore, a converter which can eliminate the need of dc-bus electrolytic capacitors will not only increase the system lifetime but will also reduce the operation and maintenance costs associated with them. Furthermore, elimination of failure-prone components without any additional component in the system will result in low Mean Time Between Failure for the system and will increase the system availability by reducing the system downtime. The next subsection presents the capital cost reduction for the proliferation of DDWTs.

1.1.2 Capital Cost of PM Generator in DDWTs

The past decade has seen remarkable growth in the installed renewable power capacity [18]. The Global Wind Energy Council has reported an increase in the global wind

installed capacity from 237.7 GW in 2011 to 493.3 GW in 2016 [1]. The developments in the wind energy conversion systems show an inclination to using high power rated wind turbines [19]. In recent decades, several wind turbine generator concepts were aimed to maximize the production of energy, reduce costs, and improve power quality. For these reasons, it has become popular to place wind farms offshore. Offshore wind turbines require new, precise design rules which take into account the particular operating specifications. A generator-converter system which eliminates the weak links (e.g. requirement of the gearbox, the electrolytic capacitors), and operates on lower dc voltage to produce the same three phase voltage output would be a robust and reliable wind energy system. The most commonly used system is a variable speed wind turbine. A variable speed wind turbine uses a Doubly-Fed Induction Generator (DFIG) whereas a fixed speed wind turbine either uses a Squirrel Cage Induction Generator (SQIG) or a Permanent Magnet Synchronous Generator (PMSG). One of the problems associated with DFIG and SQIG based wind power generation system is the presence of a gearbox, which couples the wind turbine to the generator. Gearbox faults lead to significant downtime, cause noise and vibration, and require regular maintenance [9–11]. It is worth noting that, although responsible for 20% of total wind turbine downtime, gearboxes only account for 10% of wind turbine failures [9–11]. This discrepancy is due to the fact that the bulk of gearbox failures necessitate an entire gearbox replacement, a feat which requires the use of heavy machinery and significant manpower [9]. Thus, although gearboxes are fairly reliable, failures which do occur are expensive, both in terms of repair costs and production losses. Many efforts have been made to increase the reliability of gearboxes by determining when preventive maintenance is required. These efforts, however, often require the use of expensive sensors, and retrofitting existing gearboxes is costly if it can be done at all [10]. Therefore, for many turbines especially those which are located in remote areas or offshore where maintenance fees

increase drastically, the ideal solution is to remove the gearbox altogether. Compared with gearbox coupled wind turbine generator, direct-drive PM generator has received more and more attention in wind energy application because of its self-excitation, simple structure, and high efficiency [20, 21]. There is a definite trend toward DDWTs as is predicted in the research papers and trade journals but there are some major concerns that must be overcome in order to achieve higher market penetration [19, 22]. The major concern which prevents the popularization of DDWTs is the large size of the PM generator [23, 24]. The large size of the generator is a result of the generator shaft rotating at the same speed as the turbine rotor shaft. Another reason which leads to the huge size of the PMSG is the high voltage output requirement from the power electronics interface. The commonly used power electronics interface in DDWTS when generating $690\,V$ rms line-to-line voltage at the output requires about $770\,V$ rms line-to-line voltage from the PMSG. The number of poles in the PMSG for this configuration is very high, in order to increase the frequency and magnitude of the generator output voltage. This high voltage requirement from the PMSG results in large diameter and size of the PMSG and consequently a high cost and volume for the generator. Even though PMSG based DDWTs feature high efficiencies, a 10 MW PMSG is more than 10m in diameter and weighs more than 300 tons [25]. The huge size and cost of permanent magnet materials result in high capital costs of DDWTs, decelerating their proliferation in comparison with DFIG - based wind turbines.

A topology for DDWTs with reduced volume and weight of the PMSG and high reliability will have a huge impact on the popularization of DDWTs. This research presents a new topology for the power electronics converter for DDWTs which eliminates the failure prone components and results in a reduction in the volume and weight of the generator. The existing state-of-the-art power converter topologies and wind turbine topologies are discussed in the next section.

1.2 Literature Review

In this section, the existing state-of-the-art solutions to the problems discussed in the previous section are presented. Firstly, existing wind turbine topologies and the issues associated with them are elaborated. Next the alternatives for the boost - CSI are discussed along with its technical challenges.

1.2.1 Wind Turbine Topologies

The variable speed wind turbines are commonly categorized into Indirect Drive Wind Turbines (IDWTs) and DDWTs. In IDWTs, the low-speed shaft is connected to the high-speed shaft through a gearbox, whereas DDWTs have a low-speed shaft that is directly connected to the generator [26]. The two most commonly used topologies for wind turbines are based on Doubly Fed Induction Generator (DFIG) or Permanent Magnet Synchronous Generator (PMSG) [26]. In DFIG configuration, the stator of the generator is directly connected to the grid while the rotor does not require to rotate at the fixed synchronous speed. The rotor is connected to the turbine shaft through a gearbox. In PMSG based wind turbines, the speed of the rotating magnetic field and the rotor is the same, and therefore, the generator must be connected to the grid through a power electronics interface. In other words, the PMSG based wind turbines require a power electronics interface to be connected to the grid which provides the flexibility of using these turbines with or without gearbox between the turbine shaft and the generator shaft [26]. The commonly used topologies of IDWTs and DDWTs are discussed in the following.

In IDWTs the rotor shaft is connected to the generator through a gearbox [27, 28]. These turbines have different topologies based on the type of generator and converter used for the wind power conversion. Figure 1.2 shows different topologies of IDWTs.

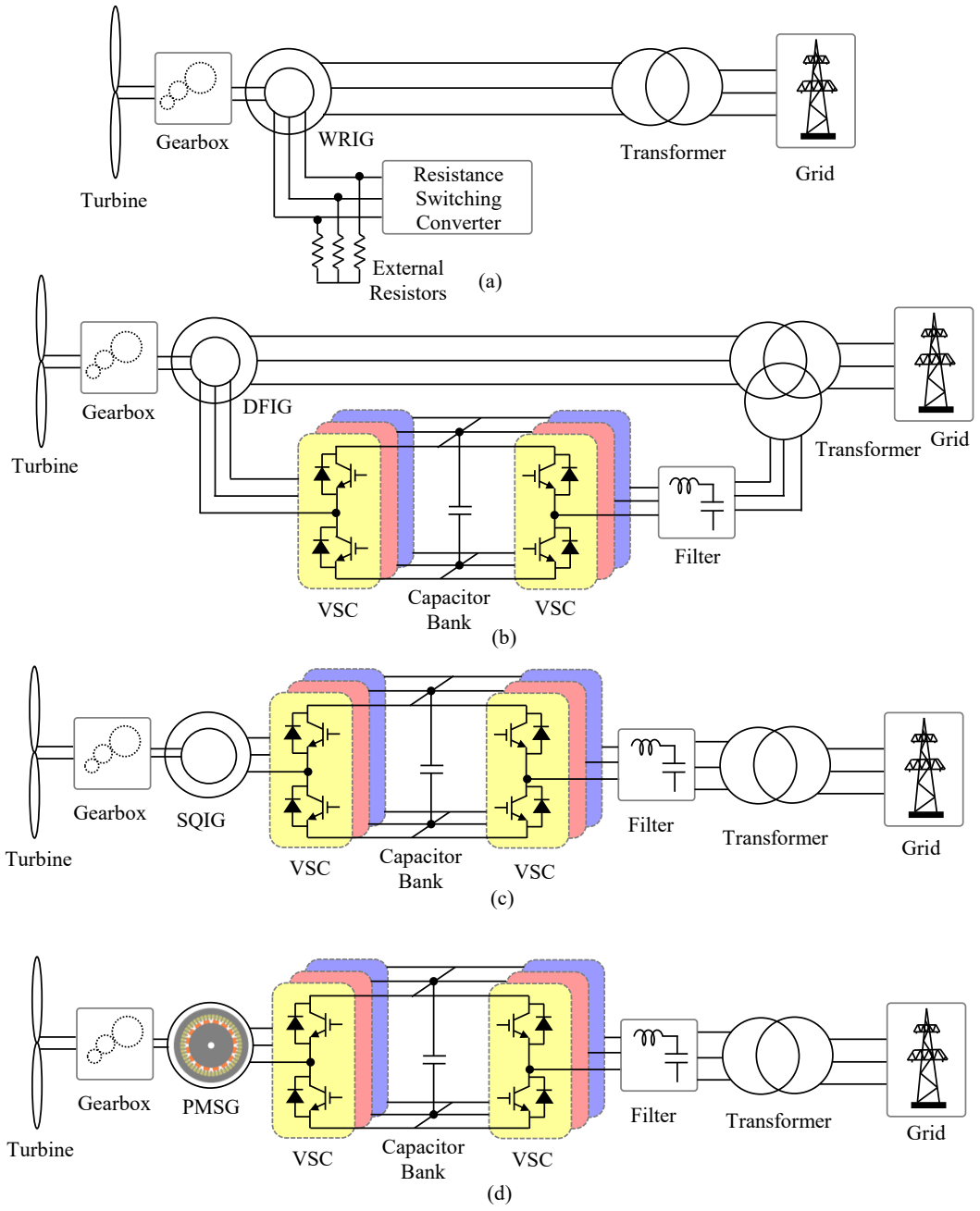

Fig. 1.2: Wind turbine system topologies for IDWTs with (a) WRIG and rotor resistance control, (b) DFIG with partly rated back-to-back VSCs for rotor connection to grid, (c) SQIG with fully rated back-to-back VSCs, and (d) PMSG with fully rated back-to-back VSCs.

Figure 1.2(a) shows an IDWT topology with a Wound Rotor Induction Generator (WRIG) with rotor resistance controller. In this topology, the output is controlled by varying the slip through variation in rotor resistance [29]. This rotor resistance is varied using the converter. Figure 1.2(b) shows an IDWT topology with DFIG. In this system, the stator of the induction generator is connected directly to the grid and the rotor feeds power to the grid through the power electronic converters. The power electronic interface between the rotor and the grid comprises of a two bidirectional converters connected at the dc-bus, formed by electrolytic capacitors. In the system shown in Figure 1.2(b), the power converters are not rated for full power transfer and they share only a fraction of the power produced. Figure 1.2(c) shows an IDWT topology with squirrel cage induction generator connected to the power electronic interface, which comprises of the back-to-back Voltage Source Converters (VSC). Unlike the system in Figure 1.2(b) the power converters for this system are rated for the full power, i.e. the full power is transferred to grid through the converters. Figure 1.2(d) shows IDWT system with a PMSG and a back-to-back VSC as the power electronic interface. In addition to the previously mentioned topologies, IDWT with wound field synchronous generator can be used with back-to-back VSCs. In this type of IDWT, an additional ac-dc converter, powered from the grid is needed to energize the air-gap magnetic field of the generator. It has been shown that the gearbox causes more downtime than any other component in an indirect drive wind turbine [9, 10, 26]. It is worth noting that, although gearboxes are responsible for 20% of total wind turbine downtime, they only account for 10% of wind turbine failures [9–11]. Recent investigations reveal that gearboxes in wind turbines, which were supposed to last 20 years, might fail in 7-10 years [12, 30]. As a result, wind farm operators may face huge potential costs to fix their turbines in the near future. The solution to the problem is to get rid of the gearbox through the deployment of DDWTs [19].

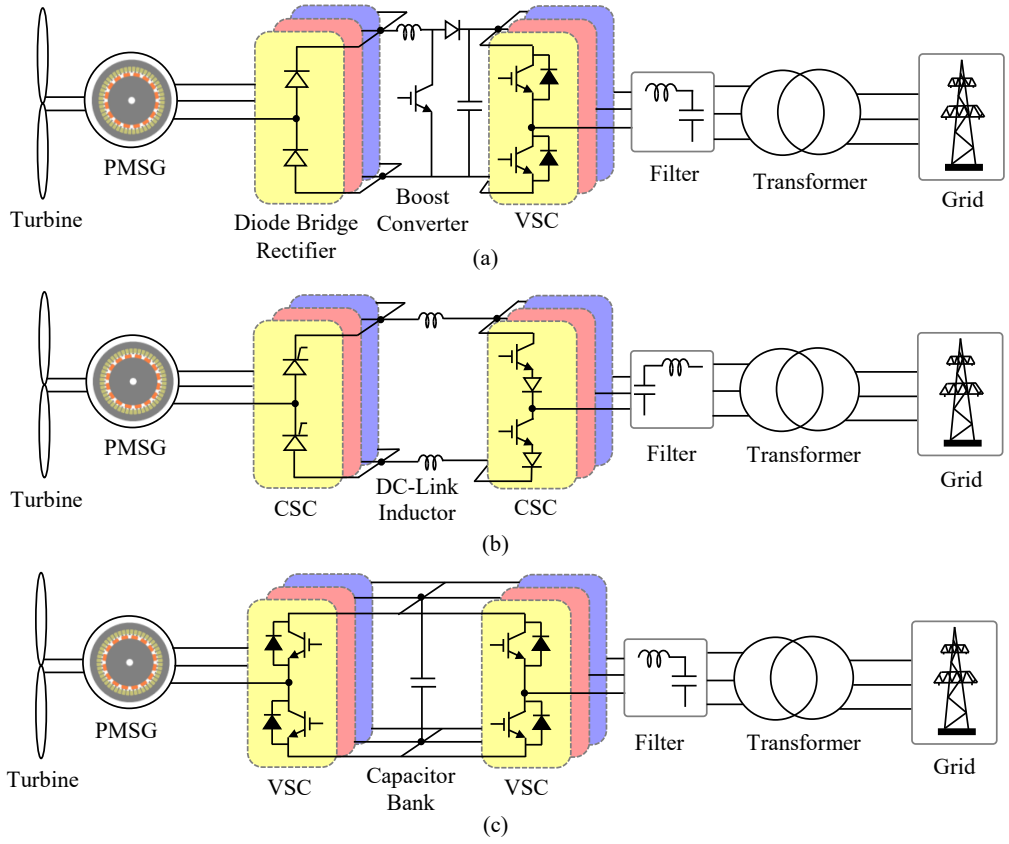

Fig. 1.3: Wind turbine system topologies for DDWTs with (a) PMSG connected to diode-bridge, boost converter and VSI, (b) PMSG connected to back-to-back CSCs, and (c) PMSG connected to back-to-back VSCs.

In DDWTs, the turbine rotor shaft is directly connected to the generator shaft, and there is no gearbox employed. Figure 1.3 shows different topologies of DDWTs. Figure 1.3(a) shows a DDWT topology with a PMSG with the power electronics interface. The power electronic interface consists of a diode bridge rectifier, a dc-dc boost converter to stabilize the dc-bus voltage, and a VSI [28, 31]. The power electronics interface is rated for full power. Another DDWT topology is shown in Figure 1.3(b) with power electronics interface consisting of back-to-back connected Current Source Converters (CSC). The generator is a multi-pole PMSG. The dc-link between the CSCs has dc-link inductors in order to have a constant current input to the second CSC [32]. Figure 1.3(c) shows the most frequently used configuration of DDWTs, comprising of PMSG connected to the grid through back-to-back connected VSCs [28, 31]. The dc-bus between the VSCs is formed by electrolytic capacitors in order to have a stable and constant dc-bus voltage. In some cases, the power electronics interface can be a back-to-back connection of multilevel converters as discussed in the previous subsection. In some DDWT applications, a wound rotor synchronous generator is used [27]. An additional ac-dc converter, which is powered by the grid, is needed to power the field of the generator. All the DDWTs discussed above either have a dc-bus formed by electrolytic capacitors or have a dc-link with inductors. The electrolytic capacitors are one of the most failure-prone components and decrease system reliability [9]. The power electronics interface is one of the most vulnerable components in wind turbines [9, 12], with the electrolytic capacitors known as the cause of more than 50% of failures [16, 33]. Many sophisticated methods which try to determine the remaining lifespan of electrolytic capacitors exist, but these methods do not serve to extend the life of the capacitors [16]. The failure of these capacitors can have a huge impact on the system maintenance costs especially in the case of offshore wind turbines [34]. The dc-link inductors are bulky and add to the system loss reducing its efficiency [34]. In some

cases, the grid side converter located away from the wind turbine and the transmission cable is used to realize the dc-link inductor [35]. Additionally, elimination of gearbox in the DDWTs leads to an increase in the size of PMSG, and thus, an increase in the capital cost of the overall system [34–37]. The other major concern which prevents the popularization of DDWTs is the large size of the PM generator [23, 24]. The large size of the generator is a result of the generator shaft rotating at the same speed as the turbine rotor shaft. The number of poles in the PMSG for this configuration is very high to increase the frequency of the generator output voltage and current waveforms. The increase in the number of poles means increase in the PM material required. The PM material are rare earth metals which are expensive and the high number pf poles further results in increasing ye cost and volume of the generator.

1.2.2 Power Electronics Interface Topologies

The incorporation of solid-state power converters in wind energy conversion systems has increased over the past decade in order to improve control of the wind turbine and to improve its interconnection issues with the grid [28]. These power converters are also used to control the active and reactive power injected into the grid. The power converters used in wind energy conversion systems can be rated for full power transfer or for partial power transfer depending upon the type of wind turbine. In this subsection, the different configurations of three-phase power converters that are used in wind turbines are described.

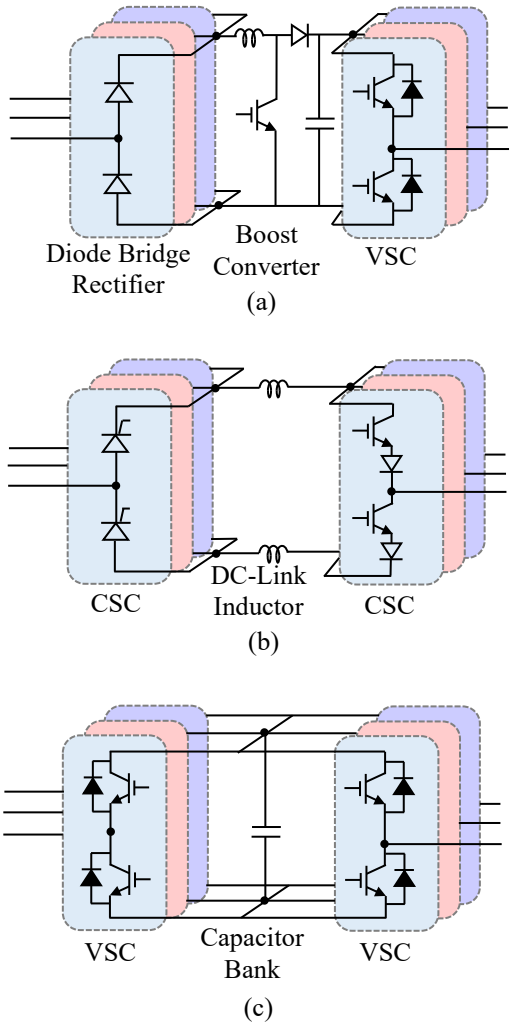

Fig. 1.4: Commonly used three-phase two-level back-to-back power converter topologies for energy conversion in wind energy conversion systems.

The most common two-level power converter topologies used for three-phase power transfer are presented in Figure 1.4. Figure 1.4(a) presents a topology with a three-phase diode bridge rectifier as the generator side converter which is cascaded with a boost dc-dc converter [6]. These converters rectify the generator voltage and boost it to the desired dc-bus voltage. The dc-bus formed by electrolytic capacitors is then connected to a three-phase two-level VSC. The drawbacks of this converter topol-

ogy is the distortion of the generator output current that results in the low-frequency torque pulsations at the generator shaft [8]. Furthermore, the dc-bus is formed using electrolytic capacitors, which are the most failure prone component for any power converter [16]. The next commonly used back-to-back converter topology used in wind energy conversion systems is shown in Figure 1.4(b). This topology is formed by a cascaded connection of Current Source Converters (CSCs), connected through dc-link inductors. This topology helps to eliminate the failure prone dc-bus capacitors but introduces another component, i.e. the dc-link inductors, which are bulky and contribute to losses in the system, reducing the overall system efficiency. The most commonly used two level back-to-back converter topology is presented in Figure 1.4(c). This topology is formed by a back-to-back connection of VSCs and electrolytic capacitors at the common dc-bus. This topology helps to eliminate the low-frequency torque pulsations at the generator shaft but still has the failure prone component. The topologies discussed so far are two-level power converters and when used for MW range of power conversion cause very high $\frac{dv}{dt}$ stress at the generator and transformer, and would require bulky filters in order to reduce this high $\frac{dv}{dt}$ stress. For high power wind turbines (multi-MW power range), multilevel power converter topologies are used in wind energy conversion systems.

Figure 1.5 shows the multilevel power converter topologies used in wind energy conversion systems. Figure 1.5(a) shows a three-level Neutral-Point diode Clamped (NPC) back-to-back converter topology. This topology adds another voltage level as compared to the two-level topologies discussed earlier in this section. the multilevel structure helps in reducing the $^{dv}/_{dt}$ stress on the IGBTs and further aids in the reduction of the size of the output filter. Even though it is a very commonly used topology, the frequently failing capacitor bank still exists in this topology and its failure rate is high due to midpoint voltage fluctuation at the diode clamp [38]. Another commonly

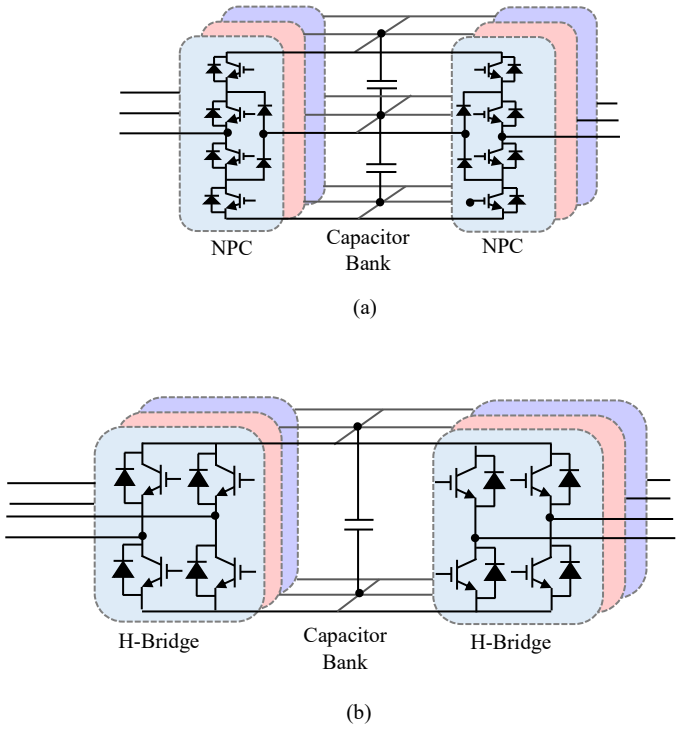

Fig. 1.5: Commonly used three-phase multilevel back-to-back power converter topologies for energy conversion in wind energy conversion systems.

used topology is the three-phase three-level H-bridge back-to-back converters shown in Figure 1.5(b). This topology eliminates the problems of dc-bus midpoint voltage fluctuations and has smaller dc-bus capacitors as compared to the NPC topology, but still employs the failure prone electrolytic capacitors to from the dc-bus. Another power converter topology is five-level NPC converter, formed by back-to-back connected five-level NPC converter which is connected at the dc-bus formed by electrolytic capacitors [39]. Similarly, back-to-back connected five-level H-bridge converters are also used in wind energy conversion systems [40]. Some wind turbines also use the back-to-back connection of a three-level NPC converter and a five-level H-bridge converter, connected at the dc-bus formed by electrolytic capacitors [41]. All the multilevel power

converters used in wind turbines comprise of a dc-bus which is formed by electrolytic capacitors that adversely affects the system reliability and adds to the system operation and maintenance costs.

1.3 Contributions of the Dissertation

The most commonly used wind turbine topologies are the IDWTs which require gearboxes. As discussed earlier, gearboxes are not the most frequently failing component but are definitely the most expensive failure associated with an IDWT. The cost associated with gearboxes is not just component cost but also the system downtime costs. This results in a very high operation and maintenance costs associated with the IDWTs. These costs will be even higher if the wind turbine is an offshore wind turbine [34]. Additionally, elimination of gearbox in the DDWTs leads to increase in the size of PMSG leading to an increased capital cost associated with them [34–37]. These issues exist due to buck nature of VSI and the low-speed input for DDWTs. This dissertation proposes a new generator - converter topology for DDWT which facilitates elimination of the failure prone component and reduction in the size of the PMSG. The main contributions of this dissertation are presented as follows:

- This dissertation proposes a new generator-converter topology for DDWTs, which eliminates the failure prone dc-bus electrolytic capacitors increasing the overall system lifetime and eliminates the dc-link inductor by utilizing the synchronous inductance of the PMSG.

- This dissertation proposes a three-phase boost - CSI as the grid-side converter for DDWTs. This converter is capable of converting a low-voltage dc-input to a higher three-phase ac voltage with boost ratio ($V_{LL,rms}/V_{dc}$) ranging up to 3.5

- A low-voltage PMSG for the proposed topology is designed which helps in reducing the weight and volume of the generator and reduces the amount of PM material required by the generator.
- The presented topology is verified through simulation and experimental results, in this dissertation.

This dissertation presents the topology, switching technique, dynamic models, control techniques, steady-state characterization of the developed converter. Furthermore, a low-voltage PMSG is required by the developed topology which helps in reducing the weight and volume of the generator and reduces the amount of PM material required by the generator.

1.4 Organization of the Dissertation

The rest of the dissertation is organized as follows:

Chapter 2 presents the proposed topology of the DDWT using the boost - CSI. The advantages of using the boost - CSI are discussed. A reliability analysis is done on existing DDWT power electronics interface and developed system to demonstrate the increase in mean time between failure. This chapter also presents the design of a low voltage PMSG for the developed topology of DDWTs. In this chapter, the designed generator is compared with an existing DDWT generator in order to emphasize the reduction in size and weight of the PMSG which is possible through the developed topology. The feasibility of the developed topology is also verified using simulation results.

The topology and switching pattern for the developed three-phase power converter is presented in Chapter 3. First, the old switching technique is reviewed and then the

modified switching technique is presented. The advantages achieved through the modified switching pattern are demonstrated through simulation and experimental results. This chapter also presents the steady state characterization of the boost - CSI. The expressions for the inverter output current, the fundamental component of the inverter output current, the ac-side voltage referred to the dc-bus, and the minimum dc-link inductance required to keep the inverter in continuous conduction mode are derived in this chapter. These equations are then verified through circuit simulations and experimental results on a laboratory scale setup for both stand-alone and grid-tied modes of operation. This chapter also presents the PQ operating region for the developed converter. A laboratory scale 2kW prototype of the boost - CSI is characterized and its efficiency and performance are compared to existing boost inverters.

Chapter 4 presents the large - signal and small - signal dynamic models for the stand - alone and grid - tied operating mode. These models are verified through circuit simulations and experimental results on the laboratory scale setup. The developed dynamic models are then used to assess the stability of the developed converter for variation in input parameters and output load conditions. The dynamic models for the stand-alone operating boost - CSI are used to design the controller for the output voltage regulation. The dynamic model for the grid - connected boost CSI is used to develop controllers for regulating active and reactive power injected into the grid and to ensure stable operation of the converter.

Chapter 5 presents details of the controllers for the developed topology of the generator - converter. The operation and function of the controllers for the back-to-back converters are explained. The performance of the developed controllers is also verified in this chapter through simulation results.

Chapter 6 presents details of the experimental setup developed for the verification of the proposed topology. This chapter also presents experimental results demonstrating

the feasibility and quality of output waveforms obtained from the system for stand-alone and grid-tied modes of operation.

Chapter 7 presents the summary of this research along with the significant contributions of this dissertation. This chapter also provides suggestions for future work on designing and optimizing a laboratory scale prototype of the entire DDWT system in order to showcase the developed technology to wind turbine manufacturers.

Chapter 2

Proposed DDWT Topolgy

In this chapter, the topology of the proposed DDWT and its power electronics interface are presented. Section 2.1 introduces the topology of the developed DDWT with details on the configuration of the power electronics interface between the PMSG and the grid transformer. Section 2.2 presents a reliability analysis of the traditional power electronics interface and the developed topology and compares the Mean Time Between Failure (MTBF) of the two topologies. Finally, Section 6.3 ends the chapter with concluding remarks.

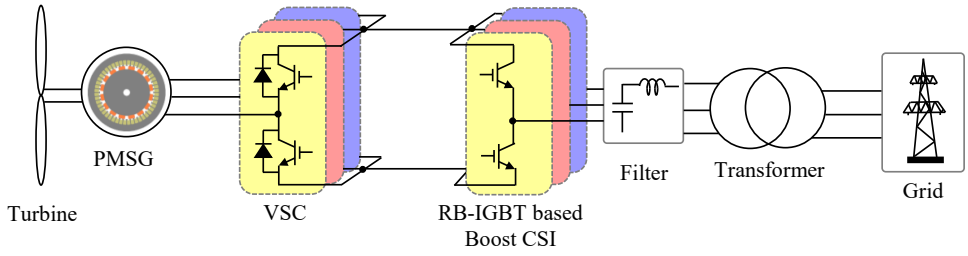

Fig. 2.1: The proposed DDWT topology with the PMSG connected to a back-to-back connected VSC and the boost - CSI equipped by RB-IGBTs.

2.1 Topology of the Developed DDWT System

The developed topology for the DDWTs is presented in Figure 2.1. In this wind turbine system, the rotor is connected directly to the PMSG. The turbine injects power to the grid through a fully rated power electronics interface, as can be seen in Figure 2.1. In this section, different parts of the developed topology for DDWTs are explained. Firstly, the power electronics interface topology is presented along with the expression for minimum per phase inductance required from the PMSG for acceptable performance of the boost-CSI. Next, the flexibility provided by this power electronics interface in the design of the PMSG is explained and the generator is elaborated upon.

2.1.1 Power Electronics Interface

The power electronics interface in the developed topology comprises a cascaded connection of a three-phase VSC and a boost - CSI as shown in Figure 2.1. In this system, the grid side VSI used in the traditional power electronics interface is replaced by boost - CSI equipped by Reverse Blocking IGBTs (RB-IGBT). It should be noted that in this topology there is no dc-bus capacitor or dc-link inductor required to form the dc-bus. A boost - CSI is modulated using the Phasor Pulse Width Modulation (PPWM) switching technique, which enables it to convert a low voltage dc-input to a higher rms line-to-line three phase ac-voltage in a single stage with a boost ratio of up to three [42–45], whereas a traditional CSI operated using space vector PWM switching provides a maximum boost ratio of about 1.2 [46]. Additionally, a boost - CSI requires a dc-link inductor [42–45]. The developed system, which is shown in Figure 2.1 eliminates the dc-link inductor needed in a conventional CSI. This inductor can be eliminated by designing the PMSG such that the generator synchronous inductance, L_s, can be used as a replacement for the dc-link inductor. In order to achieve a low To-

tal Harmonic Distortion (THD) of the inverter output voltage and current waveforms, the boost - CSI must operate in Continuous Conduction Mode (CCM). The minimum dc-link inductance, L_{dc} required to keep the inverter in CCM has been derived in in this work as will be given in Chapter 3. The computed value of the minimum inductance dc-link inductor is typically around the synchronous inductance of the generator, L_s. The low dc-side voltage required by the boost - CSI enables the design of a low voltage PMSG. The advantages gained by using a low voltage generator is discussed in the next subsection.

2.1.2 PM Synchronous Generator

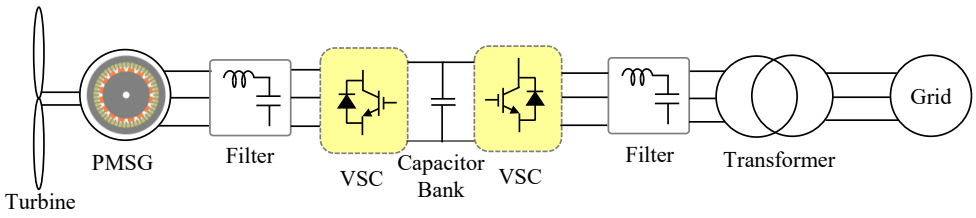

Fig. 2.2: Most common DDWT topology with the PMSG connected to back-to-back VSCs.

The developed power electronics interface provides design flexibility for the PMSG design by enabling the use of a low-voltage generator. The boost - CSI, as described above can convert a low dc-voltage to a three-phase ac-voltage with a boost ratio of over three [42, 45], for acceptable level of efficiencies, where boost ratio can be defined as

$$Boost\ Ratio = \frac{V_{LL,rms}}{V_{dc}} \tag{2.1}$$

for just the inverter and

$$Boost\ Ratio = \frac{V_{LL,rms}^{grid}}{V_{LLrms}^{generator}} \tag{2.2}$$

for a wind energy conversion system. The low dc-side voltage required by the boost - CSI further enables a low output ac-voltage from the PMSG. In a traditional DDWT topology, (as shown in Figure 2.2), in order to generate rms line-to-line voltage of $480V$ at the inverter output, about similar voltage needs to be generated at the PMSG output terminal [47–49]. If the developed topology is utilized, then rms line-to-line voltage of about $120V$ from the PM generator is sufficient to generate rms line-to-line voltage of $480V$ at the boost - CSI output. A PMSG emf equation can be expressed as $E \propto \phi N_T n_{rpm} p$ where, E is the per phase peak induced voltage, ϕ is the magnetic flux per pole, N_T is the number of turns, n_{rpm} is the speed of the generator in RPM, and p is the total number of poles [49]. The ϕ and n_{rpm} are governed by the PM material of the poles, stator construction, and the wind speed which results in $E \propto N_T p$. Therefore, for the same output power from the system, a lower output voltage required from the generator results in a lower value of $N_T p$. The reduction in the value of N_T gets limited by the minimum inductance requirement computed in (3.30), but it still allows for the reduction of number of poles in the PMSG. Furthermore, a decrease in the number of poles results in a reduction in the amount of PM material. A detailed reliability analysis of the developed power electronics interface in comparison to an existing system has been presented in the next section.

2.2 Reliability Analysis - Operation and Maintenance Cost Reduction

In this section, the reliability of a 240V, 3kW power electronics interface for the proposed and existing DDWT topologies, respectively shown in Figures 2.1 and 2.2 are examined. For the ease of this discussion, the terminologies given in [50] for reliability analysis is briefly explained first. Based on these terminologies, the Mean-Time-

Between-Failures (MTBFs) are computed for the topologies shown in Figures 2.2 and 2.1 in Subsections 2.2.2 and 2.2.3, respectively. It should be noted that the reliability analysis in this section uses the time-oriented indices based analysis, i.e. based on annual outage time and annual available time of the system.

2.2.1 Basic Terminologies

In this subsection, the basic terminologies required for the reliability evaluation of the two systems are reviewed [50].

1. Failure rate: Failure rate, λ, is the frequency of failure of a component. The failure rate of any electrical or electronic component is affected by operating conditions as voltage, current, temperature of operation, etc. [51]. Most electronic designs follow bath-tub failure rate curve and the failure rate varies over the life cycle of a system. Despite that, during most of the lifetime of a system, the failure rate of the system remains constant. The system can, therefore, be approximated to have an exponential distribution with failure rate λ.

2. Repair rate: Repair rate, μ, is the frequency of repairing of a component.

3. Mean time to failure ($MTTF$): $MTTF$ is the mean time for which a system is up and in running condition.
$$MTTF = \frac{1}{\lambda} \tag{2.3}$$

4. Mean time to repair ($MTTR$): $MTTR$ is the mean time a system is down and in repair.
$$MTTR = \frac{1}{\mu} \tag{2.4}$$

5. Mean time between failure ($MTBF$): $MTBF$ is defined as

$$MTBF = MTTF + MTTR = \frac{1}{\lambda} + \frac{1}{\mu}$$

For a system which has much higher repair rate than failure rate, MTBF can be approximated as

$$MTBF \approx MTTF = \frac{1}{\lambda} \tag{2.5}$$

6. Availability: Availability, A, is the probability of a system being in running state, and can be expressed as

$$A = \frac{\mu}{\lambda + \mu} \tag{2.6}$$

2.2.2 Reliability Analysis of Existing Power Electronics Interface

The power electronics interface shown in Figure 2.2 consists of a generator-side VSC (active rectifier), an electrolytic capacitor bank, and a grid-side VSC. The converters are formed by IGBTs, diodes, gate drivers, and snubbers. In order to compute the $MTBF$ of the system, the failure rate and repair rate of each component are needed. The failure rate of the power semiconductor devices varies with brand and model. Thus, in order to obtain uniform data, the failure rates are computed using the data provided in MIL-HDBK-217F [51]. The failure rate for IGBTs is not given in MIL-HDBK-217F, and therefore for IGBTs the failure rate is estimated based on Power MOSFETs, as the IGBT failure rate is half of an equivalent Power MOSFET [52]. Therefore, the failure rate of an IGBT is described as

$$\lambda_{IG} = 0.5\lambda_{bT}\pi_T\pi_A\pi_{QT}\pi_{ET} \tag{2.7}$$

Table 2.1: Failure rate of each component for rated power and voltage of 1 p.u.

Component	**Failure Rate λ (per million hours)**
IGBT	$\lambda_{IG} = 2.0874$
RB- IGBT	$\lambda_{RB} = 2.0883$
Electrolytic Capacitor	$\lambda_C = 6.7321$
Snubber	$\lambda_S = 0.0032$
Gate Driver	$\lambda_{GD} = 1.0021$
Diode	$\lambda_D = 1.6472$

where, λ_{bT} is the base failure rate,π_T is the temperature factor, π_A is the application factor, π_{QT} is the quality factor, and π_{ET} is the environment factor for an equivalent Power MOSFET. The failure rate is computed for a maximum junction temperature of 70^oC, and for an inverter rated at $3kW$. The failure rate is computed to be $\lambda_{IG} = 2.09$ $^{failures}/_{million-hours}$, where the subscript denotes the component type given in Table 2.1. For dc-bus electrolytic capacitors, the failure model is described as

$$\lambda_C = \lambda_{bc}\pi_{CV}\pi_{QC}\pi_{EC} \tag{2.8}$$

where, λ_{bc} base failure rate for electrolytic capacitors, π_{CV} is the capacitance factor, π_{QC} is the quality factor of the capacitor, and π_{EC} is the environment factor for the capacitor application [51]. In the case at hand, the failure rate is computed for a $1000\mu F$ capacitor, rated at $2.163p.u.$ voltage handling a dc-bus voltage of $1.803p.u.$ and with maximum rated temperature of operation as 105^oC. It should be noted that the base value considered here is the grid voltage at $208V$ and power $3kW$. The failure rate thus obtained is $\lambda_C = 6.732\,^{failures}/_{million-hours}$. The failure rates for all the other

electronic components can be calculated similarly using guidelines in [51] and [52], and their failure rates are listed in Table 2.1. The system failure rate for the DDWT shown in Figure 2.2 can be computed as [53]

$$\lambda_{sys,1} = 12\left(\lambda_{IG} + \lambda_D + \lambda_S + \lambda_{GD}\right) + \lambda_C \tag{2.9}$$

where, the subscript 1 means the power electronics interface shown in Figure 2.2. Substituting the failure rates, λ values yields

$$\lambda_{sys,1} = 0.558\, {}^{failures}/_{year}. \tag{2.10}$$

Now, using (2.5) yields

$$MTBF_1 = 15,711\, Hours\, (or\, 1.79\, Years) \tag{2.11}$$

By taking into account the system power rating, the repair time is chosen as 6 days [34]. Therefore, the repair rate can be computed as

$$\mu_{sys,1} = \frac{365}{6} = 64.03\, {}^{repairs}/_{year} \tag{2.12}$$

Accordingly, the availability of the power electronics interface of the existing DDWT shown in Figure 2.2 can be computed using (2.6), (2.10), (2.11), and (2.12) as

$$A_1 = \frac{64.03}{0.558 + 64.03} = 0.9914 \tag{2.13}$$

2.2.3 Reliability Analysis of the Developed Power Electronics Interface

The power electronics interface shown in Figure 2.1 consists of generator-side voltage source converter (active rectifier), and the single-stage boost - CSI built by Reverse Blocking-IGBTs (RB-IGBTs). The constituent components comprise of IGBTs, RB-IGBTs, diodes, gate drivers, and snubbers. The component failure rate can be calculated as described in the previous subsection and the guidelines in MIL-HDBK-217F [51] The failure rate for IGBTs is same as that calculated in the previous subsection as they have same power ratings. The failure rate of the RB-IGBTs is computed following similar guidelines for a junction temperature of 70^oC and the inverter rated at $1p.u.$ Using the failure rates given in Table 2.1, the system failure rate for the DDWT shown in Figure 2.1 can be calculated as

$$\lambda_{sys,2} = 6\left(\lambda_{IG} + \lambda_D + \lambda_{RB}\right) + 12\left(\lambda_S + \lambda_{GD}\right) \tag{2.14}$$

where, the subscript 2 means the power electronics interface shown in Figure 2.1. Substituting the failure rates, λ values yields

$$\lambda_{sys,2} = 0.412\, {}^{failures}/_{year} \tag{2.15}$$

Now, using (2.5) yields

$$MTBF_2 = 21,269\, Hours\, (or\, 2.428\, Years) \tag{2.16}$$

The system repair time is same as the one considered in the previous subsection. The repair rate is same as in (2.12). Accordingly, the availability of the proposed power

electronics interface for DDWTs shown in Figure 2.1 can be computed using (2.6), (2.12), (2.15), and (2.16) as

$$A_2 = \frac{64.03}{0.412 + 64.03} = 0.994 \tag{2.17}$$

It can be observed from (2.11) and (2.16) that the $MTBF$ for the developed system improves by about 35%. This is mainly due to the elimination of the dc-bus electrolytic capacitors, which have the highest failure rate in the power electronics interface. It should be noted that the reliability study presented in this section is performed only on the power electronics interface. Since the repair rate for electronic components is very high, i.e. they are repaired or replaced very fast, the improved $MTBF$ has very little impact on the system availability. In the case of DDWT being an off-shore turbine, the smallest improvement in $MTBF$ has a high impact on the system operation and maintenance cost [24, 54]. A 35% increase in the system MTBF will not only result in reduced maintenance cost but also decrease the system downtime for off-shore wind turbines. A reduced downtime leads to impact the system availability, reduces system operation costs, and helps in a faster payback of the wind turbine.

2.3 Capital Cost Reduction through PMSG

The use of boost - CSI as the grid-side converter facilitates the dc-link voltage to be lower than that of when using VSC. This further provides the option of keeping the generator output line-to-line voltage to be low, thus facilitating the design of a low voltage generator with a lower value of $N_T p$ as discussed in Section 2.1. In this section, a $1.5\,MW$ PMSG is designed for the proposed system and the design is compared with an existing $1.5\,MW$ PMSG in order to demonstrate the reduction in volume and weight achieved, lowering the capital costs associated with DDWTs. Firstly, an existing

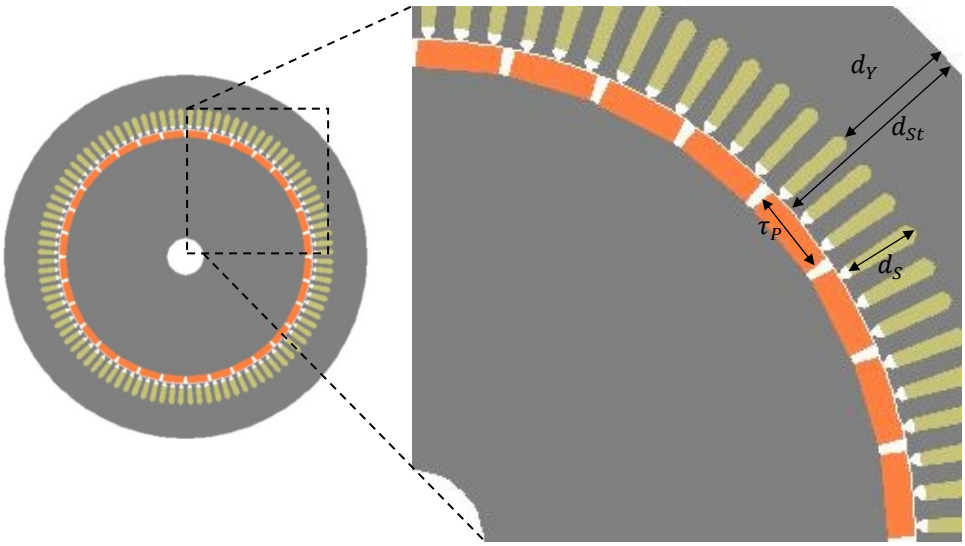

$d_Y = 350; d_{St} = 420;\ \tau_P = 260; d_S = 50;$ air-gap length $l_g = 0.6$

Fig. 2.3: Stator and rotor cross section of the designed PMSG, and their dimensions.

1.5 MW PMSG is modified for the developed system to obtain a low-voltage generator. Next, the designed generator is compared to the existing PMSG to emphasize on the weight and volume reduction achieved through the proposed topology.

2.3.1 Low-Voltage Generator Design

In this subsection, a low-voltage generator for the developed topology of DDWTs is designed. The low-voltage PMSG for the developed system is designed using GenAC toolbox of MagneForce Finite Element (FE) software. An existing 1.5 MW PMSG for DDWT is used as a base to design the low-voltage PMSG with same power rating for the developed topology [55]. The designed generator is a radial flux PMSG similar to the existing generator with the PM poles being surface mounted on the rotor. The designed generator has the rated voltage of 450 V and rated speed of19.65 RPM. The rated speed of the generator lies within the operating speed limits (15 to 20 RPM) of

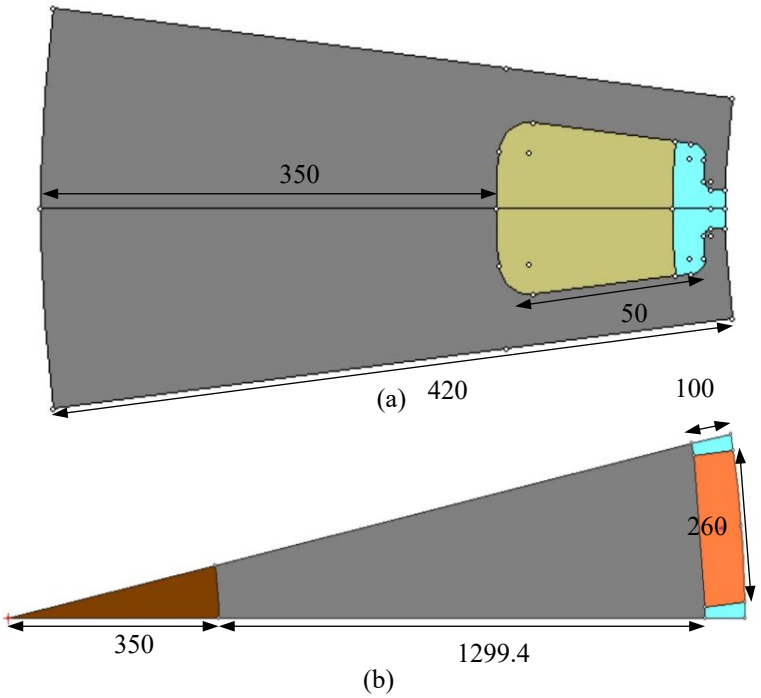

Fig. 2.4: Geometry and dimensions of (a) stator slot, and (b) rotor PM pole, obtained from the FE model.

a $1.5\,MW$ DDWT [34]. Figure 2.3 shows the stator and rotor cross section of the generator. As can be seen in Figure 2.3, the PMSG has 32 poles and 96 slots. The dimensions and geometry of the stator slots and rotor poles are shown in Figure 2.4. The armature winding is concentrated overlapping tooth coil double layered, with slot fill of about 62%, insulation thickness in the slots of $3.5\,mm$, and a current density of $4\,{}^{A}/_{mm^2}$. The length of the stator is $0.6\,m$, the inner diameter of the stator is $3.5\,m$, and the airgap length is $0.6\,mm$.

As mentioned earlier, the rotor has the surface mounted PM poles, where the PM material is NdFeB with the maximum coercive force of $24\,kOersted$, and maximum residual flux density of $1.2\,T$. The rotor poles were designed to achieve a desired value of the airgap flux density and to minimize the airgap flux density distortion. Figures

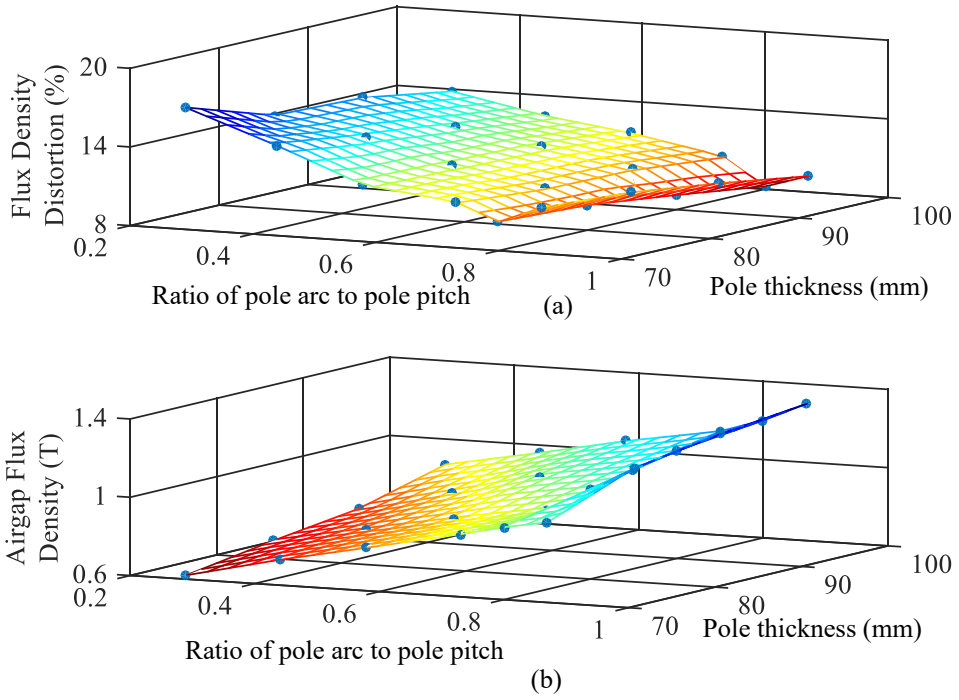

Fig. 2.5: Variation in the (a) air-gap flux density distortion, and (b) air-gap flux density with a change in the ratio of pole arc to pole pitch for different values of PM pole thickness at no load.

2.5 (a) and (b) present the airgap flux density distortion and airgap flux density with varying PM pole arc to pole pitch ratio, τ, for different thickness, respectively. The PM pole dimensions obtained through the results presented in Figure 2.5 are $260 \times 100 mm^2$ with $\tau = 0.8$ for minimum airgap flux density distortion following the analysis presented in [56].

The electromagnetic flux density distribution over the low-voltage PMSG cross section at full load ($1.5\,MW$) is presented in Figure 2.6. The FE computations indicate that the maximum flux density is about $1.15\,T$ and it is observed at the stator tooth. The parameters of the PMSG obtained through this design were implemented in MATLAB/Simulink based simulations for the verification of the developed system. The

generator line-to-line voltage and line current obtained from FE analysis and MATLAB/Simulink simulations are presented in Figure 2.7 when supplying 1 MW power. It can be observed from Figure 2.7 that the voltage and current waveforms obtained from FE analysis matches those obtained from MATLAB simulations. In the next section, the designed low-voltage generator is compared to the existing PMSG for DDWT.

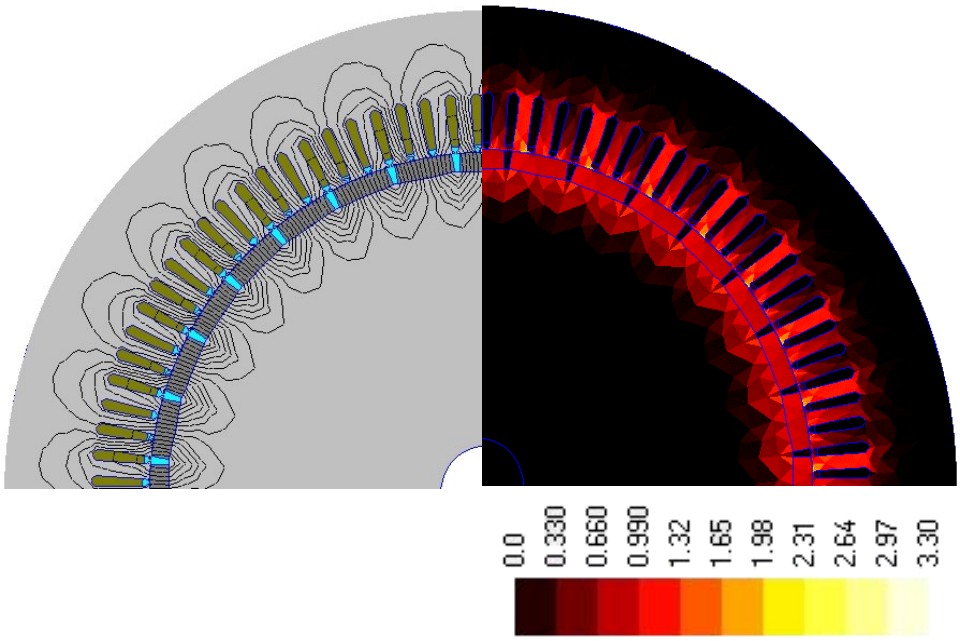

Fig. 2.6: Flux and flux density distribution (T) over the cross-section of the designed PMSG at full load.

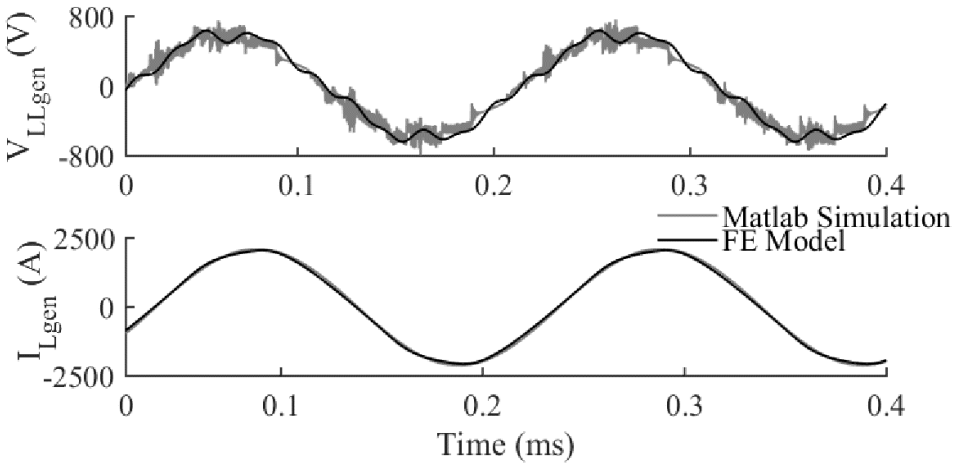

Fig. 2.7: Line-to-line voltage and line current waveforms of the designed PMSG obtained through FE computations and MATLAB simulations.

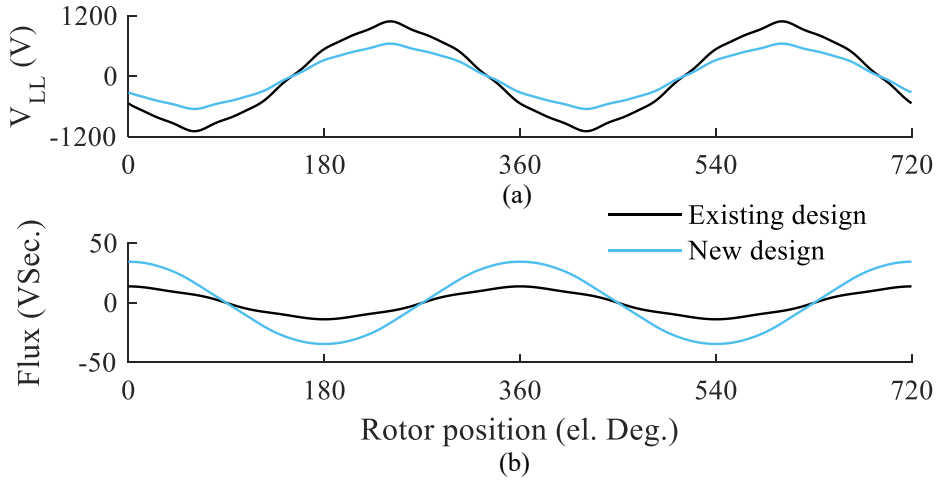

Fig. 2.8: Generator (a) line-to-line voltage, and (b) per phase flux linkage vs. rotor electrical position obtained through FE computation for the existing and new design of the PMSG.

2.3.2 Generator Parameter Comparison

In this subsection, a detailed comparison between an existing 1.5 MW PMSG for DDWT and the low-voltage PMSG design for the developed system (designed in the

previous subsection) is presented. For the purpose of this comparison, the existing generator is duplicated and modeled using FE, while the design parameters are obtained from [55]. The comparison of the generator no-load line-to-line voltage and the flux linkage with respect to rotor electrical position is presented in Figure 2.8. The no-load line-to-line voltage of the generators is shown in Figure 2.8(a). The existing generator is rated at $770\,V$ $(1.12\,p.u.)$ as compared to the modified generator as $450\,V$ $(0.652\,p.u.)$. Figure 2.8(b) presents the flux linkage with armature phase-A of the generator with respect to rotor electrical position. It can be observed from Figure 2.8(b) that the flux linkage is sinusoidal for the designed generator, with minimal distortion. It can be further observed from Figure 2.8(b) that the flux linkage for the new design is higher than that of the existing generator. This is designed so as to obtain higher per-phase inductance than in the existing generator. The higher per phase flux leads to the requirement of magnetic material with higher maximum flux density. It should be noted that even though the per phase flux is higher in the new generator design, the maximum flux density does not exceed the permissible for the core. This is possible as the maximum flux density of the core material used for the new generator design is $1.2\,T$ which is higher than that of the existing design $(1.15\,T)$.

A comparison of the existing and designed PMSG construction and design parameters is presented in Table 2.2. The rated power, rated speed, and airgap length are the same for both the generators. The existing generator is a 78 pole PMSG as compared to the new generator which is designed to be a 32 pole PMSG. This reduction in the number of poles is possible due to the low voltage output requirement in the proposed topology. It can be further observed from Table 2.2 that the there is a significant reduction in the volume and weight of the designed generator with respect to the existing generator. The axial length of the designed generator is higher than the existing generator, but the diameter is significantly smaller. This can be further observed in

Table 2.2: Comparison of the existing and designed generator.

Parameter	Existing Generator	Designed Generator
Power rating	1.5MW	1.5MW
Speed	19.65 rpm	19.65rpm
Air gap length	0.6 mm	0.6 mm
No. of poles	78	32
Line-to-line voltage	770V	450V
Stator inner diameter	4462 mm	3500 mm
Stack length	500 mm	600 mm
Number of slots	234	96
Copper weight	384.4 kg	401.3 kg
Core weight (stator)	21552 kg	19429 kg
Rotor weight	40990 kg	35870 kg

the lower weight of the designed generator. Furthermore, the amount of copper (in armature winding) in the new generator is higher but the overall generator weight is lower than the existing generator. The amount of copper in the armature winding increases in the new design as the designed generator is rated for same power with low output voltage, which results in higher rated current from the armature winding.

A detailed comparison of the existing and designed generator efficiency, total loss, core loss, and copper loss is presented in Figure 2.9. The copper loss, core loss, total loss, and efficiency data for existing and designed PMSG are presented in Figures 2.9 (a), (b), (c), and (d), respectively for the current injected into the grid ranging from $0.1\,p.u.$ to $1.25\,p.u.$ for a wind speed variation from $15\,rpm$ to $21\,rpm$ and with output impedance kept constant. It can be observed that the maximum generator efficiency occurs at about $0.8\,p.u.$ load. It can be observed from Figure 2.9(a) that the copper

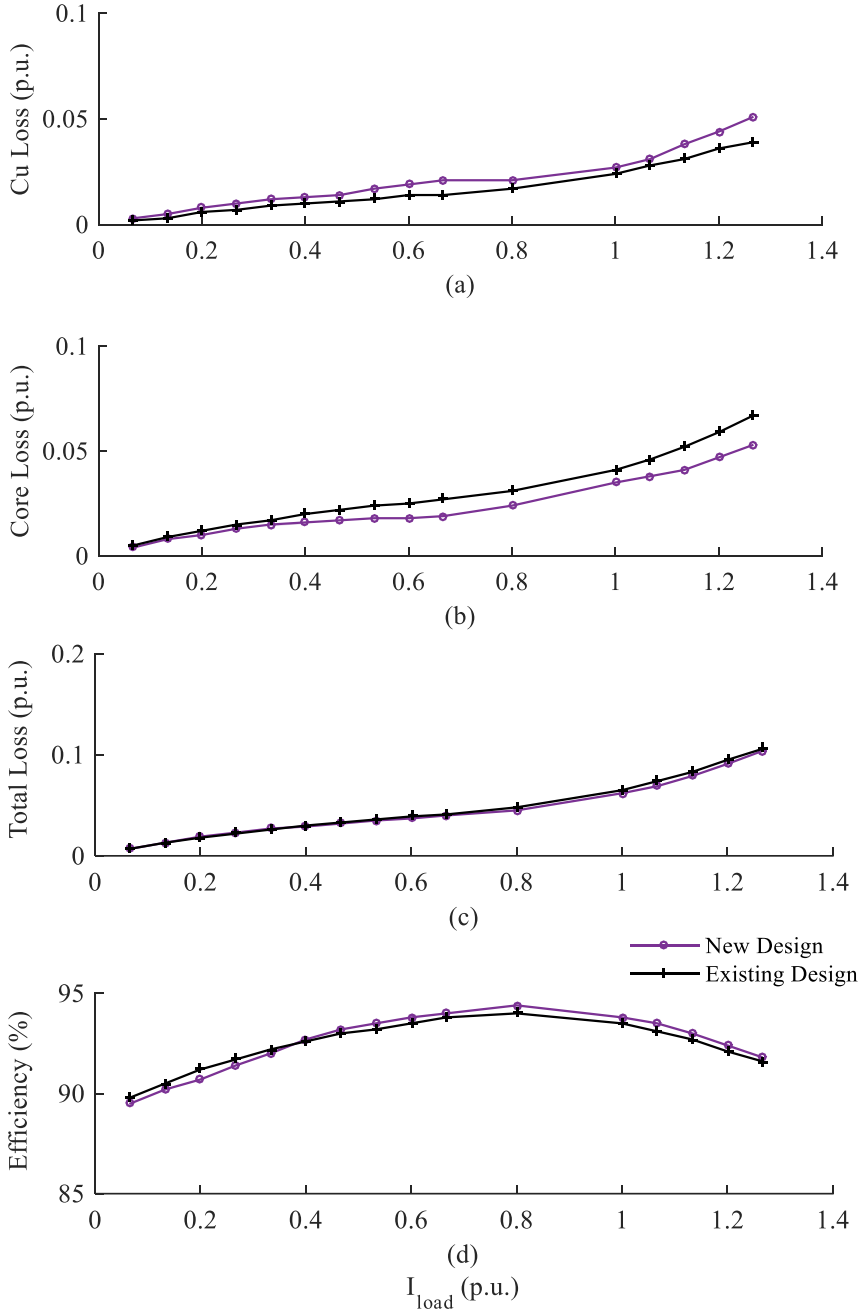

Fig. 2.9: Plot of (a) copper loss, (b) core loss, (c) total loss, and (d) efficiency for generator of existing DDWT and the generator designed for the proposed DDWT for varying output power.

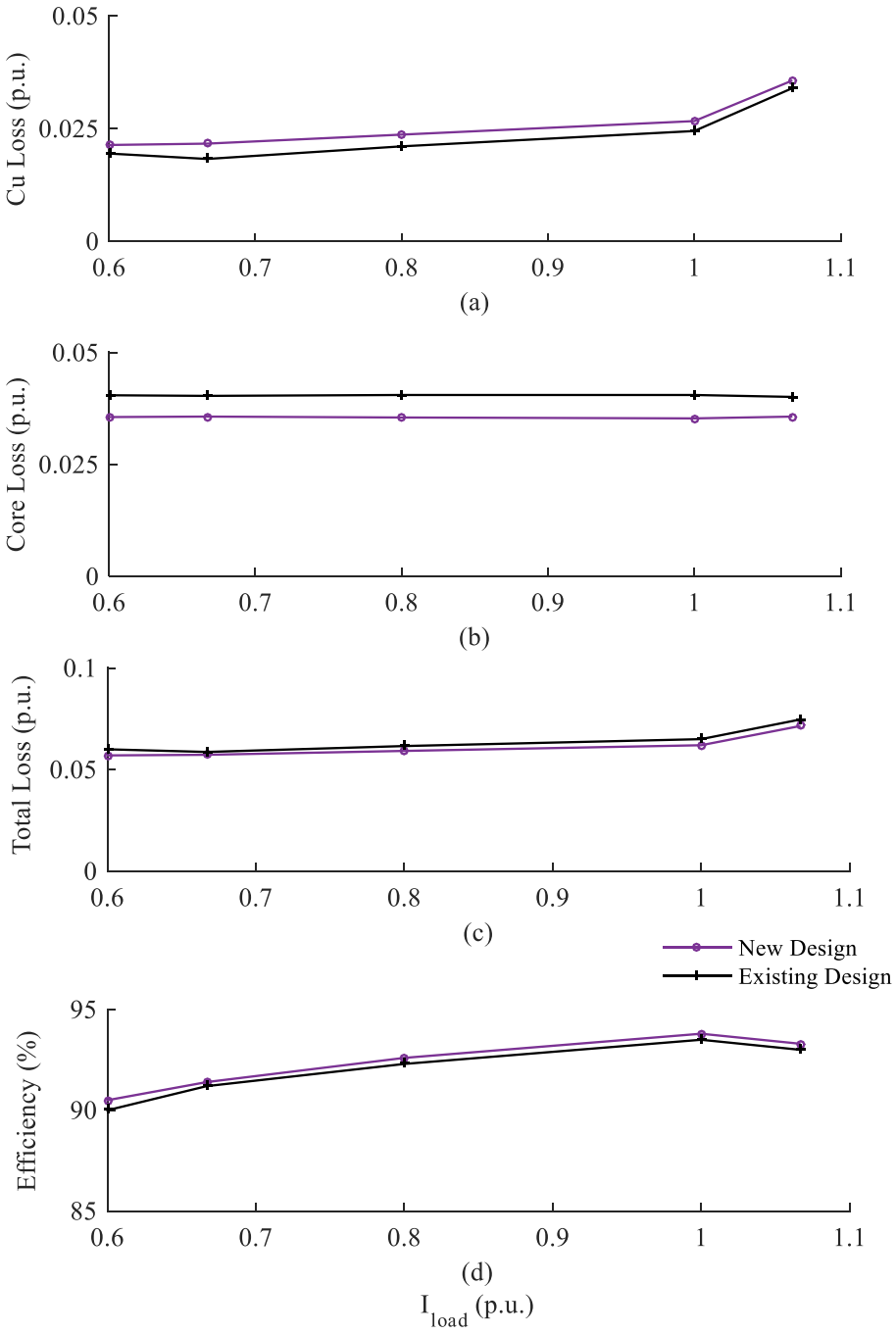

Fig. 2.10: Plot of (a) copper loss, (b) core loss, (c) total loss, and (d) efficiency of the existing and new design of PMSG for DDWT for varing output power at constant generator speed.

loss in the new design is higher than the existing generator. The copper loss in the new generator is 6.5% higher than the existing generator. This is due to the change in rated current level from the generator. The generator for the developed topology has a lower output voltage but is rated for the same output power as the existing generator. Even though the number of turns per phase in the new generator is lower leading to lower armature resistance, the output rms line current is significantly higher resulting in a higher copper loss. But, the increase in copper loss does not affect the efficiency of the new generator and it can be observed from Figure 2.9(d) that the generators have about the same efficiency, with a peak efficiency of the existing and new generators being 93.8% and 94.4%, respectively. The efficiency of the generators is about the same as the core loss in the new design is lower than the existing generator by about 9.5%, as shown in Figure 2.9(b). The reduction core loss is due to a reduction in the size of the generator. It should be noted from Figure 2.9 that the generator core losses vary with the load as the output of the generator is changed by varying the speed of the generator (which happens in the practical case through variation in wind speed) and keeping the output impedance constant. The efficiency, total loss, copper loss, and core loss comparison for the existing and designed generators for a constant speed of operation is presented in Figure 2.10. It can be observed from Figure 2.10 that the copper loss in the designed generator is higher than the existing generator but the core loss is significantly lower. The efficiency of both the generators is comparable and the maximum efficiency at constant speed is obtained for $1\,p.u.$ load.

A normalized comparison of copper loss, total loss, stator diameter, rotor weight, stator weight, volume, and PM material of the two generators is presented in Figure 2.11. Figure 2.11(a) shows the copper loss for both the generators. It can be observed from Figure 2.11(a) that the copper loss in the new generator has increased by about 6.5%. This can be contributed to the change in the current levels in the generator.

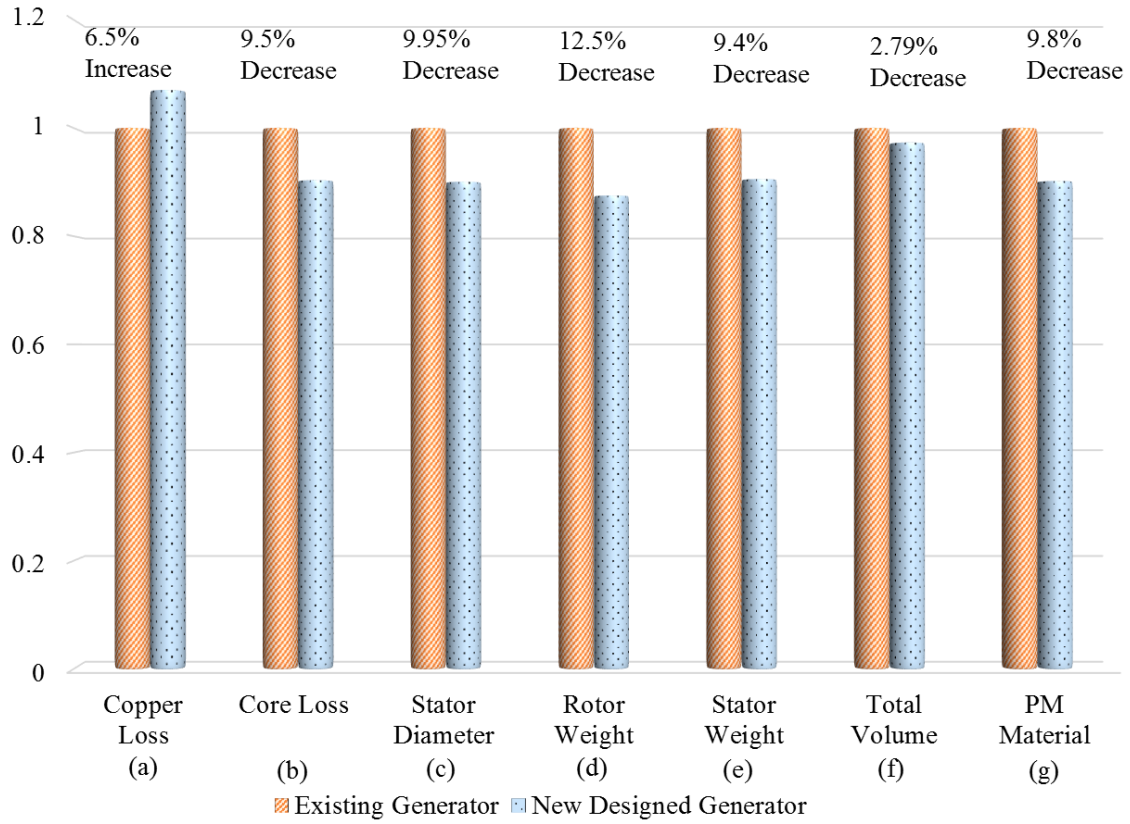

Fig. 2.11: Comparison of normalized (a) copper loss, (b) core loss, (c) stator diameter, (d) rotor weight, (e) stator weight, (f) volume, and (g) PM material of the existing and designed PM generator for DDWT using FE computation.

Even though the new design has a lower number of turns in the generator winding, i.e. lower overall stator resistance, the rms line current is significantly higher leading to higher copper loss in the designed low voltage generator. The total loss for the two generators is compared in Figure 2.11(b). It can be observed from Figures 2.11 (a) and (b) that even though the copper loss in the new design increases, the core loss for the designed generator goes down by about 9.5%. This decrease in the core loss in the designed generator can be attributed to the significant decrease in the generator iron loss which can be further extended to be caused by a decrease in stator and rotor diameters. It should be noted that the stator and rotor dimensions are decreased while

the efficiency of the generator is not compromised upon, with full load efficiency of the designed and existing generator being 94.4% and 93.8%, respectively as is also shown in Figure 2.9. Figure 2.11(c) presents the stator outer diameter for the designed and existing generators. The stator outer diameter of the designed generator is lower than that of the existing generator by about 9.95%. Figures 2.11 (d) and (e) present a comparison of the rotor and armature weights, respectively for the two generators. It should be noted that the rotor weight is the combined weight of the NdFeB PM poles and the rotor core. Similarly, the stator weight is the cumulative weight of the stator core and armature winding. It can be observed from Figures 2.11 (d) and (e) that the new designed generator has rotor and stator weight reduction by about 12.5% and 9.4%, respectively. Figure 2.11(f) presents the total volume of the two generators. The volume of the new design is lower by about 2.79% than the existing design. It can be observed that even though the decrease in the stator diameter is about 10%, it does not translate to an equivalent decrease in the overall volume of the new generator. This is because the stack length of the new generator is higher than that of the existing generator. It should be noted that the designed generator has a higher Stack Length to Diameter ($^{L}/_{D}$) ratio of 0.13 compared to the existing generator design which has a $^{L}/_{D}$ ratio of 0.11. Furthermore, a comparison for the weight of permanent magnet materials is presented in Figure 2.11(g). The dimensions of PM poles in the existing PMSG is $500 \times 142 \times 100\, mm^2$with the ratio of pole arc to pole pitch of 0.8. In the new designed generator the dimensions of the PM pole is $600 \times 260 \times 100\, mm^2$ with the pole arc to pole pitch ratio of 0.8. The new generator is a 32 pole PMSG as compared to the existing generator which is a 78 pole PMSG, which results in 9.8% reduction in the PM material.

The reduction in the PM material not only reduces the cost associated with but also reduces the dependency on the import and unstable market of PM materials. The

reduction in the weight and volume of designed generator is due to lower output rms line-to-line voltage. The lower voltage allows a lower value of $N_T p$. This results in the reduction in the overall generator volume and weight. The reduction in the generator volume and weight will further translate into reduction in the cost of the system and overall cost of energy which can be another avenue for further studies in the developed system. The reduced weight and size of the PM generator leads to a reduction in the capital cost associated with DDWTs. The current market of rare earth metals, which are used to make the PM material (NdFeB) is highly unstable and the rare earth metals have very high cost. A reduced cost generator with the more reliable converter system will have a huge commercial impact on promoting the widespread deployment of DDWTs.

2.4 System Verification

Table 2.3: Circuit parameter values (using system base).

L_s	C_{ac}	L_{ac}	f_s
23.78 p.u.	5.57p.u.	5.95 p.u.	6kHz

In this section, the generator designed in Section 2.3.1 for the developed system is implemented and the feasibility of the entire system is demonstrated through simulation results. The developed system is implemented in MATLAB/Simulink environment, using the SimPowerSystem toolbox while using the PMSG parameters obtained FE computations. The system parameters during these verifications are presented in Table 2.3.

For the first set of verification, the generator designed in the previous section is

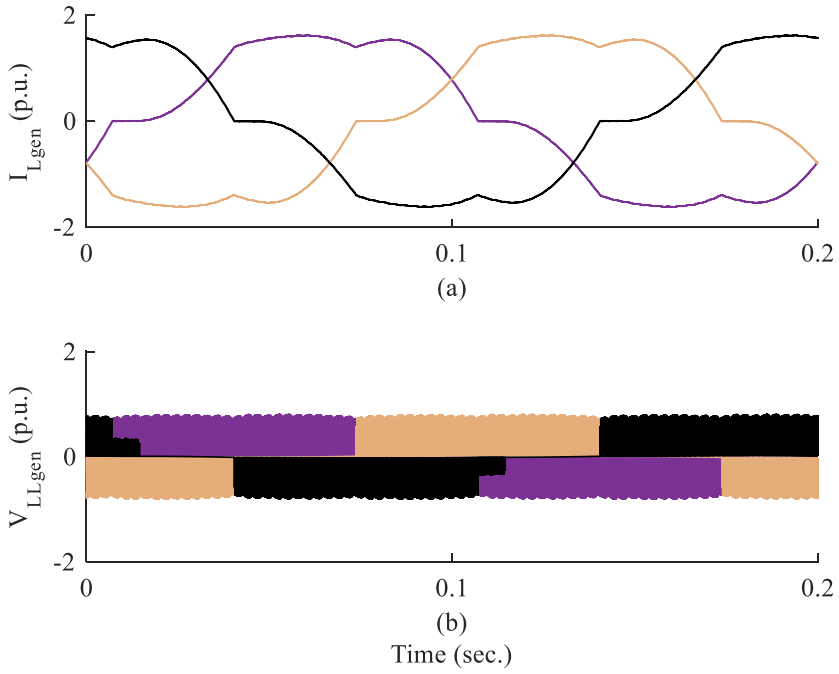

Fig. 2.12: Simulated results of generator output (a) line current waveforms, and (b) line-to-line voltage waveforms, for grid-tied system when the generator speed is 18.75 rpm and it is supplying 0.67$p.u.$ power to the grid, and the generator side converter is a diode-bridge rectifier.

implemented in MATLAB/Simulink environment and is connected to the boost - CSI while using a diode bridge rectifier as the generator side converter. The generator is run at 18.75 rpm and the system is connected to the grid with line-to-line voltage as 690 V (1$p.u.$). The average dc-side voltage is controlled through the boost - CSI such that active power injected into the grid is about 1 MW. Figure 2.12 shows the waveforms of the generator three-phase line currents and generator three-phase line-to-line voltages. The FFT analysis of these waveforms are presented in Figure 2.13. It can be observed from the generator line current waveform and its FFT spectrum (shown in Figures 2.13 (a) and (b), respectively) that the magnitude of the lower order harmonics (5^{th}, 7^{th}, etc.) content in the line current is very high. This harmonic content will result in cogging torque at the PMSG shaft decreasing its life. The waveforms of three-phase

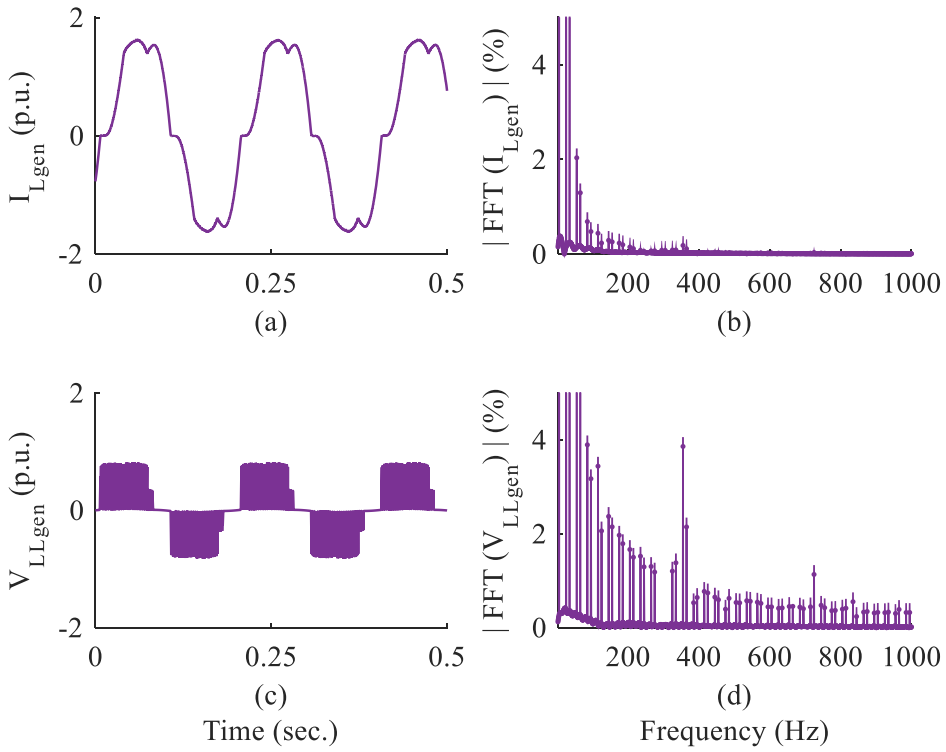

Fig. 2.13: Simulated results of generator output (a) line current waveform, (b) line current FFT spectrum, (c) line-to-line voltage waveform, and (d) line-to-line voltage FFT spectrum for grid-tied system when the generator speed is 18.75rpm and it is supplying 0.67$p.u.$ power to the grid, and the generator side converter is a diode-bridge rectifier.

line currents injected into the grid and the three-phase voltage at the point of common coupling is shown in Figure 2.14. The FFT spectrum of the line current injected into the grid and the line-to-line voltage at the point of common coupling is presented in Figure 2.15 (b) and (d), respectively. The THD of the line current injected into the grid is computed to be about 3.56%, which is within the maximum allowable limits for grid connection of distributed generation sources [57]. The results presented through this simulation demonstrate that the proposed topology is capable of providing power to the grid using a low-voltage PMSG and boost - CSI without any dc-link inductor or dc-bus capacitor, even with a diode bridge rectifier as the grid side converter. The

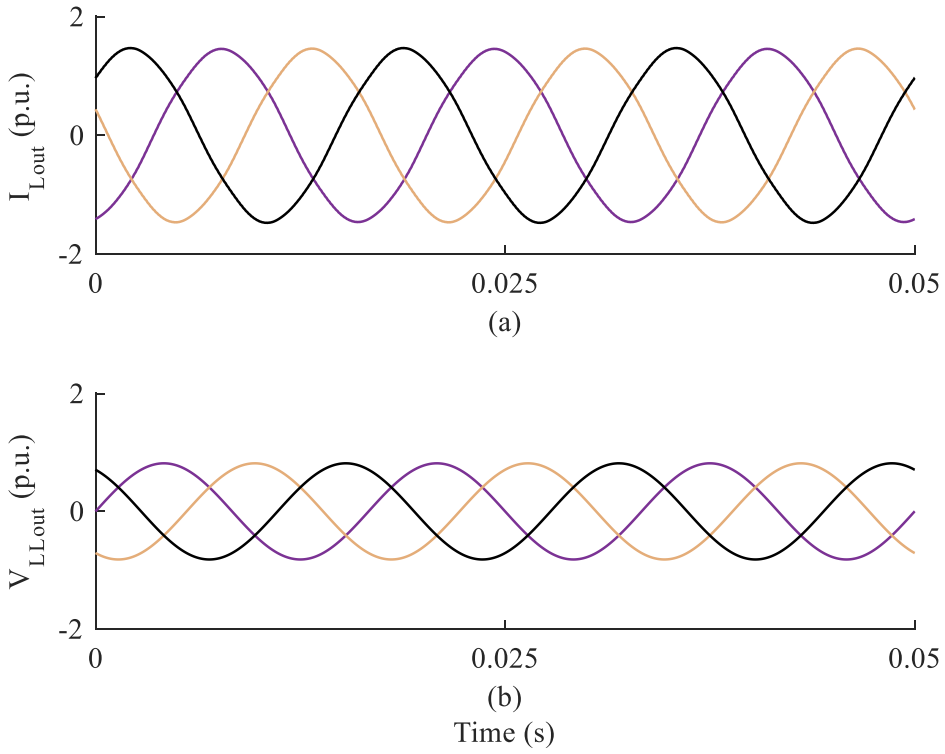

Fig. 2.14: Simulated results of output waveforms of (a) line current injected into the grid, and (b) line-to-line voltage at the point of common coupling, for grid-tied system when the generator speed is $18.75rpm$ and it is supplying $0.67p.u.$ power to the grid, and the generator side converter is a diode-bridge rectifier.

drawback of using this converter topology is a huge distortion of the generator output line current (as observed in Figure 2.13(b)), which will result in cogging torque at the PMSG shaft. This drawback of the topology can be overcome by replacing the diode bridge rectifier by a three-phase active rectifier called voltage source converter henceforth. The simulation results using the VSC as the generator side converter for the proposed topology are presented next.

The next verification is directed toward the quality of the output from the developed grid-tied system, and the results with the generator side converter as a three-phase VSC are presented in Figures 2.16 and 2.17. The rms line-to-line grid voltage was taken as $690V$ $(1p.u.)$, which is generally the transformer primary voltage for a DDWT con-

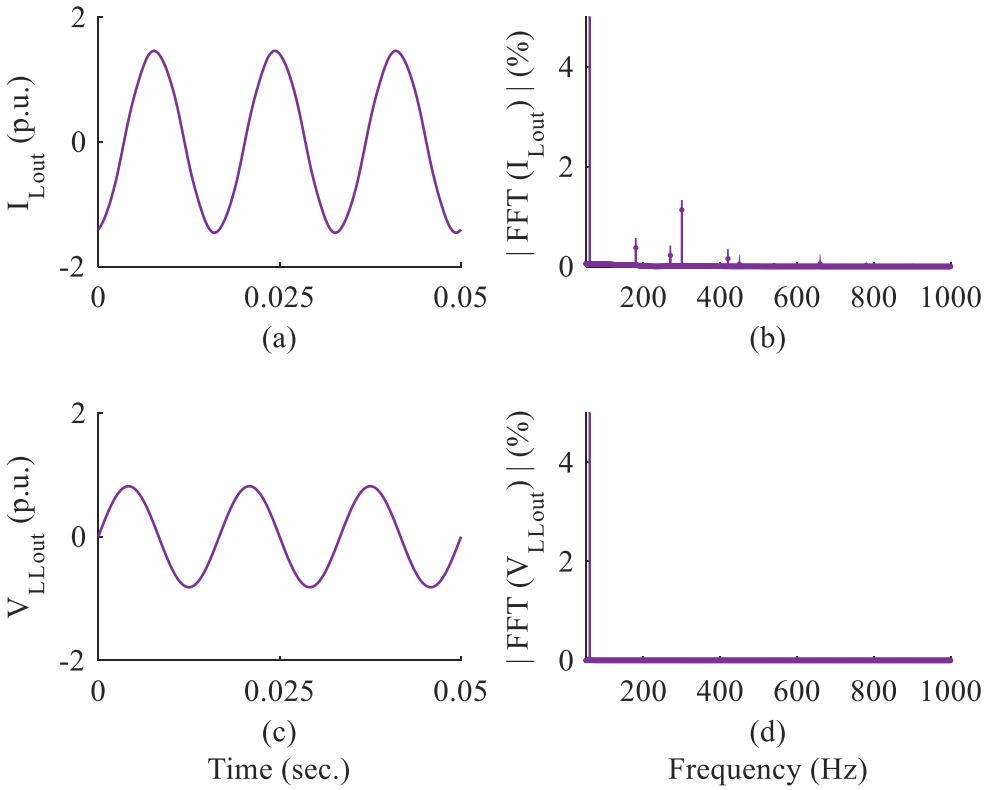

Fig. 2.15: Simulated results of (a) line current injected into the grid waveform, (b) line current FFT spectrum, (c) line-to-line voltage waveform, and (d) line-to-line voltage FFT spectrum for grid-tied system when the generator speed is $18.75 rpm$, supplying $0.67 p.u.$ power to the grid, and the generator side converter is a diode-bridge rectifier.

nected to the grid [58–61]. Figure 2.16 shows the generator output line current and line-to-line voltage waveforms along with their FFT spectra, when the system is injecting $1MW$ ($0.67 p.u.$) active power into the grid, and the generator speed is $18.75\,rpm$. It can be observed from Figure 2.16(a) that the generator current as sinusoidal current profile and the Total Harmonic Distortion (THD) of the current was computed to be about 1.2%. The absence of lower order harmonics in the generator current ensures smooth torque and elimination of any significant cogging torque on the PMSG shaft. Figure 2.17 presents the waveforms of the line current injected into the grid, and line-to-line voltage at the point of common coupling along with their harmonic spectrum

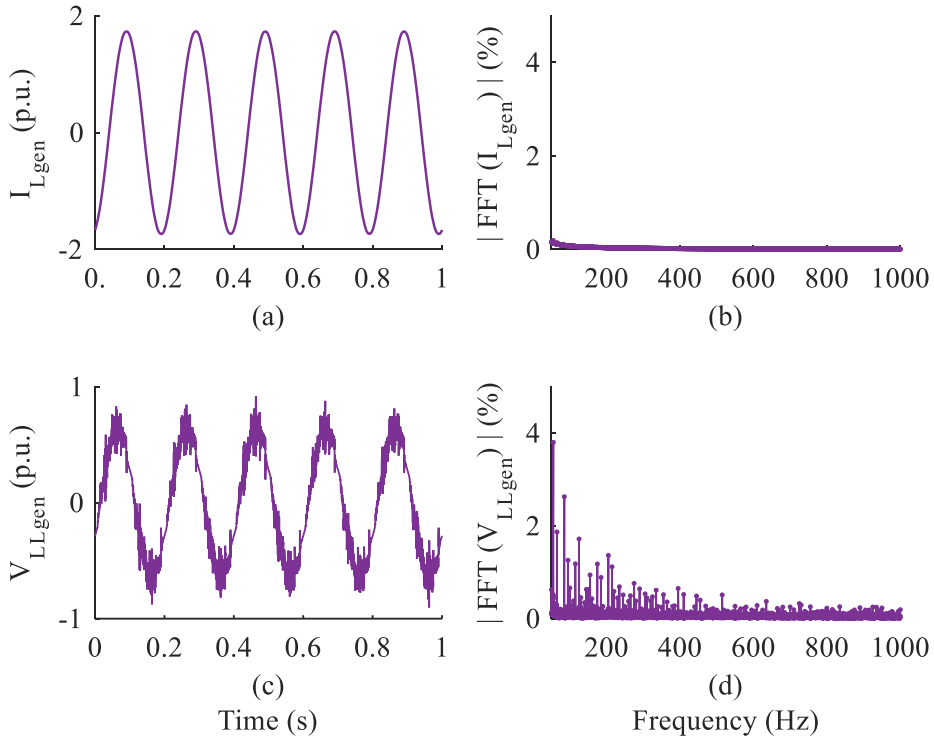

Fig. 2.16: Simulated results of generator output (a) line current waveform, (b) line current FFT analysis, (c) line-to-line voltage waveform, and (c) line-to-line voltage FFT analysis, for grid-tied system when the generator speed is $18.75rpm$ and it is supplying $0.67p.u.$ power to the grid, and the generator side converter is a VSC.

when injecting $1MW$ $(0.67p.u.)$ active power into the grid. The THD of the inverter line current is computed to be about 3.3 and it lies within the operating limits as set by the $IEEE$ 1547 standards for grid connection of distributed energy generation units [57].

2.5 Conclusion

In this chapter, an inductorless current source low-voltage generator-converter topology has been examined for DDWTs through finite-element computations and circuit simulations. The grid-side VSC in the power electronics interface of a traditional DDWT

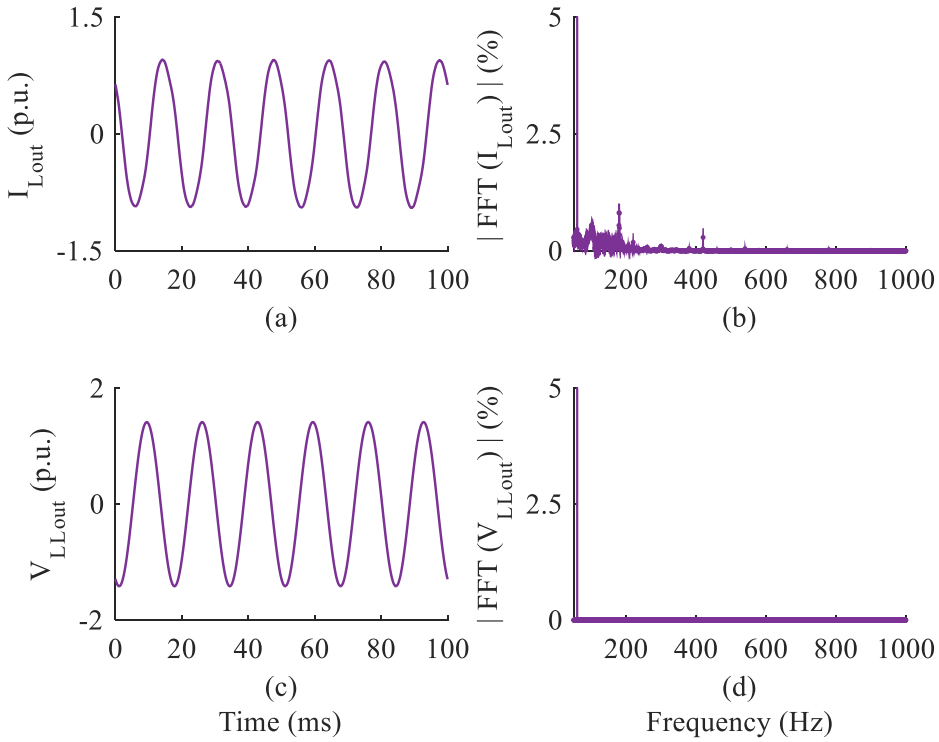

Fig. 2.17: Simulated results of inverter output (a) line current waveform, (b) line current FFT analysis, (c) line-to-line voltage waveform, and (d) line-to-line voltage FFT analysis for grid-tied system the generator speed is $18.75rpm$ and the system is injecting $0.67p.u.$ active power into the grid, and the generator side converter is a VSC.

has been replaced by the boost - CSI. The CSI topology helps in the elimination of the dc-bus electrolytic capacitors while the inherently needed dc-link inductors have been eliminated by utilizing the synchronous inductance of the PMSG. This will increase the reliability of DDWTs and decrease the overall system downtime that will have a significant impact on the maintenance costs, especially for offshore wind turbines. A reliability analysis has been performed on the existing and proposed DDWTs, showing that the proposed power electronics interface has a higher MTBF by about 35%. In this chapter, a $1.5\,MW$ proposed generator has been designed. The designed generator output has been verified through FE computations and MATLAB simulations. The designed generator has been compared to a similarly rated existing DDWT generator

using FE analysis. It has been shown that the weight, volume, and amount of PM material in the PMSG can be reduced by 9.8% by employing the new topology, when the overall system output remaining the same as the existing system. This will result in a significant reduction in the capital cost associated with the PMSG of DDWTs. Furthermore, a reduction in the amount of PM material is also demonstrated through the new generator design which will reduce the dependence on the unstable and unpredictable rare earth PM market. It has been proven that the developed DDWT system has desired performance with the synchronous inductance of PM generator utilized to eliminate the need for a dc-link inductor. It has been established that the system output waveform quality conforms to the IEEE 1547 requirements. The feasibility of the developed topology with the designed generator has also been demonstrated through simulation results in this chapter. The feasibility of the system has been demonstrated with the generator side converter as a simple diode bridge rectifier and active front rectifier as a proof-of-concept. The experimental verification will be presented in Chapter 6.

Chapter 3

Three-Phase Boost Current Source Inverter - Topology, Switching and Steady-State Characterization

This chapter introduces the topology of the three-phase boost - CSI and then details upon the developed switching technique for the control of the inverter. This chapter contains five sections. Section 3.1 describes the topology of the three-phase boost - CSI. The developed switching technique herein known as Phasor Pulse Width Modulation (PPWM) is described in Section 3.2. Section 3.2 also describes the modifications done in the developed switching pattern in order to improve the inverter output power quality. The steady state characterization equations for the boost - CSI are derived and a three-phase $3kW$ $240V$ laboratory scale boost - CSI is characterized, in Section 3.3. The expressions for the rms value of the line current being supplied by the inverter, the fundamental component of injected current, inverter ac side voltage referred to the dc-side, the minimum dc-link inductance required in order to keep the inverter in Continuous Conduction Mode (CCM) is derived in this section. The steady state

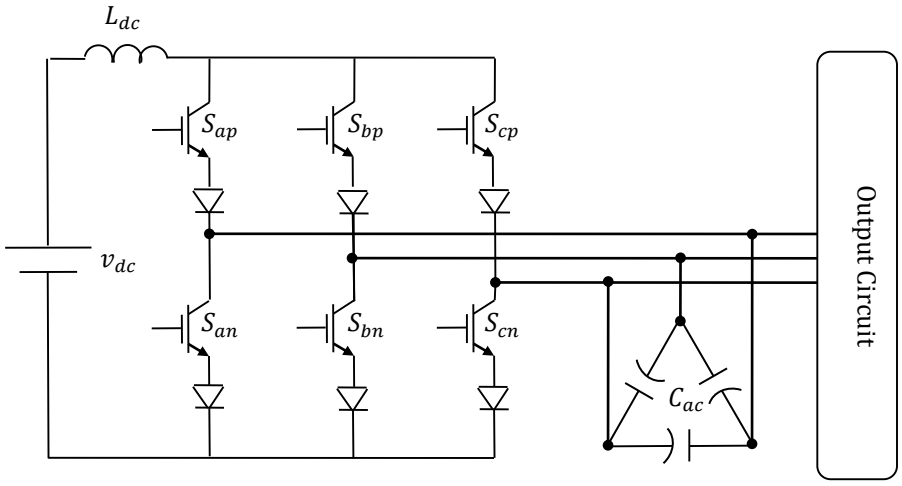

Fig. 3.1: The topology of three-phase, two-level CSI.

operating regions of the boost - CSI are also discussed in Section 3.3. The expressions derived in this chapter are verified through simulation and experimental data, and the results have also been presented in Section 3.4. Section 3.5 ends the chapter with concluding remarks.

3.1 Topology of Boost-CSI

The three-phase boost - CSI has a topology similar to a Current Source Inverter (CSI). A traditional three-phase two-level CSI is formed using six IGBTs in series with a diode. The circuit topology of a three-phase two-level CSI is shown in Figure 3.1. The three-phase boost - CSI uses Reverse Blocking – IGBTs (RB-IGBTs) as the switching devices. The circuit topology of the boost - CSI is shown in Figure 3.2. The employment of RB-IGBTs in the boost - CSI enables usage of only six switching semiconductor devices as opposed to twelve semiconductor devices in a traditional CSI. This facilitates a reduction in the switching and conduction losses associated with the boost - CSI.

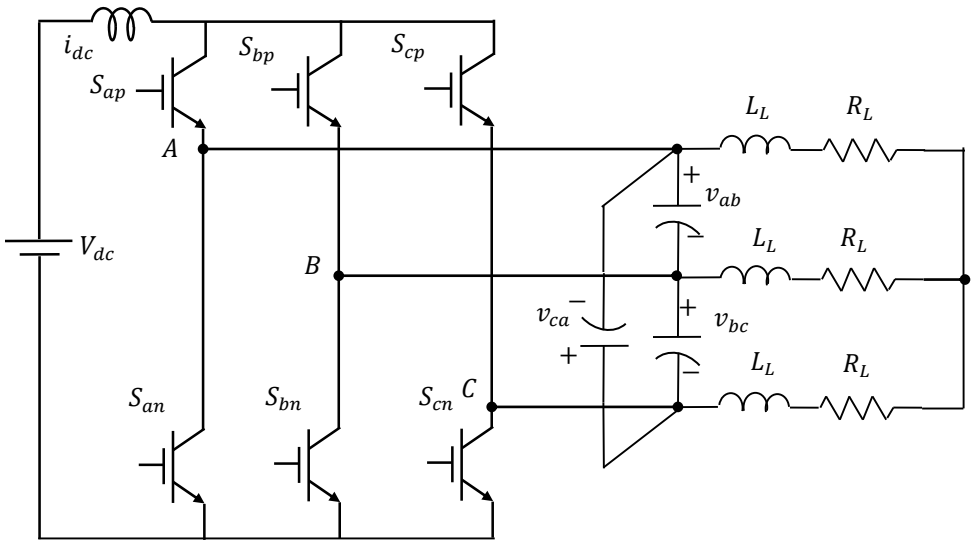

Fig. 3.2: The topology of three-phase boost - CSI equipped with RB-IGBTs.

As compared to a three-phase two-level VSI, the boost - CSI dc-side constitutes of a dc-link branch instead of a dc-bus node. The circuit topology of a three-phase two level VSI is shown in Figure 3.3. In a VSI, the dc-side comprises of a dc-bus formed by dc-bus electrolytic capacitors. The electrolytic capacitors are the most failure prone component in a power converter and it determines the system availability and lifetime [16]. This failure prone component is eliminated in the boost - CSI. The dc-side of the boost - CSI is formed by a dc-link inductor. It should be noted that even though the failure prone component is eliminated in the boost - CSI topology, the addition of dc-link inductor directly affects the system size and efficiency. The details of these effects are presented in the subsequent sections and the solution to eliminate such losses is described in the subsequent sections. The switching pattern designed for the control of the boost - CSI is discussed in the following subsection.

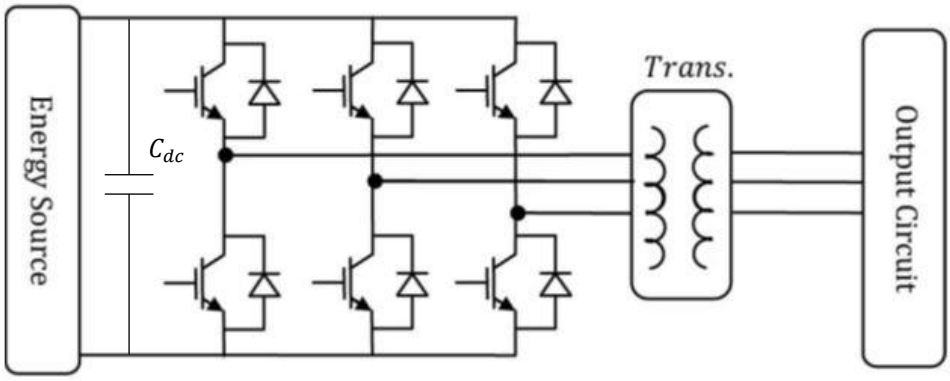

Fig. 3.3: The topology of a three-phase two level VSI.

3.2 Switching Pattern - Phasor Pulse Width Modulation

The boost - CSI topology by itself is not capable of boosting voltage in a single-stage. When the boost - CSI topology described in the previous section (see Figure 3.2) is operated using the developed switching technique PPWM it is able to provide boost ratio of about 3.5. The boost ratio is defined as

$$Boost\ Ratio = \frac{V_{LLrms}}{V_{dc}} \tag{3.1}$$

The PPWM switching technique was originally presented in [44]. It is derived from Space Vector Pulse Width Modulation (SVPWM). The six sectors in PPWM switching technique are formed by the six line-to-line voltage phasors as shown in Figure 3.4. In PPWM, one switch from the top row (S_{ap}, S_{bp}, and S_{cp}) and one switch from the bottom row (S_{an}, S_{bn}, and S_{cn}) of three-phase boost - CSI conduct at any instant, always allowing a path for the dc-link inductor current. The switches are shown in Figure 3.2.

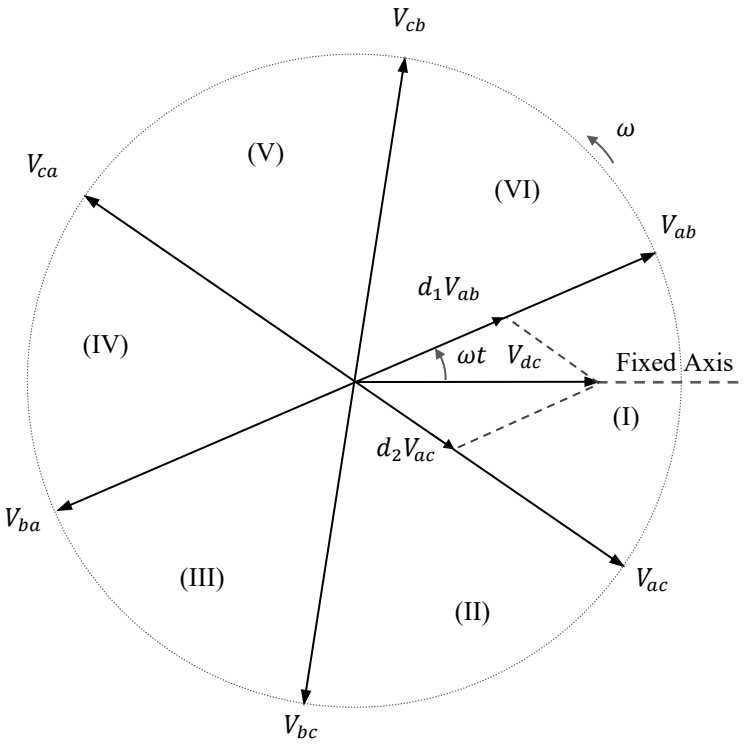

Fig. 3.4: Line-to-line voltage phasors and associated sectors for PPWM switching technique.

Every switching cycle, T_s, is divided into three time intervals (states); t_c, t_{d1}, and t_{d2}. For example, subsequent equivalent circuits of charging, C, and discharging, $D1$ and $D2$, states of Sector I, are demonstrated in Figure 3.5. During the charging state, both switches in the same leg are conducting and during each discharging state, one switch from the top row and one switch from the bottom row that are not in the same leg conduct simultaneously. For further clarification, the charging and discharging states are described as follows:

State - C: In this state, the dc circuit is shorted through two switches from a same leg. For example, in Sector I (refer to Table 3.1) S_{ap} and S_{an}, are closed and the dc-link inductor is being charged over t_c. Figure 3.5(a) shows the equivalent circuit of the converter for this state in which voltage across L_{dc} equals V_{dc}. Figure 2.6 demonstrates

Table 3.1: Sectors and switching states in PPWM switching technique.

Sector	V_1	V_2	S_{ap}	S_{an}	S_{bp}	S_{bn}	S_{cp}	S_{cn}
(I)	V_{ab}	V_{ac}	T_s	t_c	0	t_{d1}	0	t_{d2}
(II)	V_{ac}	V_{bc}	t_{d1}	0	t_{d2}	0	t_c	T_s
(III)	V_{bc}	V_{ba}	0	t_{d2}	T_s	t_c	0	t_{d1}
(IV)	V_{ba}	V_{ca}	t_c	T_s	t_{d1}	0	t_{d2}	0
(V)	V_{ca}	V_{cb}	0	t_{d1}	0	t_{d2}	T_s	t_c
(VI)	V_{cb}	V_{ab}	t_{d2}	0	t_c	T_s	t_{d1}	0

dc-link inductor current and voltage waveforms over the charging time, t_c.

State - D1: During the first discharging time-interval, t_{d1}, the inductor current is directed into phase A and returned from phase B in Sector I (refer to Table 3.1), when S_{ap} and S_{bn} are closed. Figure 3.5(b) depicts the equivalent circuit of boost - CSI during t_{d1} when the voltage across L_{dc} equals to $V_{dc} - V_1 = V_{dc} - V_{ab}$, as shown in Figure 3.6.

State - D2: During the second discharging time-interval, t_{d2}, the inductor current is directed into phase A and returned from C, when S_{ap}, and S_{cn} are closed. Figure 3.5(c) depicts the equivalent circuit of boost - CSI during t_{d2} when voltage across L_{dc} equals to $V_{dc} - V_2 = V_{dc} - V_{ac}$, as shown in Figure 3.6.

From the voltage-second balance law for the dc-link inductor voltage at steady-state conditions, the following can be written:

$$\int_0^{t_c} V_{dc} dt + \int_{t_c}^{t_{d1}} (V_{dc} - V_1)\, dt + \int_{t_{d1}}^{t_{d2}} (V_{dc} - V_2)\, dt = 0 \tag{3.2}$$

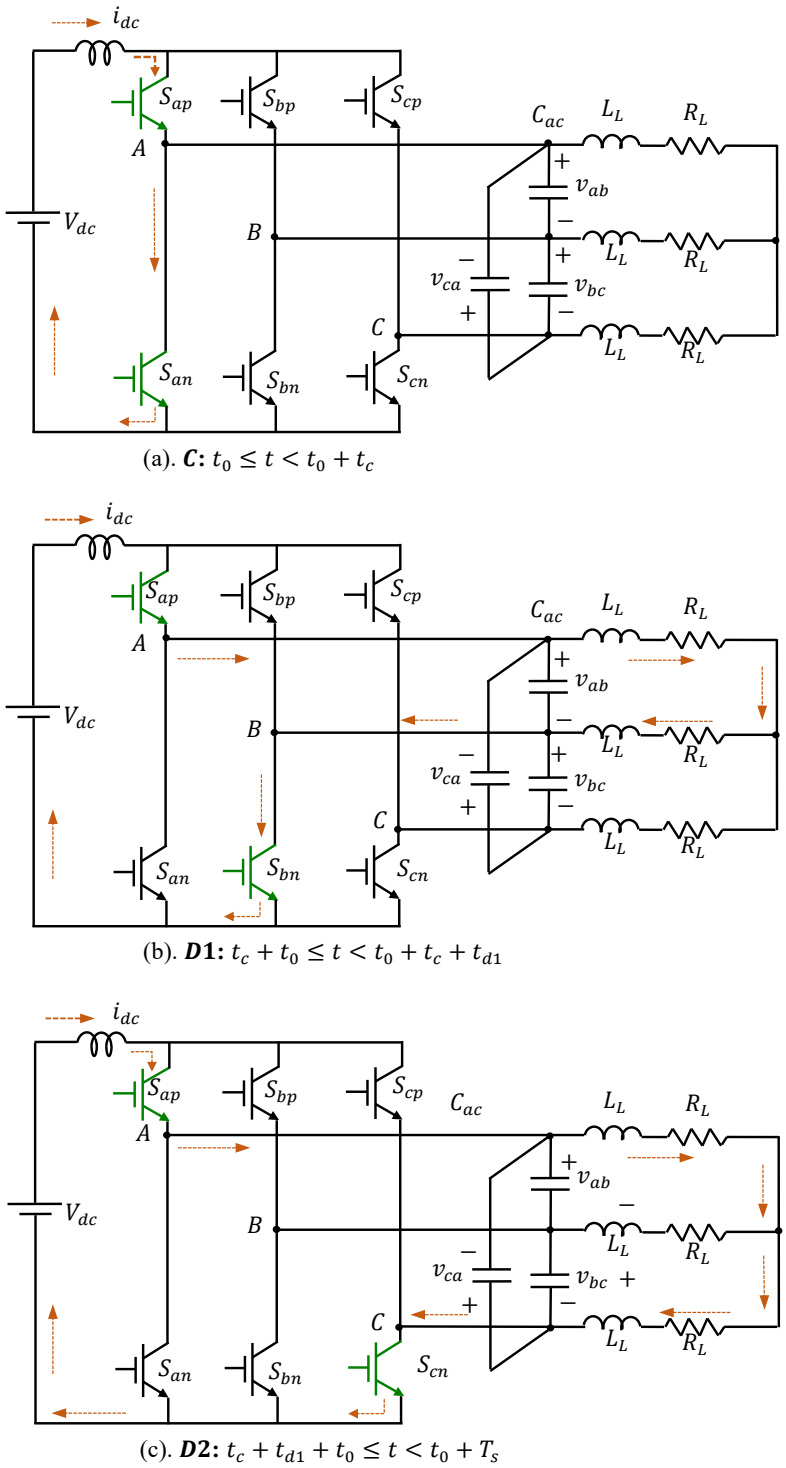

(a). ***C*:** $t_0 \leq t < t_0 + t_c$

(b). ***D1*:** $t_c + t_0 \leq t < t_0 + t_c + t_{d1}$

(c). ***D2*:** $t_c + t_{d1} + t_0 \leq t < t_0 + T_s$

Fig. 3.5: Equivalent circuit of the boost - CSI during (a) state C: charging time interval, (b) state D1: first discharging time interval, and (c) state D2: second discharging time interval of Sector I.

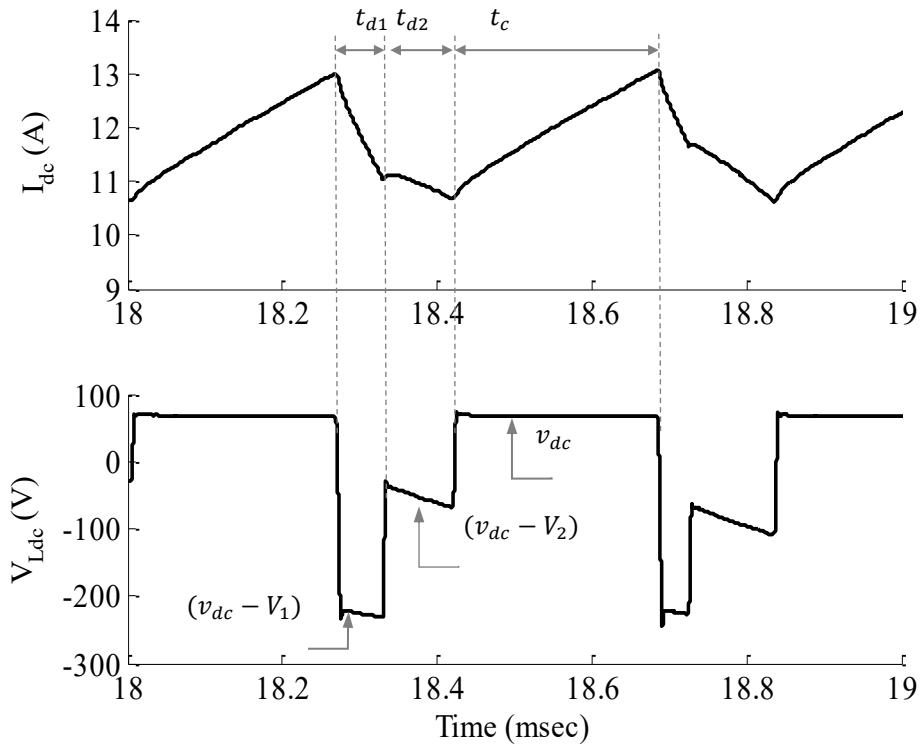

Fig. 3.6: Experimentally obtained waveforms of current and voltage of the dc-link inductor in the boost - CSI.

where, V_1 and V_2 are the corresponding line-line voltages (see Table 3.1). This equation can be simplified as

$$V_{dc}T_s = V_1 t_{d1} + V_2 t_{d2} \tag{3.3}$$

and dividing by T_s yields:

$$V_{dc} = V_1 d_1 + V_2 d_2 \tag{3.4}$$

where $d_c = t_c/T_s$, $d_1 = t_{d1}/T_s$, and $d_{d2} = t_{d2}/T_s$, are the charging and discharging duty ratios, related as follows:

$$d_c = 1 - (d_1 + d_2) \tag{3.5}$$

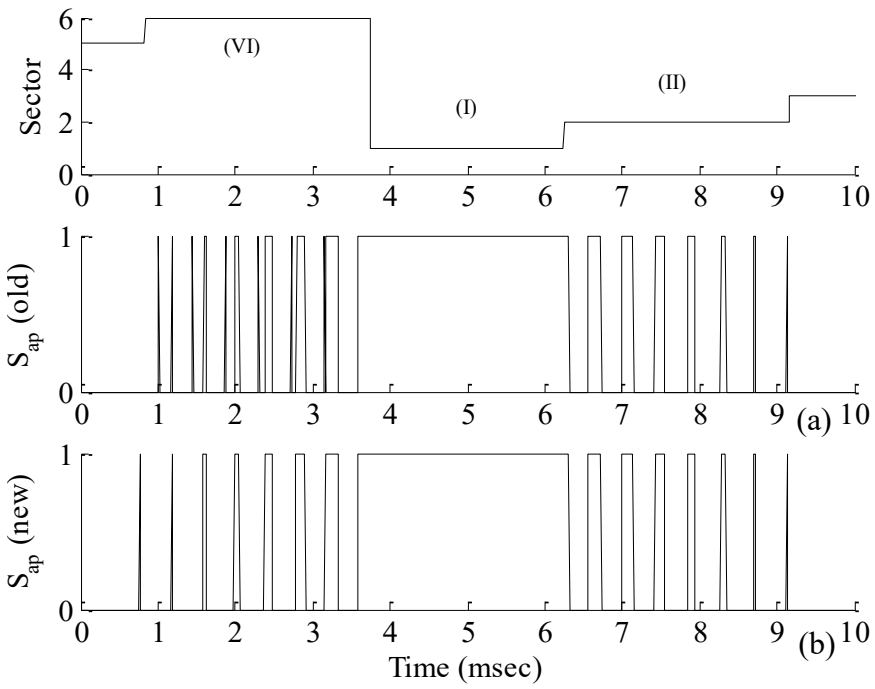

Fig. 3.7: Switching pattern of S_{ap} obtained from (a) PPWM and (b) Modified PPWM methods.

The discharging ratios, d_1 and d_2, are obtained from the law of Sines formula as $d_1 = msin\,(\pi/3 - \theta)$ and $d_2 = msin\,(\theta)$. Using (3.5), d_c is calculated as

$$d_c = 1 - msin\,(\theta - \pi/3) \tag{3.6}$$

where, m is the modulation index that must be adjusted to regulate inverter output voltage. Using a real-time calculation for d_1, d_2, and d_c, the expanded switching pattern of S_{ap} in Sectors VI, I, and II is obtained, see Figures 3.7(a) and (b). This switching pattern is not symmetric because the numbers of pulses in Sector VI and Sector I are not equal. This asymmetry is due to the inadequate resolution required for d_1, d_2, and d_c calculations and implementations, thus resulting in increased THD of the output

voltage and current waveforms. In order to resolve this problem, a modified version of PPWM method is presented in the following section to guarantee a symmetric pattern as shown in Figure 3.7(c).

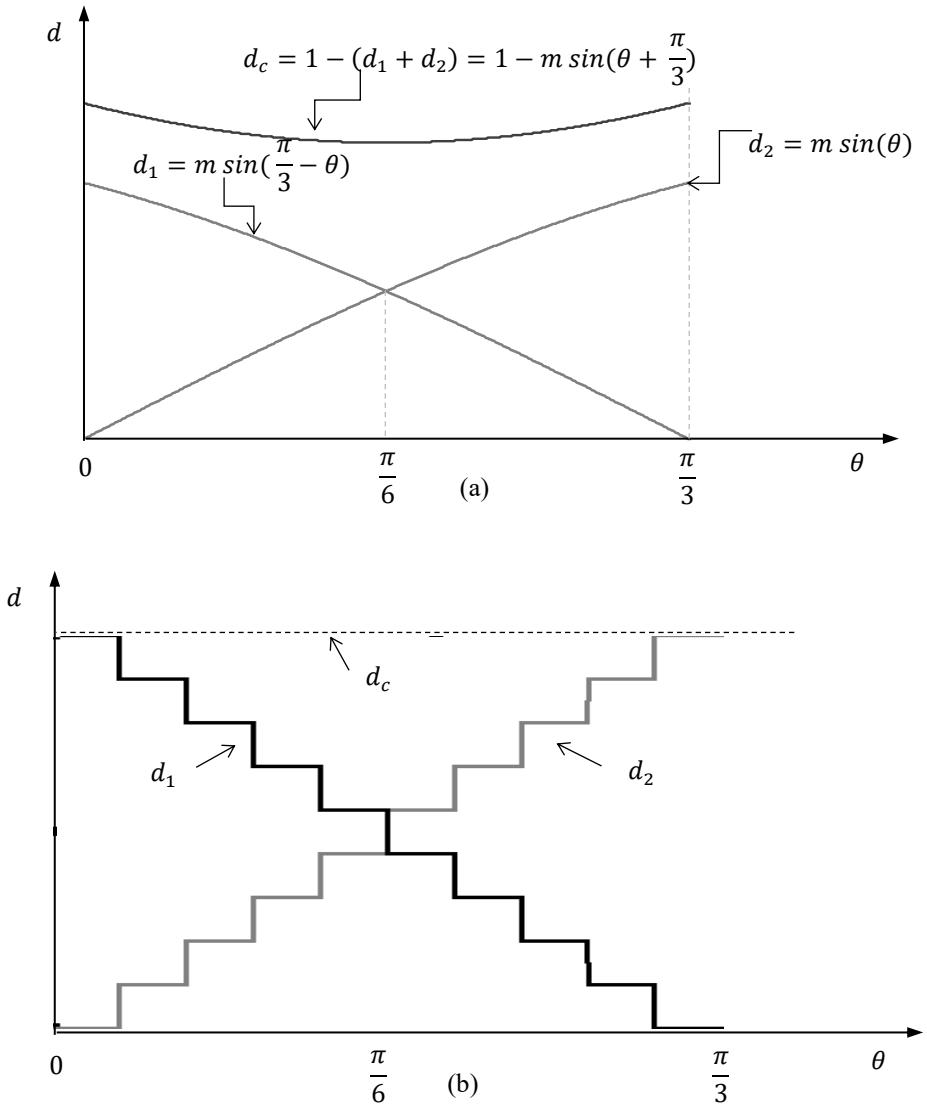

Fig. 3.8: Variations of the duty ratio d_1, d_2 and d_c versus angle, $\theta = \omega t$, for (a) the conventional PPWM and (b) the modified PPWM.

Figure 3.8(a) shows variations of charging and discharging duty ratios over one sector for the continuous PPWM derived in (3.4) – (3.6). In the modified PPWM, (i)

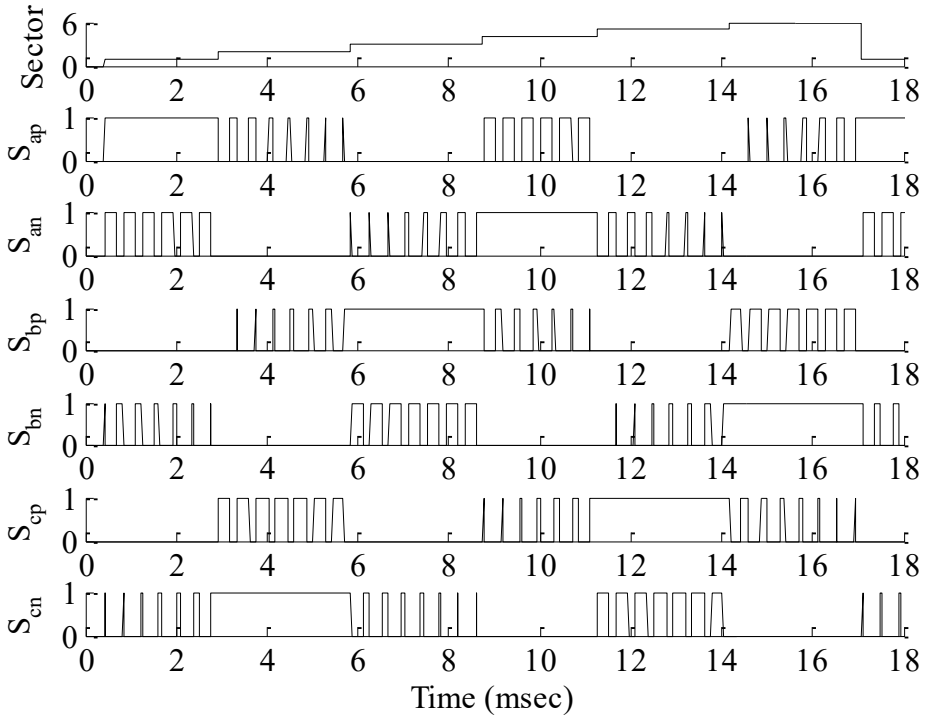

Fig. 3.9: Switching pattern obtained from using modified PPWM.

charging time remains constant over each switching cycle and (ii) discharging times are discretized as shown in Figure(3.8)(b). In this technique, n_c is obtained from the following expression.

$$n_c = \lfloor D.N_T \rfloor \tag{3.7}$$

where, $\lfloor \rfloor$is the floor function, and D is the control index in the modified PPWM instead of m in the conventional PPWM. Herein, n_1, n_2, and n_c are the number of sampling points in discharging and charging time intervals. For example, in case of implementing a $4kHz$ PWM frequency using a $500kHz$ processor, the total number of available points, N_T, is $500/4 = 125$. As shown in Figure 3.8(a), when d_1 decreases the other discharging duty ratio, d_2, increases. In the proposed method, the numbers of

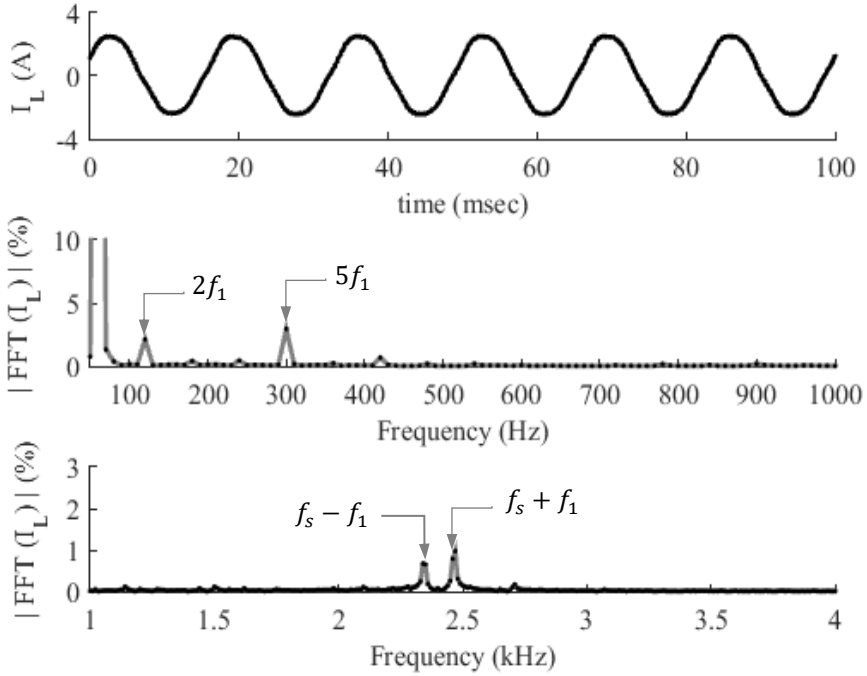

Fig. 3.10: Line current waveform for $N_T = 40$ and its FFT spectrum with THD = 3.8%, for $V_{dc} = 65V$, and $R_{load} = 70\Omega$.

points associated with the discharging time intervals are approximated by increasing and decreasing staircase functions, as shown in Figure 3.8(b). If the total number of points in every switching cycle is assumed to be N_T, the number of points in every switching cycle associated with the discharging time intervals are given by

$$n_{d1} = \lfloor (k(N_T - n_c))/(M-1) \rfloor \tag{3.8}$$

$$n_{d2} = \lfloor ((m-k)\,(N_T - n_c))/(M-1) \rfloor \tag{3.9}$$

where, $k = (M-1), \ldots, 1$, M is the predetermined number of steps over each sector, chosen based on the total number of available points, e.g. M is equal to 10 in Figure

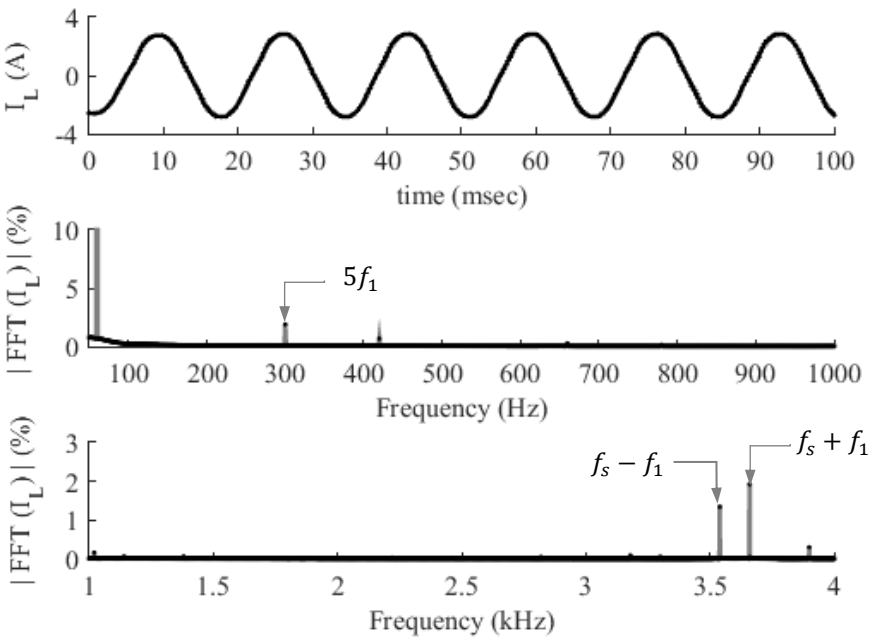

Fig. 3.11: Line current waveform for $N_T = 60$ and its FFT spectrum with $THD = 2.1$, for $V_{dc} = 65V$, and $R_{load} = 70\Omega$.

3.8(b). Using values of n_c, n_{d1}, n_{d2}, and sector number, the switching pattern for each switch can be generated, whereas n_c remains constant over each sector and the number of points for n_{d1} and n_{d2} are used to produce staircase patterns for associated discharging time intervals. The switching patterns of all switches over $18msec$, i.e. slightly more than one power cycle, are shown in Figure 3.9.

The selection of N_T is also very important in maintaining symmetrical switching pattern and ensuring quarter-wave symmetry in the output voltages and currents. N_T must be a multiple of the product of number of sectors and M. As can be seen, the switching patterns have symmetrical shapes, guaranteeing a low THD for the output current and voltage waveforms in boost - CSI. The required generate quarter-wave symmetry has been verified through simulations and the result is presented in Figures 3.10 and 3.11. Figure 3.10 and 3.11 demonstrate the line current and frequency

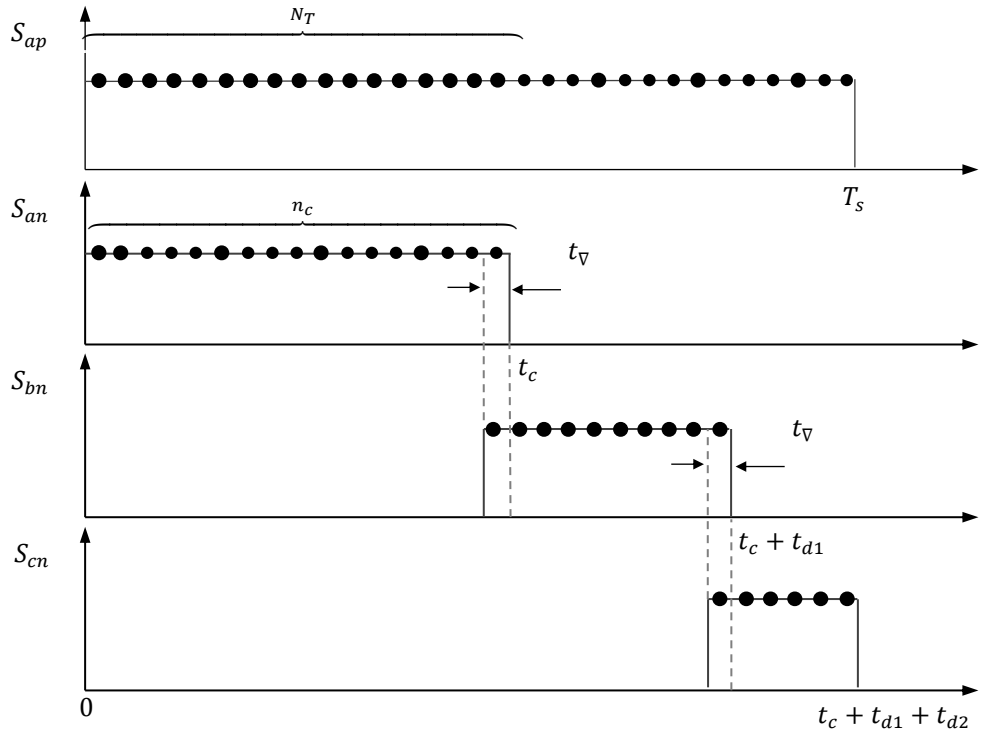

Fig. 3.12: Overlap-time, t_∇, a small duration when three switches are conducting before turn-off any switch, herein demonstrated over a switching cycle in Sector I (refer Table 3.1).

spectrum for $N_T = 40$ and $N_T = 60$, respectively. In this study, M is kept to 10 and$f_s = N_T f_1$. It can be observed from Figure 3.10, current has a second harmonic component for $N_T = 40$ while, this second harmonic component is absent for $N_T = 60$ in Figure 3.11. It should be noted that$N_T = 60$ provides an equal and integer number of sample points per sector, which results in quarter-wave symmetry in the boost - CSI output waveforms.

In a three-phase boost - CSI, a path must always exist in which dc-link current can circulate. Also, the switching pattern is based on the assumption that solid-state switches can turn on and off instantly. In reality, however, a solid-state switch has a finite switching time. In VSIs, the finite turn-off time may cause a short-circuit of the dc-bus. Therefore, dead-times must be implemented to avoid commutation overlaps

between switches. On the contrary, the presence of a dead-time in a boost - CSI during a commutation can result in a huge voltage spike across the switches causing overvoltage failure. Kavimandan et al. (2013) suggested the use of a circuit containing a switch and antiparallel diode across the dc-link inductor to resolve this problem [62]. However, this circuit complicates the control system and increases the overall cost. Singh et al. (2015) proposed an overlap-time in order always to guarantee a path for the dc-link current [45]. In a two-level voltage source inverter, a time delay between gate signals of the upper and lower switches in each leg is necessary to prevent dc-bus short circuit. This time delay is known as dead-time or blanking-time, t_{Δ}. However, the dead-time is undesired in boost - CSI, because two switches are ON at any time and there always must be a path for dc-link current to flow. The finite turn-on and turn-off times in solid-state switches can cause dead-times and consequently create huge voltage spikes across the inverter switches. This problem can be resolved by introducing an overlap-time, t_{∇}, i.e. a small duration when the three switches associated with a commutation process are conducting before turning off a switch. Meanwhile, the incorporation of the overlap-time allows the use of a smaller snubber capacitor for the boost - CSI. In Figure 3.12, the first overlap-time is naturally added to the charging time interval, which is compensated by adjusting D in (3.7) using the inverter closed-loop control scheme. However, the summation of n_c , n_{d1} and n_{d2} in each switching cycle must be equal to the total number of points, N_T, therefore n_c must be adjusted as follows:

$$n_c = N_T - (n_{d1} + n_{d2}) \tag{3.10}$$

where, n_{d1} and n_{d2} are calculated from (3.8) and (3.9). As mentioned above that the control index for the modified PPWM is D instead of m. This control index can be derived from m by averaging the charging duty ratio obtained in (3.6), over a sector.

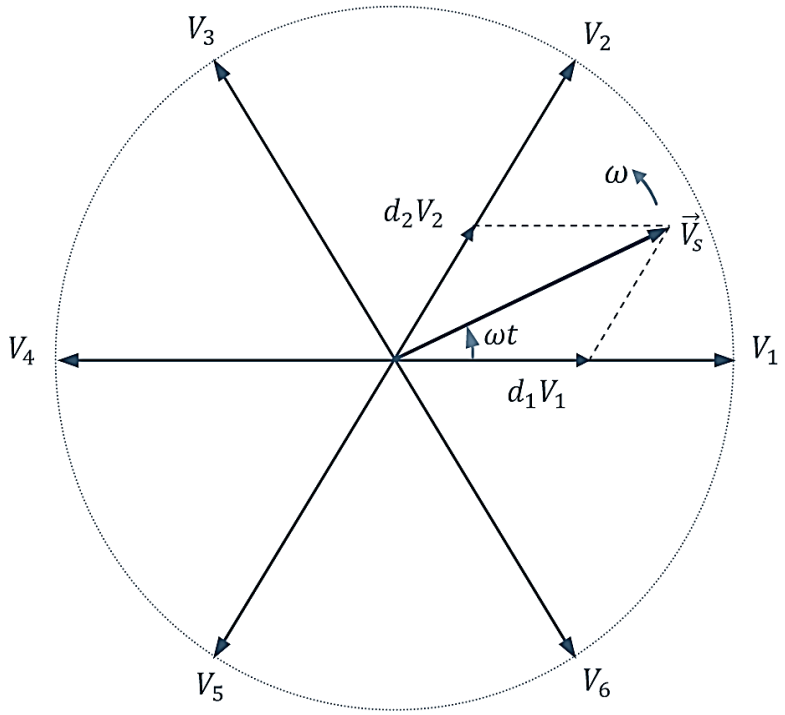

Fig. 3.13: Space vectors and associated sectors for SVPWM switching technique.

Using (3.6) and averaging over one sector, the following expression can be written:

$$D = \frac{3}{\pi} \int_0^{\pi/3} \left\{ 1 - msin\left(\theta + \frac{\pi}{3}\right) \right\} d\theta$$

which results in

$$D = 1 - \frac{3}{\pi} m \tag{3.11}$$

In spite of similarities between PPWM for boost - CSI and space-vector PWM (SVPWM) for conventional (buck) inverters, there are fundamental differences; (i) PPWM has been formulated based on phasor quantities (line-to-line voltages), not space-vectors, (ii) in SVPWM, six main switching states and two zeroes exist with three switches conducting at any given instant, however, in PPWM, six discharging and three charging states are present, with only two switches conducting at any given

instant, as shown in Figure 3.5. Additionally, in SVPWM, the resultant space vector is rotating at line frequency while the states forming the sectors are stationary as shown in Figure 3.13. In PPWM, the dc voltage is stationary and the line-to-line phasors that form the six sectors are rotating as demonstrated in Figure 3.3.

The boost - CSI bears resemblance to conventional CSIs since they share the same circuit topology. A conventional CSI is either operated based on selected harmonic elimination (SHE) modulation or SVPWM switching pattern. The SVPWM switching pattern for a CSI is formulated based on line-current space-vectors [46, 63–65]. In a SHE based CSI, the shoot-through state is prevented, and thus, it does not have the capability to boost the input voltage [66]. However, the SVPWM based CSI has a charging state, making it capable of boosting the input voltage. The boost ratio (V_{LLrms}/V_{dc}) obtained from an SVPWM based CSI is low (being slightly more than 1.1) compared to the boost ratio as high as 3.5, using a PPWM based boost - CSI.

3.3 Steady State Characterization of Boost-CSI

In this section, the steady state equations for the boost - CSI are derived and a three-phase $3kW$ $240V$ laboratory scale boost - CSI is characterized. Firstly, an expression for the rms value of the line current being supplied by the inverter is derived in Subsection 3.3.1. Secondly, the fundamental component of injected current is derived in Subsection 3.3.2. Thirdly, an expression for the inverter ac side voltage referred to the dc-side is computed in Subsection 3.3.3. Next, an expression for the minimum dc-link inductance required in order to keep the inverter in Continuous Conduction Mode (CCM) is derived in Subsection 3.3.4. The steady state operating regions of boost - CSI are discussed in Subsection 3.3.5.

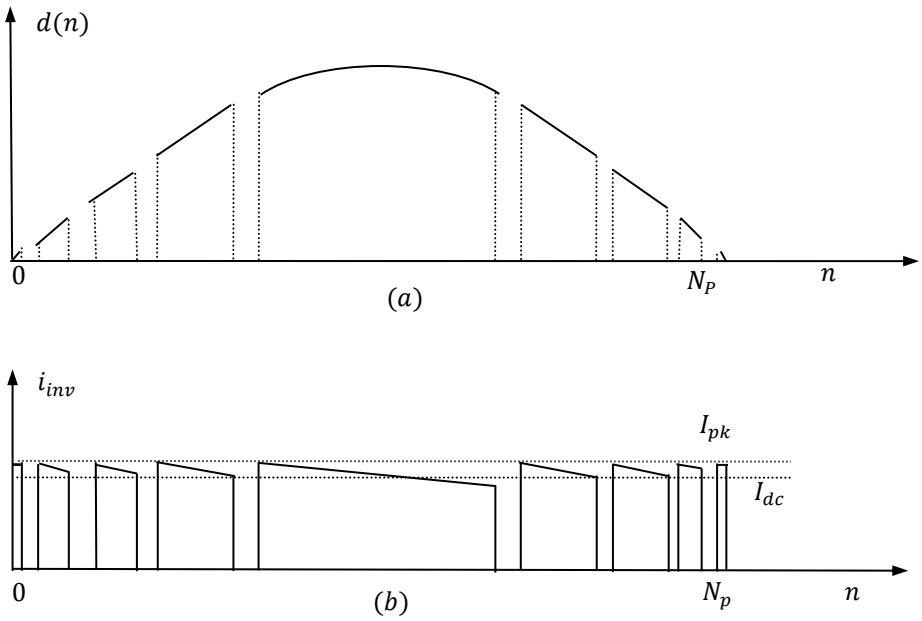

Fig. 3.14: (a) Discharging duty ratio, and (b) output current waveform before ac capacitor for phase-A over a positive half cycle.

3.3.1 Boost-CSI rms Current, I_{inv}^{rms}

In this subsection, the rms value of the inverter output current is formulated. For simplicity, the inverter output current is assumed to have rectangular-shape pulses, which implies that the dc-link current is ripple free, or $i_{dc}(t) = I_{dc}$. Accordingly, one can write the following expressions.

$$i_{inv}\,(t) \cong \begin{cases} I_{dc} & t_c < t < t_c + t_d \\ 0 & Otherwise \end{cases} \tag{3.12}$$

where, $t_d = t_{d1} + t_{d2}$. From (3.12) and Figure 3.9 the inverter output current can be calculated as follows:

$$I_{inv}^{rms} = \left(\frac{2}{T_1} \int_0^{\pi} i_{inv}^2 dt \right)^{1/2} = \left(\frac{2I_{dc}^2}{N_p} \sum_{n=0}^{N_p-1} d\,(n) \right)^{1/2} \tag{3.13}$$

where, $N_p = {}^{T_1}/_{2T_S}$. Herein, the summation over $d(n)$ has to be calculated over half power cycle, and can be calculated for a phase (e.g. phase-A) from Figure 3.14(a) and then generalized. For positive half power cycle of phase-A, sectors VI, I, and II should be analyzed and the following equation can be written:

$$d\,(n) = \begin{cases} msin\left(\frac{\pi}{N_p} n\right) & 0 \leq n < \frac{N_p}{3} \\ 2msin\left(\frac{\pi}{3} + \frac{\pi}{N_p} n\right) & \frac{N_p}{3} \leq n < \frac{2N_p}{3} \\ msin\left(\frac{\pi}{3} - \frac{\pi}{N_p} n\right) & \frac{2N_p}{3} \leq n < N_p \end{cases} \tag{3.14}$$

where, $n = 1, 2, \ldots, N_p$, and $N_p = {}^{T_1}/_{2T_S}$ is the number of pulses in any half-cycle. Substituting (3.14) in (3.13) and changing the variables to shift all the variables to interval $0 \leq n < N_p/3$ yields:

$$I_{inv}^{rms} = \left[\frac{mI_{dc}^2}{N_p} \left\{ \sum_{n=0}^{N_p/3-1} sin\left(\frac{\pi}{N_p} n\right) + \sum_{n=0}^{N_p/3-1} sin\left(\frac{\pi}{3} + \frac{\pi}{N_p} n\right) + \sum_{n=0}^{N_p/3-1} sin\left(\frac{\pi}{3} - \frac{\pi}{N_p} n\right) \right\} \right]^{1/2} \tag{3.15}$$

The following trigonometric identity can be used

$$\sum_{n=0}^{N} sin\,(nx) = \frac{sin\left(\frac{Nx}{2}\right) sin\left(\frac{1}{2}\,(N+1)\,x\right)}{sin\left(\frac{x}{2}\right)}\,; \ldots$$

$$\ldots \sum_{n=0}^{N} cos\,(nx) = \frac{cos\left(\frac{Nx}{2}\right) sin\left(\frac{1}{2}\,(N+1)\,x\right)}{sin\left(\frac{x}{2}\right)} \tag{3.16}$$

Now using (3.16), (3.11) and (3.15), the inverter output rms current can be written as follows

$$I_{inv}^{rms} = I_{dc}\sqrt{\frac{2m}{\pi}} = I_{dc}\sqrt{\frac{2}{3}(1-D)} \tag{3.17}$$

This equation is verified using simulation and experimental results later in this section.

3.3.2 Boost - CSI Fundamental Component of Current, $I_{inv}^{rms}(f_1)$

In this subsection, the fundamental component of the inverter output current is calculated. Again, assuming that the PWM switching frequency is much higher than the line frequency; from Figure 3.14 and Fourier series of $i_{inv}(t)$, the rms value of its fundamental-frequency component can be obtained as follows:

$$I_{inv}^{rms}(f_1) = \frac{I_1}{\sqrt{2}} = \frac{1}{\sqrt{2}}\frac{4}{T_1}\sum_{n=0}^{N_p} i_{inv}(n)\, sin\left(\frac{\pi}{N_p}n\right) \tag{3.18}$$

Substituting (3.14) in (3.18) and further simplification yields:

$$I_{inv}^{rms}(f_1) = \frac{\sqrt{2}I_{dc}m}{N_p}\left[\sum_{n=0}^{N_p/3-1}\frac{3}{2}\right] \tag{3.19}$$

Again, considering half power cycle, the series in (3.19) can be simplified as follows:

$$I_{inv}^{rms}(f_1) = \frac{I_{dc}m}{\sqrt{2}} = \frac{\pi I_{dc}}{3\sqrt{2}}(1-D) \tag{3.20}$$

As one can observe from (3.20), the fundamental-frequency component of the inverter output current increases with an increase in the modulation index, m. It should be noted that (3.17) and (3.20) are valid as far as the dc-link current ripples are relatively small. This low-frequency ripple will cause low order harmonics at the inverter output and affect the current THD index. Furthermore, using (3.17) and (3.19) the THD can

be calculated as

$$THD = \frac{\sqrt{I_{inv}^{rms2} - I_{inv}^{rms}\left(f_1\right)^2}}{I_{inv}^{rms}\left(f_1\right)} p.u. \tag{3.21}$$

Substituting (3.17) and (3.20) in (3.21) we get

$$THD = \sqrt{\frac{4}{m\pi} - 1} \tag{3.22}$$

It should be emphasized that the THD computed here is for the inverter current before the ac capacitors, C_{ac}, as shown in Figure 3.5.

3.3.3 AC Side Voltage Referred to DC-Bus, $u\left\langle v_{inv}\right\rangle$

In this subsection the inverter output ac voltage referred to the dc-bus is formulated as a function of system parameters. The voltage drop across the output filter can be neglected. The average value of switching function $u\left\langle v_{inv}\right\rangle$, can be approximately obtained as:

$$u\left\langle v_{inv}\right\rangle = \frac{6\sqrt{2}V_{LL}}{T_1} \sum \left\{ d_1 T_s sin\left(\frac{\pi}{N_p} n\right) + d_2 T_s sin\left(\frac{\pi}{N_p} n - \frac{2\pi}{3}\right)\right\} \tag{3.23}$$

where, T_1 is the power cycle period and ω_1 is the power cycle angular frequency. Using (3.14), (3.23) can be rewritten by expressing d_1 and d_2 in terms of modulation index m as follows:

$$u\left\langle v_{inv}\right\rangle = \frac{3\sqrt{2}V_{LL}}{N_p} \sum_{n=0}^{N_p-1} \left\{ sin\left(\frac{\pi}{N_p} n\right) sin\left(\frac{\pi}{3} - \frac{\pi}{N_p} n\right) + sin\left(\frac{\pi}{N_p} n\right) sin\left(\frac{\pi}{N_p} n - \frac{2\pi}{3}\right)\right\}$$

which can further be simplified as

$$u\left\langle v_{inv}\right\rangle = \frac{3\sqrt{2}V_{LL}T_s m}{T_1} \sum_{n=0}^{N_p-1} \left\{ cos\left(2\omega_1 T_s n\right) - 1\right\} \tag{3.24}$$

This on further mathematical simplification yields,

$$u \langle v_{inv} \rangle = \frac{3m}{\sqrt{2}} V_{LL} \tag{3.25}$$

3.3.4 DC-Link Inductor, L_{dc}

In this subsection, the minimum dc-link inductor required to keep the boost - CSI in CCM is derived. In order to achieve a low total harmonic distortion (THD) of the inverter output voltage and current, the inverter must operate in continuous conduction mode (CCM). The minimum inductance, L_{dc}, required to keep the inverter in CCM needs to be computed in order to eliminate L_{dc}.

The peak dc-link current after a charging state can be seen in Figure 3.15(b), where T_s is the switching time period. For a small T_s, the charging and discharging currents can be assumed to be linear. For the boundary condition, when the dc-link current is zero only for almost zero time, the average dc-link current can be expressed as

$$I_{dc}^{B} = \frac{1}{2} I_{pk} d_c + \frac{1}{2} \left(I_{pk} - I_M \right) d_1 + I_M d_1 + \frac{1}{2} I_M d_2 \tag{3.26}$$

where, I_M and I_{pk} are dc-link currents after the charging and first discharging time intervals, as shown in Figure 3.15(b). If the dotted line in Figure 3.15(b) is used to simplify the calculation, one can write the following expression.

$$I_{dc}^{B} = \frac{1}{2} I_{pk} d_c T_s \tag{3.27}$$

The minimum ripple in dc-link current occurs when the reflected ripple voltage is maximum, i.e. $V_1 = \sqrt{2} V_{LL}$. This occurs for d_c at $\theta = k\pi/3$. Substituting the (3.6) into (3.26) and approximating the discharging periods by the dotted line in Figure

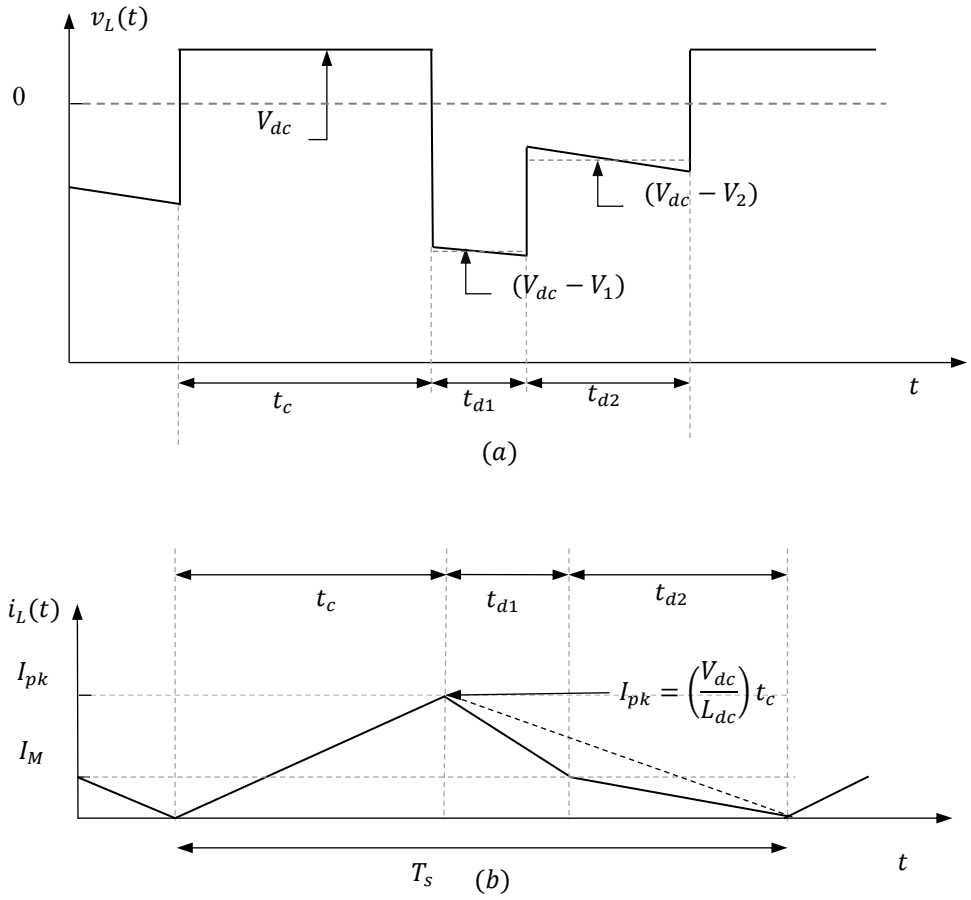

Fig. 3.15: Ideal (a) voltage and (b) current waveform of the dc-link inductor in the boost - CSI at boundary condition (BC), when it is about to enter the discontinuous mode of operation.

3.15(b) leads to

$$I_{dc}^{B} = \frac{1}{2}\frac{1}{f_s}\frac{V_{dc}}{L_{dc}}\left(1 - \frac{\sqrt{3}}{2}m\right) \tag{3.28}$$

In order to obtain the minimum inductance required to keep the boost - CSI in CCM, $I_{dc} \geq I_{dc}^{B}$. Using the dynamic equation (4.6), neglecting di_{dc}/dt and substituting $V_q = \sqrt{2}V_{LL}$ leads to the steady-state average value of I_{dc} as follows:

$$I_{dc}^{B} = \frac{V_{dc} - \sqrt{3/2}mV_{LL}}{R_{dc} + 2R_{on}} \tag{3.29}$$

The modulation index, m, for the boost - CSI depending of the boost ratio is in the range of $[0.05, 0.35]$. From (3.28) and (3.29), the minimum value of L_{dc} required to keep the three-phase single-stage boost - CSI in CCM of operation can be obtained from

$$L_{dc} > \frac{1}{2}\frac{1}{f_s}V_{dc}\frac{R_{dc}+2R_{on}}{V_{dc}-\sqrt{3/2}mV_{LL}}\left(1-\frac{\sqrt{3}}{2}m\right) \tag{3.30}$$

3.3.5 PQ Operational Region

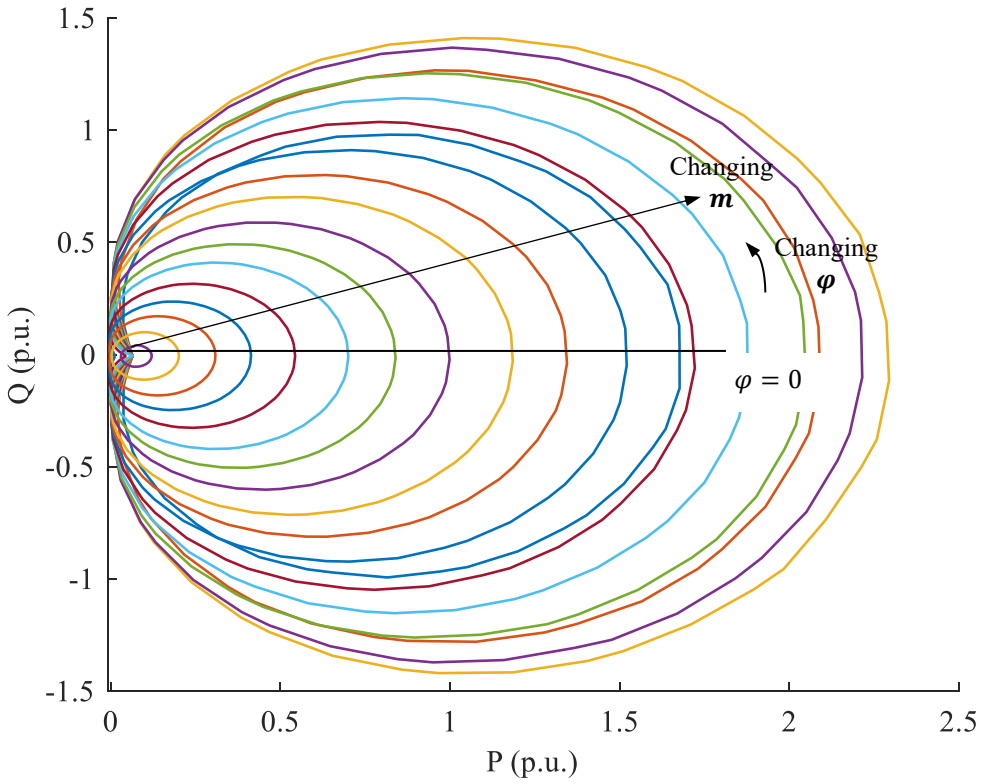

Fig. 3.16: The boost - CSI operating points for grid-tied mode obtained by varying the modulation index and phase difference between inverter and grid voltages.

In this subsection, operating points of the boost - CSI are identified in the PQ plane. The boost - CSI is formed using Reverse Blocking IGBTs (RB-IGBTs), therefore unlike

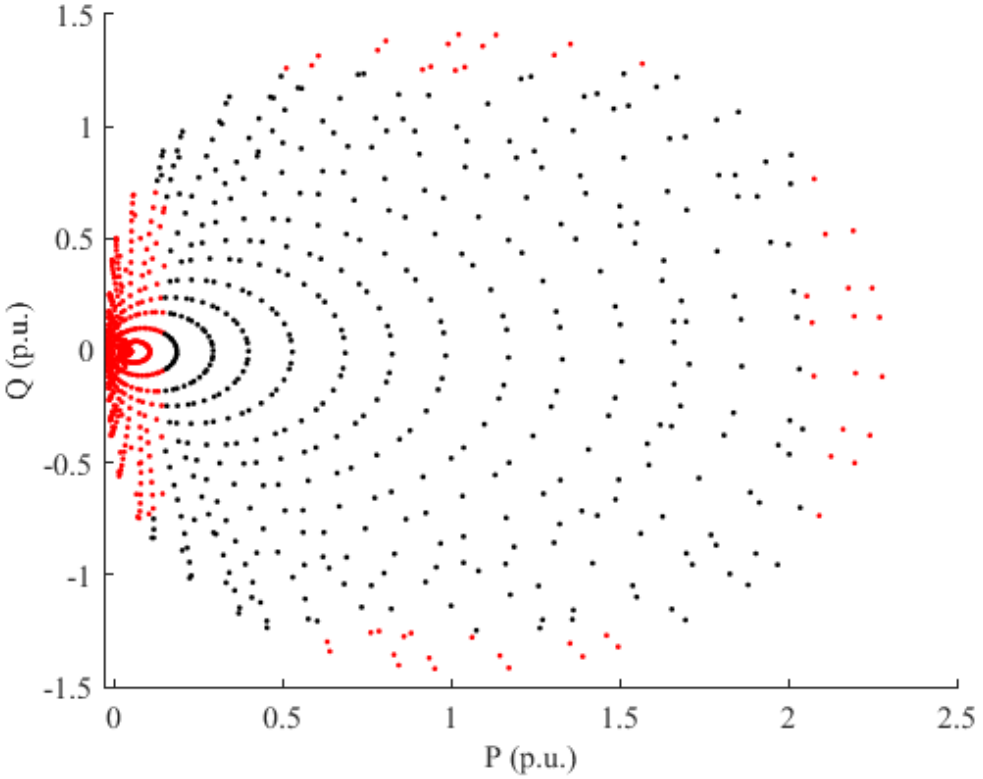

Fig. 3.17: The boost - CSI operating zone for grid-tied mode obtained by varying the modulation index and phase difference between inverter and grid voltages with the THD of the current injected to grid.

VSCs, the boost - CSI allows only unidirectional power flow, i.e. $P > 0$. In order to study the operating region of the boost - CSI, a grid-tied boost - CSI was simulated with varying modulation index, m and the phase difference between the modulated output current and the grid voltage, φ. Figure 3.16 illustrates the operating points available for a boost - CSI in the PQ plane. The base value chosen for the system is $208V$ and $2kVA$. The small negative values of P in Figure 3.16 represent the power loss in the CL filter. Figure 3.17 demonstrates the operable points in the PQ plane. The points marked in red demonstrate the operating points with high THD values in the inverter output current (more than 5%). It can be further observed that for low output active power from the inverter, the boost - CSI has high output current

THD. Again, unlike VSCs the reactive power cannot be produced for the operating points with low power factor, as shown in Figure 3.17. In the boost - CSI, a minimum magnitude of the dc-link current is necessary to generate a modulated ac-current. In other words, for a given V_{dc} if $I_{dc} = 0$ ($P_{ac} \cong P_{dc} = V_{dc}I_{dc}$), no reactive power can be generated as the boost - CSI is a unidirectional converter.

3.4 Steady-State Verification of Boost - CSI

In this subsection, the validity of the formulas developed in Section 3.3 is verified using simulation and experimental results. The efficiency and losses in the boost - CSI are also studied on a $2kW$, $240V_{LLrms}$ boost - CSI. The case study circuit parameters are given in Table 2.5.

Table 3.2: Circuit parameters for Steady State Verification.

L_{dc}	C_{ac}	L_{ac}	f_s
7.5mH	20μF	5mH	3.6kHz

Many investigations have been reported on the efficiency of boost rectifiers and single-phase boost inverters. However, only a few reports in literature can be found concerning the efficiency of three-phase boost inverters that are experimentally verified. Zhou et al. (2012) presented a three-phase boost inverter topology made of a coupling inductor, two diodes, two capacitors, and an inductor in the dc-side of a VSI [67]. In their work, a maximum efficiency of 83.4% was reported for a boost ratio of 2 (at the line-line output voltage of $220V_{rms}$) and a switching frequency of $8kHz$. Anand et al. (2014) presented a transformer-less grid-connected CSI with dc-bus capacitors, dc-link inductors, and an extra leg compared to the CSI topology [68]. However,

this inverter provided a boost ratio of about 1.33 (at the line-line output voltage of $400V_{rms}$) with a switching frequency of $7.5kHz$, and high efficiency of the inverter was only possible without the boost capability. Brito et al. (2015) presented a two-stage buck-boost integrated boost inverter, made of a cascaded dc-dc converter with a space vector PWM (SVPWM) based CSI [69]. In their work, an overall efficiency of 90% was reported for a boost ratio of 1.27 (at the line-line output voltage of $127V_{rms}$). The boost inverters reported prior to the work presented in this dissertation either have a low boost ratio or have a low efficiency. This dissertation presents a boost - CSI with high boost ratio ($V_{LL,rms}/V_{dc}$) of 3.5 and also has a high system efficiency using Reverse Blocking IGBTs (RB-IGBTs).

Table 3.3: Measured and calculated parameters of the grid-tied boost - CSI (simulation results).

v_{dc}(V)	D	I_{dc}(A)	I_{inv}^{rms}(A)		$I_{inv}^{rms}(f_1)$(A)	
		Meas.	Meas.	Calc.	Meas.	Calc.
60	0.791	10.63	3.887	3.968	1.589	1.645
65	0.773	9.76	3.713	3.797	1.593	1.640
70	0.755	9.029	3.567	3.649	1.589	1.638
75	0.737	8.408	3.459	3.521	1.594	1.637

The inverter quantities, I_{inv}^{rms} and $I_{inv}^{rms}(f_1)$ measured in simulation and calculated through the developed expressions in (3.17) and (3.20) for different input dc-voltage for grid-tied and stand-alone modes are summarized in Table 3.3 and Table 3.4, respectively. In the stand-alone mode of operation, the inverter output voltage is regulated at $208V$ for different input dc-voltage. It can be clearly observed from Table 3.3 that

the calculated results from (3.17) and (3.20) match closely to the simulated results and the error is less than 3%. In the grid-tied mode of operation, the inverter was regulated to supply $600W$ active power to the grid for varying input dc-voltages. The results for the grid-tied mode of operation are summarized in Table 3.4 with the maximum error of 3.5%.

Table 3.4: Measured and calculated parameters of the stand-alone boost - CSI (simulated results).

v_{dc}(V)	D	I_{dc}(A)	I_{inv}^{rms}(A)		$I_{inv}^{rms}(f_1)$(A)	
		Meas.	Meas.	Calc.	Meas.	Calc.
60	0.66	13.44	6.255	6.398	3.286	3.384
65	0.63	11.87	5.843	5.895	3.251	3.252
70	0.54	9.226	5.032	5.109	3.116	3.143
75	0.50	8.592	4.861	4.961	3.126	3.181

The validity of the developed characterization equations is experimentally evaluated using a laboratory scale $2kW$, $208V$ $(240V)$, $60Hz$ three-phase single-stage boost - CSI shown in Figure 3.18. Also, the efficiency of the overall system is calculated at different stages through a set of experiments for different input voltages and power levels.

The boost - CSI was designed and built using six individual reverse-blocking IGBTs (RB-IGBTs) [17], [22]-[24]. The inverter prototype, shown in Figure 3.18, contains two printed circuit boards called (i) control board and (ii) power board. The inverter is a self-powered device with control board powered directly by the dc input voltage. The IGBTs used in the boost - CSI are RB-IGBTs from Fuji, i.e. FGW85N60RB. The inverter switching is generated by Altera's DE0 FPGA development board [70], which receives a control signal from dSpace 1103.

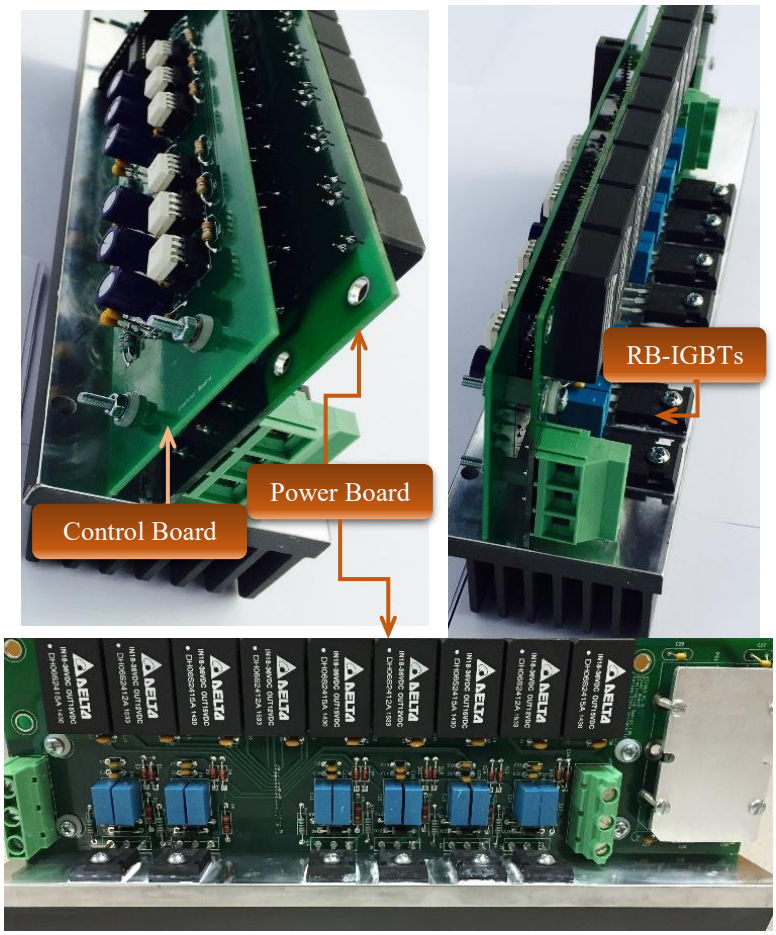

Fig. 3.18: Picture of the prototype $2kW$, $208V$ $(240V)$ three-phase single-stage boost - CSI.

In this work, the prototype boost - CSI was tested for various input dc-voltage, V_{dc}, values and load impedances. In these tests, the discretized switching pattern described earlier in Section 3.2 was implemented. In these tests, the fundamental and switching frequencies were set to $f_1 = 60Hz$ and$f_s = 3.6kHz$, respectively, with $M = 10$ and $N_T = 60$ in the discretized PPWM. The switching signals are generated by the FPGA using D and θ inputs, which are generated by the dSpace interface [70]. In this work, a simple direct PQ control scheme was implemented for the purpose of steady-state analysis of grid-tied boost - CSI. Basically, to build the closed-loop control scheme, the

grid-side line-to-line voltages and line currents are measured as feedback signals. The controller discussed in Subsection 4.2.2 was implemented in dSpace. The computed values of D and θ are then provided as input signals to the FPGA in order to generate the PPWM switching pattern described in Section 3.2.

Table 3.5: Measured and calculated parameters of the grid-tied boost - CSI (experimental results) for $P = 600W$.

v_{dc}(V)	D	I_{dc}(A)	I_{inv}^{rms}(A)		$I_{inv}^{rms}(f_1)$(A)	
		Meas.	Meas.	Calc.	Meas.	Calc.
60	0.80	10.98	3.88	4.01	1.56	1.63
65	0.78	10.11	3.70	3.87	1.59	1.64
70	0.765	9.41	3.58	3.72	1.61	1.64
75	0.74	8.71	3.51	3.63	1.61	1.68

Table 3.6: Measured and calculated parameters of the stand-alone boost - CSI (experimental results) for $V_{LL,rms} = 208V$.

v_{dc}(V)	D	I_{dc}(A)	I_{inv}^{rms}(A)		$I_{inv}^{rms}(f_1)$(A)	
		Meas.	Meas.	Calc.	Meas.	Calc.
60	0.66	14.53	6.90	6.70	3.66	3.59
65	0.64	13.57	6.64	6.32	3.62	3.54
70	0.60	10.88	5.62	5.61	3.22	3.37
75	0.58	9.87	5.22	5.25	3.07	2.99

Table 3.7: Simulated and experimentally obtained efficiency of the grid-tied boost - CSI.

v_{dc} (V)	Efficiency (%)					
	System		Inverter and Filter		Inverter	
	Sim.	Exp.	Sim.	Exp.	Sim.	Exp.
60	94.07	91.07	95.85	94.20	99.76	98.52
65	94.58	91.30	96.01	94.31	99.75	98.81
70	94.93	91.08	96.31	94.42	99.68	98.73
75	95.15	91.85	96.54	94.64	99.68	98.67

The measured and calculated quantities for grid-tied and stand-alone modes of operation are summarized in Table 3.5 and Table 3.6, respectively. The measured dc-link current was used to estimate $I_{inv}^{rms}(f_1)$ from (3.20). In order to verify the stand-alone case, the inverter was made to convert input dc-voltage to output $208V$ rms line-to-line voltage feeding a load. In the grid-tied test, the inverter injected active power to the grid for different input dc-voltages, where the desired reactive power was set to zero. The measurements were performed for many operating points and the results are given in Table 3.5, Table 3.6, and Table 3.7, as well as Figure 3.19, Figure 3.20, and Figure 3.21. It can be observed from the results given in Table 3.5 and Table 3.6 that the measured quantities closely match the calculated quantities with errors being less than 4%. During the grid-tied mode, efficiencies of the entire system, inverter with filter, and only inverter were also calculated. The efficiencies obtained through simulation and experimental results have been presented in Table 3.7. It can be observed from Table 3.7 that the overall system has an efficiency of about from $91-92\%$, for the entire operational range of the input dc voltage. The efficiency of the system, excluding the dc-link inductor loss, is more than 94%. Also, the dc-link

inductor contributes to about 1.5 to 3% of the system loss, while the filter capacitor and inductor contribute to 3 to 4% of the overall system loss.

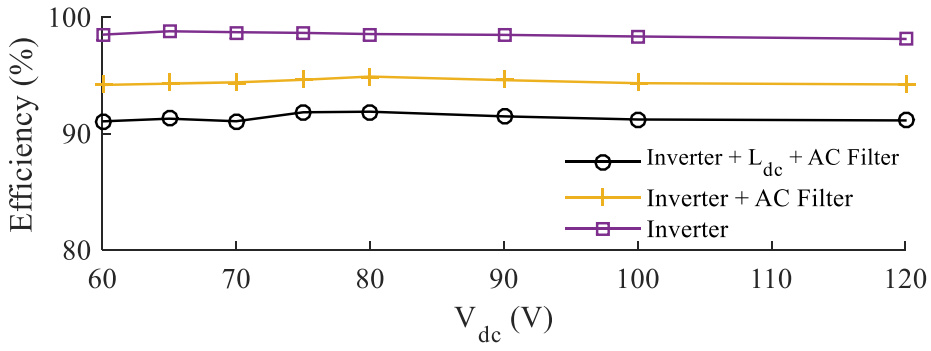

Fig. 3.19: Experimentally obtained efficiency of the prototype boost - CSI versus input dc-voltage for the grid voltage of $208V_{LL,rms}$, and $P_g = 600W$.

The inverter switching and conduction losses contribute to only about 1.5% losses, and this RB-IGBT based inverter is more than 98.5% efficient, as shown in Figure 3.19. Also, Figure 3.20 shows the efficiency of the overall system, inverter and ac filter, and inverter only versus the power injected to the grid for a constant input voltage, herein $V_{dc} = 80V$. It can be observed from Figure 3.19 and Figure 3.20 that the system efficiency is higher than 91% for the entire operating range. The efficiency of the prototype boost - CSI is comparable or better than contemporary three-phase two-stage boost - CSIs [71,72]. In Figure 3.21, the relationship between the power flow and the averaged charging duty ratio, D, is examined using experimentally obtained data. Figure 3.22 shows variation of the system efficiency and the THD of current injected to the grid with respect to power injected to the grid through experimental data. The variations of the power injected to the grid, P_g, versus the charging ratio are demonstrated in Figure 3.21(a). Herein, two main observations can be indicated; (i) an increase in the charging ratio will result in an increase in the power flow from the dc-source to the grid. In other words, the larger charging ratio means the more injected

power to the grid, and (ii) the $D-P$ relationship is almost linear. Also, the tested boost - CSI demonstrates a superior performance regarding its controllability for the boost ratios below $208V_{LLrms}/60V_{dc} = 3.47$. Figure 3.21(b) shows the relationship between the input power at the dc-source and the power injected to the grid for different values of input dc-voltage. It can be observed from Figure 3.21(b) that P_{dc} and P_g have a linear relationship regardless of the input dc-voltage level. Figure 3.22(a) shows the variation of the overall system efficiency versus P_g. It should be noted that this is the combined efficiency of the inverter, the dc-link inductor, and the ac filter. As can be seen, the system efficiency for the PPWM/RB-IGBT based single-stage boost - CSI is higher than the overall efficiency reported for the single-stage three-phase boost - CSI in [67], and for the current source inverter in [68], with similar ratings. It can be further deduced from Figure 3.22(a) that the tested system is optimal for operating around $P_g = 1kW$. Since there exists a maximum in the efficiency curves, it can be optimized by changing parameters in Table 3.2 for higher output power. Finally, Figure 3.22(b) represents variations of the current THD versus the power injected into the grid for different input dc-voltages. As can be seen, a THD of less than 5% was successfully achieved for all the operating points in the grid-tied mode of operation. It can be further observed that THDs for $V_{dc} = 120V$ and $60V$ are higher than for $V_{dc} = 80$ or $100V$. This indicates that the optimal operating input voltage (in terms of the THD level) is between $80V$ and $100V$ for the tested inverter. Figure 3.22(b) also shows that the current THD reaches almost 5% for higher boost ratios and the inverter operates best for boost ratios less than 3.5.

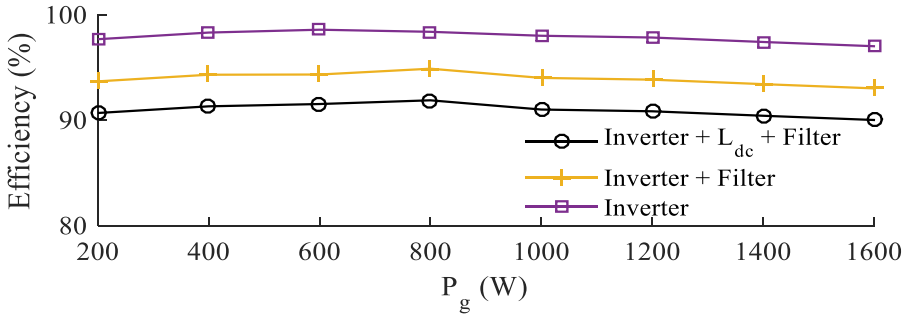

Fig. 3.20: Experimentally obtained efficiency of the prototype boost - CSI versus power injected into the grid for the input dc-voltage of $V_{dc} = 80V$.

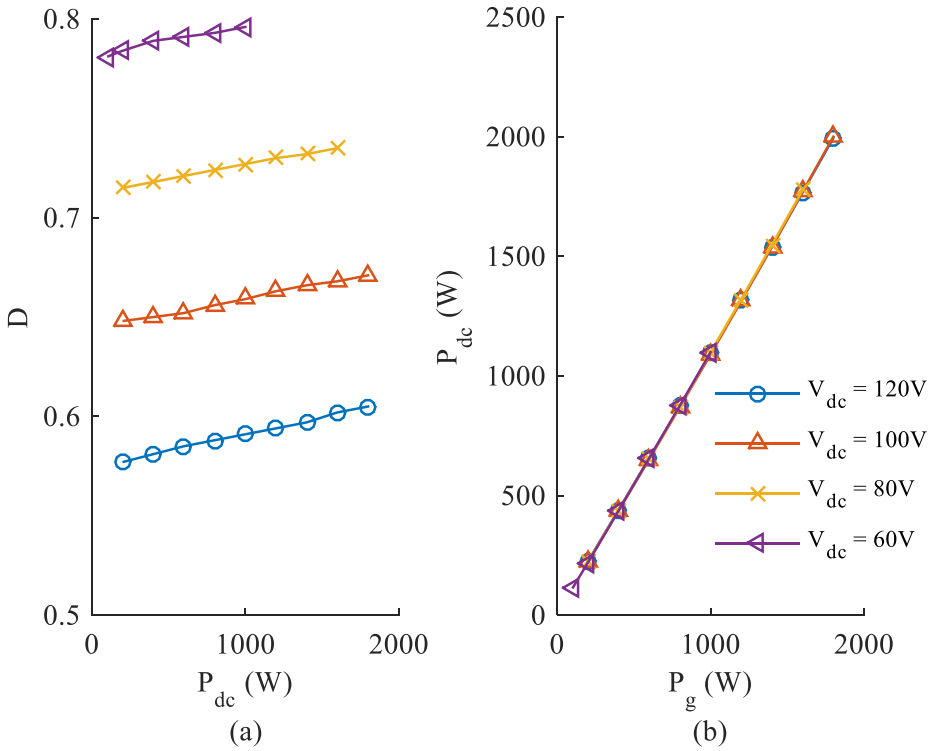

Fig. 3.21: Variations of the boost - CSI (a) charging duty ratio, D, vs. input power, P_{dc}, and (b) input power, P_{dc} vs. output power, P_g for different input dc voltages.

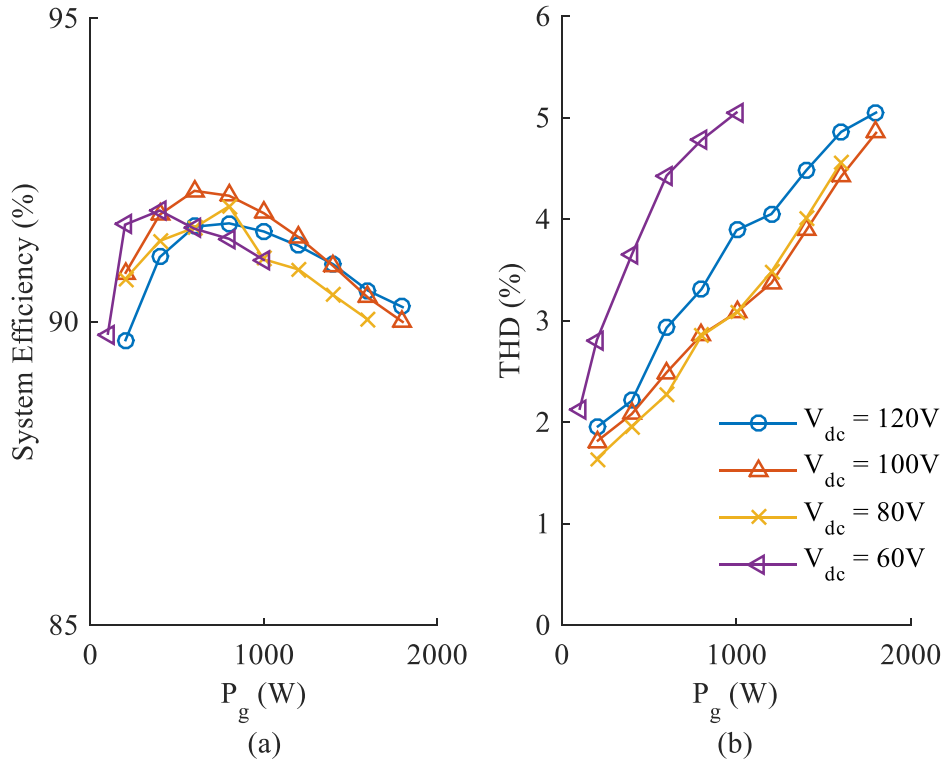

Fig. 3.22: Variations of the boost - CSI (a) system efficiency, η, vs. output power injected into the grid, and (b) THD of injected current into the grid vs. power for different input dc voltages.

3.5 Conclusion

In this chapter, the circuit topology of the three-phase single stage boost - CSI has been explained and the switching technique has been detailed. The CSI topology has been implemented using Reverse Blocking - IGBTs (RB-IGBTs) for the developed boost - CSI. In this chapter, the PPWM switching technique has been detailed and the difference between the developed PPWM switching technique and the conventional SVPWM switching technique has been explained. It has been shown that the PPWM switching developed earlier has asymmetrical pulse droppings when implemented using a low-resolution processor which results in a high THD in the inverter output voltage and current waveforms. The modified PPWM for the three-phase single stage boost

- CSI has been presented by discretizing the PPWM modulation technique to solve the problem of unsymmetrical switching. The finite on and off times associated with the switching devices might lead to a dead time during the switching transitions between devices. This will result in a high voltage spike across the devices. In this chapter, an overlap-time technique has been presented as a solution to suppress the voltage spikes across the RB-IGBTs in the boost - CSI and ensures that a path always exists for dc-link current. This chapter also provided a detailed steady-state analysis of both stand-alone and grid-tied PPWM based boost - CSI. This chapter formed the knowledge base for the steady-state analysis of the boost - CSI. The switching technique generates desired inverter output waveforms with THDs below 5% from low-voltage dc-sources, with higher efficiencies in comparison with two-stage dc-ac boost converters. Furthermore, characterization equations have been derived and verified using simulation and experimental results. The simulation and experimentally obtained data have been presented in order to validate the derived equation for both stand-alone and grid-tied modes of operation. The efficiency of the overall circuit, the inverter with the filter, and just the inverter has also been examined using simulation and experimentally obtained data. It has been verified experimentally that the efficiency of the prototype inverter and filter is comparable to commercial three-phase boost converters. The family of curves representing power injected to the grid with varying the charging duty ratio has been also presented for different input dc-voltages in this paper. The presented results demonstrate that the PPWM based three-phase single-stage boost - CSI is an efficient alternative for two-stage dc-ac boost converters. The application of the developed three-phase boost - CSI and the developed DDWT topology in the next chapter.

Chapter 4

Dynamic Models and Controllers for Boost-CSI

This chapter is focused on the development of the boost - CSI dynamic models, and controllers. This chapter is divided into three sections. Section 4.1 presents the development of the inverter dynamic models for both stand-alone and grid-tied modes of operation. The large-signal and small signal models of the boost - CSI are developed in stand-alone and grid-tied modes of operation. The boost - CSI controllers for voltage regulation in the stand-alone mode of operation, and active-reactive power control in the grid-tied mode are presented in Section 4.2. The conclusion of this chapter is provided in Section 4.3.

4.1 Dynamic Models of Boost-CSI: Stand-Alone and Grid-Tied Modes

In this section, the state space averaged model of the boost - CSI feeding a resistive-inductive (RL) load and connected to the grid is derived. In this work, the inverter

PWM frequency is assumed adequately higher than the frequency of fundamental ac waveforms, therefore, the averaging theorem described in [73], can be applied. The large-signal and small signal models for stand-alone and grid - tied boost - CSI are derived in this section. In addition to these models, the *dq* equivalent circuit of the boost - CSI is obtained from these models. A stability analysis of the system is also performed using these models. The developed models are verified using simulation and experimental data and the results are also presented in this section.

4.1.1 Stand-Alone Model

The state space averaged model of a three-phase boost - CSI feeding a resistive-inductive (RL) load is derived in this subsection. It should be noted that on-state resistance and voltage-drop of the solid-state switches are taken into account for developing the boost - CSI dynamic models. The state space model is developed in two steps. First, the boost - CSI equivalent circuits which represent boost - CSI behaviors in charging and discharging times are combined using averaging method. This results in six distinct state-space models, which are then converted into a single state space representation using a rotating reference frame transformation. Also, the small signal model of the boost - CSI is obtained by linearizing the large-signal model.

The circuit diagrams, corresponding state-space equations for each switching state of the boost - CSI feeding a resistive-inductive load, R_L,L_L, are summarized in Table 2.2. The boost - CSI circuit leads to three state space representations over a switching cycle, corresponding to the three switching states. In these state-space representations, the state vector x consists of state variables of the system, i.e. $x = \begin{bmatrix} i_{dc} & v_{ab} & v_{bc} & i_a & i_b \end{bmatrix}^T$, as shown in Figure 3.2. It should be noted that v_{ca} can always be rewritten in terms of v_{ab} and v_{bc}, therefore, the state space variables can remain the same for all six sectors. Similarly, i_c can be written in terms of i_a and i_b.

Table 4.1: Simplified circuit diagrams and state-space equations of the three-phase single-stage boost - CSI in the stand-alone and CCM of operation for Sector I.

C: $0 \le t < t_c$	*D1:* $t_c \le t < t_c + t_{d1}$	*D2:* $t_c + t_{d1} \le t < T_S$
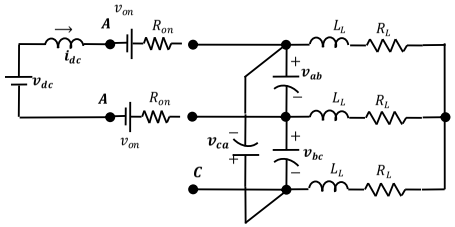	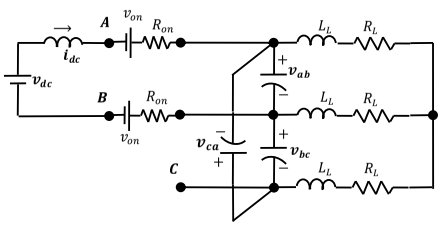	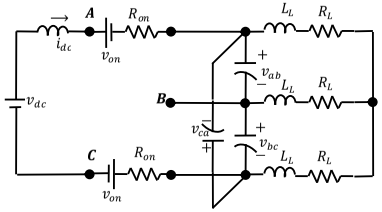
$\dot{\boldsymbol{x}} = \boldsymbol{A_{C1}x} + \boldsymbol{B_{C1}u}$	$\dot{\boldsymbol{x}} = \boldsymbol{A_{D1}x} + \boldsymbol{B_{D1}u}$	$\dot{\boldsymbol{x}} = \boldsymbol{A_{D2}x} + \boldsymbol{B_{D2}u}$
$\boldsymbol{A_{C1}} = \begin{bmatrix} \frac{-R_{dc}-2R_{on}}{L_{dc}} & 0 & 0 & 0 & 0 \\ 0 & 0 & 0 & \frac{-1}{3C_{ac}} & \frac{1}{3C_{ac}} \\ 0 & 0 & 0 & \frac{-1}{3C_{ac}} & \frac{-2}{3C_{ac}} \\ 0 & \frac{2}{3L_L} & \frac{1}{3L_L} & \frac{-R_L}{L_L} & 0 \\ 0 & \frac{-1}{3L_L} & \frac{1}{3L_L} & 0 & \frac{-R_L}{L_L} \end{bmatrix}$	$\boldsymbol{A_{D1}} = \begin{bmatrix} \frac{-R_{dc}-2R_{on}}{L_{dc}} & \frac{-1}{L_{dc}} & 0 & 0 & 0 \\ \frac{2}{3C_{ac}} & 0 & 0 & \frac{-1}{3C_{ac}} & \frac{1}{3C_{ac}} \\ \frac{-1}{3C_{ac}} & 0 & 0 & \frac{-1}{3C_{ac}} & \frac{-2}{3C_{ac}} \\ 0 & \frac{2}{3L_L} & \frac{1}{3L_L} & \frac{-R_L}{L_L} & 0 \\ 0 & \frac{-1}{3L_L} & \frac{1}{3L_L} & 0 & \frac{-R_L}{L_L} \end{bmatrix}$	$\boldsymbol{A_{D2}} = \begin{bmatrix} \frac{-R_{dc}-2R_{on}}{L_{dc}} & \frac{-1}{L_{dc}} & \frac{-1}{L_{dc}} & 0 & 0 \\ \frac{1}{3C_{ac}} & 0 & 0 & \frac{-1}{3C_{ac}} & \frac{1}{3C_{ac}} \\ \frac{1}{3C_{ac}} & 0 & 0 & \frac{-1}{3C_{ac}} & \frac{-2}{3C_{ac}} \\ 0 & \frac{2}{3L_L} & \frac{1}{3L_L} & \frac{-R_L}{L_L} & 0 \\ 0 & \frac{-1}{3L_L} & \frac{1}{3L_L} & 0 & \frac{-R_L}{L_L} \end{bmatrix}$
$\boldsymbol{x} = [i_{dc} \quad v_{ab} \quad v_{bc} \quad i_a \quad i_b]^T, \quad \boldsymbol{u} = v_{dc} - 2v_{on}, \quad \boldsymbol{B_{C1}} = \boldsymbol{B_{D1}} = \boldsymbol{B_{D2}} = \boldsymbol{B} = \left[\frac{1}{L_{dc}} \quad 0 \quad 0 \quad 0 \quad 0\right]^T, \quad and \quad T_S = t_c + t_{d1} + t_{d2}$		

Also, the input vector u is the dc-source voltage such that $u = v_{dc}$. Applying periodic averaging technique to these models results in $\dot{\widetilde{x}} = \bar{A}_I \widetilde{x} + \bar{B}u$ state space representation for Sector I where, $\widetilde{x}$ is the approximate state vector and $\bar{A}_I$ is the averaged state matrix of Sector (I) obtained from $\bar{A}_I = [d_c A_{C1} + d_1 A_{D1} + d_2 A_{D2}]$. Therefore, there are six time varying state space representations of the boost - CSI corresponding to the six sectors of PPWM, which are presented in Appendix (A). Transferring these six state space representations to the synchronously rotating dq reference frame results in a time-invariant state space averaged model, using (4.1).

$$\begin{bmatrix} \widetilde{v}_{ab} \\ \widetilde{v}_{bc} \end{bmatrix} = \begin{bmatrix} cos\left(\theta_f\right) & sin\left(\theta_f\right) \\ cos\left(\theta_f - \frac{2\pi}{3}\right) & sin\left(\theta_f - \frac{2\pi}{3}\right) \end{bmatrix} \begin{bmatrix} \widetilde{v}_q \\ \widetilde{v}_d \end{bmatrix} \tag{4.1}$$

where, θ_f is the angular displacement of the rotating dq reference frame. The duty cycles d_1, d_2, and d_c are replaced using

$$d_1 = msin\left(\frac{\pi}{3} - \theta\right) \tag{4.2}$$

$$d_2 = msin\left(\theta\right) \tag{4.3}$$

and

$$d_c = 1 - (d_1 + d_2) \tag{4.4}$$

The averaged matrix obtained for the six sectors in dq reference frame are same i.e., $\bar{A}_{dqI} = \bar{A}_{dqII} = \ldots = \bar{A}_{dqVI} = \bar{A}_{dq}$, . Therefore, $\bar{A}_{dq}$ forms the matrix A of the large-signal model [74].

The state-space-averaged representation of the boost - CSI feeding an R-L load in the rotating dq-frame of reference can be written as in (4.5) [45].

$$\frac{d}{dt}\begin{bmatrix} \widetilde{i}_{dc} \\ \widetilde{v}_q \\ \widetilde{v}_d \\ \widetilde{i}_q \\ \widetilde{i}_d \end{bmatrix} = \begin{bmatrix} \frac{-R_{dc}-2R_{on}}{L_{dc}} & \frac{-\sqrt{3}m}{L_{dc}} & 0 & 0 & 0 \\ \frac{\sqrt{3}m}{L_{dc}} & 0 & -\omega & \frac{-1}{2C_{ac}} & \frac{-\sqrt{3}}{6C_{ac}} \\ 0 & \omega & 0 & \frac{\sqrt{3}}{6C_{ac}} & \frac{-1}{2C_{ac}} \\ 0 & \frac{1}{2L_L} & \frac{-\sqrt{3}}{6L_L} & \frac{-R_L}{L_L} & -\omega \\ 0 & \frac{\sqrt{3}}{6L_L} & \frac{1}{2L_L} & \omega & \frac{-R_L}{L_L} \end{bmatrix} \begin{bmatrix} \widetilde{i}_{dc} \\ \widetilde{v}_q \\ \widetilde{v}_d \\ \widetilde{i}_q \\ \widetilde{i}_d \end{bmatrix} + \begin{bmatrix} \frac{1}{L_{dc}} \\ 0 \\ 0 \\ 0 \\ 0 \end{bmatrix} v_{dc} \qquad (4.5)$$

where, ω is the angular frequency of the reference line voltage and m is the modulation index. Equation (4.5) represents large-signal model of the boost - CSI. In order to study the inverter dynamics in the *dq*-reference frame for various loads, the *dq*-equivalent circuit representation of the system is important. Therefore, the *dq*-equivalent circuit representations of the boost - CSI must be obtained.

The *dq*-equivalent circuits for the three-phase single-stage boost - CSI are derived from the developed state-space model presented in (4.5). The order-five state-space model in (4.5) can be broken down to *q*-axis equations, *d*-axis equations on the ac-side and dc side equation linking the dc-side input circuit to the *d* and *q* quantities. The input dc-side dynamics of the boost - CSI can be expressed as

$$v_{dc} = (R_{dc} + 2R_{on})\, i_{dc} + L_{dc}\frac{di_{dc}}{dt} + \frac{\sqrt{3}}{2} m v_q \qquad (4.6)$$

The dc-voltage equation in (4.6) contains *q*-axis component which can be modelled as a dependent voltage source. Thus, the q-axis component in (4.6) links the dc-input to the ac *dq* quantities. It is therefore necessary to find the *q*-axis dynamics, which can be expressed as follows:

$$i_q = \frac{2\sqrt{3}}{3} m i_{dc} - 2C_{ac}\omega v_d - \frac{\sqrt{3}}{3} i_d - 2C_{ac}\frac{dv_q}{dt} \qquad (4.7)$$

$$v_q = 2R_L i_q + 2L_L \frac{di_q}{dt} + \frac{\sqrt{3}}{3} v_d + 2L_L \omega i_d \tag{4.8}$$

where, the voltage equation in (4.8) contains d-axis components. These terms can again be modelled as dependent voltage sources. Similarly, the current equation in (4.7) contains d-axis components, which can be modelled as dependent current sources. This leads to a need for obtaining d-axis dynamics, which can be expressed as

$$i_d = 2C_{ac} \omega v_q + \frac{\sqrt{3}}{3} i_q - 2C_{ac} \frac{dv_d}{dt} \tag{4.9}$$

$$v_d = 2R_L i_d + 2L_L \frac{di_d}{dt} - \frac{\sqrt{3}}{3} v_q - 2L_L \omega i_q \tag{4.10}$$

These equations can form the dq-equivalent circuits for the boost - CSI. Equation (4.6) can be represented as a circuit forming the dc-input, (4.7) and (4.8) form the q-axis, and (4.9) and (4.10) form the d-axis equivalent circuits. These circuits are shown in Figure 4.1 (a), (b), and (c), respectively [45]. As can be seen in Figure 4.1, the q-axis and d-axis equivalent circuits are formed by passive elements as well as dependent voltage and current sources. In Figure 4.1(a), the independent voltage source, v_{dc}, in the dc-equivalent circuit forms the system input, while a dependent voltage source makes the link between ac and dc sides of the circuit quantities. The dq-equivalent circuits can be used for analysis of a boost - CSI coupled with dynamic loads, as now the entire system can be represented in the same frame of reference. The dq-equivalent circuit representation can create a knowledge base for analysis of the boost - CSI. The dq-equivalent circuits in Figure 4.1 and equation (4.5) represent a linear time-invariant system, assuming that m, and ω are constant. However, the modulation index is commonly used as the input control signal to regulate inverter output voltage. Therefore, a small-signal model of the boost - CSI is needed.

The small-signal model of the three-phase boost - CSI feeding a resistive-inductive

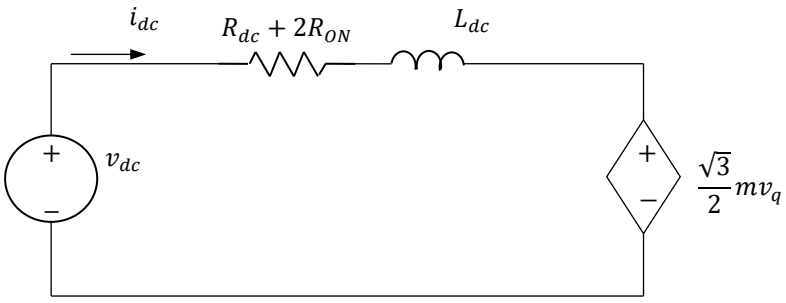

(a)

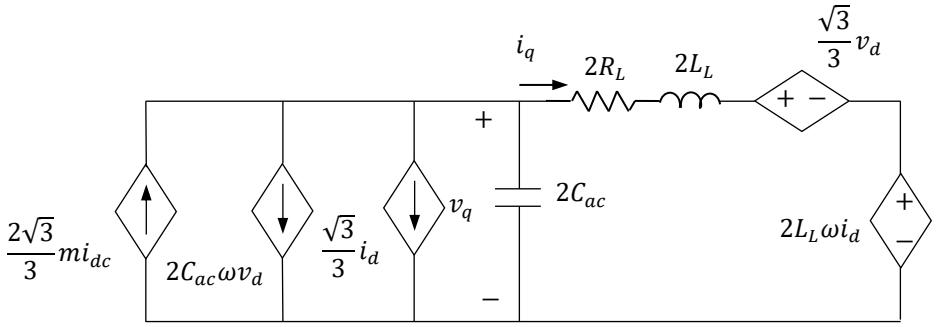

(b)

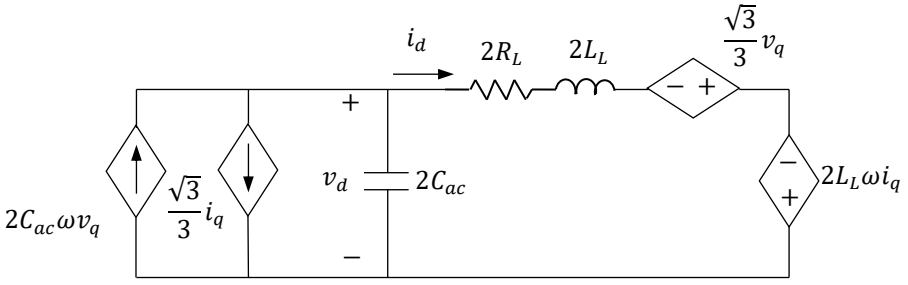

(c)

Fig. 4.1: The boost - CSI equivalent circuits; (a) dc-side equivalent circuit, (b) q-axis equivalent circuit; and (c) d-axis equivalent circuit in stand-alone mode of operation.

load is derived using the large signal model in (4.5). As illustrated in (4.5), v_{dc} represents the system input for constant values of m and ω. In practice, m is used to regulate the output voltage in stand-alone mode. Therefore, (4.5) cannot be considered a linear equation. However, (4.5) can be linearized around a steady-state operating point by defining small perturbations for the system variables as $\bar{x}_{dq} = \bar{X}_{dq} + \delta\bar{x}_{dq}$, $v_{dc} = V_{dc} + \delta v_{dc}$, $m = M + \delta m$, $\omega = \Omega + \delta\omega$, where $\widetilde{x}_{dq} = \begin{bmatrix} \widetilde{i}_{dc} & \widetilde{v}_{ab} & \widetilde{v}_{bc} & \widetilde{i}_a & \widetilde{i}_b \end{bmatrix}^T$ is the state vector, δ denotes small-signal perturbation, and capital quantities represent the steady-state operating point. The linearized (small-signal) model can be written as in (4.11) [45]. Equation (4.11) can be used to perform different linear control designs and small-signal stability studies on the boost - CSI for stand-alone applications.

$$\frac{d}{dt}\begin{bmatrix} \delta\widetilde{i}_{dc} \\ \delta\widetilde{v}_q \\ \delta\widetilde{v}_d \\ \delta\widetilde{i}_q \\ \delta\widetilde{i}_d \end{bmatrix} = \begin{bmatrix} \frac{-R_{dc}-2R_{on}}{L_{dc}} & \frac{-\sqrt{3}m}{2L_{dc}} & 0 & 0 & 0 \\ \frac{\sqrt{3}m}{3C_{ac}} & 0 & -\Omega & \frac{-1}{2C_{ac}} & \frac{-\sqrt{3}}{6C_{ac}} \\ 0 & \Omega & 0 & \frac{\sqrt{3}}{6C_{ac}} & \frac{-1}{2C_{ac}} \\ 0 & \frac{1}{2L_L} & \frac{-\sqrt{3}}{6L_L} & \frac{-R_L}{L_L} & -\Omega \\ 0 & \frac{\sqrt{3}}{6L_L} & \frac{1}{2L_L} & \Omega & \frac{-R_L}{L_L} \end{bmatrix}\begin{bmatrix} \delta\widetilde{i}_{dc} \\ \delta\widetilde{v}_q \\ \delta\widetilde{v}_d \\ \delta\widetilde{i}_q \\ \delta\widetilde{i}_d \end{bmatrix} + \ldots$$

$$\ldots \begin{bmatrix} \frac{1}{L_{dc}} & \frac{-\sqrt{3}}{2L_{dc}}\widetilde{V}_q & 0 \\ 0 & \frac{\sqrt{3}}{3C_{ac}}\widetilde{I}_{dc} & -\widetilde{V}_d \\ 0 & 0 & \widetilde{V}_q \\ 0 & 0 & -\widetilde{I}_d \\ 0 & 0 & \widetilde{I}_q \end{bmatrix}\begin{bmatrix} \delta v_{dc} \\ \delta m \\ \delta\omega \end{bmatrix} \tag{4.11}$$

The developed models for large and small signal dynamics of the boost - CSI for the stand-alone mode of operation are presented in (4.5) and (4.11), respectively. These models are verified first using a circuit simulation and then using a laboratory test setup. The values of main circuit parameters for the laboratory setup are given in

Table 4.2: System parameters.

Parameter	Nominal values
v_{dc}	65 V
L_{dc}	10 mH
R_{dc}	0.5 Ω
C_{ac}	20 μF
L_L	7.5 mH
R_L	70 Ω
$v_{LL\,rms}$	208 V

Table 4.2. The dc-link inductor, ac-filter inductors, and PWM switching frequency have not been optimized for this study. In order to verify the validity of the developed state-space-averaged model, a laboratory-scale three-phase single-stage boost - CSI, feeding an RL load, has been modeled and simulated in MATLAB/Simulink using the SimPowerSystems toolbox.

Firstly, the dynamic behaviors of the boost - CSI, when generates a line-to-line rms voltage of $208V$ from a $65V_{dc}$ with a PWM frequency of $2.4kHz$, are studied using circuit simulations. In Figure 4.2, the boost - CSI response to a step change of v_{dc}, from zero to $65V$, is demonstrated. In this figure, the gray color waveforms demonstrate the results obtained from the circuit simulation and the black color waveforms are obtained from solving (4.5). As can be seen, the results obtained from solving the averaged model in (4.5) are in very good agreement with the circuit simulation results. In Figure 4.3, the system response to a small step change in the duty ratio, D, or the modulation index, m, is shown. Again, the relationship between the charging duty ratio, D, and the modulation index, m, is $D = 1 - \frac{3}{\pi}m$, as discussed earlier in Chapter 3. In Figure 4.3, a step change to the modulation index, m, is applied at $t = 5msec$.

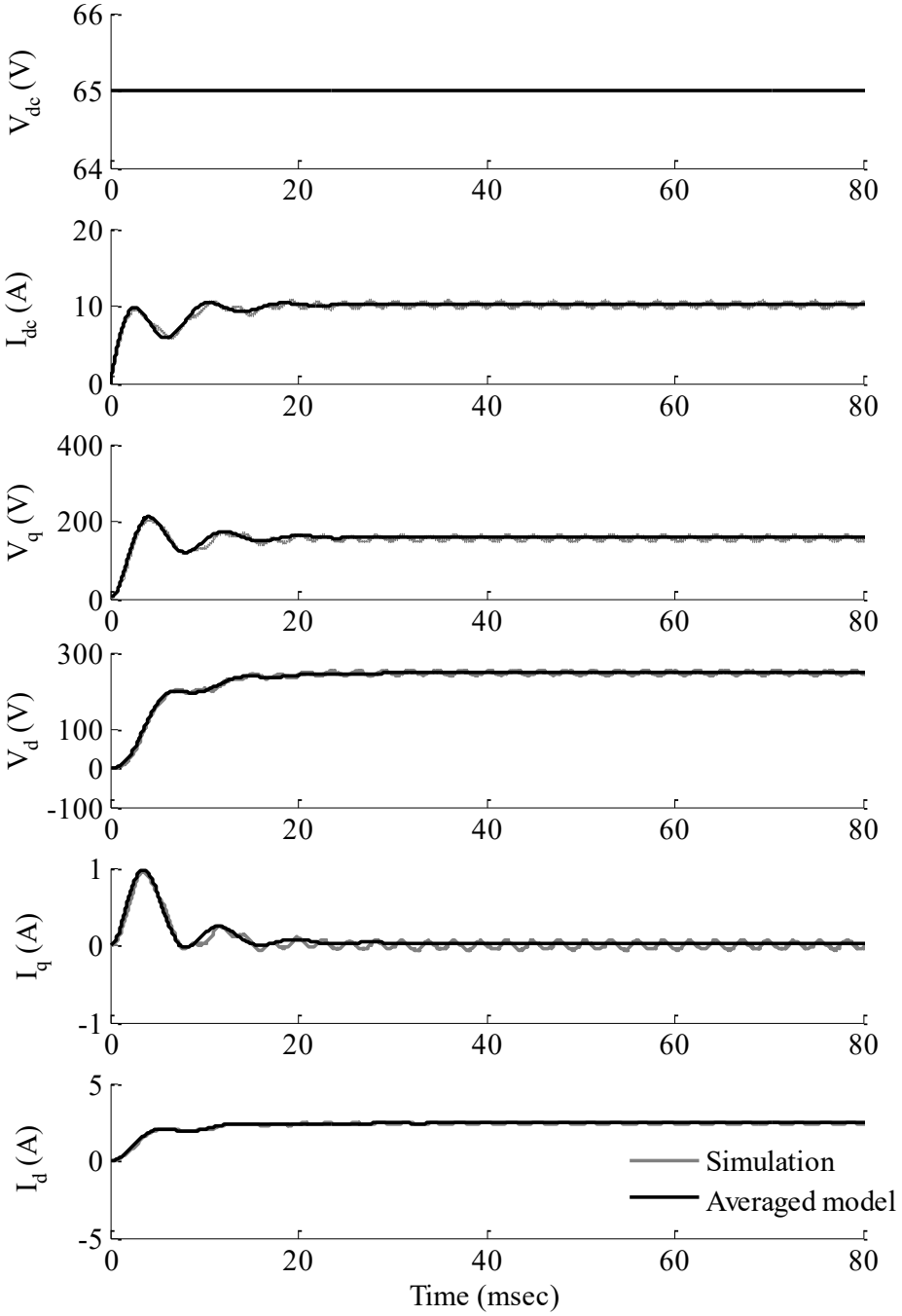

Fig. 4.2: Simulated (Gray) and model (Black) waveforms of v_{dc}, i_{dc}, v_q, v_d, i_q and i_d during startup.

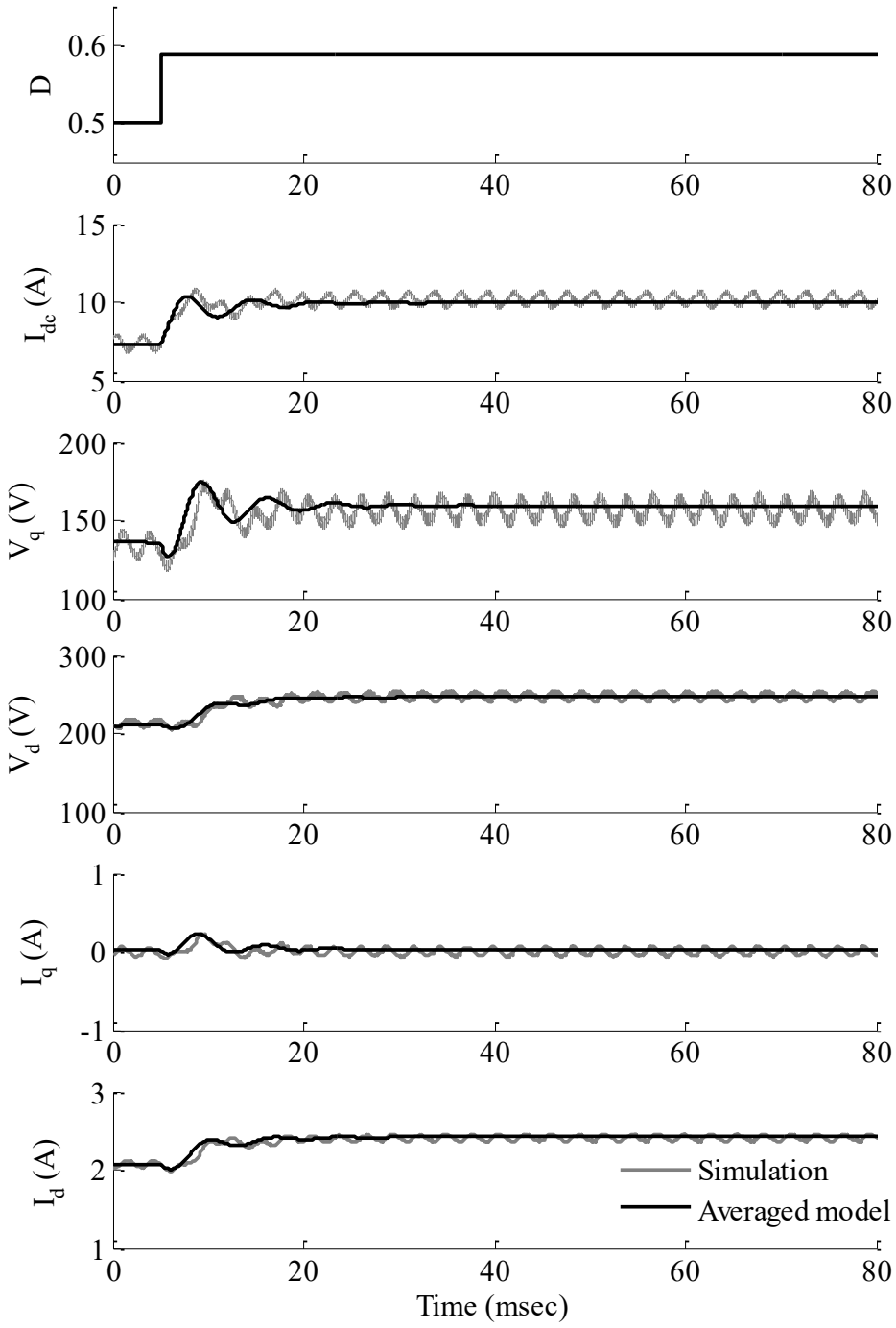

Fig. 4.3: Simulated (Gray) and model (Black) waveforms of D, i_{dc}, v_q, v_d, i_q and i_d for a step change in D.

In this example, m suddenly decreases from 0.51 to 0.433, i.e. D increases from 0.49 to 0.589. In this figure, the black color waveforms were obtained from solving (4.11), and the gray color waveforms are from the circuit simulation that contains the inverter PWM switching transients. These two case scenarios were repeated in the laboratory to further confirm the validity of the developed state space models in (4.5) and (4.11). In order to verify the validity of the developed state-space-averaged model, a $2kW$, $208/240V$ boost - CSI made of reverse-blocking IGBTs (RB-IGBTs) was designed and built in the laboratory. The system parameters in the developed setup are the same as the ones applied in the circuit simulation and summarized in Table 4.2. The prototype boost - CSI was switched at $f_s = 2.4kHz$. The switching signals were implemented using a dSpace 1103 as the interface circuit between computer and hardware in the setup. The dSpace provides rapid control prototyping for power electronic circuits using Matlab/Simulink programming. Furthermore, the experimental results presented in this section were acquired using a LeCroy Waverunner 64XI oscilloscope equipped with ADP305 differential high-voltage probes ($100MHz$ bandwidth) and CP031 high-current ($50MHz$ bandwidth) probes.

The experimentally obtained data from the prototype boost - CSI and the state-space-averaged models in (4.5) and (4.11) are plotted in Figure 4.4 and Figure 4.5. As shown in these figures, the outputs of the state-space-averaged models are in good agreement with the experimentally obtained data. The start-up transient results in which the dc-source voltage is switched from zero to $65V$ are shown in Figure 4.4. In this test scenario, the input dc voltage, v_{dc}, increases exponentially from zero to $65V$ over around $20msec$. The same input dc voltage waveform is given to the model in (4.5), and both experimental and model results are plotted in Figure 4.4. Moreover, in order to verify the small-signal model in (4.11), the model was solved for a step change in D, from 0.49 to 0.59 at $t = 20msec$, and the same was performed in the

control scheme of the prototype boost - CSI. As shown in Figure 4.5, the experimental results satisfactorily match the results obtained from the developed state-space models in (4.5) and (4.11).

4.1.2 Grid - Connected Model

The models presented in this subsection, are derived assuming the inverter PWM frequency is adequately higher than the frequency of fundamental ac voltages and currents. These assumptions allow the averaging theorem described in [73] to be applied to obtain the averaged models. The state-space representation of the boost - CSI operating in stand-alone mode has been derived in [45]. Similarly, the state-space representation for a grid-connected three-phase boost - CSI operated by Phasor PWM (PPWM) technique described in [42,43,45] can be obtained. For the six sectors of PPWM, there are six different sets of equations, and consequently six distinct state matrices, namely $\overline{A_I}$, $\overline{A_{II}}$, $\overline{A_{III}}$, $\overline{A_{IV}}$, $\overline{A_V}$, and $\overline{A_{VI}}$,see Appendix A. The state-space-averaged representation of grid-connected boost - CSI in the rotating dq-frame of reference can be written as in (4.12). In (4.12), $\widetilde{v}_q$ and $\widetilde{v}_d$ are the dq components of inverter line-to-line voltages, v_q^g and v_d^g are dq components of the grid voltage, $\widetilde{i}_q$ and $\widetilde{i}_d$ are dq components of inverter line currents,$\widetilde{i}_{dc}$ is the dc-link current, and v_{dc} is the input dc voltage.

$$\frac{d}{dt}\begin{bmatrix} \widetilde{i}_{dc} \\ \widetilde{v}_q \\ \widetilde{v}_d \\ \widetilde{i}_q \\ \widetilde{i}_d \end{bmatrix} = \begin{bmatrix} \frac{-R_{dc}}{L_{dc}} & \frac{-\sqrt{3}mcos(\phi)}{2L_{dc}} & \frac{-\sqrt{3}msin(\phi)}{2L_{dc}} & 0 & 0 \\ \frac{\sqrt{3}mcos(\phi)}{3C_{ac}} & 0 & -\omega_g & \frac{-1}{2C_{ac}} & \frac{-\sqrt{3}}{6C_{ac}} \\ \frac{\sqrt{3}msin(\phi)}{3C_{ac}} & \omega_g & 0 & \frac{\sqrt{3}}{6C_{ac}} & \frac{-1}{2C_{ac}} \\ 0 & \frac{1}{2L_g} & \frac{-\sqrt{3}}{6L_g} & \frac{-R_g}{L_g} & -\omega_g \\ 0 & \frac{\sqrt{3}}{6L_g} & \frac{1}{2L_g} & \omega_g & \frac{-R_g}{L_g} \end{bmatrix} \begin{bmatrix} \widetilde{i}_{dc} \\ \widetilde{v}_q \\ \widetilde{v}_d \\ \widetilde{i}_q \\ \widetilde{i}_d \end{bmatrix} + \dots$$

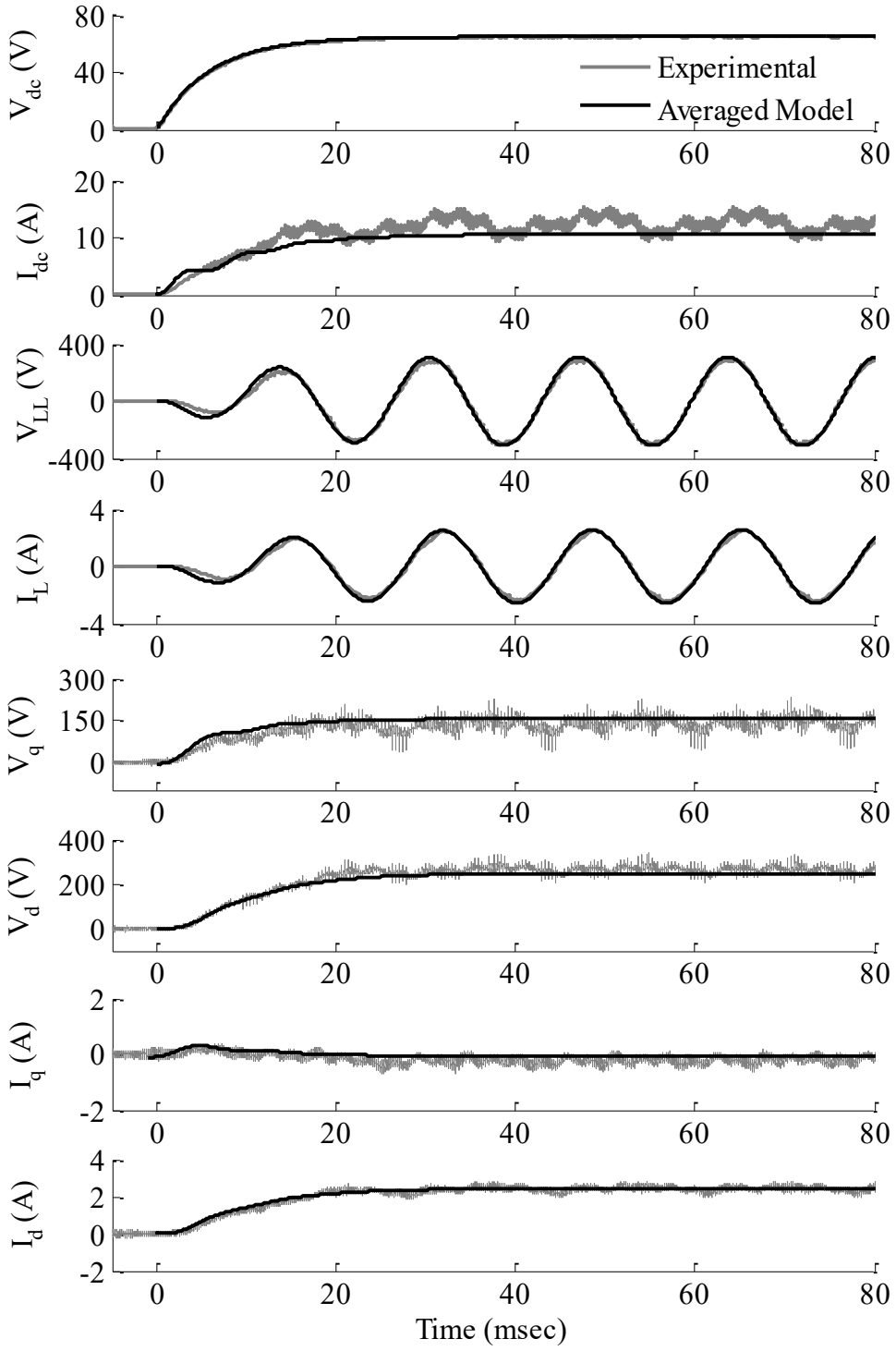

Fig. 4.4: Experimental (Gray) and model (Black) waveforms of v_{dc}, i_{dc}, v_{LL}, i_L, v_q, v_d, i_q and i_d during startup.

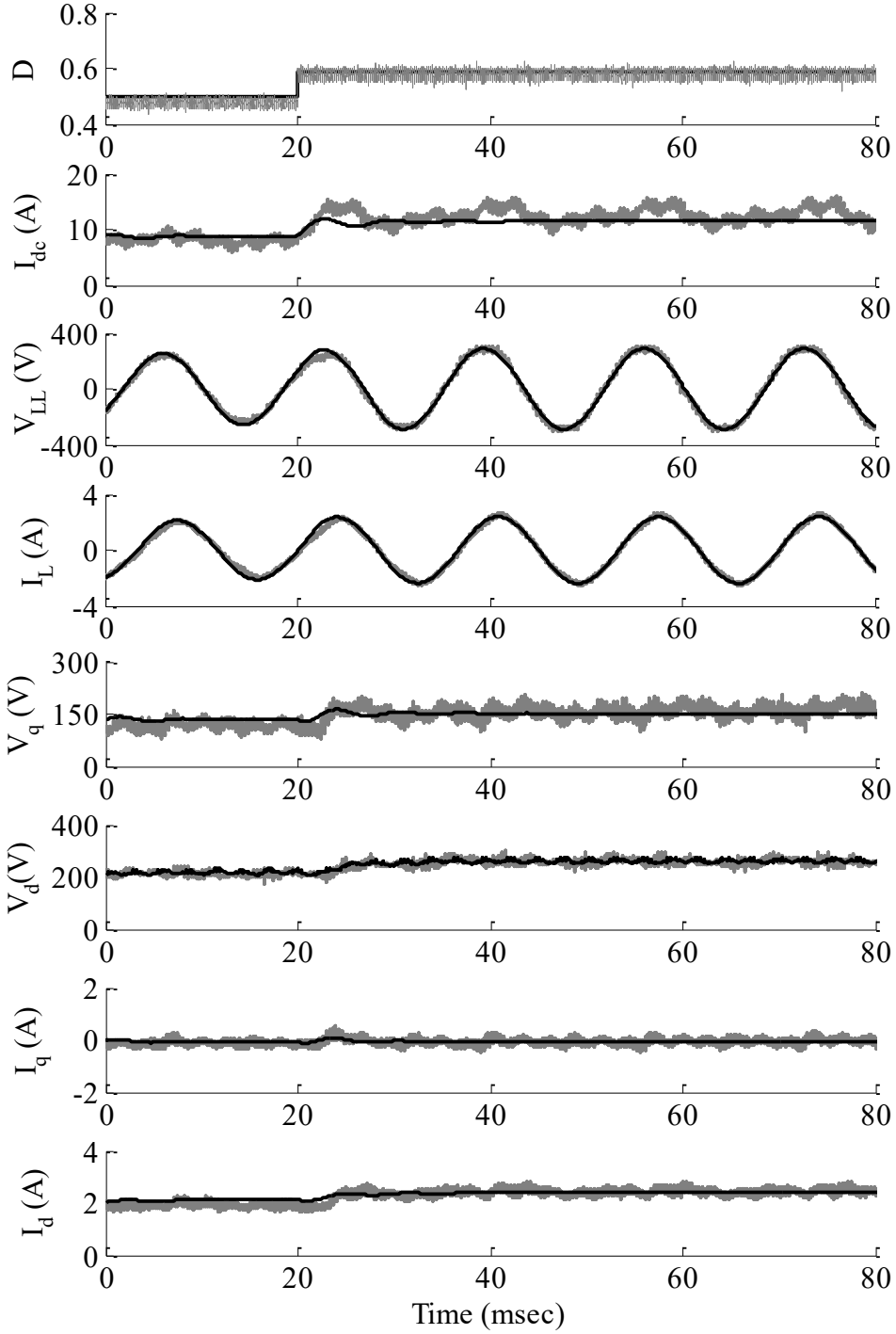

Fig. 4.5: Experimental (Gray) and model (Black) waveforms of D, i_{dc}, v_{LL}, i_L, v_q, v_d, i_q and i_d for a step change in D.

$$\ldots + \begin{bmatrix} \frac{1}{L_{dc}} & 0 & 0 \\ 0 & 0 & 0 \\ 0 & 0 & 0 \\ 0 & -\frac{1}{2L_g} & \frac{\sqrt{3}}{6L_g} \\ 0 & -\frac{\sqrt{3}}{6L_g} & -\frac{1}{2L_g} \end{bmatrix} \begin{bmatrix} v_{dc} \\ v_q^g \\ v_d^g \end{bmatrix} \tag{4.12}$$

The model in (4.12) represents the linear time-invariant state-space model of the boost - CSI assuming that m, and the phase angle between the output voltage of the single-stage boost - CSI, v_{ab}, and the grid voltage, v_{ab}^g, ϕ are constant. However, in practice, m and ϕ can be used to control the injected power to the grid. In this case, (4.12) will be a non-linear model. Thus, by linearizing (4.12) around an operating point, the small signal model can be obtained as in (4.13), where, $\widetilde{V}_q$, $\widetilde{V}_d$, $\widetilde{M}$, and $\widetilde{I}_{dc}$ correspond to the operating point. In order to study inverter dynamics for different operating points and stability analysis of open and closed loop grid-connected inverter in dq-frame of reference the dq- equivalent circuit representation of the system is very important.

$$\frac{d}{dt}\begin{bmatrix} \delta\widetilde{i}_{dc} \\ \delta\widetilde{v}_q \\ \delta\widetilde{v}_d \\ \delta\widetilde{i}_q \\ \delta\widetilde{i}_d \end{bmatrix} = \begin{bmatrix} \frac{-R_{dc}}{L_{dc}} & \frac{-\sqrt{3}\widetilde{M}cos(\phi)}{2L_{dc}} & \frac{-\sqrt{3}\widetilde{M}sin(\phi)}{2L_{dc}} & 0 & 0 \\ \frac{\sqrt{3}\widetilde{M}cos(\phi)}{3C_{ac}} & 0 & -\omega_g & \frac{-1}{2C_{ac}} & \frac{-\sqrt{3}}{6C_{ac}} \\ \frac{\sqrt{3}\widetilde{M}sin(\phi)}{3C_{ac}} & \omega_g & 0 & \frac{\sqrt{3}}{6C_{ac}} & \frac{-1}{2C_{ac}} \\ 0 & \frac{1}{2L_g} & \frac{-\sqrt{3}}{6L_g} & \frac{-R_g}{L_g} & -\omega_g \\ 0 & \frac{\sqrt{3}}{6L_g} & \frac{1}{2L_g} & \omega_g & \frac{-R_g}{L_g} \end{bmatrix} \begin{bmatrix} \delta\widetilde{i}_{dc} \\ \delta\widetilde{v}_q \\ \delta\widetilde{v}_d \\ \delta\widetilde{i}_q \\ \delta\widetilde{i}_d \end{bmatrix} + \ldots$$

$$\ldots + \begin{bmatrix} \frac{1}{L_{dc}} & 0 & 0 & \frac{-\sqrt{3}\left[cos(\phi)\widetilde{V}_q + sin(\phi)\widetilde{V}_d\right]}{2L_{dc}} & \frac{-\sqrt{3}\widetilde{M}\left[sin(\phi)\widetilde{V}_q + cos(\phi)\widetilde{V}_d\right]}{2L_{dc}} & 0 \\ 0 & 0 & 0 & \frac{\sqrt{3}cos(\phi)\widetilde{I}_{dc}}{3C_{ac}} & \frac{-\sqrt{3}\widetilde{M}sin(\phi)\widetilde{I}_{dc}}{3C_{ac}} & -\widetilde{V}_d \\ 0 & 0 & 0 & \frac{\sqrt{3}sin(\phi)\widetilde{I}_{dc}}{3C_{ac}} & \frac{\sqrt{3}\widetilde{M}cos(\phi)\widetilde{I}_{dc}}{3C_{ac}} & \widetilde{V}_q \\ 0 & \frac{-1}{2L_g} & \frac{\sqrt{3}}{6L_g} & 0 & 0 & -\widetilde{I}_d \\ 0 & \frac{-\sqrt{3}}{6L_g} & \frac{-1}{2L_g} & 0 & 0 & \widetilde{I}_q \end{bmatrix} \begin{bmatrix} \delta v_{dc} \\ \delta v_q^g \\ \delta v_d^g \\ \delta m \\ \delta \phi \\ \delta \omega \end{bmatrix} \tag{4.13}$$

The dq-equivalent circuits for the grid-connected three-phase boost - CSI are derived from the linearized average state-space model presented in (4.13). The fifth order dynamic model developed in (4.13) can be used to get q-axis equations, d-axis equations for the ac side of the inverter and the dc-bus equation in order to link the input dc side to the output ac side. The equation representing the input dc-side of the grid-connected inverter can be expressed as

$$v_{dc} = R_{dc}i_{dc} + L_{dc}\frac{di_{dc}}{dt} + \frac{\sqrt{3}mcos\left(\phi\right)}{2}v_q + \frac{\sqrt{3}msin\left(\phi\right)}{2}v_d \tag{4.14}$$

The dc-side equation in (4.14) has both q-axis and d-axis components which link the input side equation to the output dq quantities of the inverter. This makes it essential to obtain the d-axis and q-axis equations in order to obtain the full dynamic model. The q-axis equations for the inverter can be expressed as follows:

$$i_q = \frac{2mcos\left(\phi\right)}{\sqrt{3}}i_{dc} - 2C_{ac}\omega v_d - \frac{1}{\sqrt{3}}i_d - 2C_{ac}\frac{dv_q}{dt} \tag{4.15}$$

$$v_q = 2R_g i_q + 2L_g\frac{di_q}{dt} + \frac{1}{\sqrt{3}}v_d + 2L_g\omega_g i_d + v_q^g - \frac{1}{\sqrt{3}}v_d^g \tag{4.16}$$

Equations in (4.15) and (4.16) represent the q-axis dynamics of the boost - CSI. Both

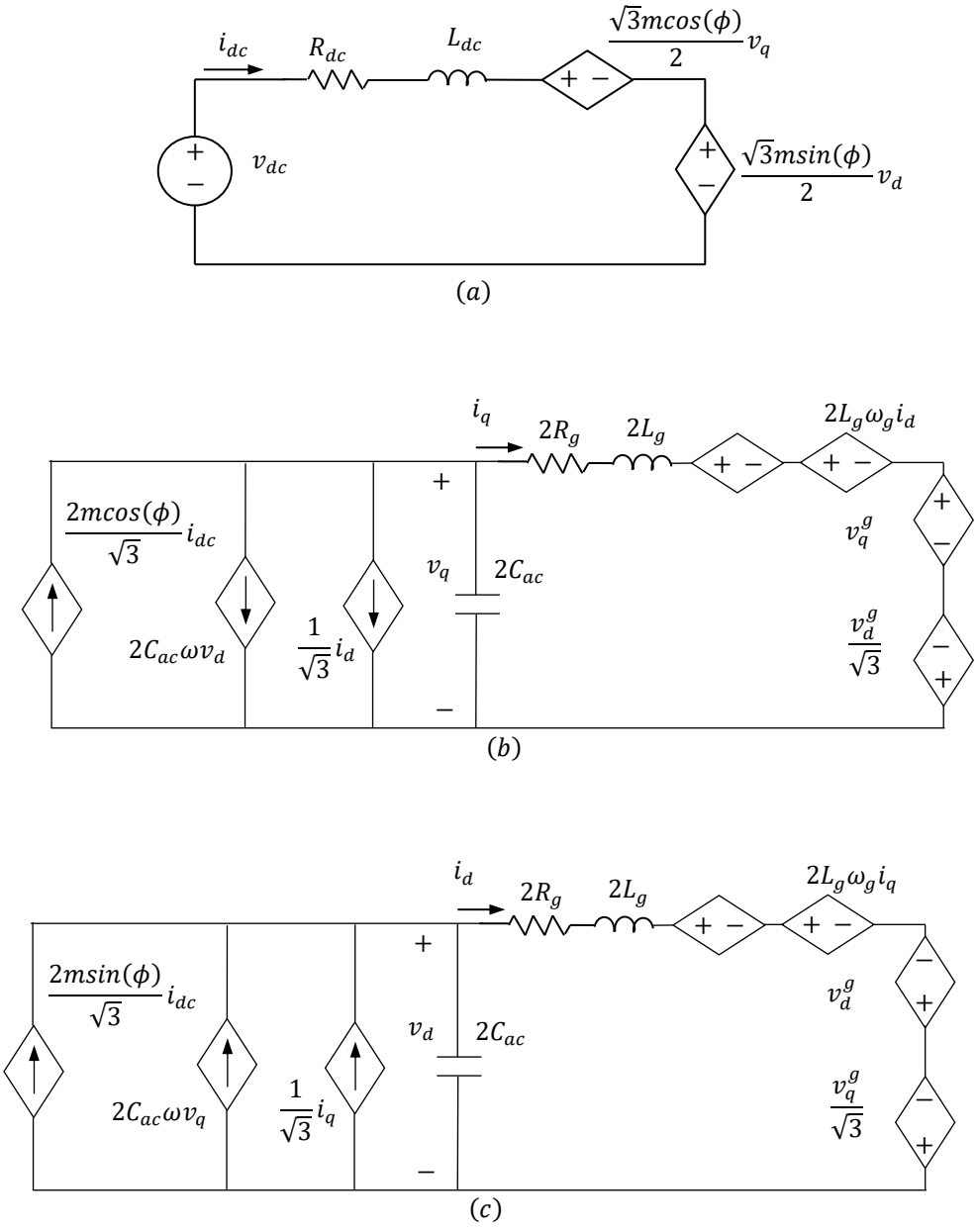

Fig. 4.6: The boost - CSI equivalent circuits; (a) dc-side equivalent circuit, (b) q-axis equivalent circuit; and (c) d-axis equivalent circuit in the grid-tied mode of operation.

the input side dynamic equation, and q-axis dynamic equations have d-axis components associated with them which makes it necessary to obtain the d-axis dynamic equation for the inverter. The d-axis dynamics can be expressed as

$$i_d = \frac{2msin\,(\phi)}{\sqrt{3}} i_{dc} + 2C_{ac}\omega v_q - \frac{1}{\sqrt{3}} i_q - 2C_{ac}\frac{dv_d}{dt} \tag{4.17}$$

$$v_d = 2R_g i_d + 2L_g \frac{di_d}{dt} - \frac{1}{\sqrt{3}} v_q - 2L_g \omega_g i_q + v_d^g - \frac{1}{\sqrt{3}} v_q^g \tag{4.18}$$

These equations can be used to form the dq-equivalent circuits for the grid-connected three-phase boost - CSI. Equation (4.14) forms the input dc-side circuit for the inverter, (4.15) and (4.16) form the q-axis circuits, and (4.17) and (4.18) form the d-axis circuit. These circuits are presented in Figure 4.6(a), (b), and (c), respectively. The independent dc-source in Figure 4.6(a) forms the input to the system, while the dependent sources act as the link between the input dc-side and the output ac-side of the boost - CSI.

4.2 Controllers for Boost-CSI

4.2.1 Stand - Alone System

Stability of the boost - CSI with respect to the variation in input signals, i.e. m and ω, as well as load parameters are studied using the developed small-signal model, represented by (4.11). The study is based on the experimental setup that is built in the laboratory for test and verification. The parameters of the developed setup are summarized in Table 4.2. Substituting these values into (4.11) results in the state vector equilibrium point of $X_{dq} = \begin{bmatrix} 12.30 & 178.75 & 234.71 & 0.23 & 2.83 \end{bmatrix}^T$, which corresponds to a line-to-line rms voltage of $208.5V$ and a line rms current of $2.01A$. The eigenvalues

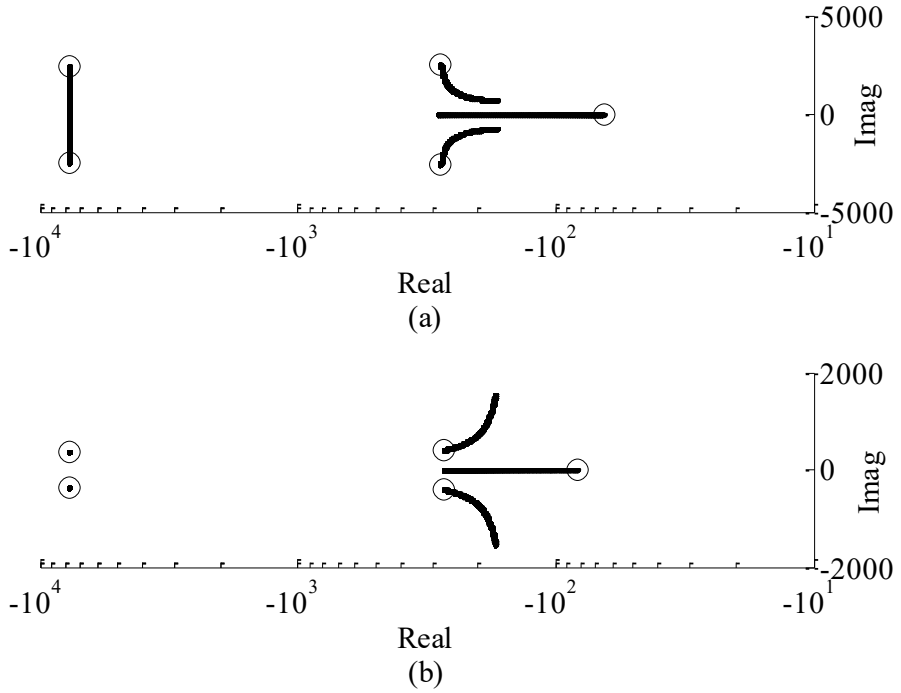

Fig. 4.7: Root locus of small-signal poles (eigenvalues) of the stand-alone boost - CSI as (a) ω, or f varies from $10Hz$ to $400Hz$; (b) m, or D varies from 0.1 to 0.9.

of the system at this operating point are obtained as $\lambda_1 = -220.7$, $\lambda_{2,3} = -202.0 \pm j705.7$, and $\lambda_{4,5} = -7.713 \times 10^3 \pm j376.9$. These five eigenvalues are located in the left-half s-plane, indicating a stable system. However, this does not necessarily mean that the system will be stable for input signal variations and load parameter changes. Therefore, variations of the overall system eigenvalues with respect to changes in the input control signals and load parameters must be studied.

The system eigenvalues are shown in Figure 4.7(a), in which the frequency varies from $10Hz(62.83\,rad/sec)$ to $400Hz$ $(2513.3\,rad/sec)$, with all nominal parameter values provided in Table 4.2. The range of frequency is chosen based on the typical frequency range used in adjustable speed drive systems [75, 76]. As shown in Figure 4.7(a), the eigenvalues move toward the origin as the system frequency increases, and

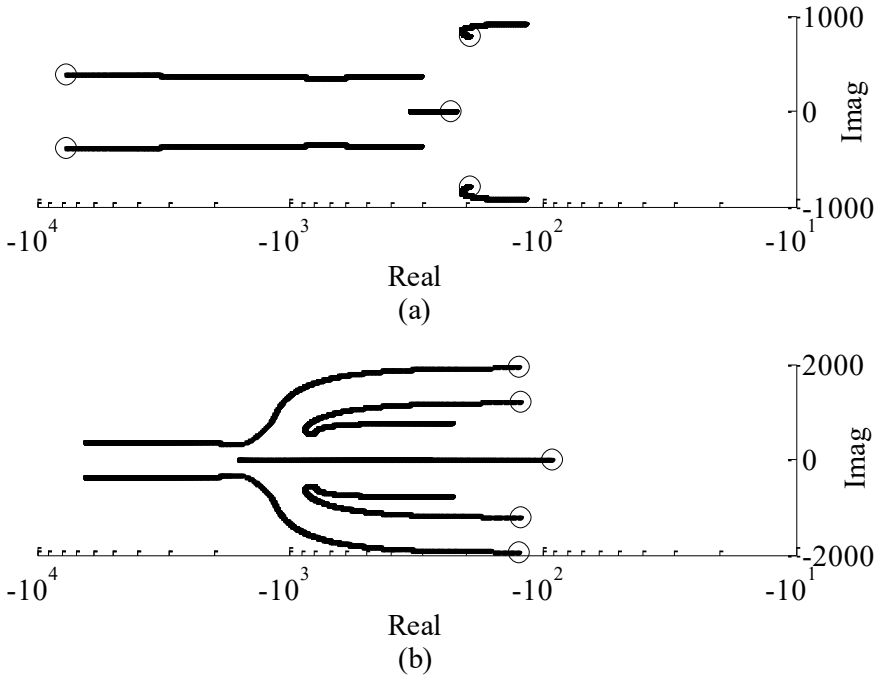

Fig. 4.8: Root locus of small-signal poles (eigenvalues) of the stand-alone boost - CSI as (a) power factor varies from 0.999 to 0.799; (b) R_L varies from $0.06p.u.$ to $2.5p.u.$.

therefore the damping factor of the system decreases, when the overall system remains stable. The root locus of small signal poles (eigenvalues) of the stand-alone boost - CSI as m varies from 0.1047 to 0.9425 is shown in Figure 4.7(b). This range of m corresponds to the charging ratio, D, variation from 0.1 to 0.9, as the relationship between these parameters has been given in Section 3.2. This variation in D covers the entire operating range of the boost - CSI corresponding to the system parameters given in Table 4.2. It can be observed that the eigenvalues of the boost - CSI lie on the left half of the s-plane for the entire operating range, indicating the stability of the boost - CSI over the range. As can be seen, the imaginary part absolute values of λ_2 and λ_3 increase whereas the real part absolute values decrease as m increases. Unlike λ_2 and λ_3, λ_1 moves away from the imaginary axis as m increases. However,

since the pair eigenvalues, λ_2 and λ_3, have higher weights than the single one, it can be expected that the overall system response becomes more oscillatory as m increases. Nevertheless, the overall system remains stable for the entire range of m variation.

The system eigenvalues as the load power factor varies from 1 to 0.8 is shown in Figure 4.8(a). In this case, the load power factor changes while the load impedance is kept constant. This power factor range is chosen to analyze the system stability for common power factors encountered in loads. It can be observed from Figure 4.8(a) that with the decrease in power factor, λ_2, λ_3, λ_4 and λ_5 eigenvalues move toward right, staying in the left-half s-plane and λ_1 eigenvalue toward the left. In this case, even though four eigenvalues move toward right, they always stay in the left-half s-plane even for lower power factor values. Thus, the system is stable with variation in load power factor. Figure 4.8(b) demonstrates the root locus of small signal poles (eigenvalues) of the stand-alone boost - CSI as the load resistance, R_L varies from $0.06p.u.$ to $2.5p.u.$ Here, the base values for the power and line-to-line voltage are chosen based on the laboratory setup rated values, i.e., base power is $2kW$ and base voltage is $240V$. It can be clearly observed from Figure 4.8(b) that as the load resistance increases all the eigenvalues move to the left half s-plane. As the load resistance increases λ_1, λ_4 and λ_5 move toward left in the s-plane, and λ_2 and λ_3 move to the right. For the entire range of variation, again the eigenvalues remain in the left half s-plane and thus establishing the stable operation of the boost - CSI. It can be observed from the above four cases that changes in the input control parameters, i.e. ω and m, mainly affect the three eigenvalues λ_1, λ_2 and λ_3. However, changes in load parameters (power factor and load resistance), have impact on all the system eigenvalues. It can be thereby concluded that λ_1, λ_2 and λ_3 are input dominant eigenvalues. Thus, to design a controller for a boost - CSI, the dynamic model of the inverter can be reduced to a third-order system.

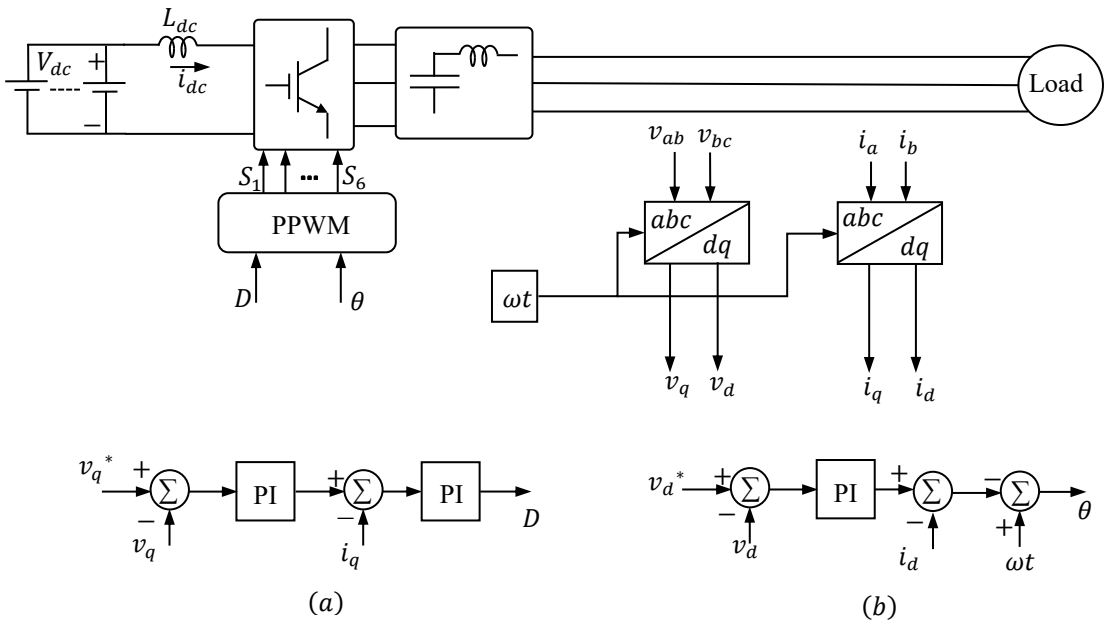

Fig. 4.9: Block diagram of the controller for output voltage regulation of a three-phase boost - CSI in the stand-alone mode of operation.

The controller of the stand-alone system is designed to regulate the output line-to-line rms voltage. The block diagram of the controller is presented in Figure 4.9. The load line-to-line load voltages and line currents are converted to *dqo*-reference frame to obtain v_q, v_d, i_q, and i_d. These measured values are then compared with the desired values v_q^* and v_d^* obtained from the desired value of the output rms line-to-line voltage. The controller generates the charging duty ratio D and the phase shift from the reference angle. This is then used as input in order to generate the inverter switching signals, as shown in Figure 4.9.

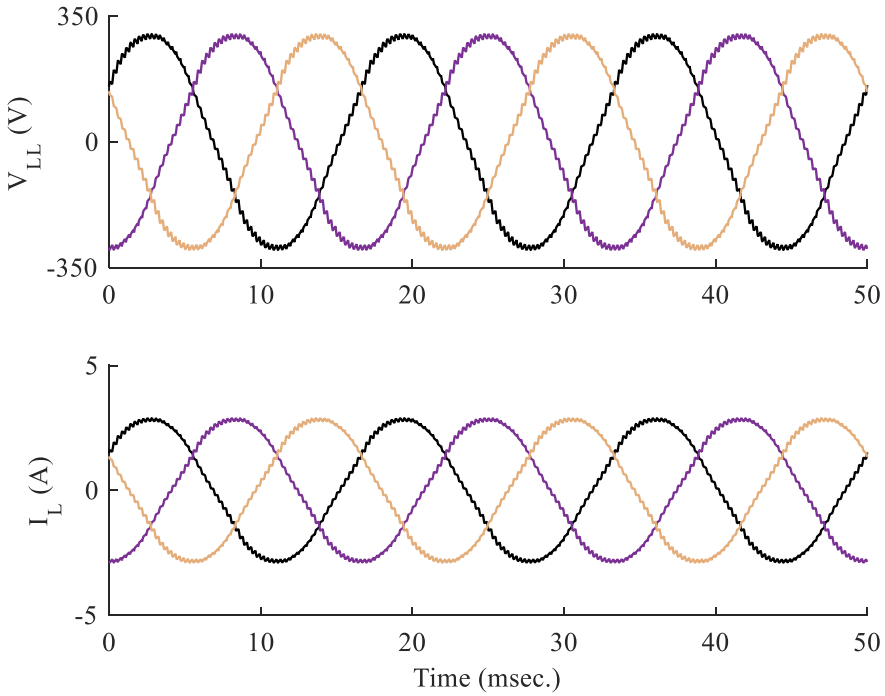

Fig. 4.10: Measured output line-to-line voltage and line current waveforms of the boost - CSI for the input voltage of $V_{dc} = 65V$, load resistance of $R_L = 70\Omega$, and switching frequency of $2.4kHz$, when the output rms line-to-line voltage is regulated at $208V$.

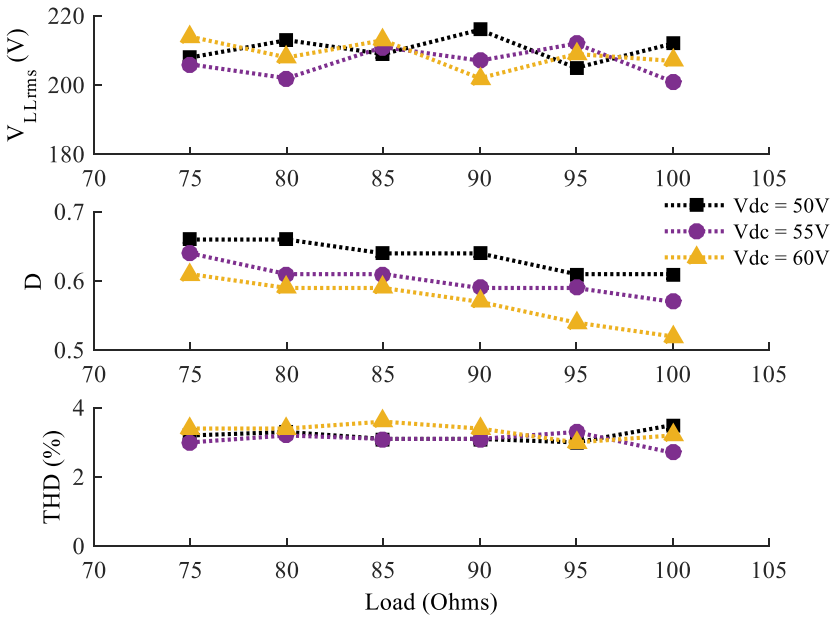

Fig. 4.11: Simulation result for voltage regulation, THD of output line current, and D variation with change in load for various input dc voltages.

Figure 4.10 presents the three-phase line-to-line voltage and line current waveforms of a boost - CSI operating in stand-alone mode, feeding a resistive load of 70Ω while the output voltage is regulated at $208V_{rms}$. The THD of the output voltage and current waveforms are measured to be about 2.3% and 2.7% respectively. The next verification of the controller is done by changing the load while keeping the desired output line-to-line rms voltage constant at $208V_{rms}$. Figure 4.11 presents the results of voltage regulation, THD of the output line current, and D obtained using the controller shown in Figure 4.9 with variation in load and for various input dc voltages. It can be clearly observed from Figure 4.11 that the output rms line-to-line voltage was maintained at $208V$ with voltage regulation of less than 5%. The THD of the output line current is less than 4% for all loads and input dc voltages which is well within the allowed distortion of the line current.

4.2.2 Grid - Tied System

Table 4.3: System parameters for grid-tied inverter.

Parameter	Nominal values
v_{dc}	65 V
L_{dc}	10 mH
R_{dc}	0.5 Ω
C_{ac}	20 μF
L_L	7.5 mH
R_g	0.1 Ω
V_{LL}^g	208 V

Stability of the boost - CSI with respect to the variation in input signals, i.e. m and ϕ, are studied using the developed small-signal model, represented by (4.13). The study is based on the experimental setup that is built in the laboratory for test and verification. The parameters of the developed setup are summarized in Table 4.3. The starting point is when the inverter is injecting $500W$ active power into the grid at unity power factor i.e., $\phi = 0$. Substituting these values into (4.13) results in the state vector equilibrium point of $X_{dq} = \begin{bmatrix} 7.69 & 294.2 & 0 & 1.96 & 0 \end{bmatrix}^T$, which corresponds to a line-to-line rms grid voltage of $208V$ and while injecting $500W$ active power into the grid. The eigenvalues of the system at this operating point are obtained as $\lambda_1 = 75.3$, $\lambda_{2,3} = 237.1 \pm j921.5$, and $\lambda_{4,5} = -313.1 \pm j1624.8$. Out of the five eigenvalues of the system for this operating point, three are located in the right half of the s-plane and two are located in the left half of the s-plane indicative of the system being unstable at this operating point. This indicates that the developed inverter in an open-loop structure has unstable operating points which need to be identified and a controller is designed for stable system operation. Therefore, variations of the overall system eigenvalues with respect to changes in the modulation index and inverter phase angle with respect to the grid must be studied.

The system eigenvalues are shown in Figure 4.12(a), in which the modulation index, m varies from 0.2 to 0.7 , with all nominal parameter values provided in Table 4.3. This range of m corresponds to the charging ratio, D, variation from 0.33 to 0.81, as the relationship between these parameters has been given in Section 3.2. The range of modulation index is chosen based on the active power injected into the grid for the laboratory prototype. As shown in Figure 4.12(a), the eigenvalues of the system are located on both sides of the s-plane indicative of the system being unstable for the entire operating region. As can be seen, the imaginary part absolute values of λ_2 and λ_3 increase whereas the real part absolute values decrease as m increases. Unlike λ_2

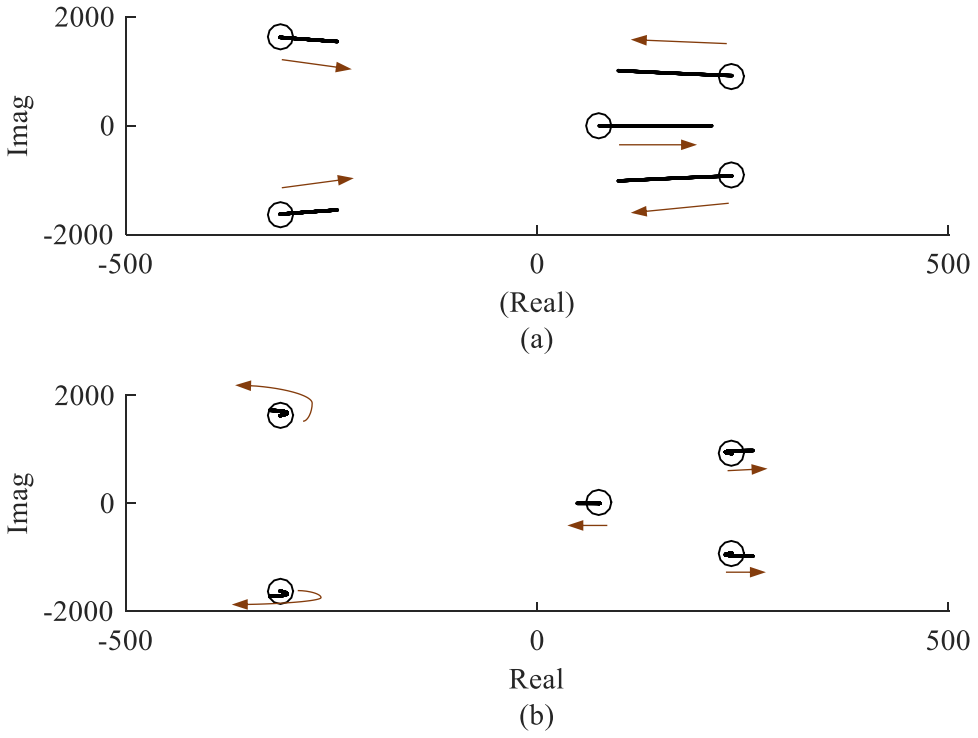

Fig. 4.12: Root locus of small-signal poles (eigenvalues) of the grid-tied boost - CSI as (a) m, varies from 0.2 to 0.7; (b) ϕ varies from 0^o to 45^o.

and λ_3, λ_1 moves away from the imaginary axis as m increases. However, since the pair eigenvalues, λ_2 and λ_3, have higher weights than the single one, it can be expected that the overall system response becomes more oscillatory as m increases. Nevertheless, the overall system remains unstable for the entire range of m variation. The root locus of small signal poles (eigenvalues) of the grid-tied boost - CSI as the inverter angle with respect to the grid, ϕ varies from 0^o to 45^o is shown in Figure 4.12(b). This variation in ϕ covers the entire operating range of the boost - CSI corresponding to reactive power injection into the grid. It can be observed from Figure 4.12 that the eigenvalues of the boost - CSI lie on both left and right half of the s-plane for the operating range, indicating that the boost - CSI is unstable over the range.

The controller of the grid-tied system is designed to control the active and reactive

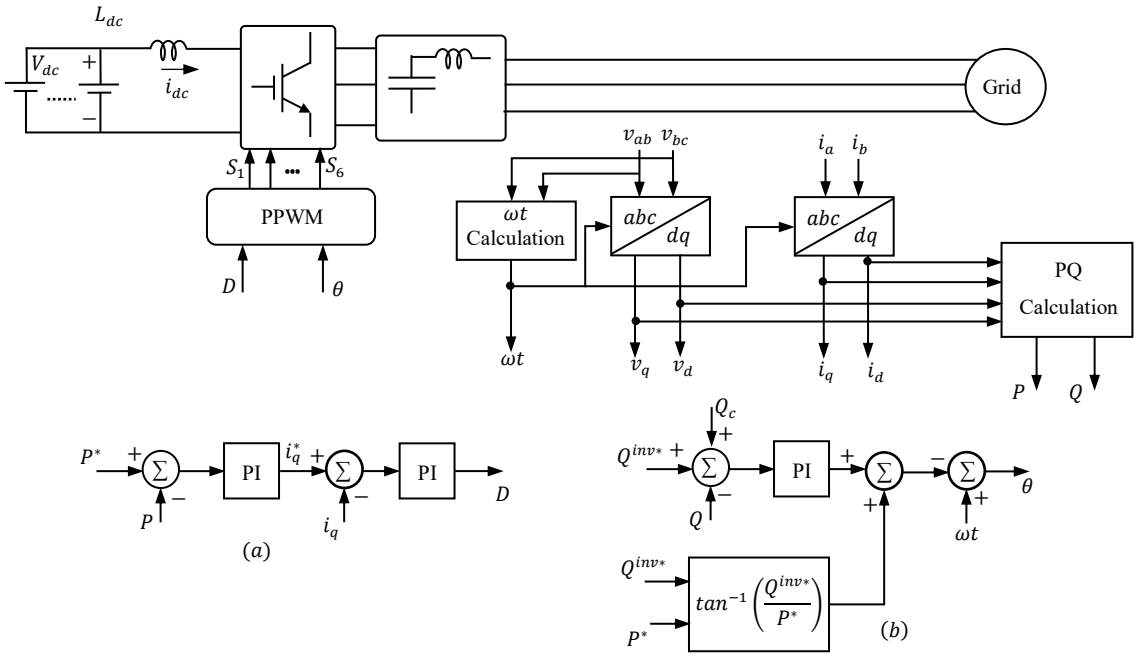

Fig. 4.13: Block diagram of the controller for regulation of active and reactive power injected into the grid for the three-phase grid-tied boost - CSI.

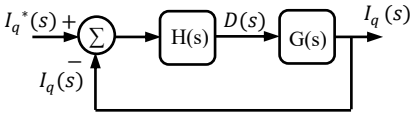

Fig. 4.14: Block diagram for i_q control.

power injected into the grid and ensure a stable operation of the grid-tied closed loop boost - CSI. The block diagram of the controller is presented in Figure 4.13. In order to control the active power injected into the grid, the computed value of P to the grid is compared with the desired active power and the error is compensated using a PI controller which generates the desired q-axis current, i_q^*. This generated i_q^* is then compared with the measured i_q, and the error is compensated by a PI controller, which generates the charging duty ratio D.

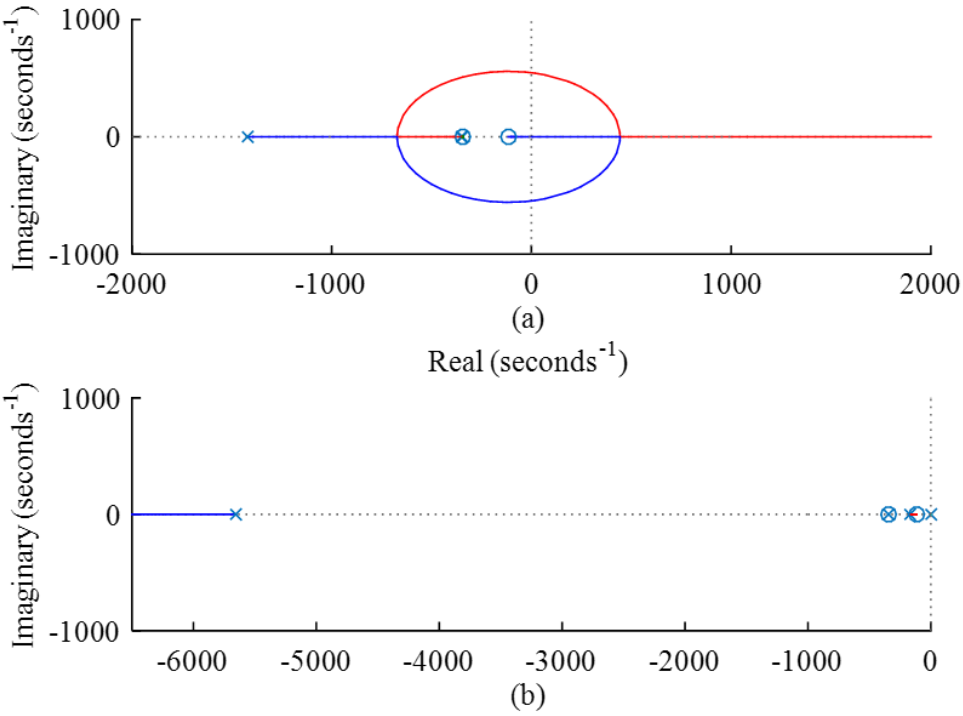

Fig. 4.15: Root-locus for the reduced order (a) open-loop, and (b) closed-loop grid-tied boost-CSI.

The active power controller is detailed in Figure 4.13(a). The control technique formulated in this section is derived from (4.13). To control the active power injected into the grid, P, the control variables are i_q and D. The transfer function $G(s)$ shown in Figure 4.14 can be obtained by reducing the order of the small signal model derived in (4.13).

For the grid connected inverter, one can assume $dv_q/dt = dv_d/dt$ are negligible as the grid is assumed as an infinite bus and is not a weak grid; all inputs perturbation to the system is neglected except that of δm. Thus, the open-loop reduced-order transfer function between $I_q(s)$ and $M(s)$ can be obtained as

$$G(s) = \frac{a_2 s^2 + a_1 s + a_0}{b_3 s^3 + b_2 s^2 + b_1 s + b_0} \tag{4.19}$$

For the circuit parameters and operating point given in Table 4.3, the open-loop transfer function can be obtained in which $a_o = -1.7257 \times 10^3$, $a_1 = -20.0783$, $a_2 = -0.0438$, $b_o = 1.8663 \times 10^3$, $b_1 = 12.0222$, $b_2 = 0.0229$, and $b_3 = 0.1081 \times 10^{-4}$. Now applying the closed loop control as shown in Figure 4.13 and Figure 4.14, the closed loop transfer function can be obtained as $T(s) = \frac{H(s)G(s)}{(1+H(s)G(s))}$. Using the Routh-Hurwitz criterion for stability of a fourth-order system [77], and applying the bound on m for the operating range ($0.2 \leq m \leq 0.7$), conditions on K_i and K_p are obtained as $K_p > 1.673 \times 10^{-4}$ and $K_i K_p < 2.018 \times 10^{-5}$. Thus, using these conditions K_i and K_p have been chosen for the Figure 4.13(a). The root-locus for the open-loop and reduced order closed-loop system are presented in Figure 4.15 (a) and (b), respectively. It can be observed from Figure 4.15 that the open-loop system may go to the unstable region while the closed-loop boost - CSI is always stable. This can be further verified from Figure 4.16, which shows the eigenvalue variation of the closed-loop transfer function with varying m and ϕ, as K_i and K_p remain same as in Figure 4.16.

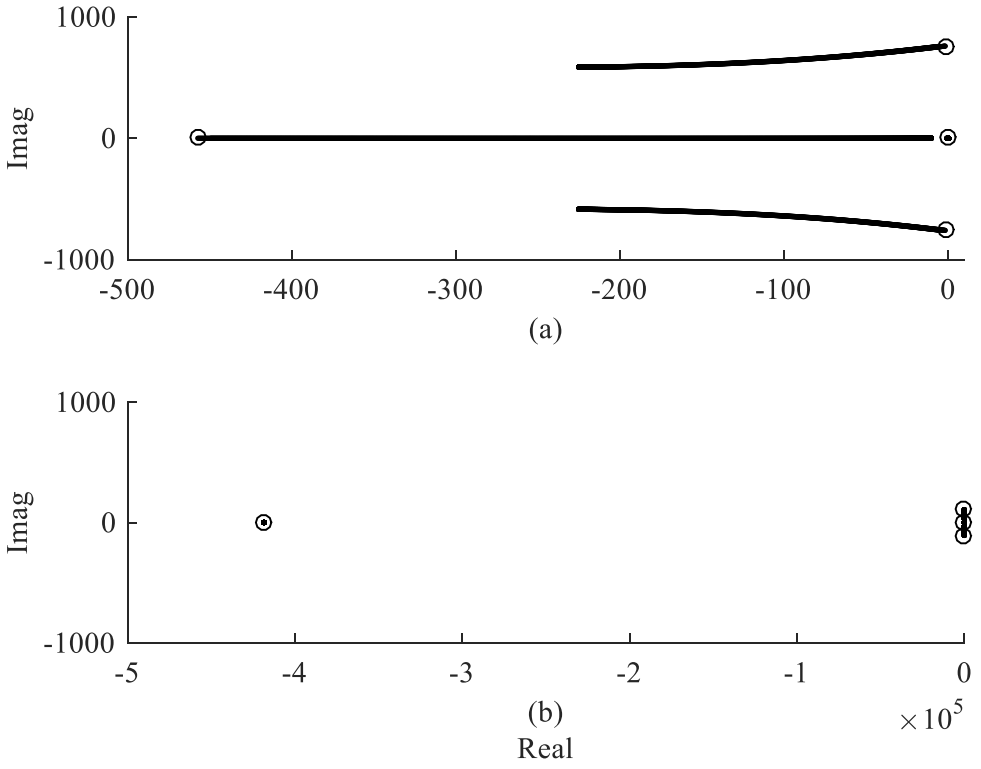

Fig. 4.16: Root locus of reduced-order, closed-loop transfer function (eigenvalues) of the grid-connected boost - CSI as (a) m varies from 0.2 to 0.7; (b) ϕ varies from $-\pi/4$ to $\pi/4$.

In order to control the reactive power injected into the grid, the desired active power, P^* and desired reactive power,$Q^{inv*}$are used to compute the phase shift required in the voltage generated from the inverter to inject the desired power to the grid. The error between desired reactive power at the grid and measured reactive power at the PCC, Q is compensated by a PI controller and the result is added to the obtained phase shift. This phase shift is then introduced in grid reference angle ωt to obtain the switching pattern reference angle, θ. The reactive power controller has been detailed in Figure 4.13(b). While the error between desired reactive power at the grid and measured Q is computed, the reactive power generated from the ac-capacitors has been added it to Q^{inv*} value. The P^* and Q^{inv*} make the charging duty ratio D and reference angle θ. This is then used to generate the PWM switching pulses for the boost - CSI.

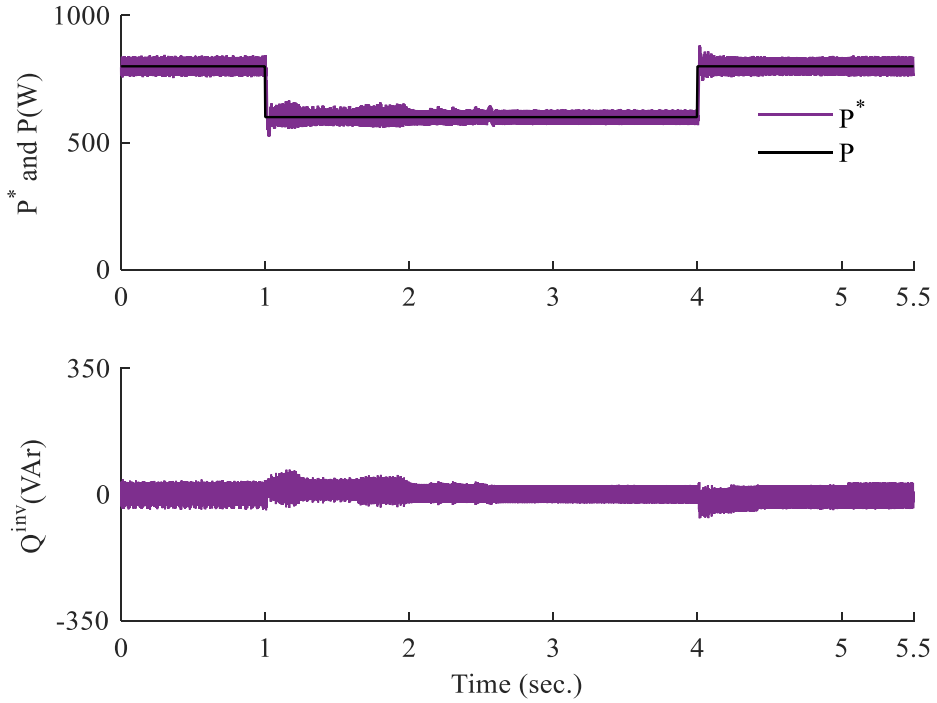

Fig. 4.17: Simulation results for (a) $P^*$and P, and (b) Q injected into the grid for the boost - CSI regulated by the developed control technique when $P^*$is given step changes at $t = 1sec$ and $t = 4sec$.

The verification of the controller is presented through simulation and experimental results. The boost - CSI along with the developed control scheme is simulated in Simulink/MATLAB environment in order to validate the developed control scheme for the independent control of active and reactive power. In order to verify the performance and decoupled behavior of the active and reactive power controllers, two cases were simulated. Figure 4.17 shows the results for the verification of the active power controller and its decoupling with the reactive power control. For this verification, P^* is first set to $800W$, which is then given a step change to $600W$ at $t = 1sec$, and at $t = 4sec$, P^* was given a step change back to $800W$. During this time, Q^{inv*} is constant at $0\,VAr$. It can be observed from Figure 4.17 (a) and (b) that the P closely follows the command P^*, and reactive power from the inverter remains zero. The sec-

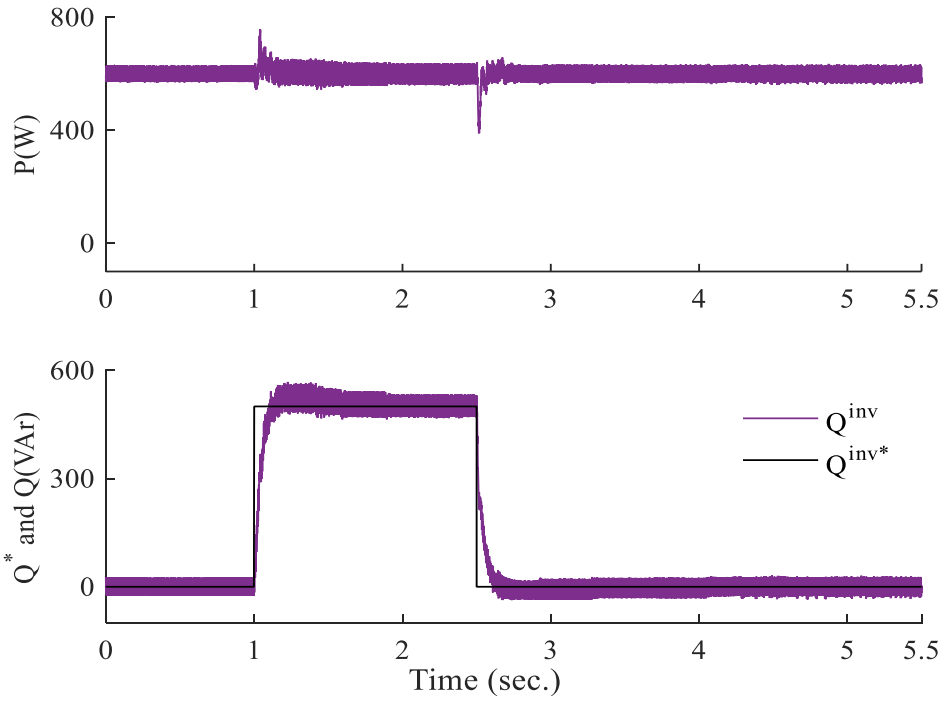

Fig. 4.18: Simulation results for (a) P, and (b) Q^{inv*} and Q injected into the grid for the boost - CSI regulated by the developed control technique when Q^{inv*} is given step changes at $t = 1sec$ and $t = 2.5sec$.

ond verification is for the reactive power controller and its decoupling with the active power control. For this verification, Q^{inv*} was set to $0\,VAr$ initially, then at $t = 1sec$, Q^{inv*} was stepped to $500\,VAr$, and at$t = 2.5sec$, Q^{inv*} was brought back to $0\,VAr$. During this validation P^* was set constant at $600W$. It can be observed from Figure 4.18(a) that the P injected into the grid remains constant at $600W$, while Figure 4.18(b) shows that the Q follows the command Q^{inv*}. The experimentally obtained waveforms of the inverter output line-to-line voltage, line-to-line voltage at the point of common coupling, current injected into the grid, and inverter output line current are shown in Figure 4.19 when the inverter is injecting $1kW$ active power into the grid. The THD of the current injected into the grid was computed to be about 3.16%, which is within the limits as per IEEE 1547 standards for grid connection [57].

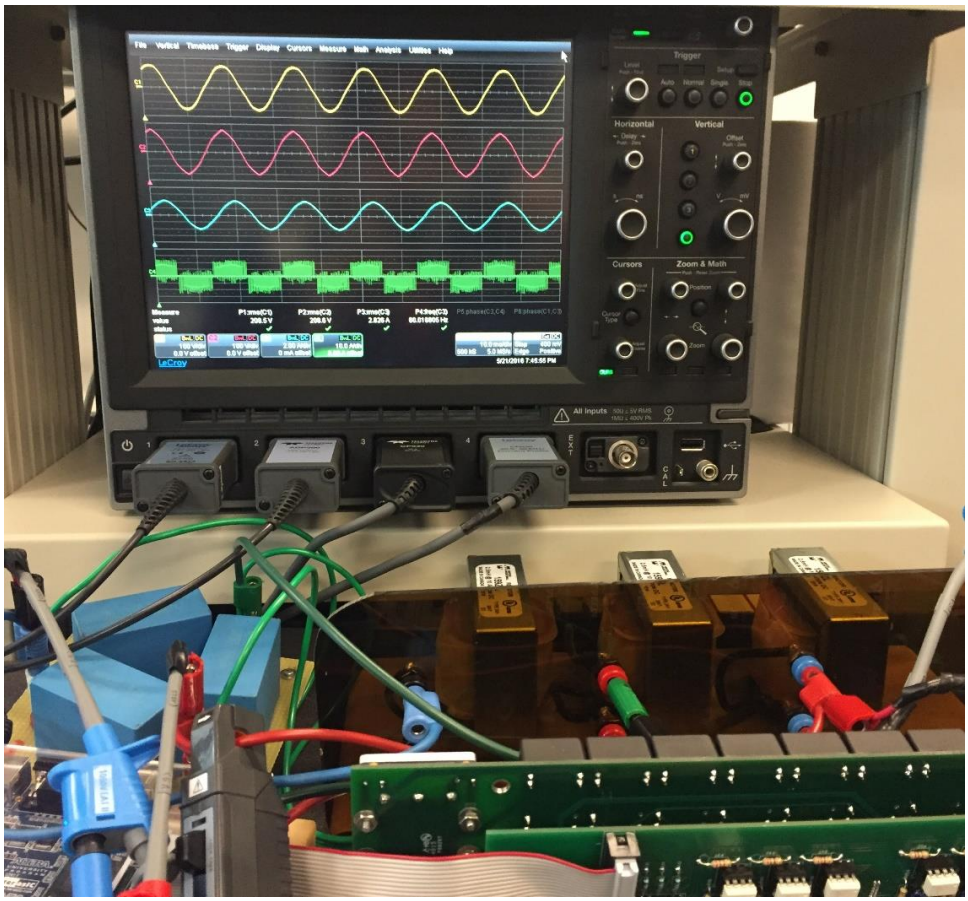

Fig. 4.19: The waveforms from the top to the bottom of the oscilloscope screen are: voltage at the ac capacitors, grid line-to-line voltage, injected current into the grid, and inverter output current before the ac capacitors.

4.3 Conclusion

In order to realize the boost - CSI capabilities, and to assist the penetration of the boost - CSI into renewable energy systems, the boost - CSI dynamic behaviors and models have been presented in this chapter for both stand-alone and grid-tied modes of operation. The boost - CSI *dq*-equivalent circuits have been developed using the state-space averaged model of the boost - CSI transferred into a *dq*-frame of reference. The boost - CSI small-signal model has also been developed to analyze the boost - CSI stability. In this paper, the root locus studies on small signal poles of the boost - CSI

have been performed and revealed that the boost - CSI stays stable as control inputs and load parameters vary within the boost - CSI's operating limits for stand-alone operation but is unstable for open-loop operation. These investigations demonstrate that the boost - CSI can be a suitable dc-ac converter to generate three-phase voltage from a parallel set of small dc voltage sources, which is typically more reliable than the series connected voltage sources, paving the path for the boost - CSI into renewable energy generation systems (e.g., photovoltaic arrays, fuel cells, etc.). The developed dynamic models are used to design the controller for closed-loop operation in stand-alone and grid-tied modes. The controller for the stand-alone mode is used to regulate the output voltage of the boost - CSI. The controller for the grid-tied operation controls the active and reactive power injected into the grid while maintaining stable operation of the boost - CSI. The developed models and controllers have been verified using simulation and experimental results. The control scheme for the proposed DDWT topology is presented in the next chapter.

Chapter 5

Control Schemes for the Proposed DDWT

In this chapter, the control scheme for the boost - CSI as part of the back-to-back converter in DDWTs is explained. Section 5.1 provides the details about the control technique and the functionality of controllers developed for the power converters. Section 5.2 provides the results verifying the effectiveness of the developed controllers. Section 5.3 ends the chapter with concluding remarks.

5.1 Control Technique

The block diagram of the controller is shown in Figure 5.1. The controller for the developed system is a two-part controller with the first controller for the VSC and the second for the boost - CSI. The VSC controller is used for Maximum Power Point Tracking (MPPT) and it delivers the maximum power available dependent on the generator speed (governed by the wind speed) to the dc-side. The boost - CSI controller is used to maintain a constant average dc-side voltage while controlling the reactive

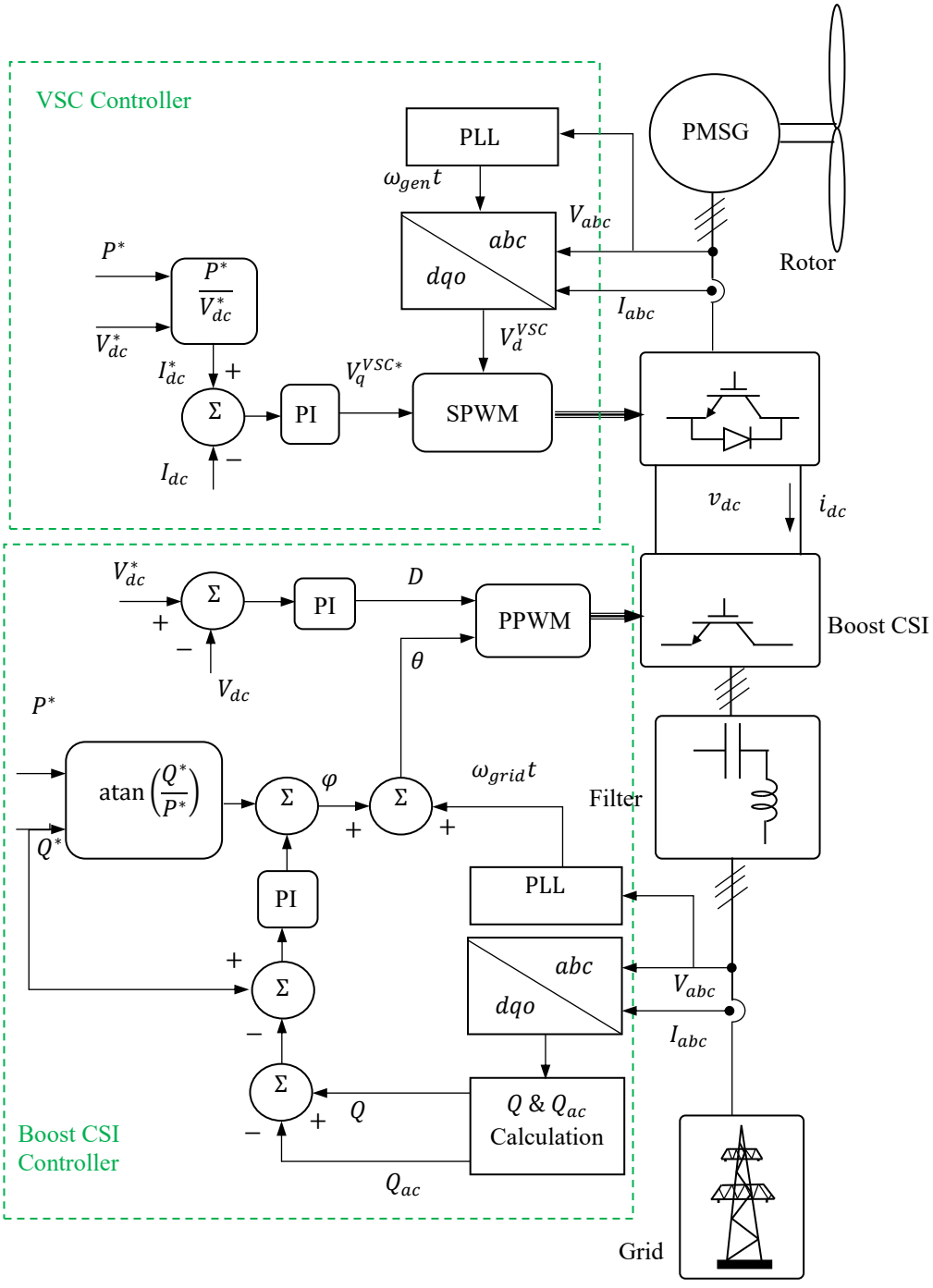

Fig. 5.1: Block diagram of the controller for the proposed power electronics interface for DDWTs .

power injected into the grid. Thus, the VSC controller modulates the active power injected into the grid while the boost - CSI controller regulates the average of the dc-bus voltage and the reactive power injected into the grid.

5.1.1 VSC Controller

The VSC controller receives the generator line-to-line voltages, line currents, dc-side voltage, and dc-side current as feedback signals. The three-phase quantities are then transferred to the dqo reference frame rotating at generator electrical speed, ω_{gen}. The measured power on the dc-side is compared to the desired active power signal, P^* and the error is forced to zero through a PI controller, while generating the desired q-axis voltage, V_q^{VSC*} for the converter input. The desired active power, P^* signal is generated from the generator rotor speed, using the most common MPPT technique, where $P^* = K_{opt}\omega_R^3$, [60, 78]. The generated V_q^{VSC*} and the measured V_d^{VSC} are used to compute the reference signals for generating the switching signals for the VSC using Sine PWM (SPWM) switching technique.

5.1.2 Boost - CSI Controller

The boost - CSI controller receives the line-to-line voltages at the point of common coupling, line current injected into the grid, and dc-side voltage as inputs. The average dc-side voltage, V_{dc} is compared to the desired dc-side voltage, V_{dc}^* and the error is forced to zero through a PI controller, as shown in Figure 5.1. This generates the modulation index, D required for implementing the PPWM switching technique as described in [19]. The measured three-phase quantities are transferred to the *dqo* frame of reference, rotating at grid frequency. The measured reactive power injected into the grid, Q is corrected by the amount of reactive power compensated by the ac filter capacitors, Q_{ac}

and then compared to the desired reactive power, Q^*. A PI controller is then used to make the error zero while generating the correction factor for the phase shift between the inverter and grid voltages, φ, as can be seen in Figure 5.1. This generates the boost - CSI reference angle, θ which is needed for generating the PPWM switching pattern [45]. The verification of these controllers is presented in the next section.

5.2 Simulation Results

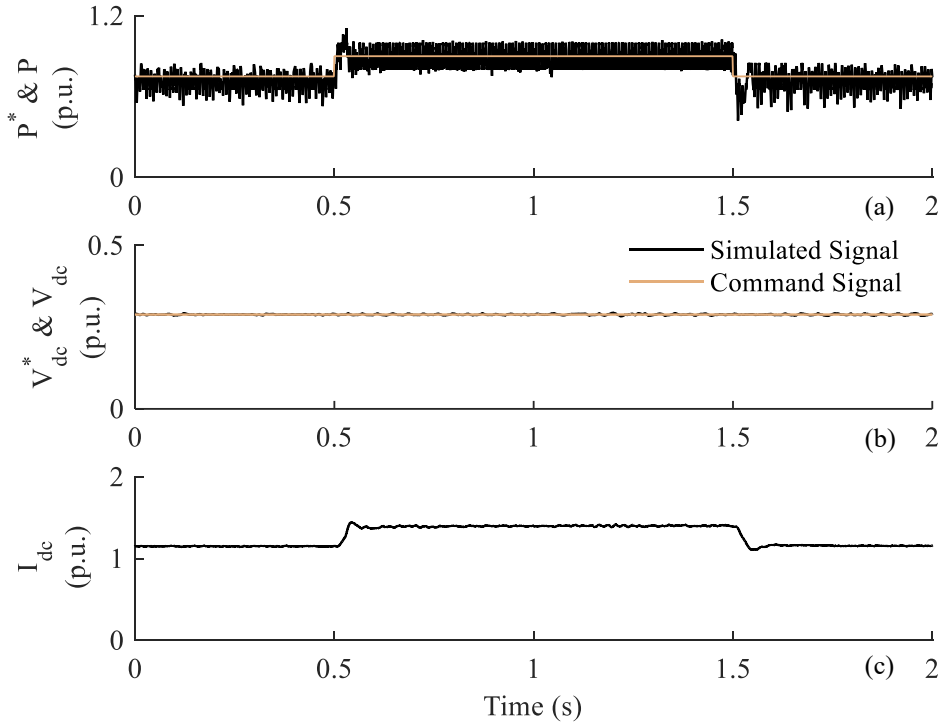

Fig. 5.2: Simulation results showing (a) P^* and P, (b) V_{dc}^* and V_{dc}, and (c) I_{dc} for a step change in P^* at $t = 0.5s$ and $t = 1.5s$ while $V_{dc}^* = 0.725p.u.$ and $Q^* = 0$.

The controllers developed in Section 5.1 are verified through the next set of results presented in Figures 5.2, 5.3, and 5.4. For the first set of verification, step changes were provided to the desired power command,P^* from $0.75\,p.u.$ to $0.9\,p.u.$ at $t = 0.5\,sec$ and back to $0.75\,p.u.$ at $t = 1.5\,sec$. During this interval the desired average dc-side

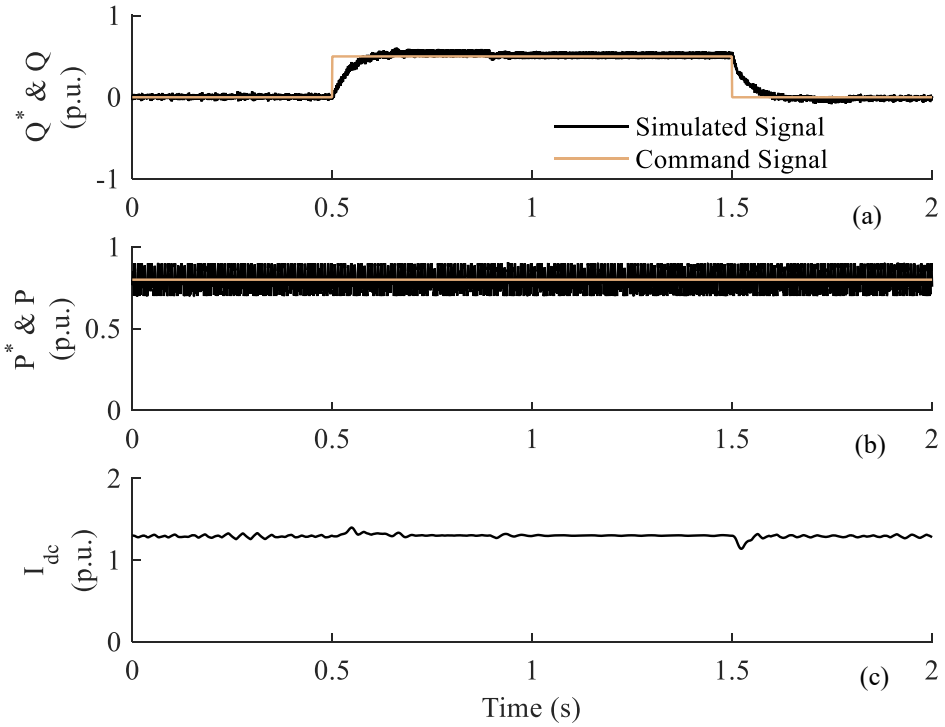

Fig. 5.3: Simulation results showing (a) Q^* and Q, (b) P^* and P, and (c) I_{dc} for a step change in Q^* at $t = 0.5s$ and $t = 1.5s$ while $V_{dc}^* = 0.725p.u.$ and $P^* = 0.8p.u.$

voltage, $V_{dc}{}^* = 0.725\,p.u.$, and the desired reactive power, $Q^* = 0$. The active power command signal, measured power injected into the grid, command dc-side voltage, measures average dc-side voltage, and the dc-side current for this test case is presented in Figure 5.2. It can be observed from Figure 5.2 that the power injected into the grid follows the desired power command, while the dc-side voltage remains unchanged. The dc-side current changes to accommodate the active power requirement.

For the next verification, step changes were provided to Q^* from 0 to $0.5\,p.u.$ at $t = 0.5\,sec$ and back to $0\,p.u.$ at $t = 1.5\,sec$, while P^* is constant at $0.8\,p.u.$, and V_{dc}^* is constant at $0.725\,p.u.$ The resulting Q^*, Q, P^*, active power injected into the grid, and I_{dc} are shown in Figure 5.3. It can be observed from Figure 5.3 that Q follows Q^* while the active power injected into the grid remains unchanged.

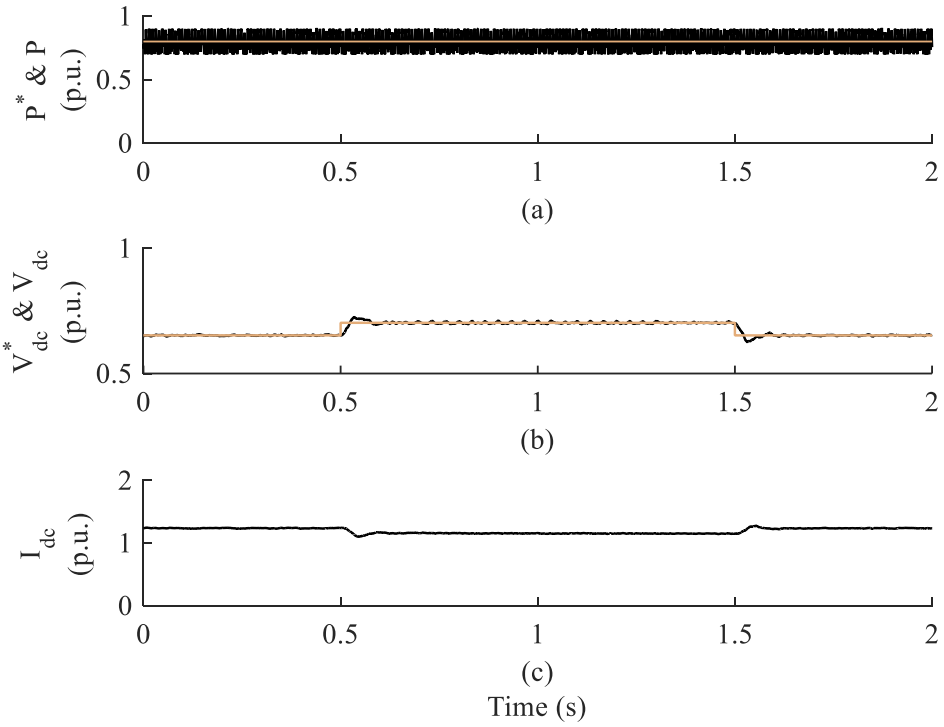

Fig. 5.4: Simulation results showing (a) P^* and P, (b) V_{dc}^* and V_{dc}, and (c) I_{dc} for a step change in V_{dc}^* at $t = 0.5s$ and $t = 1.5s$ while $P^* = 0.8p.u.$ and $Q^* = 0p.u.$

The next verification is through a change in V_{dc}^* as shown in Figure 5.4. It should be noted that such a case does not occur in a wind turbine and this result is presented for validation of the decoupled operation of the controllers. In this case, V_{dc}^* is given step changes from $0.65\,p.u.$ to $0.70\,p.u.$ at $t = 0.5\,sec$ and back to $0.65\,p.u.$ at $t = 1.5\,sec$, while P^* remains constant at $0.8\,p.u.$ during this time. It can be seen in Figure 5.4(a) that the measure active power injected into the grid follows P^*. Figure 5.4(b) shows V_{dc}^* and V_{dc} and it can be seen that V_{dc} follows the command signal, while I_{dc} changes to keep the power output constant.

The results presented in Figures 5.2, 5.3, and 5.4 demonstrate that the controllers for the VSC and the boost - CSI work together to follow their respective command signals. It can be observed from the results presented in Figures 5.2, 5.3, and 5.4 that

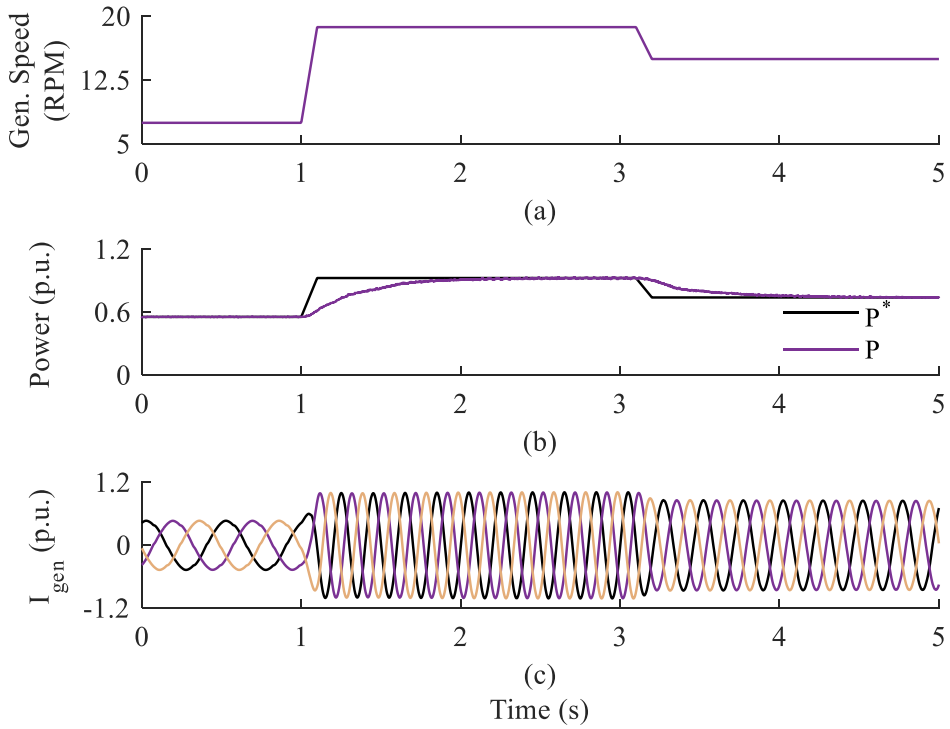

Fig. 5.5: Simulated results of (a) generator speed governed by wind speed, (b) p.u. desired and measured power injected into the grid, and (c) p.u. three-phase generator line current for the developed system when the wind speed is varying.

a low dc-side voltage is used to inject power into the grid (1p.u.).

Figure 5.5 demonstrates the feasibility of the developed system and its controllers for variable wind speed. The input wind speed is varied over a period of 5 *sec*. Figure 5.5(a) shows the resulting generator speed over this interval. From $t = 0\,sec$ to $t = 1\,sec$ the generator speed is $7.5\,rpm$. At $t = 1\,sec$ the speed gradually increases to $18.75\,rpm$ and at $t = 3.1\,sec$ the speed decreases gradually to $15\,rpm$. The speed profile chosen here consists of sudden changes in the wind speed, which is used to demonstrate the robustness of the controllers. The generator speed is used to compute P^*. Figure 5.5(b) shows P^* and the measured active power injected into the grid. It can be observed from Figure 5.5(b) that the power injected into the grid closely follows P^*. The waveforms of the three-phase current output from the PMSG is shown in Figure 5.5(c). Figure

5.5 demonstrates that the controllers have acceptable performance while maintaining the quality of the output waveforms.

5.3 Conclusion

In this chapter, the control technique for the developed power electronics interface has been developed and verified through simulations for different operating conditions. It has been proven that the developed DDWT system has desired performance with the synchronous inductance of PM generator utilized to eliminate the need for a dc-link inductor. It has been demonstrated that the controllers for the converters work in tandem to effectively control the active and reactive power injected into the grid. The performance of the controller has also been verified for sudden changes in wind speed profile.

Chapter 6

Experimental Setup and Verifications

In this chapter, the laboratory scale experimental setup developed for the proposed system is explained and the developed system is verified through experimental results. The details of the $1.5\,kW$, $240\,V$ laboratory scale prototype of the developed system is explained in Section 6.1. The developed experimental setup is then used to verify the performance and feasibility of the proposed topology of DDWT, and the results are presented in Section 6.2. The chapter ends with concluding remarks presented in Section 6.3.

6.1 Experimental Setup

In this section, the details of a laboratory scale $1.5\,kW$, $240\,V$ prototype of the developed topology of DDWT is presented. The laboratory setup has four main parts:

1. Wind Turbine Emulator - prime mover
2. PMSG

3. Active rectifier or VSC along with input filter

4. Boost - CSI with output filter

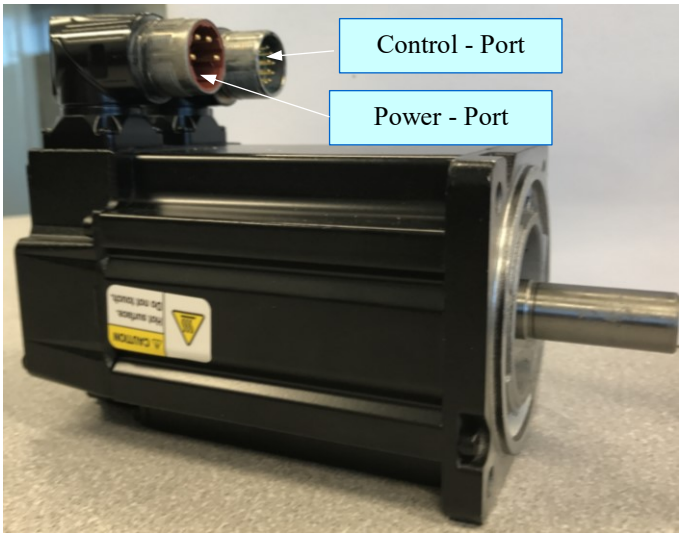

Fig. 6.1: Servo motor which acts as the prime mover in the wind turbine emulator.

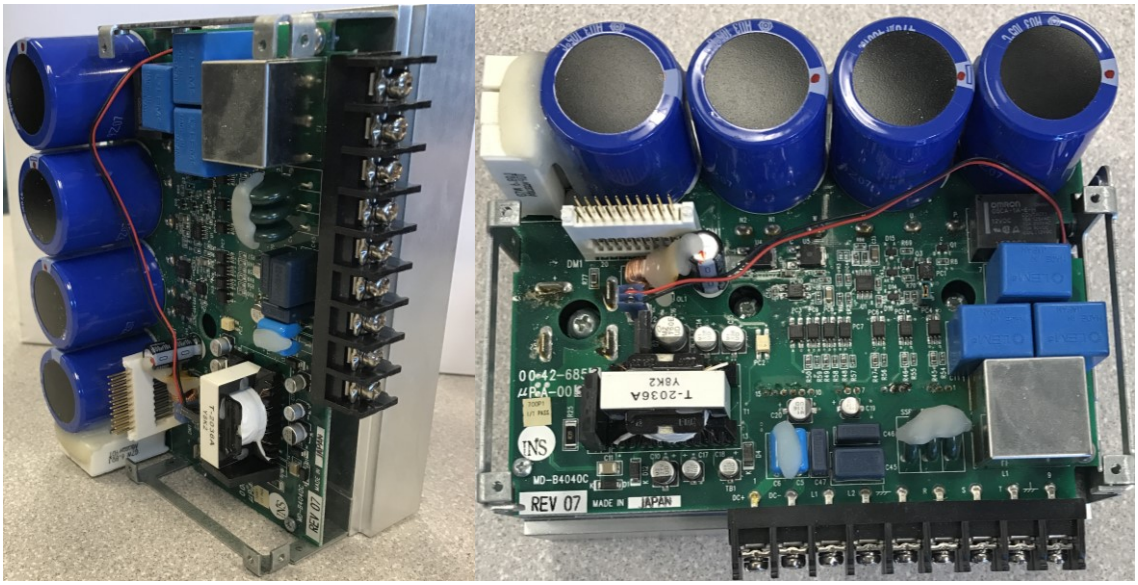

Fig. 6.2: Servo drive to control and power the servo motor for the wind turbine emulator.

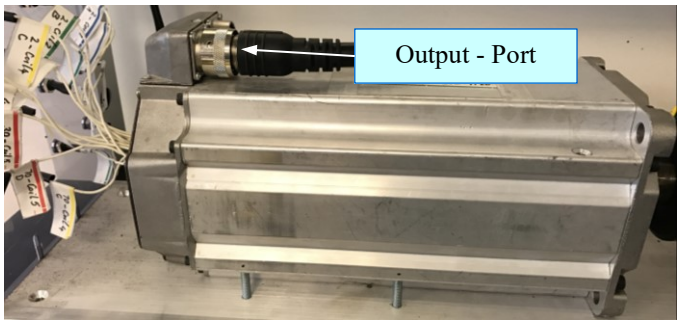

Fig. 6.3: PMSG used in the laboratory scale setup of the developed system.

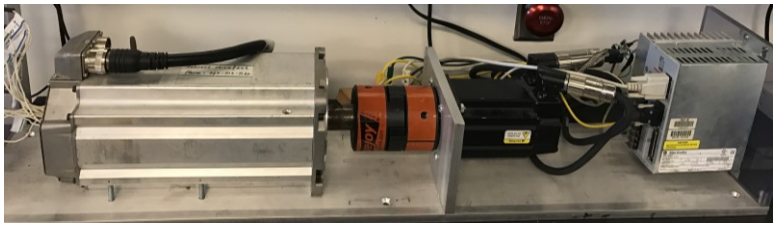

Fig. 6.4: The wind-turbine emulator and PMSG dyne setup.

The wind turbine emulator has been developed using a $1.5\,kW$, $110\,V$ servo-motor along with a servo drive to control the motor. The servo motor used is an Allen-Bradely Kinetix series MPL–A320P-SK72AA motor, shown in Figure 6.1. The motor receives three-phase power supply through the power port (shown in Figure 6.1) from a $2\,kW$, $110\,V$ Allen-Bradely servo drive: 2098-DSD-020X which is shown in Figure 6.2. The servo drive is also used to control the speed of the servo motor which acts as the prime mover for the generator. The control of the servo drive is done through Ultraware software named Ultra 3000 version 1.82 from Allen-Bradely. The servo motor and the drive together form the wind turbine emulator for the developed setup. The servomotor is then coupled to an $8-pole$, $7\,hp$, $480\,V$ PMSG shown in Figure 6.3. It should be noted that the PMSG being used here is not designed specifically for this system and an existing permanent magnet motor is used as a generator for the experimental verification of the topology of the proposed system. The entire wind turbine emulator

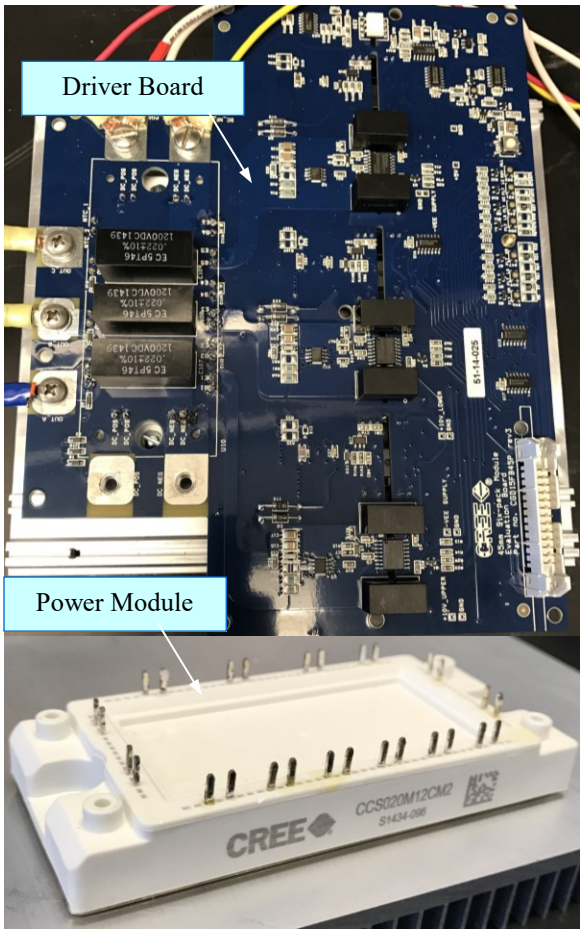

Fig. 6.5: The generator side converter (VSC) setup developed using SiC MOSFETS.

- PMSG dyne bench is shown in Figure 6.4.

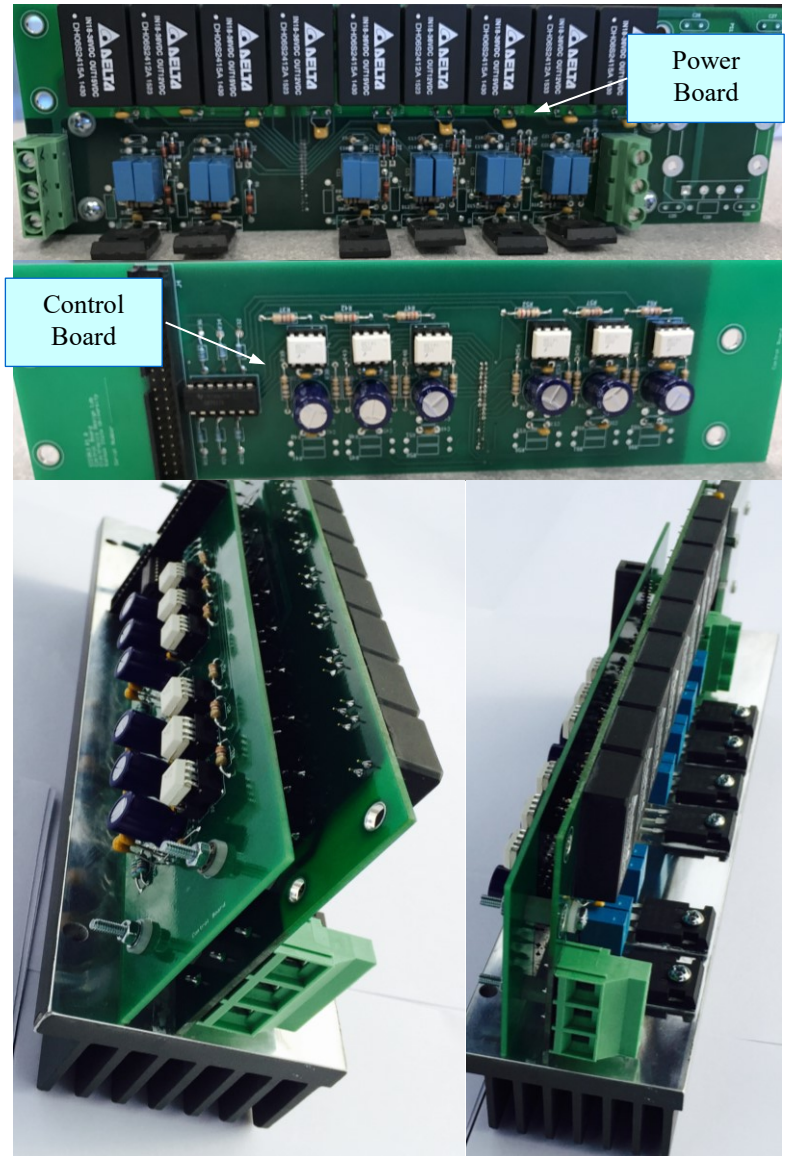

Fig. 6.6: The boost - CSI setup developed using RB-IGBTs.

The VSC used in the laboratory setup is CREE CCS020M12CM2 and CREE CGD15FB45P based converter formed using SiC MOSFETs. The power converter is shown in Figure 6.5. The boost - CSI converter is a $2\,kW$, $240\,V$, $60\,Hz$ three-phase converter developed using six individual RB-IGBTs [45]. The IGBTs used in the boost inverter are RB-IGBTs from Fuji, i.e. FGW85N60RB. The inverter prototype, which is

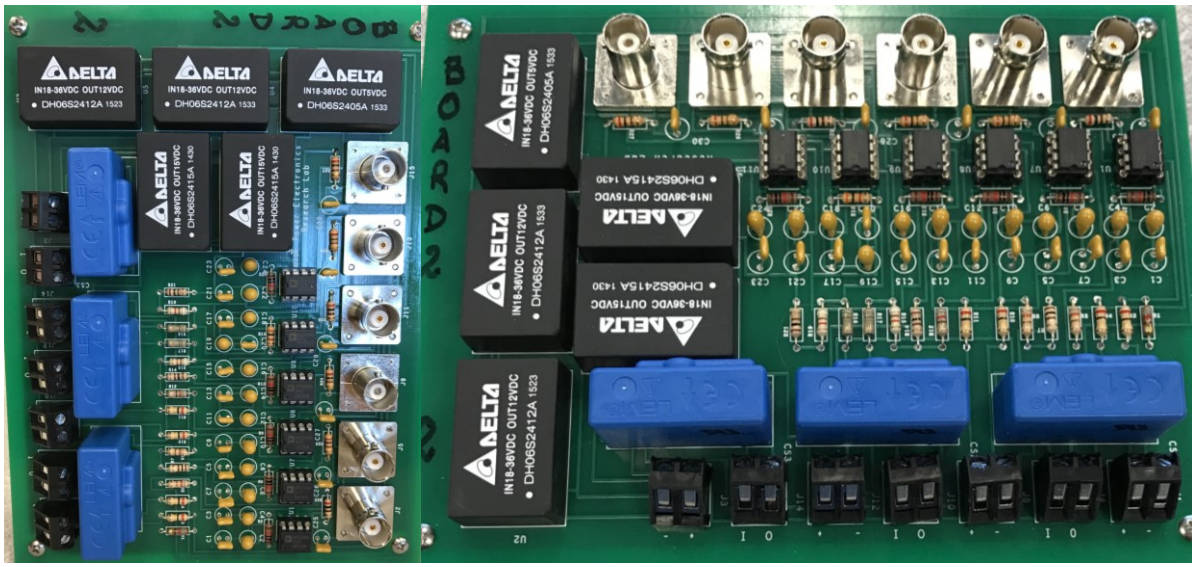

Fig. 6.7: Measurement board for sending feedback to the controller implemented in dSPACE.

shown in Figure 6.6, contains two printed circuit boards called 1) control board and 2) power board. The inverter is a self-powered device with control board powered directly by the dc input voltage. A detailed circuit drawing for the boost - CSI is presented in Appendix B. The inverter switching is generated by Altera's DE0 FPGA development board [70]. The controllers for the system are implemented in dSPACE 1103. The feedback signals are measured from the experimental setup using the measurement board shown in Figure 6.7 and it sends the feedback signals to the dSPACE. Two such measurement boards are implemented in the final setup to sense and send feedback for controllers of the VSC and boost - CSI. The setup developed in this section is used for system verification and the results are presented in the following section.

6.2 System Verification

This section presents experimental results demonstrating proof-of-concept of the proposed topology where the grid-side VSC is replaced by three-phase boost - CSI, en-

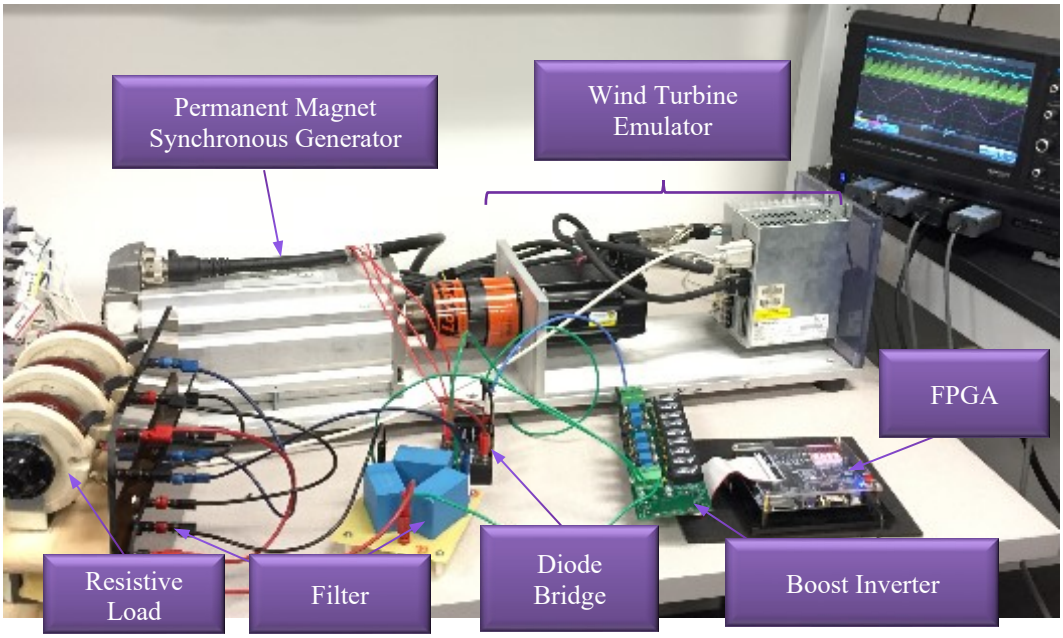

Fig. 6.8: Laboratory scale setup of the proposed system with the wind turbine emulator, the PMSG, a diode bridge rectifier, and the 2kW 240V three-phase boost - CSI operating in the stand-alone mode feeding a resistive load.

abling elimination of dc-bus electrolytic capacitors. The verification is provided for both stand-alone and grid-tied modes of operation of the system. The experimental verification is done using a laboratory scale $1.5\,kW$, $240\,V$ setup described in the previous section.

6.2.1 Stand-Alone Operation

The first set of verification of the proposed topology is done on a stand-alone system comprising the wind turbine emulator, generator, diode-bridge as the generator-side converter, and boost - CSI is presented through experimental results using the laboratory scale boost - CSI. A wind turbine emulator is used to run a PMSG as shown in Figure 6.8. The output of the generator is connected to a diode bridge rectifier, and

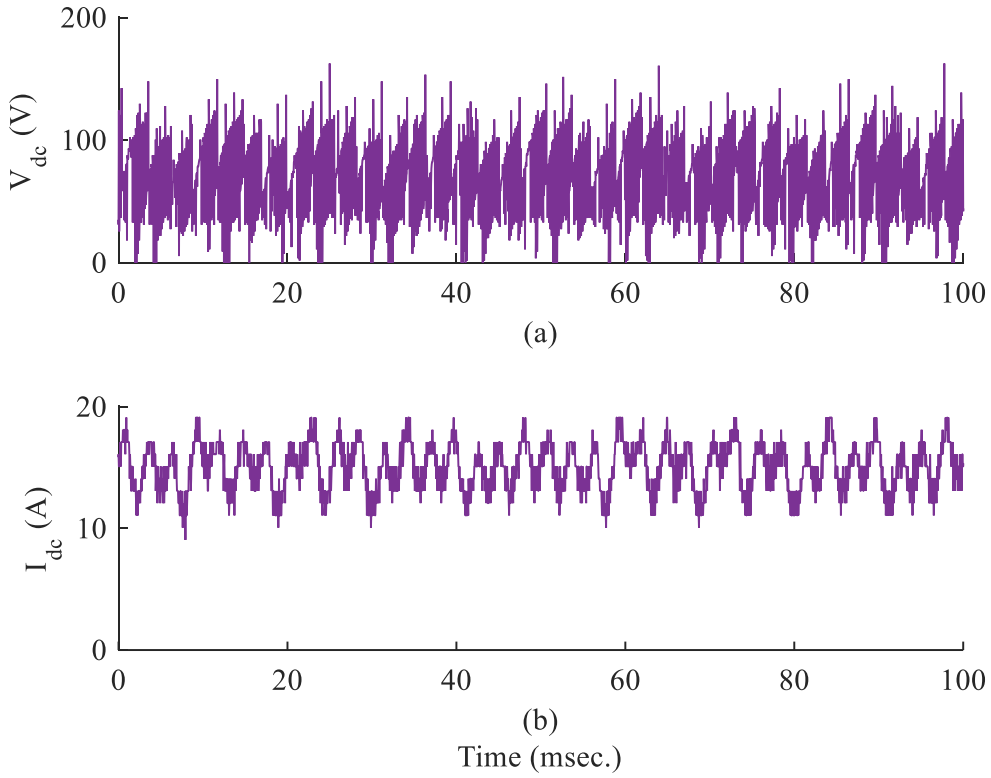

Fig. 6.9: Experimentally obtained waveforms of (a) dc-side voltage, and (b) dc-link current for the stand-alone mode of operation of the system with a diode bridge as the generator-side converter.

the dc output of the rectifier is connected to the three-phase boost - CSI operating in stand-alone mode feeding resistive load through a filter. The generator side filter is a three-phase $3\,mH$ inductor. The boost - CSI switching frequency was set to $f_s = 6\,kHz$ and the output filter values are $C_{ac} = 20\,\mu F$, and $L_{ac} = 5\,mH$ with a load resistance of $50\,\Omega$ per phase. The generator used for the experimental verification of the topology is a three-phase, $7\,hp$, 8-pole, $480\,V$ PMSG. Again it should be noted that the PMSG used to obtain the experimental results is not designed for the proposed system and is used just as the proof-of-concept for the developed topology. The generator was run at $450\,rpm$ corresponding to $30\,Hz$ frequency of the generator output voltage and current. The output dc-side voltage corresponding to this speed of the wind emulator

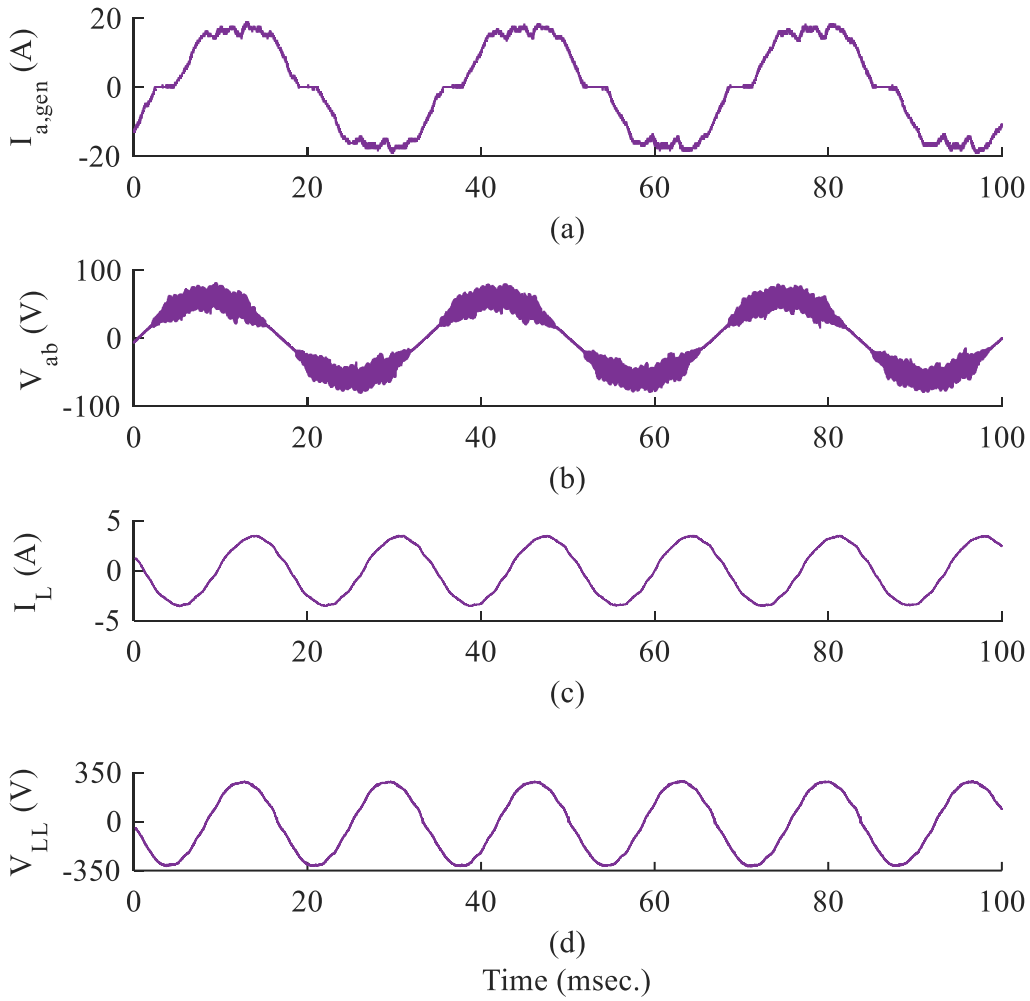

Fig. 6.10: Experimentally obtained waveforms of (a) generator output line current, (b) generator output line-to-line voltage, (c) inverter output line current, and (d) inverter output line-to-line voltage for the stand-alone mode of operation of the system with a diode bridge rectifier as the generator-side converter.

is obtained $60\,V$.

Figure 6.9 presents the dc link voltage and current waveforms for the system feeding a resistive stand-alone load, when the inverter output is regulated to provide line-to-line rms voltage of $208\,V$. The average dc link voltage was obtained to be about $60\,V$. The generator and the output line-to-line voltage and line current waveforms are shown

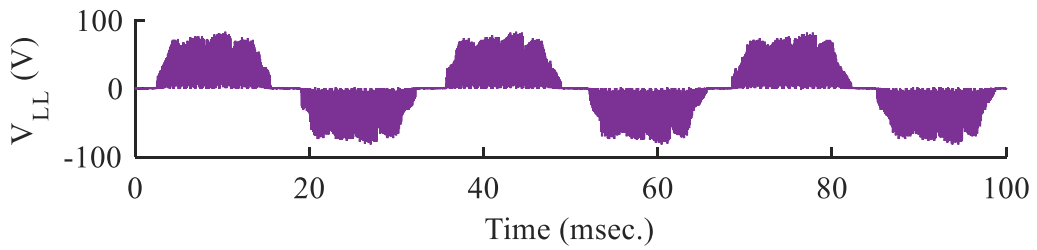

Fig. 6.11: Experimentally obtained waveform of input to the active rectifier.

in Figure 6.10. Figures 6.10 (a) and (b) show the experimentally obtained waveform of the generator output line current and line-to-line voltage, respectively. It can be clearly observed that the generator output current is similar to the current from a three-phase source connected to a full-bridge diode rectifier. The output voltage and current waveforms from the generator are distorted because a diode-bridge rectifier is used as the generator-side converter. This distortion can be eliminated by replacing the diode-bridge rectifier with an active rectifier. The generator line current will be sinusoidal if the system is implemented with the generator-side converter as an active rectifier. Figures 6.10 (c) and (d) present the inverter output line-to-line voltage and line current, respectively. The THD of the output voltage and current was computed to be 2.7% and 3.1%, respectively. Figure 6.11 shows the generator line-to-line voltage as seen by the diode bridge rectifier. It can be observed from Figure 6.10 that the inverter is able to boost a dc voltage of $\sim 60\,V$ to $208\,V$ demonstrating boost ratio of about 3.5. The inverter output voltage and current waveforms demonstrate that the quality of the power from the converter is not compromised. The results presented in Figure 6.10 demonstrate the feasibility of a new topology for a DDWT system but the generator line current is highly distorted with low-order harmonics which will result in a cogging torque at the generator shaft. This distortion in the generator line current is eliminated by replacing the diode bridge rectifier by an active rectifier is presented

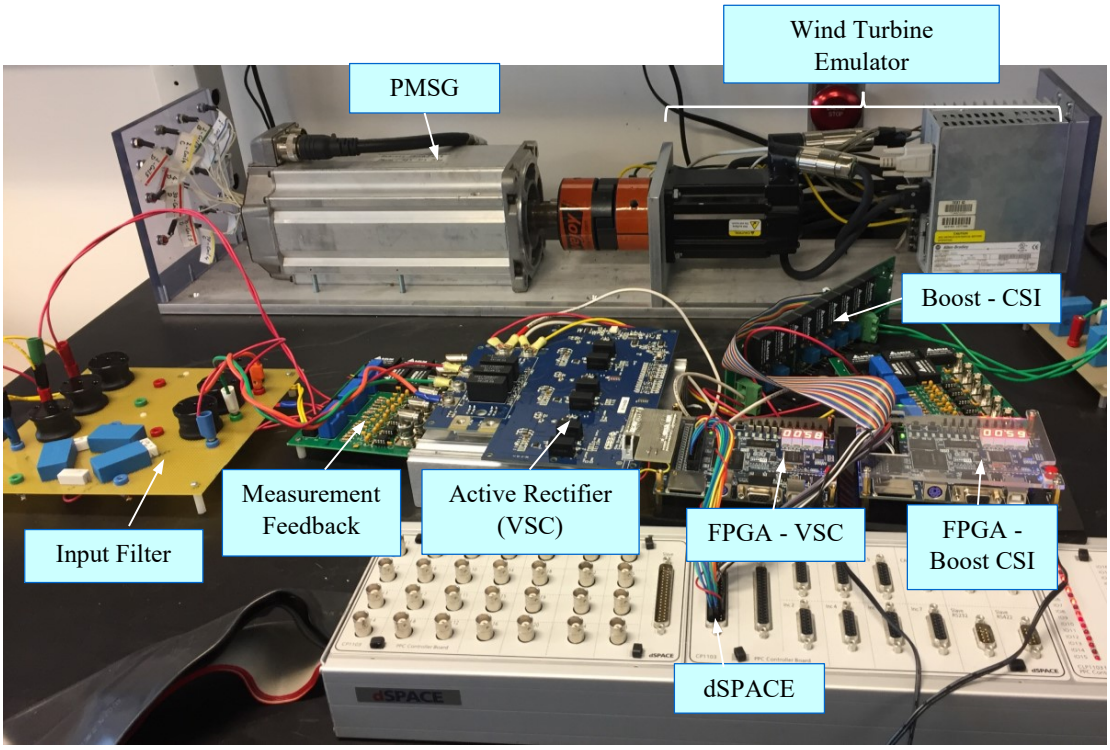

Fig. 6.12: Laboratory scale setup of the proposed system with the wind turbine emulator, the PMSG, an active VSC, and the 2kW 240V three-phase boost CSI operating in stand-alone mode feeding a resistive load.

next.

The next verification is for a wind turbine emulator, PMSG, a VSC as the generator-side converter, and boost - CSI. The operating conditions for the generator are kept same as in the previous case. The experimental setup for this verification is shown in Figure 6.12. The generator speed is $450\,rpm$, which generates a line-to-line voltage of $\sim 45\,V$. The generator side converter hereby referred as the VSC is controlled to maintain the average dc-side voltage at $70\,V$. The switching frequency of the VSC is $25\,kHz$ and was connected to the PMSG through a three-phase L filter of $3\,mH$. The boost - CSI was controlled to regulate the output rms line-to-line voltage at $208\,V$, while switching at $6\,kHz$ and connected to a three-phase resistive load of $50\,\Omega$ through

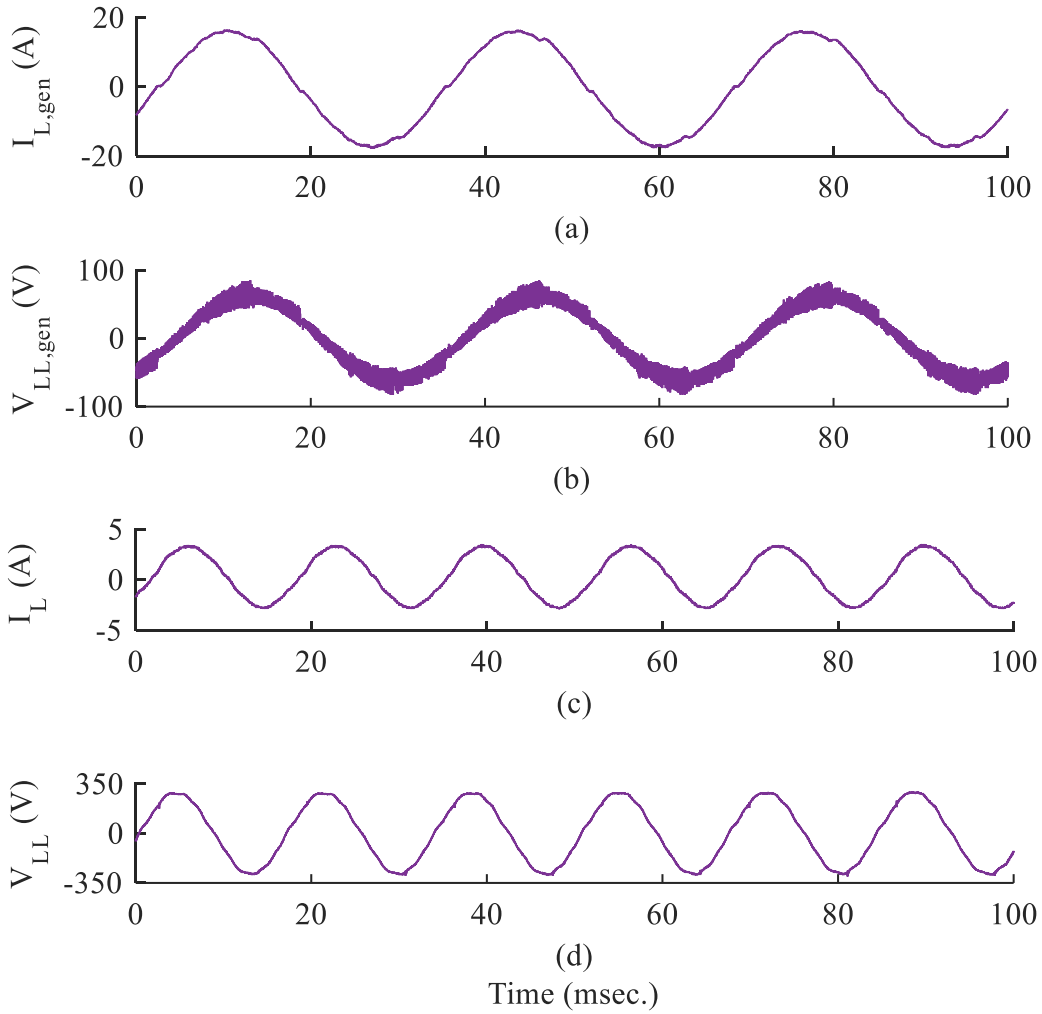

Fig. 6.13: Experimentally obtained waveforms of (a) generator output line current, (b) generator output line-to-line voltage, (c) inverter output line current, and (d) inverter output line-to-line voltage of the system with a VSC as the generator-side converter, when the output of the system is regulated at $208V$ for the stand-alone mode of operation when the PMSG speed is $450\,rpm$.

a three-phase CL filter with $C_{ac} = 20\mu F$ and $L_{ac} = 5\,mH$. Figure 6.13 shows the experimentally obtained waveforms of the generator output line current, generator output line-to-line voltage, load current, and load line-to-line voltage. The FFT analyses of these waveforms are presented in Figures 6.14 and 6.15. The THD of the generator current is calculated to be 2.9%. It can be observed from the waveforms of the genera-

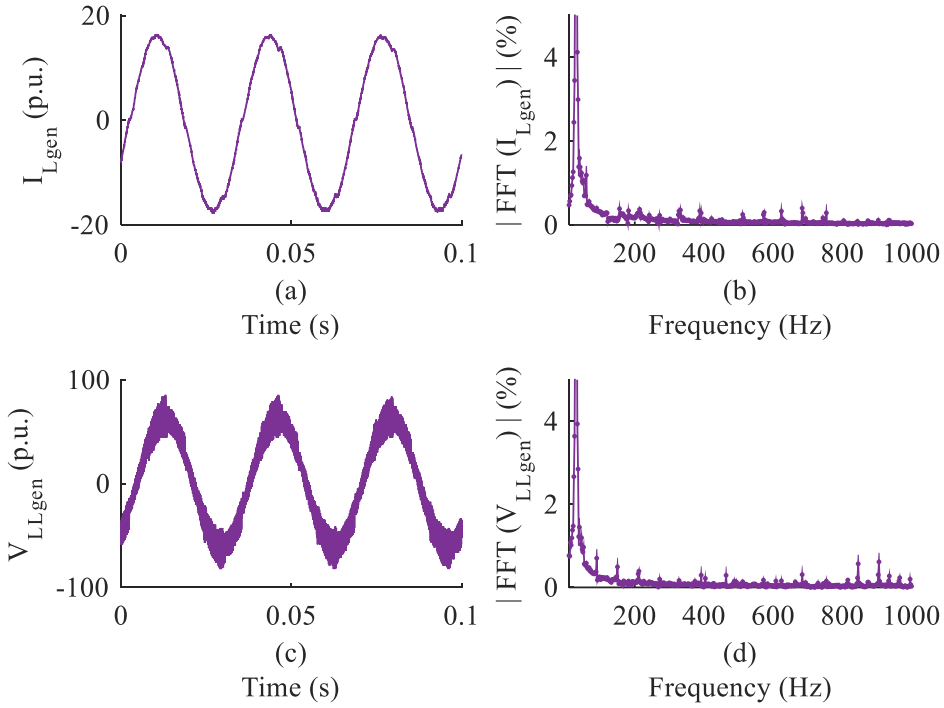

Fig. 6.14: Experimentally obtained generator output (a) line current waveform, (b) line current FFT spectrum, (c) line-to-line voltage waveform, and (d) line-to-line voltage FFT spectrum for the system when the output of the system supplying about 856W active power to a three-phase stand-alone load.

tor output line current and line-to-line voltage and their FFT spectra shown in Figures 6.14(b) and (d) that the low order harmonics have been eliminated. The elimination of the low order harmonics is especially essential for generator line current and it can be evidently observed in Figure 6.10(a) and Figure 6.13(a). This low order harmonic reduction from generator line current results in the elimination of a detrimental cogging torque in the generator.

The next verification is for a wind turbine emulator, PMSG, a VSC as the generator-side converter, and boost - CSI. The operating conditions for the generator are different than the previous case. The generator speed is $600\,rpm$, which generates a line-to-line voltage of about $64\,V$. The generator side converter hereby referred as the VSC is controlled to maintain the average dc-side voltage at $110\,V$. The switching frequency

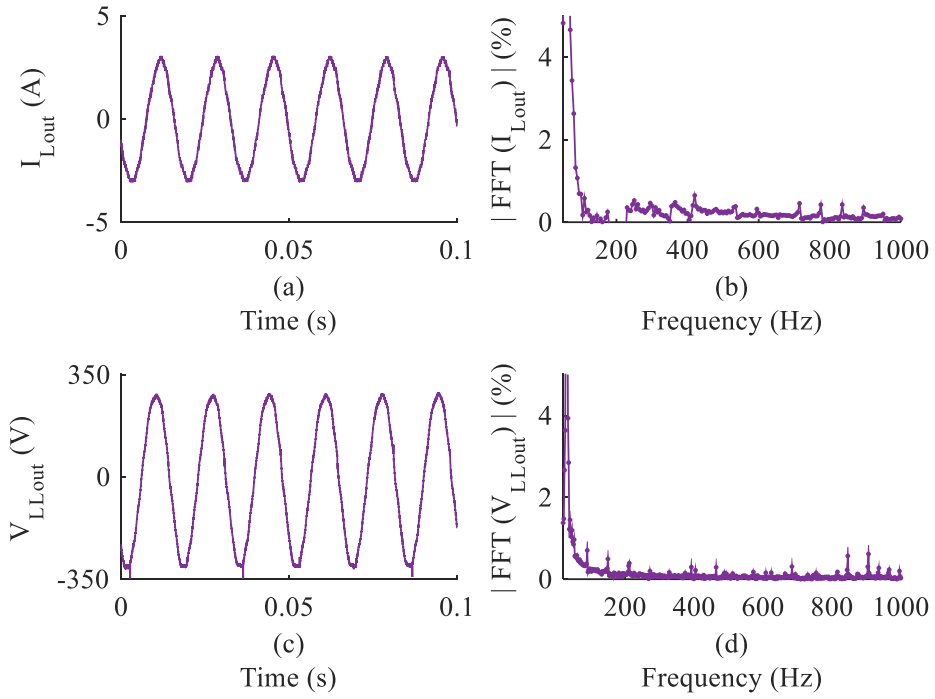

Fig. 6.15: Experimentally obtained load (a) line current waveform, (b) line current FFT spectrum, (c) line-to-line voltage waveform, and (d) line-to-line voltage FFT spectrum for the system when output is regulated at 208V and it is supplying about 856W active power to a three-phase stand-alone load.

of the VSC is $25\,kHz$ and was connected to the PMSG through a three-phase L filter of $3\,mH$. The boost - CSI was controlled to regulate the output rms line-to-line voltage at $208\,V$, while switching at $6\,kHz$ and connected to a three-phase resistive load of $50\,\Omega$ through a three-phase CL filter with $C_{ac} = 20\mu F$ and $L_{ac} = 5\,mH$. Figure 6.16 shows the experimentally obtained waveforms of the generator output line current, generator output line-to-line voltage, load current, and load line-to-line voltage. The THD of the generator current is calculated to be 2.7%. The THD of the load line-to-line voltage and the load current is computed to be 2.8% and 3.01%, respectively. It can be observed from the presented results that the quality of the system output is maintained, while utilizing low voltage from the generator. For a conventional DDWT,

in order to generate this 208 V line-to-line voltage, $\sim$ 220 V rms line-to-line voltage

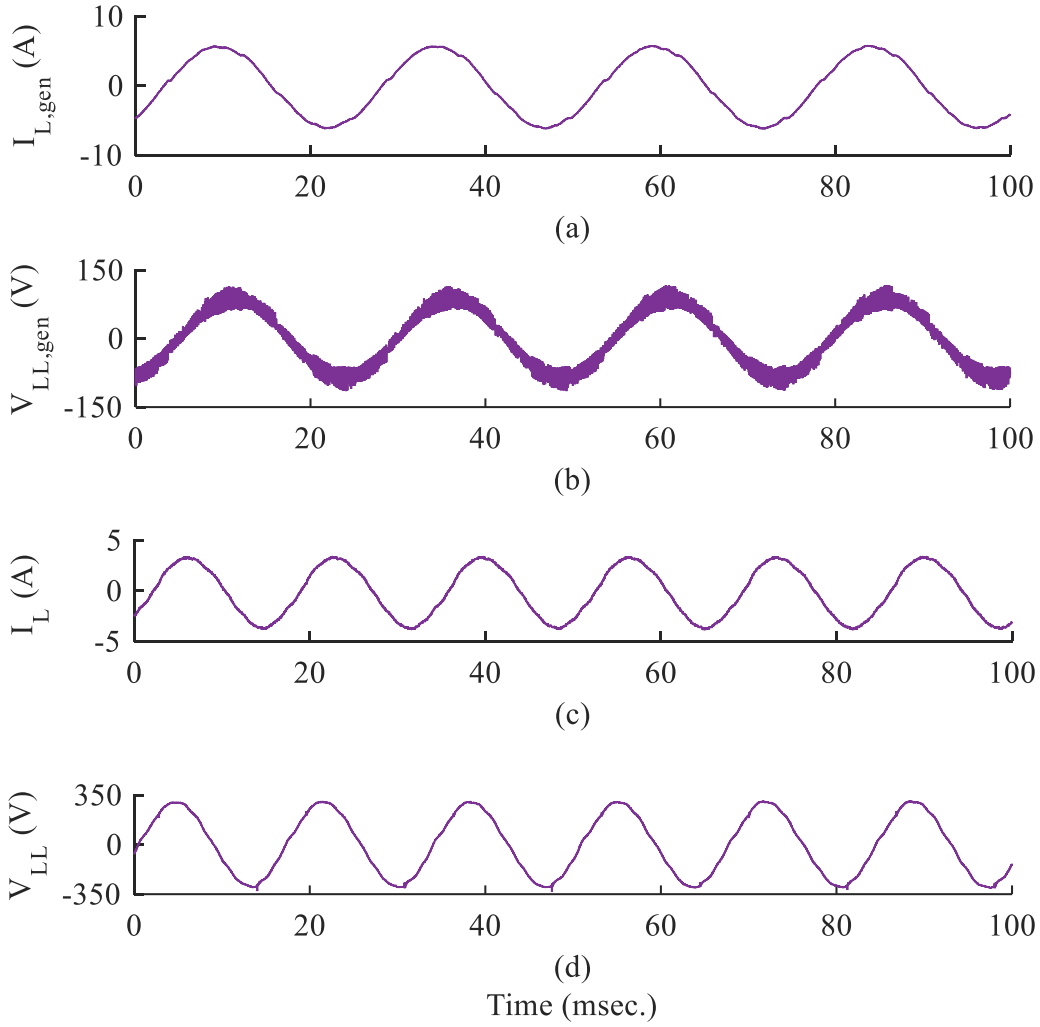

Fig. 6.16: Experimentally obtained waveforms of (a) generator output line current, (b) generator output line-to-line voltage, (c) inverter output line current, and (d) inverter output line-to-line voltage of the system with a VSC as the generator-side converter, when the output of the system is regulated at 208V for stand-alone mode of operation, when the PMSG speed is 600 rpm.

is required from the generator when the power electronics interface is back-to-back VSCs . It is shown from the experimental results that about 64 V line-to-line voltage is sufficient to provide the same output as in a traditional DDWT.

The results presented in this subsection demonstrate the feasibility of the developed system for the stand-alone mode of operation. The developed system is capable of delivering power to a local load while regulating the output voltage and dc-side voltage without compromising the quality of the system. The results also demonstrate that the generator line current does not contain low order harmonics that could create a cogging torque which is detrimental for the generator shaft. In the next subsection, the developed system is verified for grid-tied operation.

6.2.2 Grid-Tied Operation

In this subsection, the feasibility of the developed system is demonstrated for the grid-tied mode of operation. The experimental setup shown in Figure 6.12 is used for this verification. The circuit parameters for this verification is presented in Table 6.1. For this verification the generator is run at $450\,rpm$, resulting in about $45\,V$ rms line-to-line voltage. The VSC is controlled to transfer about $510\,W$ active power to the dc-side considering 98% efficiency of the boost - CSI, i.e. $500\,W$ to be injected into the grid. The boost - CSI is controlled to maintain the average dc-side voltage at $70\,V$. Figure 6.17 shows the generator output line current, generator output line-to-line voltage, line current injected into the grid, and line-to-line voltage at the point of common coupling when the system is injecting $500\,W$ active power into the grid. The THD of the grid line-to-line voltage shown in Figure 6.17(d) is computed to be about 5.1% with a very prominent 5^{th} and 7^{th}harmonic content. This high harmonic content in the available

Table 6.1: Circuit parameter values for experimental verification.

L_s	C_{ac}	L_{ac}	$f_{s,VSC}$	$f_{s,CSI}$
3mH	20µF	5mH	25kHz	6kHz

grid voltage leads to high THD of the current injected into the grid. The THD of the

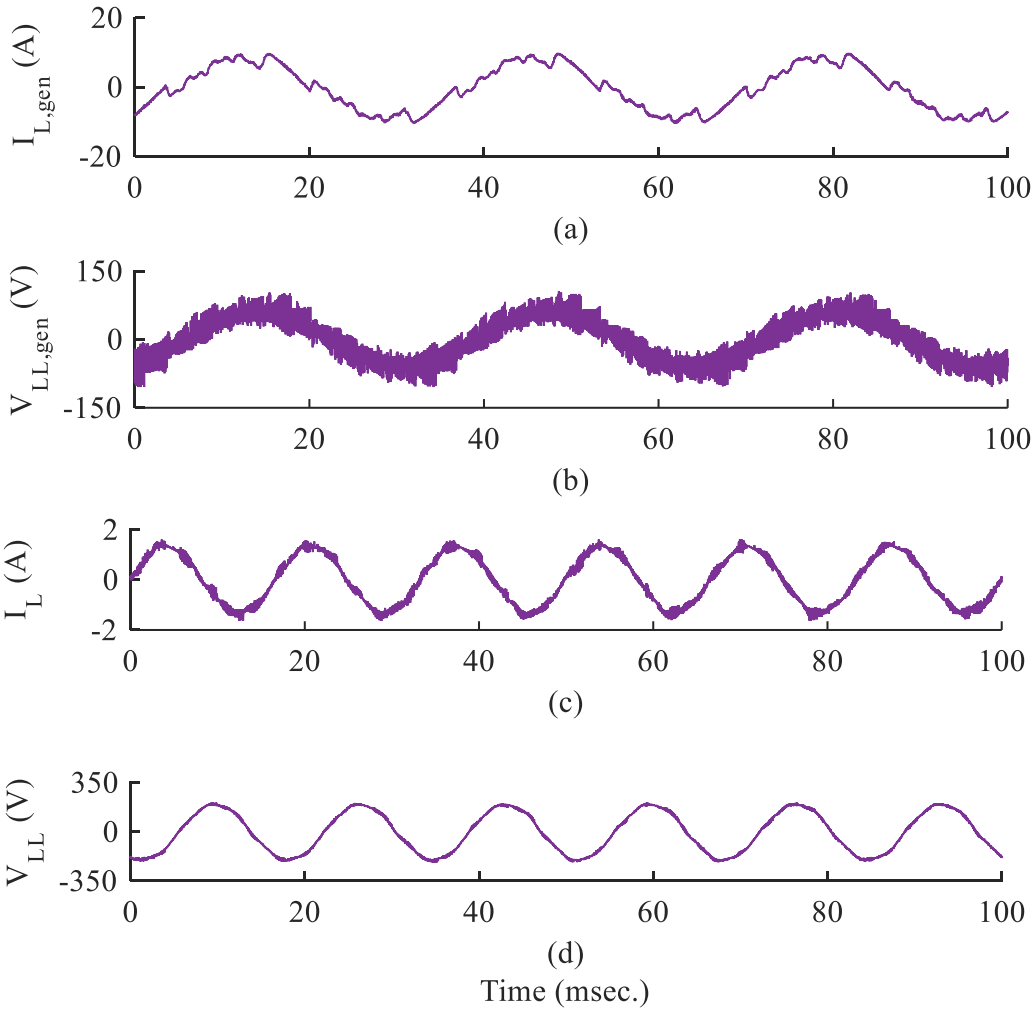

Fig. 6.17: Experimentally obtained waveforms of (a) generator output line current, (b) generator output line-to-line voltage, (c) line current injected into the grid, and (d) line-to-line voltage at the point of common coupling of the system with VSC as the generator-side converter, when the system is injecting $500\,W$ active power into the grid.

line current injected into the grid is computed to be about 5.4%. Even though this THD is high but that is a result of the highly distorted grid, which is further evident from the stand-alone results which have very low distortion of the system output voltage and current waveforms. The efficiency of the entire system was computed to be about

95%. The results shown in Figure 6.17 demonstrate the feasibility of the developed system and its controllers for the grid-tied mode of operation.

6.3 Conclusion

In this chapter, the experimental setup developed for the verification of the proposed topology of DDWTs has been explained. This chapter also presented experimental results on a $1.5\,kW$, $240\,V$ laboratory scale prototype of a boost - CSI in order to show its superior performance. In this chapter, the proof-of-concept of the proposed system has been demonstrated through experimental results on a wind-turbine emulator, PM generator with boost - CSI. The developed system has been verified for both stand-alone and grid-tied modes of operation and the results show the feasibility of the developed topology and its controllers. It has been demonstrated through the presented results that the proposed DDWT topology is feasible and it does not compromise the quality of the system output voltage and current waveforms. The failure prone electrolytic capacitor bank has been eliminated from the DDWT system and no additional component is required for the viability of the proposed system. It has been shown that the developed topology of DDWT is capable of operating with a low voltage generator, and has the potential of reduction in the size of the generator.

Chapter 7

Conclusions and Suggestions for Future Work

In this chapter, the main accomplishments of this dissertation are summarized and the contributions are highlighted. This chapter also includes the suggestions for possible future investigations and research in this topic.

7.1 Summary and Conclusions

This dissertation presents the three-phase single-stage boost CSI as an alternative for multi-stage boost inverters. The application of the boost - CSI for DDWTs has also been presented in this dissertation. This dissertation includes the background and the problem statement for the issue addressed through this dissertation. The motivation behind the research findings presented in this dissertation has been described. The importance of renewable energy deployment is described and the growth in different renewable energy sources has been elaborated. In the introductory chapter, the literature review for the state-of-the-art power converter topologies and wind turbine

topologies have been presented. The challenges that exist which need to be overcome for the proliferation of DDWTs have been discussed.

In this dissertation, topology of the boost - CSI has been described and a review of the switching pattern has been presented. The switching pattern (termed as PPWM) for the boost - CSI has been modified in order to achieve symmetrical switching and lower harmonic content in the inverter output. The modified switching technique has been verified using simulation and experimental results.

The dissertation also forms a knowledge base for the developed boost - CSI. The dynamic models for the inverter have been presented for stand-alone and grid-tied modes of operation. The stability of the inverter has been investigated for different operating conditions. It has been demonstrated that the boost - CSI has a stable operation for stand-alone mode while it is unstable for open-loop grid-tied operation. The inverter controllers have been developed for both stand-alone and grid-tied modes of operation. The steady state characterization equations of the inverter have been developed and a laboratory scale boost - CSI has been characterized. It has been shown that the boost - CSI is an efficient alternative for two-stage boost inverters. It has been demonstrated through simulation and experimental results that the boost inverter is capable of converting a low-voltage dc-input to a higher line-to-line three-phase output voltage with a boost ratio of ~ 3.5.

In this dissertation, the developed boost - CSI is implemented for the DDWT application. The grid-side converter in a conventional DDWT has been replaced by the boost - CSI. It has been demonstrated that the implementation of the boost - CSI as the grid side converter eliminates the need for the failure prone dc-bus electrolytic capacitors. The dc-link inductor which is inherently needed by the boost - CSI has been eliminated by utilizing the synchronous inductance of the PMSG. Furthermore, it has been demonstrated that the developed topology for DDWTs is capable of operating

with a low voltage generator as compared to a traditional DDWT. The low-voltage requirement from the generator has been used to design a PMSG for a 1.5MW system and it has been compared with a generator for existing DDWTs. It has been demonstrated that the developed topology provides flexibility in the generator design and leads to a substantial reduction in the generator volume, weight, and amount of permanent magnet material without affecting the efficiency of the generator. The key contributions of this dissertation are listed as follows:

- A three-phase boost - CSI has been developed, characterized along with its dynamic models. It has been demonstrated capable of converting a low voltage dc-input to a higher line-to-line three-phase output with boost ratio of about 3.5 in single-stage and exhibits efficiency higher than a two-stage counterpart.

- A new generator - converter topology for DDWTs has been introduced in which the boost - CSI has been used as the grid-side converter.

- The developed topology eliminates the failure prone dc-bus electrolytic capacitor bank without any additional component in the system. The synchronous inductance of the PMSG has been utilized to eliminate the dc-link inductor required. It has been shown through reliability analysis of the power electronics interface that the MTBF increases by about 35% for the developed system. The increase in MTBF directly impacts the system operation and maintenance costs especially in case of off-shore wind turbines.

- The developed topology also provides flexibility in the design of the PMSG. It has been shown that a low-voltage generator is required by using the proposed topology of DDWTs. Furthermore, it has been demonstrated that a substantial reduction in the volume, weight, and amount of PM material can be achieved

through a low-voltage PMSG design. This directly impacts the capital cost associated with DDWTs. A lower volume and weight of the PMSG results not only in capital cost reduction but also installation cost reduction. Additionally, in the current unstable and unpredictable market of rare-earth minerals, a low PM material requirement will further help in the proliferation of DDWTs.

7.2 Suggestions for Future Work

This dissertation presents a new generator-converter topology for DDWTs which has a low-voltage PMSG connected to a power electronics interface comprising of cascaded connection of a VSC and a boost - CSI. While the developed system is verified and the advantages are demonstrated, the low voltage generator has not been manufactured and tested. A laboratory scale low-voltage PMSG for the proposed system can be optimally designed and manufactured for a complete system. This will also help in showcasing the developed topology in conferences and to the industry. The optimization of the PMSG for the system can also be an avenue of research.

Furthermore, this dissertation presents a reliability analysis and comparison for the power electronics interface. A detailed reliability analysis of the developed PMSG can be done and compared with the reliability analysis of the existing PMSG for conventional DDWT. The DDWT topology proposed in this dissertation uses a low-voltage generator for the same power rating as an existing DDWT. This results in a higher current rating of the PMSG. A lifetime analysis of the cooling system and demagnetization of the permanent magnet poles can also be done in the future.

It has been shown in Chapter 3 that the boost - CSI has two - quadrant operation due to unidirectional switches (RB-IGBTs) used for the inverter. The inverter operation can be developed for four-quadrant by implementing the inverter using bidi-

rectional switches used in matrix converters and modifying the switching code for the bidirectional operation of the converter.

Bibliography

[1] "Renewables 2016 global status report," 2015. [Online]. Available: http://www.ren21.net/status-of-renewables/global-status-report/

[2] D. Boroyevich, I. Cvetkovic, R. Burgos, and D. Dong, "Intergrid: A future electronic energy network?" *IEEE Jour. of Emerg. and Sel. Topics in Power Electron.*, vol. 1, no. 3, pp. 127–138, Sep. 2013.

[3] B. K. Bose, "Global energy scenario and impact of power electronics in 21st century," *IEEE Trans. on Ind. Electron.*, vol. 60, no. 7, pp. 2638–2651, Jul. 2013.

[4] J. Popovic-Gerber, J. A. Oliver, N. Cordero, T. Harder, J. A. Cobos, M. Hayes, S. C. O'Mathuna, and E. Prem, "Power electronics enabling efficient energy usage: Energy savings potential and technological challenges," *IEEE Trans. on Power Electron.*, vol. 27, no. 5, pp. 2338–2353, May 2012.

[5] M. Liserre, T. Sauter, and J. Y. Hung, "Future energy systems: Integrating renewable energy sources into the smart power grid through industrial electronics," *IEEE Ind. Electron. Mag.*, vol. 4, no. 1, pp. 18–37, Mar. 2010.

[6] F. Blaabjerg, Y. Yang, and K. Ma, "Power electronics - key technology for renewable energy systems - status and future," in *Electric Power and Energy Conversion Systems (EPECS), 2013 3rd International Conference on*, Oct. 2013, pp. 1–6.

[7] F. Blaabjerg, Z. Chen, and S. B. Kjaer, "Power electronics as efficient interface in dispersed power generation systems," *IEEE Trans. on Power Electron.*, vol. 19, no. 5, pp. 1184–1194, Sep. 2004.

[8] F. Blaabjerg, R. Teodorescu, M. Liserre, and A. V. Timbus, "Overview of control and grid synchronization for distributed power generation systems," *IEEE Trans. on Ind. Electron.*, vol. 53, no. 5, pp. 1398–1409, Oct. 2006.

[9] J. Ribrant and L. M. Bertling, "Survey of failures in wind power systems with focus on swedish wind power plants during 1997 ndash;2005," *IEEE Trans. Energy Convers.*, vol. 22, no. 1, pp. 167–173, Mar. 2007.

[10] Z. Daneshi-Far, G. A. Capolino, and H. Henao, "Review of failures and condition monitoring in wind turbine generators," in *Electrical Machines (ICEM), 2010 XIX International Conference on*, Sept. 2010, pp. 1–6.

[11] P. J. Tavnet, G. J. W. V. Bussel, and F. Spinato, "Machine and converter reliabilities in wind turbines," in *Power Electronics, Machines and Drives, 2006. The 3rd IET International Conference on*, Apr. 2006, pp. 127–130.

[12] H. Polinder, F. F. A. van der Pijl, G. J. de Vilder, and P. J. Tavner, "Comparison of direct-drive and geared generator concepts for wind turbines," *IEEE Trans. Energy Convers.*, vol. 21, no. 3, pp. 725–733, Sep. 2006.

[13] A. M. Imam, D. M. Divan, R. G. Harley, and T. G. Habetler, "Real-time condition monitoring of the electrolytic capacitors for power electronics applications," in *APEC 07 - Twenty-Second Annual IEEE Applied Power Electronics Conference and Exposition*, Feb. 2007, pp. 1057–1061.

[14] P. Venet, H. Darnand, and G. Grellet, "Detection of faults of filter capacitors in a converter. application to predictive maintenance," in *Telecommunications Energy*

Conference, INTELEC '93. 15th International, vol. 2, Sep. 1993, pp. 229–234 vol.2.

[15] P. Venet, F. Perisse, M. H. El-Husseini, and G. Rojat, "Realization of a smart electrolytic capacitor circuit," *IEEE Ind. Appl. Mag.*, vol. 8, no. 1, pp. 16–20, Jan. 2002.

[16] A. Lahyani, P. Venet, G. Grellet, and P. J. Viverge, "Failure prediction of electrolytic capacitors during operation of a switchmode power supply," *IEEE Trans. Power Electron.*, vol. 13, no. 6, pp. 1199–1207, Nov. 1998.

[17] K. Harada, A. Katsuki, and M. Fujiwara, "Use of esr for deterioration diagnosis of electrolytic capacitor," *IEEE Trans. on Power Electron.*, vol. 8, no. 4, pp. 355–361, Oct. 1993.

[18] W. Tong, *Wind power generation and wind turbine design.* WIT Press, 2010.

[19] H. Li, Z. Chen, and H. Polinder, "Optimization of multibrid permanent-magnet wind generator systems," *IEEE Trans. Energy Convers.*, vol. 24, no. 1, pp. 82–92, Mar. 2009.

[20] M. Chinchilla, S. Arnaltes, and J. C. Burgos, "Control of permanent-magnet generators applied to variable-speed wind-energy systems connected to the grid," *IEEE Trans. on Energy Convers.*, vol. 21, no. 1, pp. 130–135, Mar. 2006.

[21] J. Chen, C. V. Nayar, and L. Xu, "Design and finite-element analysis of an outer-rotor permanent-magnet generator for directly coupled wind turbines," *IEEE Trans. on Magn.*, vol. 36, no. 5, pp. 3802–3809, Sep. 2000.

[22] Y. K. Wu, C. Y. Lee, C. R. Chen, K. W. Hsu, and H. T. Tseng, "Optimization of the wind turbine layout and transmission system planning for a large-scale offshore

windfarm by ai technology," *IEEE Trans. Ind. Appl.*, vol. 50, no. 3, pp. 2071–2080, May 2014.

[23] K. Leban, E. Ritchie, and A. Argeseanu, "Design preliminaries for direct drive under water wind turbine generator," in *Electrical Machines (ICEM), 2012 XXth International Conference on*, Sep. 2012, pp. 190–195.

[24] D. McMillan and G. W. Ault, "Techno-economic comparison of operational aspects for direct drive and gearbox-driven wind turbines," *IEEE Trans. Energy Convers.*, vol. 25, no. 1, pp. 191–198, Mar. 2010.

[25] D. Bang, H. Polinder, G. Shrestha, and J. A. Ferreira, "Review of generator systems for direct-drive wind turbines," in *European Wind Energy Conference & Exhibition, Belgium*, 2008, pp. 1–11.

[26] J. F. Manwell, J. G. McGowan, and A. L. Rogers, *Wind energy explained*. Wiley, 2009.

[27] Z. Chen, J. M. Guerrero, and F. Blaabjerg, "A review of the state of the art of power electronics for wind turbines," *IEEE Trans. Power Electron.*, vol. 24, no. 8, pp. 1859–1875, Aug. 2009.

[28] F. Blaabjerg, M. Liserre, and K. Ma, "Power electronics converters for wind turbine systems," *IEEE Trans. Ind. Appl.*, vol. 48, no. 2, pp. 708–719, Mar. 2012.

[29] T. Sun, Z. Chen, and F. Blaabjerg, "Voltage recovery of grid-connected wind turbines after a short-circuit fault," in *Industrial Electronics Society, 2003. IECON '03. The 29th Annual Conference of the IEEE*, vol. 3, Nov. 2003, pp. 2723–2728 Vol.3.

[30] F. Spinato, P. J. Tavner, G. J. W. V. Bussel, and E. Koutoulakos, "Reliability of wind turbine subassemblies," *IET Renew. Power Gener.*, vol. 3, no. 4, pp. 387–401, Dec. 2009.

[31] F. Blaabjerg and K. Ma, "Future on power electronics for wind turbine systems," *IEEE Jour. of Emerg. and Sel. Topics in Power Electron.*, vol. 1, no. 3, pp. 139–152, Sep. 2013.

[32] J. Dai, D. Xu, and B. Wu, "A novel control scheme for current-source-converter-based pmsg wind energy conversion systems," *IEEE Trans. Power Electron.*, vol. 24, no. 4, pp. 963–972, Apr. 2009.

[33] H. Wang, M. Liserre, and F. Blaabjerg, "Toward reliable power electronics: Challenges, design tools, and opportunities," *IEEE Ind. Electron. Mag.*, vol. 7, no. 2, pp. 17–26, Jun. 2013.

[34] A. Zavvos, A. Mcdonald, and M. Mueller, "Optimisation tools for large permanent magnet generators for direct drive wind turbines," *IET Renew. Power Gener.*, vol. 7, no. 2, pp. 163–171, Mar. 2013.

[35] P. Tenca, A. A. Rockhill, T. A. Lipo, and P. Tricoli, "Current source topology for wind turbines with decreased mains current harmonics, further reducible via functional minimization," *IEEE Trans. on Power Electron.*, vol. 23, no. 3, pp. 1143–1155, May. 2008.

[36] Z. Zhang, Y. Zhao, W. Qiao, and L. Qu, "A space-vector-modulated sensorless direct-torque control for direct-drive pmsg wind turbines," *IEEE Trans. on Ind. Appl.*, vol. 50, no. 4, pp. 2331–2341, Jul. 2014.

[37] J. H. J. Potgieter and M. J. Kamper, "Design optimization of directly grid-connected pm machines for wind energy applications," *IEEE Trans. Ind. Appl.*, vol. 51, no. 4, pp. 2949–2958, Jul. 2015.

[38] R. Teichmann and S. Bernet, "A comparison of three-level converters versus two-level converters for low-voltage drives, traction, and utility applications," *IEEE Trans. on Ind. Appl.*, vol. 41, no. 3, pp. 855–865, May 2005.

[39] S. Kouro, M. Malinowski, K. Gopakumar, J. Pou, L. G. Franquelo, B. Wu, J. Rodriguez, M. A. Perez, and J. I. Leon, "Recent advances and industrial applications of multilevel converters," *IEEE Trans. on Ind. Electron.*, vol. 57, no. 8, pp. 2553–2580, Aug. 2010.

[40] H. Hosoda and S. Peak, "Multi-level converters for large capacity motor drive," in *The 2010 International Power Electronics Conference - ECCE ASIA -*, Jun. 2010, pp. 516–522.

[41] M. Altin, . GÃ¶ksu, R. Teodorescu, P. Rodriguez, B. B. Jensen, and L. Helle, "Overview of recent grid codes for wind power integration," in *2010 12th International Conference on Optimization of Electrical and Electronic Equipment*, May 2010, pp. 1152–1160.

[42] A. Singh, A. A. Milani, and B. Mirafzal, "Voltage regulation in single-stage boost inverter for stand-alone applications," in *2014 IEEE Applied Power Electronics Conference and Exposition - APEC 2014*, Mar. 2014, pp. 3011–3016.

[43] ——, "Modified phasor pulse width modulation method for three-phase single-stage boost inverter," in *2014 IEEE Applied Power Electronics Conference and Exposition - APEC 2014*, Mar. 2014, pp. 1276–1280.

[44] B. Mirafzal, M. Saghaleini, and A. K. Kaviani, "An SVPWM-based switching pattern for stand-alone and grid-connected three-phase single-stage boost inverters," *IEEE Trans. Power Electron.*, vol. 26, no. 4, pp. 1102–1111, Apr. 2011.

[45] A. Singh, A. K. Kaviani, and B. Mirafzal, "On dynamic models and stability analysis of three-phase phasor PWM-based CSI for stand-alone applications," *IEEE Trans. Ind. Electron.*, vol. 62, no. 5, pp. 2698–2707, May 2015.

[46] Z. Wang, B. Wu, D. Xu, and N. R. Zargari, "A current-source-converter-based high-power high-speed pmsm drive with 420-hz switching frequency," *IEEE Trans. on Ind. Electron.*, vol. 59, no. 7, pp. 2970–2981, Jul. 2012.

[47] D. G. Holmes and T. A. Lipo, *Pulse width modulation for power converters: principles and practice*, 1st ed. Wiley & Sons, 2003.

[48] N. Mohan, T. Undeland, and W. Robbins, *Power Electronics: Converters, Applications and Design*, 3rd ed. Wiley, 2003.

[49] A. E. Fitzgerald, C. Kingsley, S. D. Umans, and B. James, *Electric machinery*. McGraw-Hill New York, 2003, vol. 5.

[50] E. Koutroulis and F. Blaabjerg, "Design optimization of transformerless grid-connected pv inverters including reliability," *IEEE Trans. on Power Electron.*, vol. 28, no. 1, pp. 325–335, Jan. 2013.

[51] *Military handbook reliability prediction of electronic equipment.* Department of Defense, 1986.

[52] M. Aten, G. Towers, C. Whitley, P. Wheeler, J. Clare, and K. Bradley, "Reliability comparison of matrix and other converter topologies," *IEEE Transactions on Aerosp. and Electron. Syst.*, vol. 42, no. 3, pp. 867–875, Jul. 2006.

[53] X. Yu and A. M. Khambadkone, "Reliability analysis and cost optimization of parallel-inverter system," *IEEE Trans. on Ind. Electron.*, vol. 59, no. 10, pp. 3881–3889, Oct. 2012.

[54] I. A. Dinwoodie and D. Mcmillan, "Operational strategies for offshore wind turbines to mitigate failure rate uncertainty on operational costs and revenue," *IET Renew. Power Gen.*, vol. 8, no. 4, pp. 359–366, May 2014.

[55] G. Bywaters, P. Mattila, D. Costin, J. Stowell, V. John, S. Hoskins, J. Lynch, T. Cole, A. Cate, C. Badger, and B. Freeman, "Northern power nw 1500 direct-drive generator," *National Renewable Energy Laboratory, Report*, 2006.

[56] Y. Guo, H. Lin, P. Jin, J. Yan, J. Wang, and Z. Jia, "Analytical modeling of air-gap field distributions in permanent magnet embedded salient pole wind generator," *IEEE Trans. Magn.*, vol. 49, no. 12, pp. 5756–5760, Dec. 2013.

[57] "IEEE Standard for Interconnecting Distributed Resources with Electric Power Systems," *IEEE Std. 1547-2003*, pp. 1–28, Jul. 2003.

[58] H. Polinder, D. Bang, R. P. J. O. M. van Rooij, A. S. McDonald, and M. A. Mueller, "10 mw wind turbine direct-drive generator design with pitch or active speed stall control," in *2007 IEEE International Electric Machines Drives Conference*, vol. 2, May 2007, pp. 1390–1395.

[59] H. Polinder, J. A. Ferreira, B. B. Jensen, A. B. Abrahamsen, K. Atallah, and R. A. McMahon, "Trends in wind turbine generator systems," *IEEE Trans. Emerg. Sel. Topics Power Electron.*, vol. 1, no. 3, pp. 174–185, Sep. 2013.

[60] X. Yuan and Y. Li, "Control of variable pitch and variable speed direct-drive wind turbines in weak grid systems with active power balance," *IET Renew. Power Gener.*, vol. 8, no. 2, pp. 119–131, March 2014.

[61] N. M. A. Freire, J. O. Estima, and A. J. M. Cardoso, "Open-circuit fault diagnosis in pmsg drives for wind turbine applications," *IEEE Trans. Ind. Electron.*, vol. 60, no. 9, pp. 3957–3967, Sep. 2013.

[62] A. Kavimandan and S. P. Das, "Control and protection strategy for a three-phase single-stage boost type grid-connected current source inverter for pv applications," in *Industrial Technology (ICIT), 2013 IEEE International Conference on*, Feb. 2013, pp. 1722–1727.

[63] B. Wu, J. Pontt, J. Rodriguez, S. Bernet, and S. Kouro, "Current-source converter and cycloconverter topologies for industrial medium-voltage drives," *IEEE Trans. on Ind. Electron.*, vol. 55, no. 7, pp. 2786–2797, Jul. 2008.

[64] Y. W. Li, M. Pande, N. R. Zargari, and B. Wu, "Dc-link current minimization for high-power current-source motor drives," *IEEE Trans. on Power Electron.*, vol. 24, no. 1, pp. 232–240, Jan. 2009.

[65] M. Salo and H. Tuusa, "vector-controlled pwm current-source-inverter-fed induction motor drive with a new stator current control method," *IEEE Trans. on Ind. Electron.*, vol. 52, no. 2, pp. 523–531, Apr. 2005.

[66] S. R. Bowes and P. R. Clark, "Transputer-based harmonic-elimination pwm control of inverter drives," *IEEE Trans. on Ind. Appl.*, vol. 28, no. 1, pp. 72–80, Jan. 1992.

[67] Y. Zhou and W. Huang, "Single-stage boost inverter with coupled inductor," *IEEE Trans. on Power Electron.*, vol. 27, no. 4, pp. 1885–1893, Apr. 2012.

[68] S. Anand, S. K. Gundlapalli, and B. G. Fernandes, "Transformer-less grid feeding current source inverter for solar photovoltaic system," *IEEE Trans. on Ind. Electron.*, vol. 61, no. 10, pp. 5334–5344, Oct. 2014.

[69] M. de Brito, L. Sampaio, G. Melo, and C. A. Canesin, "Three-phase tri-state buck-boost integrated inverter for solar applications," *IET Renew. Power Gener.*, vol. 9, no. 6, pp. 557–565, 2015.

[70] J. Lamb, A. Singh, and B. Mirafzal, "Rapid implementation of solid-state based converters in power engineering laboratories," *IEEE Trans. Power Syst.*, vol. 31, no. 4, pp. 2957–2964, Jul. 2016.

[71] U. R. Prasanna and A. K. Rathore, "A novel single-reference six-pulse-modulation (srspm) technique-based interleaved high-frequency three-phase inverter for fuel cell vehicles," *IEEE Trans. on Power Electron.*, vol. 28, no. 12, pp. 5547–5556, Dec. 2013.

[72] ——, "Dual three-pulse modulation-based high-frequency pulsating dc link two-stage three-phase inverter for electric/hybrid/fuel cell vehicles applications," *IEEE Jour. of Emerg. and Sel. Topics in Power Electron.*, vol. 2, no. 3, pp. 477–486, Sep. 2014.

[73] S. R. Sanders, J. M. Noworolski, X. Z. Liu, and G. C. Verghese, "Generalized averaging method for power conversion circuits," *IEEE Trans. on Power Electron.*, vol. 6, no. 2, pp. 251–259, Apr. 1991.

[74] A. K. Kaviani, "Dynamic modeling and analysis of single-stage boost inverters under normal and abnormal conditions," *Ph.D. Disseration, FIU*, 2012.

[75] U. R. Prasanna and A. K. Rathore, "Small-signal modeling of active-clamped zvs current-fed full-bridge isolated dc/dc converter and control system implementation using psoc," *IEEE Trans. on Ind. Electron.*, vol. 61, no. 3, pp. 1253–1261, Mar. 2014.

[76] R. Lai, F. Wang, R. Burgos, D. Boroyevich, D. Jiang, and D. Zhang, "Average modeling and control design for vienna-type rectifiers considering the dc-link voltage balance," *IEEE Trans. on Power Electron.*, vol. 24, no. 11, pp. 2509–2522, Nov. 2009.

[77] R. C. Dorf and R. H. Bishop, *The relative stability of feedback control systems*, 23rd ed. Pearson, 2011.

[78] F. Fateh, W. N. White, and D. Gruenbacher, "A maximum power tracking technique for grid-connected dfig-based wind turbines," *IEEE Jour. Emerg. and Sel. Topics Power Electron.*, vol. 3, no. 4, pp. 957–966, Dec 2015.

Appendix A

Dynamic Model Derivations

Stand-Alone System

The averaged state matrices for the six sectors are as follows:

$$\overline{A}_I = \begin{bmatrix} \frac{-R_{dc}-2R_{ON}}{L_{dc}} & \frac{-(d_1+d_2)}{L_{dc}} & \frac{-d_2}{L_{dc}} & 0 & 0 \\ \frac{2d_1+d_2}{3C_{ac}} & 0 & 0 & \frac{-1}{3C_{ac}} & \frac{1}{3C_{ac}} \\ \frac{-d_1+d_2}{3C_{ac}} & 0 & 0 & \frac{-1}{3C_{ac}} & \frac{-2}{3C_{ac}} \\ 0 & \frac{2}{3L_L} & \frac{1}{3L_L} & \frac{-R_L}{L_L} & 0 \\ 0 & \frac{-1}{3L_L} & \frac{1}{3L_L} & 0 & \frac{-R_L}{L_L} \end{bmatrix} \tag{A.1}$$

$$\overline{A}_{II} = \begin{bmatrix} \frac{-R_{dc}-2R_{ON}}{L_{dc}} & \frac{-d_1}{L_{dc}} & \frac{-(d_1+d_2)}{L_{dc}} & 0 & 0 \\ \frac{d_1-d_2}{3C_{ac}} & 0 & 0 & \frac{-1}{3C_{ac}} & \frac{1}{3C_{ac}} \\ \frac{d_1+2d_2}{3C_{ac}} & 0 & 0 & \frac{-1}{3C_{ac}} & \frac{-2}{3C_{ac}} \\ 0 & \frac{2}{3L_L} & \frac{1}{3L_L} & \frac{-R_L}{L_L} & 0 \\ 0 & \frac{-1}{3L_L} & \frac{1}{3L_L} & 0 & \frac{-R_L}{L_L} \end{bmatrix} \tag{A.2}$$

$$\overline{A}_{III} = \begin{bmatrix} \frac{-R_{dc}-2R_{ON}}{L_{dc}} & \frac{d_2}{L_{dc}} & \frac{-d_1}{L_{dc}} & 0 & 0 \\ \frac{-(d_1+2d_2)}{3C_{ac}} & 0 & 0 & \frac{-1}{3C_{ac}} & \frac{1}{3C_{ac}} \\ \frac{2d_1+d_2}{3C_{ac}} & 0 & 0 & \frac{-1}{3C_{ac}} & \frac{-2}{3C_{ac}} \\ 0 & \frac{2}{3L_L} & \frac{1}{3L_L} & \frac{-R_L}{L_L} & 0 \\ 0 & \frac{-1}{3L_L} & \frac{1}{3L_L} & 0 & \frac{-R_L}{L_L} \end{bmatrix} \tag{A.3}$$

$$\overline{A}_{IV} = \begin{bmatrix} \frac{-R_{dc}-2R_{ON}}{L_{dc}} & \frac{d_1+d_2}{L_{dc}} & \frac{d_2}{L_{dc}} & 0 & 0 \\ \frac{-(2d_1+d_2)}{3C_{ac}} & 0 & 0 & \frac{-1}{3C_{ac}} & \frac{1}{3C_{ac}} \\ \frac{d_1-d_2}{3C_{ac}} & 0 & 0 & \frac{-1}{3C_{ac}} & \frac{-2}{3C_{ac}} \\ 0 & \frac{2}{3L_L} & \frac{1}{3L_L} & \frac{-R_L}{L_L} & 0 \\ 0 & \frac{-1}{3L_L} & \frac{1}{3L_L} & 0 & \frac{-R_L}{L_L} \end{bmatrix} \tag{A.4}$$

$$\overline{A}_{V} = \begin{bmatrix} \frac{-R_{dc}-2R_{ON}}{L_{dc}} & \frac{d_1}{L_{dc}} & \frac{d_1+d_2}{L_{dc}} & 0 & 0 \\ \frac{-d_1+d_2}{3C_{ac}} & 0 & 0 & \frac{-1}{3C_{ac}} & \frac{1}{3C_{ac}} \\ \frac{-(d_1+2d_2)}{3C_{ac}} & 0 & 0 & \frac{-1}{3C_{ac}} & \frac{-2}{3C_{ac}} \\ 0 & \frac{2}{3L_L} & \frac{1}{3L_L} & \frac{-R_L}{L_L} & 0 \\ 0 & \frac{-1}{3L_L} & \frac{1}{3L_L} & 0 & \frac{-R_L}{L_L} \end{bmatrix} \tag{A.5}$$

$$\overline{A}_{VI} = \begin{bmatrix} \frac{-R_{dc}-2R_{ON}}{L_{dc}} & \frac{-d_2}{L_{dc}} & \frac{d_1}{L_{dc}} & 0 & 0 \\ \frac{d_1+2d_2}{3C_{ac}} & 0 & 0 & \frac{-1}{3C_{ac}} & \frac{1}{3C_{ac}} \\ \frac{-(2d_1+d_2)}{3C_{ac}} & 0 & 0 & \frac{-1}{3C_{ac}} & \frac{-2}{3C_{ac}} \\ 0 & \frac{2}{3L_L} & \frac{1}{3L_L} & \frac{-R_L}{L_L} & 0 \\ 0 & \frac{-1}{3L_L} & \frac{1}{3L_L} & 0 & \frac{-R_L}{L_L} \end{bmatrix} \tag{A.6}$$

It can be shown that these matrices have the same eigenvalues which indicates that

these are similar matrices. Equation (A.1)for Sector I can be re-written as

$$\begin{bmatrix} \frac{d}{dt}\widetilde{i}_{dc} \\ \frac{d}{dt}\widetilde{v}_{LL} \\ \frac{d}{dt}\widetilde{i}_{L} \end{bmatrix} = \begin{bmatrix} \overline{A}_{I(1,1)} & \overline{A}_{I(1,2)} & \overline{A}_{I(1,3)} \\ \overline{A}_{I(2,1)} & \overline{A}_{I(2,2)} & \overline{A}_{I(2,3)} \\ \overline{A}_{I(3,1)} & \overline{A}_{I(3,2)} & \overline{A}_{I(3,3)} \end{bmatrix} \begin{bmatrix} \widetilde{i}_{dc} \\ \widetilde{v}_{LL} \\ \widetilde{i}_{L} \end{bmatrix} + \begin{bmatrix} \overline{B}_{(1,1)} \\ O \end{bmatrix} v_{dc} \tag{A.7}$$

where, $\overline{A}_{I(1,1)} = \frac{-R_{dc}}{L_{dc}}$, $\overline{A}_{I(1,2)} = \begin{bmatrix} \frac{-(d_{\cdot 1}+d_2)}{L_{dc}} & \frac{-d_2}{L_{dc}} \end{bmatrix}$, $\overline{A}_{I(1,3)} = \begin{bmatrix} 0 & 0 \end{bmatrix}$, $\overline{A}_{I(2,1)} = \begin{bmatrix} \frac{2d_1+d_2}{3C_{ac}} \\ \frac{-d_1+d_2}{3C_{ac}} \end{bmatrix}$, $\overline{A}_{I(2,2)} = \begin{bmatrix} 0 & 0 \\ 0 & 0 \end{bmatrix}$, $\overline{A}_{I(2,3)} = \begin{bmatrix} \frac{-1}{3C_{ac}} & \frac{1}{3C_{ac}} \\ \frac{-1}{3C_{ac}} & \frac{-2}{3C_{ac}} \end{bmatrix}$, $\overline{A}_{I(3,1)} = \begin{bmatrix} 0 \\ 0 \end{bmatrix}$, $\overline{A}_{I(3,2)} = \begin{bmatrix} \frac{2}{3L_L} & \frac{1}{3L_L} \\ \frac{-1}{3L_L} & \frac{1}{3L_L} \end{bmatrix}$, $\overline{A}_{I(3,3)} = \begin{bmatrix} \frac{-R_L}{L_L} & 0 \\ 0 & \frac{-R_L}{L_L} \end{bmatrix}$, $\widetilde{v}_{LL} = \begin{bmatrix} \widetilde{v}_{ab} \\ \widetilde{v}_{bc} \end{bmatrix}$, $\widetilde{i}_L = \begin{bmatrix} \widetilde{i}_a \\ \widetilde{i}_b \end{bmatrix}$, $\overline{B}_{(1,1)} = \frac{1}{L_{dc}}$, $O = \begin{bmatrix} 0 & 0 & 0 & 0 \end{bmatrix}^T$.

Using equation (4.1)

$$\widetilde{v}_{LL} = M\widetilde{v}_{qd} \tag{A.8}$$

Accordingly, the derivative of $\widetilde{v}_{LL}$ with respect to time is obtained as:

$$\frac{d}{dt}\widetilde{v}_{LL} = \left(\frac{d}{dt}M\right)\widetilde{v}_{qd} + M\left(\frac{d}{dt}\right)\widetilde{v}_{qd} \tag{A.9}$$

Using the (A.7) and (A.8), one can write:

$$\frac{d}{dt}\widetilde{i}_{dc} = \overline{A}_{I(1,1)}\widetilde{i}_{dc} + \overline{A}_{I(1,2)}M\widetilde{v}_{qd} + \overline{B}_{(1,1)}v_{dc} \tag{A.10}$$

Using the second row of (A.7) and (A.9),

$$\left(\frac{d}{dt}M\right)\widetilde{v}_{qd} + M\left(\frac{d}{dt}\widetilde{v}_{qd}\right) = \overline{A}_{I(2,1)}\widetilde{i}_{dc} + \overline{A}_{I(2,3)}M\widetilde{v}_{qd} + Ov_{dc} \tag{A.11}$$

Using (A.11), the derivative of $\widetilde{v}_{qd}$ with respect to time can be expressed as

$$\frac{d}{dt}\widetilde{v}_{qd} = M^{-1}\overline{A}_{I(2,1)}\widetilde{i}_{dc} - \left[\begin{array}{cc} \frac{1}{3R_LC_{ac}}I & M^{-1}\frac{d}{dt}M \end{array}\right]\widetilde{v}_{qd} + Ov_{dc} \tag{A.12}$$

Using (A.10) and (A.12), (A.7) can be expressed as

$$\frac{d}{dt}\left[\begin{array}{c} \widetilde{i}_{dc} \\ \widetilde{v}_{qd} \end{array}\right] = \overline{A}_{dqI}\left[\begin{array}{c} \widetilde{i}_{dc} \\ \widetilde{v}_{qd} \end{array}\right] + \left[\begin{array}{c} \frac{1}{L_{dc}} \\ O \end{array}\right] v_{dc} \tag{A.13}$$

where,

$$\overline{A}_{dqI} = \left[\begin{array}{ccc} \frac{-R_{dc}-2R_{ON}}{L_{dc}} & \frac{-\left[d_1cos(\theta)+d_2cos\left(\theta-\frac{\pi}{3}\right)\right]}{L_{dc}} & \cdots \\ \frac{2\left[d_1cos(\theta)+d_2cos\left(\theta-\frac{\pi}{3}\right)\right]}{3C_{ac}} & 0 & \cdots \\ \frac{2\left[d_1sin(\theta)+d_2sin\left(\theta-\frac{\pi}{3}\right)\right]}{3C_{ac}} & \omega & \cdots \\ 0 & \frac{1}{2L_L} & \cdots \\ 0 & \frac{\sqrt{3}}{6L_L} & \cdots \end{array}\right] \cdots$$

$$\cdots = \left[\begin{array}{cccc} \cdots & \frac{-\left[d_1sin(\theta)+d_2sin\left(\theta-\frac{\pi}{3}\right)\right]}{L_{dc}} & 0 & 0 \\ \cdots & -\omega & \frac{-1}{2C_{ac}} & \frac{-\sqrt{3}}{6C_{ac}} \\ \cdots & 0 & \frac{\sqrt{3}}{6C_{ac}} & \frac{-1}{2C_{ac}} \\ \cdots & \frac{-\sqrt{3}}{6L_L} & \frac{-R_L}{L_L} & -\omega \\ \cdots & \frac{1}{2L_L} & \omega & \frac{-R_L}{L_L} \end{array}\right] \tag{A.14}$$

The averaged system matrices for other sectors in the dq-frame of reference can be obtained similarly. The averaged matrices in dq - frame of reference are presented as follows:

$$\overline{A}_{dqI} = \begin{bmatrix} \frac{-R_{dc}-2R_{ON}}{L_{dc}} & \frac{-d_1 cos\left(\theta-\frac{\pi}{3}\right)+d_2 cos\left(\theta+\frac{\pi}{3}\right)}{L_{dc}} & \cdots \\ \frac{2\left[d_1 cos\left(\theta-\frac{\pi}{3}\right)-d_2 cos\left(\theta+\frac{\pi}{3}\right)\right]}{3C_{ac}} & 0 & \cdots \\ \frac{2\left[d_1 sin\left(\theta-\frac{\pi}{3}\right)-d_2 sin\left(\theta+\frac{\pi}{3}\right)\right]}{3C_{ac}} & \omega & \cdots \\ 0 & \frac{1}{2L_L} & \cdots \\ 0 & \frac{\sqrt{3}}{6L_L} & \cdots \end{bmatrix} \cdots$$

$$\cdots = \begin{bmatrix} \cdots & \frac{-d_1 sin\left(\theta-\frac{\pi}{3}\right)+d_2 sin\left(\theta+\frac{\pi}{3}\right)}{L_{dc}} & 0 & 0 \\ \cdots & -\omega & \frac{-1}{2C_{ac}} & \frac{-\sqrt{3}}{6C_{ac}} \\ \cdots & 0 & \frac{\sqrt{3}}{6C_{ac}} & \frac{-1}{2C_{ac}} \\ \cdots & \frac{-\sqrt{3}}{6L_L} & \frac{-R_L}{L_L} & -\omega \\ \cdots & \frac{1}{2L_L} & \omega & \frac{-R_L}{L_L} \end{bmatrix} \tag{A.15}$$

$$\overline{A}_{dqIII} = \begin{bmatrix} \frac{-R_{dc}-2R_{ON}}{L_{dc}} & \frac{d_1 cos\left(\theta+\frac{\pi}{3}\right)+d_2 cos(\theta)}{L_{dc}} & \frac{d_1 sin\left(\theta+\frac{\pi}{3}\right)+d_2 sin(\theta)}{L_{dc}} & 0 & 0 \\ \frac{-2\left[d_1 cos\left(\theta+\frac{\pi}{3}\right)-d_2 cos(\theta)\right]}{3C_{ac}} & 0 & -\omega & \frac{-1}{2C_{ac}} & \frac{-\sqrt{3}}{6C_{ac}} \\ \frac{-2\left[d_1 sin\left(\theta+\frac{\pi}{3}\right)-d_2 sin(\theta)\right]}{3C_{ac}} & \omega & 0 & \frac{\sqrt{3}}{6C_{ac}} & \frac{-1}{2C_{ac}} \\ 0 & \frac{1}{2L_L} & \frac{-\sqrt{3}}{6L_L} & \frac{-R_L}{L_L} & -\omega \\ 0 & \frac{\sqrt{3}}{6L_L} & \frac{1}{2L_L} & \omega & \frac{-R_L}{L_L} \end{bmatrix} \tag{A.16}$$

$$\overline{A}_{dqIV} = \begin{bmatrix} \frac{-R_{dc}-2R_{ON}}{L_{dc}} & \frac{d_1 cos(\theta)+d_2 cos\left(\theta-\frac{\pi}{3}\right)}{L_{dc}} & \frac{d_1 sin(\theta)+d_2 sin\left(\theta-\frac{\pi}{3}\right)}{L_{dc}} & 0 & 0 \\ \frac{-2\left[d_1 cos(\theta)-d_2 cos\left(\theta-\frac{\pi}{3}\right)\right]}{3C_{ac}} & 0 & -\omega & \frac{-1}{2C_{ac}} & \frac{-\sqrt{3}}{6C_{ac}} \\ \frac{-2\left[d_1 sin(\theta)-d_2 sin\left(\theta-\frac{\pi}{3}\right)\right]}{3C_{ac}} & \omega & 0 & \frac{\sqrt{3}}{6C_{ac}} & \frac{-1}{2C_{ac}} \\ 0 & \frac{1}{2L_L} & \frac{-\sqrt{3}}{6L_L} & \frac{-R_L}{L_L} & -\omega \\ 0 & \frac{\sqrt{3}}{6L_L} & \frac{1}{2L_L} & \omega & \frac{-R_L}{L_L} \end{bmatrix} \tag{A.17}$$

$$\overline{A}_{dqV} = \begin{bmatrix} \frac{-R_{dc}-2R_{ON}}{L_{dc}} & \frac{d_1 cos\left(\theta-\frac{\pi}{3}\right)-d_2 cos\left(\theta+\frac{\pi}{3}\right)}{L_{dc}} & \cdots \\ \frac{-2\left[d_1 cos\left(\theta-\frac{\pi}{3}\right)-d_2 cos\left(\theta+\frac{\pi}{3}\right)\right]}{3C_{ac}} & 0 & \cdots \\ \frac{-2\left[d_1 sin\left(\theta-\frac{\pi}{3}\right)-d_2 sin\left(\theta+\frac{\pi}{3}\right)\right]}{3C_{ac}} & \omega & \cdots \\ 0 & \frac{1}{2L_L} & \cdots \\ 0 & \frac{\sqrt{3}}{6L_L} & \cdots \end{bmatrix} \cdots$$

$$\cdots = \begin{bmatrix} \cdots & \frac{d_1 sin\left(\theta-\frac{\pi}{3}\right)-d_2 sin\left(\theta+\frac{\pi}{3}\right)}{L_{dc}} & 0 & 0 \\ \cdots & -\omega & \frac{-1}{2C_{ac}} & \frac{-\sqrt{3}}{6C_{ac}} \\ \cdots & 0 & \frac{\sqrt{3}}{6C_{ac}} & \frac{-1}{2C_{ac}} \\ \cdots & \frac{-\sqrt{3}}{6L_L} & \frac{-R_L}{L_L} & -\omega \\ \cdots & \frac{1}{2L_L} & \omega & \frac{-R_L}{L_L} \end{bmatrix} \tag{A.18}$$

$$\overline{A}_{dqVI} = \begin{bmatrix} \frac{-R_{dc}-2R_{ON}}{L_{dc}} & \frac{-d_1 cos\left(\theta+\frac{\pi}{3}\right)-d_2 cos(\theta)}{L_{dc}} & \frac{-d_1 sin\left(\theta+\frac{\pi}{3}\right)-d_2 sin(\theta)}{L_{dc}} & 0 & 0 \\ \frac{2\left[d_1 cos\left(\theta+\frac{\pi}{3}\right)+d_2 cos(\theta)\right]}{3C_{ac}} & 0 & -\omega & \frac{-1}{2C_{ac}} & \frac{-\sqrt{3}}{6C_{ac}} \\ \frac{2\left[d_1 sin\left(\theta+\frac{\pi}{3}\right)+d_2 sin(\theta)\right]}{3C_{ac}} & \omega & 0 & \frac{\sqrt{3}}{6C_{ac}} & \frac{-1}{2C_{ac}} \\ 0 & \frac{1}{2L_L} & \frac{-\sqrt{3}}{6L_L} & \frac{-R_L}{L_L} & -\omega \\ 0 & \frac{\sqrt{3}}{6L_L} & \frac{1}{2L_L} & \omega & \frac{-R_L}{L_L} \end{bmatrix} \tag{A.19}$$

The discharging duty ratios in the above equations are replaced using (4.2), (4.3), and (4.4). Assuming $\theta_f = \theta$, i.e. synchronously rotating frame of reference the averaged

system matrices for all sectors are obtained as follows

$$\overline{A}_{dq} = \overline{A}_{dqI} = \overline{A}_{dqII} = \ldots = \overline{A}_{dqVI} = \begin{bmatrix} \frac{-R_{dc}-2R_{ON}}{L_{dc}} & \frac{-\sqrt{3}m}{2L_{dc}} & 0 & 0 & 0 \\ \frac{\sqrt{3}m}{3C_{ac}} & 0 & -\omega & \frac{-1}{2C_{ac}} & \frac{-\sqrt{3}}{6C_{ac}} \\ 0 & \omega & 0 & \frac{\sqrt{3}}{6C_{ac}} & \frac{-1}{2C_{ac}} \\ 0 & \frac{1}{2L_L} & \frac{-\sqrt{3}}{6L_L} & \frac{-R_L}{L_L} & -\omega \\ 0 & \frac{\sqrt{3}}{6L_L} & \frac{1}{2L_L} & \omega & \frac{-R_L}{L_L} \end{bmatrix} \quad \text{(A.20)}$$

Grid-Tied System

The averaged state matrices for the six sectors are as follows:

$$\overline{A}_I = \begin{bmatrix} \frac{-R_{dc}-2R_{ON}}{L_{dc}} & \frac{-(d_1+d_2)}{L_{dc}} & \frac{-d_2}{L_{dc}} & 0 & 0 \\ \frac{2d_1+d_2}{3C_{ac}} & 0 & 0 & \frac{-1}{3C_{ac}} & \frac{1}{3C_{ac}} \\ \frac{-d_1+d_2}{3C_{ac}} & 0 & 0 & \frac{-1}{3C_{ac}} & \frac{-2}{3C_{ac}} \\ 0 & \frac{2}{3L_g} & \frac{1}{3L_g} & \frac{-R_L}{L_g} & 0 \\ 0 & \frac{-1}{3L_g} & \frac{1}{3L_g} & 0 & \frac{-R_L}{L_g} \end{bmatrix} \quad \text{(A.21)}$$

$$\overline{A}_{II} = \begin{bmatrix} \frac{-R_{dc}-2R_{ON}}{L_{dc}} & \frac{-d_1}{L_{dc}} & \frac{-(d_1+d_2)}{L_{dc}} & 0 & 0 \\ \frac{d_1-d_2}{3C_{ac}} & 0 & 0 & \frac{-1}{3C_{ac}} & \frac{1}{3C_{ac}} \\ \frac{d_1+2d_2}{3C_{ac}} & 0 & 0 & \frac{-1}{3C_{ac}} & \frac{-2}{3C_{ac}} \\ 0 & \frac{2}{3L_g} & \frac{1}{3L_g} & \frac{-R_g}{L_g} & 0 \\ 0 & \frac{-1}{3L_g} & \frac{1}{3L_g} & 0 & \frac{-R_L}{L_g} \end{bmatrix} \quad \text{(A.22)}$$

$$\overline{A}_{III} = \begin{bmatrix} \frac{-R_{dc}-2R_{ON}}{L_{dc}} & \frac{d_2}{L_{dc}} & \frac{-d_1}{L_{dc}} & 0 & 0 \\ \frac{-(d_1+2d_2)}{3C_{ac}} & 0 & 0 & \frac{-1}{3C_{ac}} & \frac{1}{3C_{ac}} \\ \frac{2d_1+d_2}{3C_{ac}} & 0 & 0 & \frac{-1}{3C_{ac}} & \frac{-2}{3C_{ac}} \\ 0 & \frac{2}{3L_g} & \frac{1}{3L_g} & \frac{-R_g}{L_g} & 0 \\ 0 & \frac{-1}{3L_g} & \frac{1}{3L_g} & 0 & \frac{-R_L}{L_g} \end{bmatrix} \tag{A.23}$$

$$\overline{A}_{IV} = \begin{bmatrix} \frac{-R_{dc}-2R_{ON}}{L_{dc}} & \frac{d_{1+}d_2}{L_{dc}} & \frac{d_2}{L_{dc}} & 0 & 0 \\ \frac{-(2d_1+d_2)}{3C_{ac}} & 0 & 0 & \frac{-1}{3C_{ac}} & \frac{1}{3C_{ac}} \\ \frac{d_1-d_2}{3C_{ac}} & 0 & 0 & \frac{-1}{3C_{ac}} & \frac{-2}{3C_{ac}} \\ 0 & \frac{2}{3L_g} & \frac{1}{3L_g} & \frac{-R_g}{L_g} & 0 \\ 0 & \frac{-1}{3L_g} & \frac{1}{3L_g} & 0 & \frac{-R_L}{L_g} \end{bmatrix} \tag{A.24}$$

$$\overline{A}_{V} = \begin{bmatrix} \frac{-R_{dc}-2R_{ON}}{L_{dc}} & \frac{d_1}{L_{dc}} & \frac{d_1+d_2}{L_{dc}} & 0 & 0 \\ \frac{-d_1+d_2}{3C_{ac}} & 0 & 0 & \frac{-1}{3C_{ac}} & \frac{1}{3C_{ac}} \\ \frac{-(d_1+2d_2)}{3C_{ac}} & 0 & 0 & \frac{-1}{3C_{ac}} & \frac{-2}{3C_{ac}} \\ 0 & \frac{2}{3L_g} & \frac{1}{3L_g} & \frac{-R_g}{L_g} & 0 \\ 0 & \frac{-1}{3L_g} & \frac{1}{3L_g} & 0 & \frac{-R_L}{L_g} \end{bmatrix} \tag{A.25}$$

$$\overline{A}_{VI} = \begin{bmatrix} \frac{-R_{dc}-2R_{ON}}{L_{dc}} & \frac{-d_2}{L_{dc}} & \frac{d_1}{L_{dc}} & 0 & 0 \\ \frac{d_1+2d_2}{3C_{ac}} & 0 & 0 & \frac{-1}{3C_{ac}} & \frac{1}{3C_{ac}} \\ \frac{-(2d_1+d_2)}{3C_{ac}} & 0 & 0 & \frac{-1}{3C_{ac}} & \frac{-2}{3C_{ac}} \\ 0 & \frac{2}{3L_g} & \frac{1}{3L_g} & \frac{-R_g}{L_g} & 0 \\ 0 & \frac{-1}{3L_g} & \frac{1}{3L_g} & 0 & \frac{-R_L}{L_g} \end{bmatrix} \tag{A.26}$$

and

$$\overline{B} = \begin{bmatrix} \frac{1}{L_{dc}} & 0 & 0 \\ 0 & 0 & 0 \\ 0 & 0 & 0 \\ 0 & \frac{-2}{3L_g} & \frac{-1}{3L_g} \\ 0 & \frac{1}{3L_g} & \frac{-1}{3L_g} \end{bmatrix} \tag{A.27}$$

It can be shown that these matrices have the same eigenvalues, which indicates that they are similar matrices. Equation (A.21)for Sector I can be re-written as

$$\begin{bmatrix} \frac{d}{dt}\widetilde{i}_{dc} \\ \frac{d}{dt}\widetilde{v}_{LL} \\ \frac{d}{dt}\widetilde{i}_{L} \end{bmatrix} = \begin{bmatrix} \overline{A}_{I(1,1)} & \overline{A}_{I(1,2)} & \overline{A}_{I(1,3)} \\ \overline{A}_{I(2,1)} & \overline{A}_{I(2,2)} & \overline{A}_{I(2,3)} \\ \overline{A}_{I(3,1)} & \overline{A}_{I(3,2)} & \overline{A}_{I(3,3)} \end{bmatrix} \begin{bmatrix} \widetilde{i}_{dc} \\ \widetilde{v}_{LL} \\ \widetilde{i}_{L} \end{bmatrix} + \begin{bmatrix} \overline{B}_{(1,1)} & \overline{B}_{(1,2)} \\ \overline{B}_{(2,1)} & \overline{B}_{(2,2)} \\ \overline{B}_{(3,1)} & \overline{B}_{(3,2)} \end{bmatrix} \begin{bmatrix} v_{dc} \\ v_{LL}^{g} \end{bmatrix} \tag{A.28}$$

where, $\overline{A}_{I(1,1)} = \frac{-R_{dc}}{L_{dc}}$, $\overline{A}_{I(1,2)} = \begin{bmatrix} \frac{-(d_1+d_2)}{L_{dc}} & \frac{-d_2}{L_{dc}} \end{bmatrix}$, $\overline{A}_{I(1,3)} = \begin{bmatrix} 0 & 0 \end{bmatrix}$, $\overline{A}_{I(2,1)} = \begin{bmatrix} \frac{2d_1+d_2}{3C_{ac}} \\ \frac{-d_1+d_2}{3C_{ac}} \end{bmatrix}$, $\overline{A}_{I(2,2)} = \begin{bmatrix} 0 & 0 \\ 0 & 0 \end{bmatrix}$, $\overline{A}_{I(2,3)} = \begin{bmatrix} \frac{-1}{3C_{ac}} & \frac{1}{3C_{ac}} \\ \frac{-1}{3C_{ac}} & \frac{-2}{3C_{ac}} \end{bmatrix}$, $\overline{A}_{I(3,1)} = \begin{bmatrix} 0 \\ 0 \end{bmatrix}$, $\overline{A}_{I(3,2)} = \begin{bmatrix} \frac{2}{3L_L} & \frac{1}{3L_L} \\ \frac{-1}{3L_L} & \frac{1}{3L_L} \end{bmatrix}$, $\overline{A}_{I(3,3)} = \begin{bmatrix} \frac{-R_L}{L_L} & 0 \\ 0 & \frac{-R_L}{L_L} \end{bmatrix}$, $\widetilde{v}_{LL} = \begin{bmatrix} \widetilde{v}_{ab} \\ \widetilde{v}_{bc} \end{bmatrix}$, $\widetilde{i}_{L} = \begin{bmatrix} \widetilde{i}_{a} \\ \widetilde{i}_{b} \end{bmatrix}$, $\overline{B}_{(1,1)} = \frac{1}{L_{dc}}$, $\overline{B}_{(1,2)} = 0$, $\overline{B}_{(2,1)} = \begin{bmatrix} 0 \\ 0 \end{bmatrix}$, $\overline{B}_{(2,2)} = \begin{bmatrix} 0 & 0 \\ 0 & 0 \end{bmatrix}$, $\overline{B}_{(3,1)} = \begin{bmatrix} 0 \\ 0 \end{bmatrix}$, $\overline{B}_{(2,2)} = \begin{bmatrix} \frac{-2}{3L_g} & \frac{-1}{3L_g} \\ \frac{1}{3L_g} & \frac{-1}{3L_g} \end{bmatrix}$.

Using equation (4.1)

$$\widetilde{v}_{LL} = M\widetilde{v}_{qd} \tag{A.29}$$

Accordingly, the derivative of $\widetilde{v}_{LL}$ with respect to time is obtained as:

$$\frac{d}{dt}\widetilde{v}_{LL} = \left(\frac{d}{dt}M\right)\widetilde{v}_{qd} + M\left(\frac{d}{dt}\right)\widetilde{v}_{qd} \tag{A.30}$$

Using the (A.28) and (A.29), one can write:

$$\frac{d}{dt}\widetilde{i}_{dc} = \overline{A}_{I(1,1)}\widetilde{i}_{dc} + \overline{A}_{I(1,2)}M\widetilde{v}_{qd} + \overline{B}_{(1,1)}v_{dc} \tag{A.31}$$

Using the second row of (A.28) and (A.30),

$$\left(\frac{d}{dt}M\right)\widetilde{v}_{qd} + M\left(\frac{d}{dt}\widetilde{v}_{qd}\right) = \overline{A}_{I(2,1)}\widetilde{i}_{dc} + \overline{A}_{I(2,3)}M\widetilde{i}_{qd} \tag{A.32}$$

Using (A.32), the derivative of $\widetilde{v}_{qd}$ with respect to time can be expressed as

$$\frac{d}{dt}\widetilde{v}_{qd} = M^{-1}\overline{A}_{I(2,1)}\widetilde{i}_{dc} + M^{-1}\overline{A}_{I(2,3)}M\widetilde{i}_{qd} - M^{-1}\frac{d}{dt}M\widetilde{v}_{qd} \tag{A.33}$$

Similarly, $\widetilde{i}_{qd}$ with respect to time can be expressed as

$$\frac{d}{dt}\widetilde{i}_{qd} = M^{-1}\overline{A}_{I(3,2)}M\widetilde{v}_{qd} + \left(M^{-1}\overline{A}_{I(3,3)}M - M^{-1}\frac{d}{dt}M\right)\widetilde{i}_{qd} - M^{-1}\overline{B}_{(3,2)}Mv^{g}_{qd} \tag{A.34}$$

Using (A.31) and (A.33), (A.28) can be expressed as

$$\frac{d}{dt}\begin{bmatrix} \widetilde{i}_{dc} \\ \widetilde{v}_{qd} \\ \widetilde{i}_{qd} \end{bmatrix} = \overline{A}_{dqI}\begin{bmatrix} \widetilde{i}_{dc} \\ \widetilde{v}_{qd} \\ \widetilde{i}_{qd} \end{bmatrix} + B\begin{bmatrix} v_{dc} \\ v^{g}_{qd} \end{bmatrix} \tag{A.35}$$

where,

$$\overline{A}_{dqI} = \begin{bmatrix} \frac{-R_{dc}-2R_{ON}}{L_{dc}} & \frac{-\left[d_1 cos\left(\theta_f\right)+d_2 cos\left(\theta_f-\frac{\pi}{3}\right)\right]}{L_{dc}} & \cdots \\ \frac{2\left[d_1 cos\left(\theta_f\right)+d_2 cos\left(\theta_f-\frac{\pi}{3}\right)\right]}{3C_{ac}} & 0 & \cdots \\ \frac{2\left[d_1 sin\left(\theta_f\right)+d_2 sin\left(\theta_f-\frac{\pi}{3}\right)\right]}{3C_{ac}} & \dot{\theta}_f & \cdots \\ 0 & \frac{1}{2L_g} & \cdots \\ 0 & \frac{\sqrt{3}}{6L_g} & \cdots \end{bmatrix} \cdots$$

$$\cdots = \begin{bmatrix} \cdots & \frac{-\left[d_1 sin\left(\theta_f\right)+d_2 sin\left(\theta_f-\frac{\pi}{3}\right)\right]}{L_{dc}} & 0 & 0 \\ \cdots & -\dot{\theta}_f & \frac{-1}{2C_{ac}} & \frac{-\sqrt{3}}{6C_{ac}} \\ \cdots & 0 & \frac{\sqrt{3}}{6C_{ac}} & \frac{-1}{2C_{ac}} \\ \cdots & \frac{-\sqrt{3}}{6L_g} & \frac{-R_g}{L_g} & -\dot{\theta}_f \\ \cdots & \frac{1}{2L_g} & \dot{\theta}_f & \frac{-R_g}{L_g} \end{bmatrix} \tag{A.36}$$

The averaged system matrices for other sectors in the dq-frame of reference can be obtained similarly. The averaged matrices in dq - frame of reference are presented as follows:

$$\overline{A}_{dqII} = \begin{bmatrix} \frac{-R_{dc}-2R_{ON}}{L_{dc}} & \frac{-d_1 cos\left(\theta_f-\frac{\pi}{3}\right)+d_2 cos\left(\theta_f+\frac{\pi}{3}\right)}{L_{dc}} & \cdots \\ \frac{2\left[d_1 cos\left(\theta_f-\frac{\pi}{3}\right)-d_2 cos\left(\theta_f+\frac{\pi}{3}\right)\right]}{3C_{ac}} & 0 & \cdots \\ \frac{2\left[d_1 sin\left(\theta_f-\frac{\pi}{3}\right)-d_2 sin\left(\theta_f+\frac{\pi}{3}\right)\right]}{3C_{ac}} & \dot{\theta}_f & \cdots \\ 0 & \frac{1}{2L_g} & \cdots \\ 0 & \frac{\sqrt{3}}{6L_g} & \cdots \end{bmatrix} \cdots$$

$$\ldots = \begin{bmatrix} \ldots & \frac{-d_1 sin\left(\theta_f - \frac{\pi}{3}\right) + d_2 sin\left(\theta_f + \frac{\pi}{3}\right)}{L_{dc}} & 0 & 0 \\ \ldots & -\dot{\theta}_f & \frac{-1}{2C_{ac}} & \frac{-\sqrt{3}}{6C_{ac}} \\ \ldots & 0 & \frac{\sqrt{3}}{6C_{ac}} & \frac{-1}{2C_{ac}} \\ \ldots & \frac{-\sqrt{3}}{6L_g} & \frac{-R_g}{L_g} & -\dot{\theta}_f \\ \ldots & \frac{1}{2L_g} & \dot{\theta}_f & \frac{-R_g}{L_g} \end{bmatrix} \tag{A.37}$$

$$\overline{A}_{dqIII} = \begin{bmatrix} \frac{-R_{dc} - 2R_{ON}}{L_{dc}} & \frac{d_1 cos\left(\theta_f + \frac{\pi}{3}\right) + d_2 cos\left(\theta_f\right)}{L_{dc}} & \frac{d_1 sin\left(\theta_f + \frac{\pi}{3}\right) + d_2 sin\left(\theta_f\right)}{L_{dc}} & 0 & 0 \\ \frac{-2\left[d_1 cos\left(\theta_f + \frac{\pi}{3}\right) - d_2 cos\left(\theta_f\right)\right]}{3C_{ac}} & 0 & -\dot{\theta}_f & \frac{-1}{2C_{ac}} & \frac{-\sqrt{3}}{6C_{ac}} \\ \frac{-2\left[d_1 sin\left(\theta_f + \frac{\pi}{3}\right) - d_2 sin\left(\theta_f\right)\right]}{3C_{ac}} & \dot{\theta}_f & 0 & \frac{\sqrt{3}}{6C_{ac}} & \frac{-1}{2C_{ac}} \\ 0 & \frac{1}{2L_g} & \frac{-\sqrt{3}}{6L_g} & \frac{-R_g}{L_g} & -\dot{\theta}_f \\ 0 & \frac{\sqrt{3}}{6L_g} & \frac{1}{2L_g} & \dot{\theta}_f & \frac{-R_g}{L_g} \end{bmatrix} \tag{A.38}$$

$$\overline{A}_{dqIV} = \begin{bmatrix} \frac{-R_{dc} - 2R_{ON}}{L_{dc}} & \frac{d_1 cos\left(\theta_f\right) + d_2 cos\left(\theta_f - \frac{\pi}{3}\right)}{L_{dc}} & \frac{d_1 sin\left(\theta_f\right) + d_2 sin\left(\theta_f - \frac{\pi}{3}\right)}{L_{dc}} & 0 & 0 \\ \frac{-2\left[d_1 cos\left(\theta_f\right) - d_2 cos\left(\theta_f - \frac{\pi}{3}\right)\right]}{3C_{ac}} & 0 & -\dot{\theta}_f & \frac{-1}{2C_{ac}} & \frac{-\sqrt{3}}{6C_{ac}} \\ \frac{-2\left[d_1 sin\left(\theta_f\right) - d_2 sin\left(\theta_f - \frac{\pi}{3}\right)\right]}{3C_{ac}} & \dot{\theta}_f & 0 & \frac{\sqrt{3}}{6C_{ac}} & \frac{-1}{2C_{ac}} \\ 0 & \frac{1}{2L_g} & \frac{-\sqrt{3}}{6L_g} & \frac{-R_g}{L_g} & -\dot{\theta}_f \\ 0 & \frac{\sqrt{3}}{6L_g} & \frac{1}{2L_g} & \dot{\theta}_f & \frac{-R_g}{L_g} \end{bmatrix} \tag{A.39}$$

$$\overline{A}_{dqV} = \begin{bmatrix} \frac{-R_{dc} - 2R_{ON}}{L_{dc}} & \frac{d_1 cos\left(\theta_f - \frac{\pi}{3}\right) - d_2 cos\left(\theta_f + \frac{\pi}{3}\right)}{L_{dc}} & \ldots \\ \frac{-2\left[d_1 cos\left(\theta_f - \frac{\pi}{3}\right) - d_2 cos\left(\theta_f + \frac{\pi}{3}\right)\right]}{3C_{ac}} & 0 & \ldots \\ \frac{-2\left[d_1 sin\left(\theta_f - \frac{\pi}{3}\right) - d_2 sin\left(\theta_f + \frac{\pi}{3}\right)\right]}{3C_{ac}} & \dot{\theta}_f & \ldots \\ 0 & \frac{1}{2L_g} & \ldots \\ 0 & \frac{\sqrt{3}}{6L_g} & \ldots \end{bmatrix} \ldots$$

$$\ldots = \begin{bmatrix} \ldots & \frac{d_1 sin\left(\theta_f - \frac{\pi}{3}\right) - d_2 sin\left(\theta_f + \frac{\pi}{3}\right)}{L_{dc}} & 0 & 0 \\ \ldots & -\dot{\theta}_f & \frac{-1}{2C_{ac}} & \frac{-\sqrt{3}}{6C_{ac}} \\ \ldots & 0 & \frac{\sqrt{3}}{6C_{ac}} & \frac{-1}{2C_{ac}} \\ \ldots & \frac{-\sqrt{3}}{6L_g} & \frac{-R_g}{L_g} & -\dot{\theta}_f \\ \ldots & \frac{1}{2L_g} & \dot{\theta}_f & \frac{-R_g}{L_g} \end{bmatrix} \tag{A.40}$$

$$\overline{A}_{dqVI} = \begin{bmatrix} \frac{-R_{dc} - 2R_{ON}}{L_{dc}} & \frac{-d_1 cos\left(\theta_f + \frac{\pi}{3}\right) - d_2 cos\left(\theta_f\right)}{L_{dc}} & \frac{-d_1 sin\left(\theta_f + \frac{\pi}{3}\right) - d_2 sin(\theta)}{L_{dc}} & 0 & 0 \\ \frac{2\left[d_1 cos\left(\theta_f + \frac{\pi}{3}\right) + d_2 cos\left(\theta_f\right)\right]}{3C_{ac}} & 0 & -\dot{\theta}_f & \frac{-1}{2C_{ac}} & \frac{-\sqrt{3}}{6C_{ac}} \\ \frac{2\left[d_1 sin\left(\theta_f + \frac{\pi}{3}\right) + d_2 sin\left(\theta_f\right)\right]}{3C_{ac}} & \dot{\theta}_f & 0 & \frac{\sqrt{3}}{6C_{ac}} & \frac{-1}{2C_{ac}} \\ 0 & \frac{1}{2L_g} & \frac{-\sqrt{3}}{6L_g} & \frac{-R_g}{L_g} & -\dot{\theta}_f \\ 0 & \frac{\sqrt{3}}{6L_g} & \frac{1}{2L_g} & \dot{\theta}_f & \frac{-R_g}{L_g} \end{bmatrix} \tag{A.41}$$

and

$$\overline{B} = \begin{bmatrix} \frac{1}{L_{dc}} & 0 & 0 \\ 0 & 0 & 0 \\ 0 & 0 & 0 \\ 0 & \frac{-2}{3L_g} & \frac{-1}{3L_g} \\ 0 & \frac{1}{3L_g} & \frac{-1}{3L_g} \end{bmatrix} \tag{A.42}$$

The discharging duty ratios in the above equations are replaced using (4.2), (4.3), and (4.4). Assuming $\theta_f - \theta = \phi$ and $\dot{\theta}_f = \omega_g$, i.e. synchronously rotating frame of reference

the averaged system matrices for all sectors are obtained as follows

$$\overline{A}_{dq} = \overline{A}_{dqI} = \overline{A}_{dqII} = ... = \overline{A}_{dqVI} = \begin{bmatrix} \frac{-R_{dc}-2R_{ON}}{L_{dc}} & \frac{-\sqrt{3}mcos\phi}{2L_{dc}} & \frac{-\sqrt{3}msin\phi}{2L_{dc}} & 0 & 0 \\ \frac{\sqrt{3}mcos\phi}{3C_{ac}} & 0 & -\omega_g & \frac{-1}{2C_{ac}} & \frac{-\sqrt{3}}{6C_{ac}} \\ \frac{\sqrt{3}msin\phi}{3C_{ac}} & \omega_g & 0 & \frac{\sqrt{3}}{6C_{ac}} & \frac{-1}{2C_{ac}} \\ 0 & \frac{1}{2L_g} & \frac{-\sqrt{3}}{6L_g} & \frac{-R_g}{L_g} & -\omega_g \\ 0 & \frac{\sqrt{3}}{6L_g} & \frac{1}{2L_g} & \omega_g & \frac{-R_g}{L_g} \end{bmatrix} \tag{A.43}$$

and the large signal model can be written as

$$\frac{d}{dt}\begin{bmatrix} \widetilde{i}_{dc} \\ \widetilde{v}_q \\ \widetilde{v}_d \\ \widetilde{i}_q \\ \widetilde{i}_d \end{bmatrix} = \begin{bmatrix} \frac{-R_{dc}}{L_{dc}} & \frac{-\sqrt{3}mcos(\phi)}{2L_{dc}} & \frac{-\sqrt{3}msin(\phi)}{2L_{dc}} & 0 & 0 \\ \frac{\sqrt{3}mcos(\phi)}{3C_{ac}} & 0 & -\omega_g & \frac{-1}{2C_{ac}} & \frac{-\sqrt{3}}{6C_{ac}} \\ \frac{\sqrt{3}msin(\phi)}{3C_{ac}} & \omega_g & 0 & \frac{\sqrt{3}}{6C_{ac}} & \frac{-1}{2C_{ac}} \\ 0 & \frac{1}{2L_g} & \frac{-\sqrt{3}}{6L_g} & \frac{-R_g}{L_g} & -\omega_g \\ 0 & \frac{\sqrt{3}}{6L_g} & \frac{1}{2L_g} & \omega_g & \frac{-R_g}{L_g} \end{bmatrix} \begin{bmatrix} \widetilde{i}_{dc} \\ \widetilde{v}_q \\ \widetilde{v}_d \\ \widetilde{i}_q \\ \widetilde{i}_d \end{bmatrix} + \dots$$

$$\dots + \begin{bmatrix} \frac{1}{L_{dc}} & 0 & 0 \\ 0 & 0 & 0 \\ 0 & 0 & 0 \\ 0 & -\frac{1}{2L_g} & \frac{\sqrt{3}}{6L_g} \\ 0 & -\frac{\sqrt{3}}{6L_g} & -\frac{1}{2L_g} \end{bmatrix} \begin{bmatrix} v_{dc} \\ v_q^g \\ v_d^g \end{bmatrix} \tag{A.44}$$

The large signal model presented in (A.44) has the modulation index, m and phase shift, ϕ as parameters in the state-space A matrix, while these are the parameters used for controlling the system. Equation (A.44) presents a time-invariant non-linear model of the grid connected three-phase boost - CSI. The linear, time-invariant dynamic model of the three-phase boost - CSI can be obtained by linearizing the model in (A.44). The following presents the linearzing of the large-signal model using the perturbation

technique.

Linearization of the I_{dc} equation:

$$\frac{d}{dt}\left(\widetilde{I}_{dc}+\delta\widetilde{i}_{dc}\right)=-\frac{R_{dc}}{L_{dc}}\left(\widetilde{I}_{dc}+\delta\widetilde{i}_{dc}\right)-\frac{\sqrt{3}\left(M+\delta m\right)cos\left(\phi+\delta\phi\right)}{2L_{dc}}\left(\widetilde{V}_{q}+\delta\widetilde{v}_{q}\right)-...$$

$$...\frac{\sqrt{3}\left(M+\delta m\right)sin\left(\phi+\delta\phi\right)}{2L_{dc}}\left(\widetilde{V}_{d}+\delta\widetilde{v}_{d}\right)+\frac{1}{L_{dc}}\left(\widetilde{V}_{dc}+\delta\widetilde{v}_{dc}\right)$$

which can be simplified as

$$\dot{\delta\widetilde{i}}_{dc}=-\frac{R_{dc}}{L_{dc}}\delta\widetilde{i}_{dc}-\frac{\sqrt{3}M}{2L_{dc}}cos\left(\phi+\delta\phi\right)\left(\widetilde{V}_{q}+\delta\widetilde{v}_{q}\right)-\frac{\sqrt{3}\delta m}{2L_{dc}}cos\left(\phi+\delta\phi\right)\left(\widetilde{V}_{q}+\delta\widetilde{v}_{q}\right)-...$$

$$...\frac{\sqrt{3}M}{2L_{dc}}sin\left(\phi+\delta\phi\right)\left(\widetilde{V}_{d}+\delta\widetilde{v}_{d}\right)-\frac{\sqrt{3}\delta m}{2L_{dc}}sin\left(\phi+\delta\phi\right)\left(\widetilde{V}_{d}+\delta\widetilde{v}_{d}\right)+\frac{1}{L_{dc}}\delta\widetilde{v}_{dc}$$

which results in

$$\dot{\delta\widetilde{i}}_{dc}=-\frac{R_{dc}}{L_{dc}}\delta\widetilde{i}_{dc}-\frac{\sqrt{3}Mcos\phi}{2L_{dc}}\delta\widetilde{v}_{q}-\frac{\sqrt{3}Msin\phi}{2L_{dc}}\delta\widetilde{v}_{d}+\frac{1}{L_{dc}}\delta\widetilde{v}_{dc}-\frac{\sqrt{3}}{2L_{dc}}\left(\widetilde{V}_{q}cos\phi+\widetilde{V}_{d}sin\phi\right)\delta m+...$$

$$...\frac{\sqrt{3}M}{2L_{dc}}\left(\widetilde{V}_{q}sin\phi+\widetilde{V}_{d}cos\phi\right)\delta\phi \tag{A.45}$$

Equation (A.45) presents the linearized dynamic equation for I_{dc}.

Linearization of the V_q equation:

$$\frac{d}{dt}\left(\widetilde{V}_{q}+\delta\widetilde{v}_{q}\right)=\frac{\sqrt{3}\left(M+\delta m\right)cos\left(\phi+\delta\phi\right)}{3C_{ac}}\left(\widetilde{I}_{dc}+\delta\widetilde{i}_{dc}\right)-\left(\Omega+\delta\omega\right)\left(\widetilde{V}_{d}+\delta\widetilde{v}_{d}\right)-...$$

$$...\frac{1}{2C_{ac}}\left(\widetilde{I}_q+\delta\widetilde{i}_q\right)-\frac{\sqrt{3}}{6C_{ac}}\left(\widetilde{I}_d+\delta\widetilde{i}_d\right)$$

which can be simplified as

$$\delta\dot{\widetilde{v}}_q=\frac{\sqrt{3}M}{3C_{ac}}cos\left(\phi+\delta\phi\right)\left(\widetilde{I}_{dc}+\delta\widetilde{i}_{dc}\right)+\frac{\sqrt{3}\delta m}{3C_{ac}}cos\left(\phi+\delta\phi\right)\left(\widetilde{I}_{dc}+\delta\widetilde{i}_{dc}\right)-\Omega\delta\widetilde{v}_d-\widetilde{V}_d\delta\omega-...$$

$$...\frac{1}{2C_{ac}}\delta\widetilde{i}_q-\frac{\sqrt{3}}{6C_{ac}}\delta\widetilde{i}_d$$

which can be re-written as

$$\delta\dot{\widetilde{v}}_q=\left(-\frac{\sqrt{3}M}{3C_{ac}}\widetilde{I}_{dc}sin\phi\right)\delta\phi+\left(\frac{\sqrt{3}M}{3C_{ac}}cos\phi\right)\delta\widetilde{i}_{dc}+\left(\frac{\sqrt{3}}{3C_{ac}}\widetilde{I}_{dc}cos\phi\right)\delta m-\frac{1}{2C_{ac}}\delta\widetilde{i}_q-...$$

$$...\frac{\sqrt{3}}{6C_{ac}}\delta\widetilde{i}_d-\Omega\delta\widetilde{v}_d-\widetilde{V}_d\delta\omega$$

which can be rearranged as

$$\delta\dot{\widetilde{v}}_q=\frac{\sqrt{3}M}{3C_{ac}}cos\phi\delta\widetilde{i}_{dc}-\Omega\delta\widetilde{v}_d-\frac{1}{2C_{ac}}\delta\widetilde{i}_q-\frac{\sqrt{3}}{6C_{ac}}\delta\widetilde{i}_d+\frac{\sqrt{3}}{3C_{ac}}\widetilde{I}_{dc}cos\phi\delta m-\frac{\sqrt{3}M}{3C_{ac}}\widetilde{I}_{dc}sin\phi\delta\phi-\widetilde{V}_d\delta\omega \tag{A.46}$$

Equation (A.46) provides the linearized dynamic equation for V_q.

Linearization of the V_d equation

$$\frac{d}{dt}\left(\widetilde{V}_d+\delta\widetilde{v}_d\right)=\frac{\sqrt{3}\left(M+\delta m\right)sin\left(\phi+\delta\phi\right)}{3C_{ac}}\left(\widetilde{I}_{dc}+\delta\widetilde{i}_{dc}\right)-\left(\Omega+\delta\omega\right)\left(\widetilde{V}_q+\delta\widetilde{v}_q\right)-...$$

$$...\frac{\sqrt{3}}{6C_{ac}}\left(\widetilde{I}_q+\delta\widetilde{i}_q\right)-\frac{1}{2C_{ac}}\left(\widetilde{I}_d+\delta\widetilde{i}_d\right)$$

which can be simplified as

$$\delta\dot{\widetilde{v}}_d = \frac{\sqrt{3}M}{3C_{ac}} sin\left(\phi + \delta\phi\right)\left(\widetilde{I}_{dc} + \delta\widetilde{i}_{dc}\right) + \frac{\sqrt{3}\delta m}{3C_{ac}} sin\left(\phi + \delta\phi\right)\left(\widetilde{I}_{dc} + \delta\widetilde{i}_{dc}\right) + \Omega\delta\widetilde{v}_q + \widetilde{V}_q\delta\omega + ...$$

$$... \frac{\sqrt{3}}{6C_{ac}}\delta\widetilde{i}_q - \frac{1}{2C_{ac}}\delta\widetilde{i}_d$$

which can be rewritten as

$$\delta\dot{\widetilde{v}}_d = \left(\frac{\sqrt{3}M}{3C_{ac}}\widetilde{I}_{dc}cos\phi\right)\delta\phi + \left(\frac{\sqrt{3}M}{3C_{ac}}sin\phi\right)\delta\widetilde{i}_{dc} + \left(\frac{\sqrt{3}}{3C_{ac}}\widetilde{I}_{dc}sin\phi\right)\delta m - \frac{1}{2C_{ac}}\delta\widetilde{i}_d + ...$$

$$... \frac{\sqrt{3}}{6C_{ac}}\delta\widetilde{i}_q + \Omega\delta\widetilde{v}_q + \widetilde{V}_q\delta\omega$$

on further rearrangement results in

$$\delta\dot{\widetilde{v}}_d = \frac{\sqrt{3}M}{3C_{ac}}sin\phi\delta\widetilde{i}_{dc} + \Omega\delta\widetilde{v}_d + \frac{\sqrt{3}}{6C_{ac}}\delta\widetilde{i}_q - \frac{1}{2C_{ac}}\delta\widetilde{i}_d + \frac{\sqrt{3}}{3C_{ac}}\widetilde{I}_{dc}sin\phi\delta m + \frac{\sqrt{3}M}{3C_{ac}}\widetilde{I}_{dc}cos\phi\delta\phi + \widetilde{V}_q\delta\omega \tag{A.47}$$

Equation (A.47) presents the linearized model for V_d.

Linearization of the $I_q$equation:

$$\frac{d}{dt}\left(\widetilde{I}_q + \delta\widetilde{i}_q\right) = \frac{1}{2L_g}\left(\widetilde{V}_q + \delta\widetilde{v}_q\right) - \frac{\sqrt{3}}{6L_g}\left(\widetilde{V}_d + \delta\widetilde{v}_d\right) - \frac{R_g}{L_g}\left(\widetilde{I}_q + \delta\widetilde{i}_q\right) - (\Omega + \delta\omega)\left(\widetilde{I}_d + \delta\widetilde{i}_d\right) - ...$$

$$... \frac{1}{2L_g}\left(V_q^g + \delta v_q^g\right) + \frac{\sqrt{3}}{6L_g}\left(V_d^g + \delta v_d^g\right)$$

which can be simplified as

$$\delta\dot{\widetilde{i}}_q = \frac{1}{2L_g}\delta\widetilde{v}_q - \frac{\sqrt{3}}{6L_g}\delta\widetilde{v}_d - \frac{R_g}{L_g}\delta\widetilde{i}_q - \Omega\delta\widetilde{i}_d - \widetilde{I}_d\delta\omega - \frac{1}{2L_g}\delta v_q^g + \frac{\sqrt{3}}{6L_g}\delta v_d^g$$

which can be rearranged as

$$\dot{\delta\widetilde{i}}_q = \frac{1}{2L_g}\delta\widetilde{v}_q - \frac{\sqrt{3}}{6L_g}\delta\widetilde{v}_d - \frac{R_g}{L_g}\delta\widetilde{i}_q - \Omega\delta\widetilde{i}_d - \frac{1}{2L_g}\delta v_q^g + \frac{\sqrt{3}}{6L_g}\delta v_d^g - \widetilde{I}_d\delta\omega \tag{A.48}$$

Equation (A.48) presents the linearized dynamic model for I_q.

Linearization if the I_d:

$$\frac{d}{dt}\left(\widetilde{I}_d + \delta\widetilde{i}_d\right) = \frac{\sqrt{3}}{6L_g}\left(\widetilde{V}_q + \delta\widetilde{v}_q\right) + \frac{1}{2L_g}\left(\widetilde{V}_d + \delta\widetilde{v}_d\right) + (\Omega + \delta\omega)\left(\widetilde{I}_q + \delta\widetilde{i}_q\right) - \frac{R_g}{L_g}\left(\widetilde{I}_d + \delta\widetilde{i}_d\right) - \ldots$$

$$\ldots\frac{\sqrt{3}}{6L_g}\left(V_q^g + \delta v_q^g\right) - \frac{1}{2L_g}\left(V_d^g + \delta v_d^g\right)$$

which can be simplified as

$$\dot{\delta\widetilde{i}}_d = \frac{1}{2L_g}\delta\widetilde{v}_d + \frac{\sqrt{3}}{6L_g}\delta\widetilde{v}_q - \frac{R_g}{L_g}\delta\widetilde{i}_d + \Omega\delta\widetilde{i}_q + \widetilde{I}_q\delta\omega - \frac{1}{2L_g}\delta v_d^g - \frac{\sqrt{3}}{6L_g}\delta v_q^g$$

which can be rearranged as

$$\dot{\delta\widetilde{i}}_d = \frac{\sqrt{3}}{6L_g}\delta\widetilde{v}_q + \frac{1}{2L_g}\delta\widetilde{v}_d + \Omega\delta\widetilde{i}_q - \frac{R_g}{L_g}\delta\widetilde{i}_d - \frac{\sqrt{3}}{6L_g}\delta v_q^g - \frac{1}{2L_g}\delta v_d^g - \widetilde{I}_q\delta\omega \tag{A.49}$$

Combining equations (A.45), (A.46), (A.47), (A.48), and (A.49) we get the linearized small signal dynamic model as follows

$$\frac{d}{dt}\begin{bmatrix} \delta\widetilde{i}_{dc} \\ \delta\widetilde{v}_q \\ \delta\widetilde{v}_d \\ \delta\widetilde{i}_q \\ \delta\widetilde{i}_d \end{bmatrix} = \begin{bmatrix} \frac{-R_{dc}}{L_{dc}} & \frac{-\sqrt{3}\widetilde{M}cos(\phi)}{2L_{dc}} & \frac{-\sqrt{3}\widetilde{M}sin(\phi)}{2L_{dc}} & 0 & 0 \\ \frac{\sqrt{3}\widetilde{M}cos(\phi)}{3C_{ac}} & 0 & -\omega_g & \frac{-1}{2C_{ac}} & \frac{-\sqrt{3}}{6C_{ac}} \\ \frac{\sqrt{3}\widetilde{M}sin(\phi)}{3C_{ac}} & \omega_g & 0 & \frac{\sqrt{3}}{6C_{ac}} & \frac{-1}{2C_{ac}} \\ 0 & \frac{1}{2L_g} & \frac{-\sqrt{3}}{6L_g} & \frac{-R_g}{L_g} & -\omega_g \\ 0 & \frac{\sqrt{3}}{6L_g} & \frac{1}{2L_g} & \omega_g & \frac{-R_g}{L_g} \end{bmatrix}\begin{bmatrix} \delta\widetilde{i}_{dc} \\ \delta\widetilde{v}_q \\ \delta\widetilde{v}_d \\ \delta\widetilde{i}_q \\ \delta\widetilde{i}_d \end{bmatrix} + \ldots$$

$$\ldots + \begin{bmatrix} \frac{1}{L_{dc}} & 0 & 0 & \frac{-\sqrt{3}\left[cos(\phi)\widetilde{V}_q + sin(\phi)\widetilde{V}_d\right]}{2L_{dc}} & \frac{-\sqrt{3}\widetilde{M}\left[sin(\phi)\widetilde{V}_q + cos(\phi)\widetilde{V}_d\right]}{2L_{dc}} & 0 \\ 0 & 0 & 0 & \frac{\sqrt{3}cos(\phi)\widetilde{I}_{dc}}{3C_{ac}} & \frac{-\sqrt{3}\widetilde{M}sin(\phi)\widetilde{I}_{dc}}{3C_{ac}} & -\widetilde{V}_d \\ 0 & 0 & 0 & \frac{\sqrt{3}sin(\phi)\widetilde{I}_{dc}}{3C_{ac}} & \frac{\sqrt{3}\widetilde{M}cos(\phi)\widetilde{I}_{dc}}{3C_{ac}} & \widetilde{V}_q \\ 0 & \frac{-1}{2L_g} & \frac{\sqrt{3}}{6L_g} & 0 & 0 & -\widetilde{I}_d \\ 0 & \frac{-\sqrt{3}}{6L_g} & \frac{-1}{2L_g} & 0 & 0 & \widetilde{I}_q \end{bmatrix} \begin{bmatrix} \delta v_{dc} \\ \delta v_q^g \\ \delta v_d^g \\ \delta m \\ \delta \phi \\ \delta \omega \end{bmatrix} \tag{A.50}$$

where, $\widetilde{I}_{dc}$, $\widetilde{V}_q$, $\widetilde{V}_d$, $\widetilde{I}_q$, and $\widetilde{I}_d$ represent the steady state operating point around which the system is linearized.

Appendix B

Developed Hardware

The circuit drawings along with rating of all the parts for the power and control board of the developed three-phase boost - CSI is presented in this Appendix. The drawings are presented supplemental files.